Final Report 2000-26

Research

Development Length of GFRP Reinforcement in Concrete Bridge Decks

Technical Report Documentation Page

1. Report No.	2.	3. Recipient's Accession No.
MN/RC – 2000-26		

4. Title and Subtitle	5. Report Date
DEVELOPMENT LENGTH OF GRFP REINFORCEMENT IN CONCRETE BRIDGE DECKS	July 2000
	6.

7. Author(s)	8. Performing Organization Report No.
Joe Hanus Carol Shield Catherine W. French	

9. Performing Organization Name and Address	10. Project/Task/Work Unit No.
University of Minnesota Department of Civil Engineering 122 CivE Bldg 500 Pillsbury Dr, SE Minneapolis, MN 55455-0220	11. Contract (C) or Grant (G) No. c) 74708 wo) 25

12. Sponsoring Organization Name and Address	13. Type of Report and Period Covered
Minnesota Department of Transportation 395 John Ireland Boulevard St. Paul, MN 55155	Final Report 1997-2000
	14. Sponsoring Agency Code

15. Supplementary Notes

16. Abstract (Limit: 200 words)

This report summarizes an experimental program that investigated the development length and variability in bond of glass-fiber-reinforced-polymer (GFRP) reinforcement in concrete. The variables in the study were manufacturer (Marshall Industries Composites, Inc. [M1] and Corrosion Proof Products/Hughes Brothers [M2], bar size (No. 5 and 6), cover (2 and 3 bar diameters), and embedment length (10 through 47 inc.). Eighty-four inverted half-beam bond specimens were tested while monitoring load, loaded-end slip, free-end slip, cracking, and acoustic emissions on the embedded bar and concrete.

Neither bar was recommended for immediate use as a reinforcement in bridge decks. The M1 rebar exhibited cracking and splitting along the outer coating of the bar, which damaged bar deformations. Additionally, these bars exhibited larger COVs for bar failures with average ultimate loads below the reported manufacturer's value. The M2 rebar exhibited a smaller COV for tensile test bar failures and a similar ultimate load average when compared to the manufacturer's reported strength. However, both GFRP rebar had 47.0 in. embedment length bond tests, which exhibited bar failures with ultimate loads less than the tensile test average minus two standard deviations.

17. Document Analysis/Descriptors	18. Availability Statement
Bond, GFRP Rebar, Bridge Decks	

19. Security Class (this report)	20. Security Class (this page)	21. No. of Pages	22. Price
Unclassified	Unclassified	371	

Development Length of GFRP Reinforcement in Concrete Bridge Decks

Final Report

Prepared by

Joe P. Hanus
Carol K. Shield
Catherine W. French

Department of Civil Engineering
University of Minnesota

July 2000

Published by

Minnesota Department of Transportation
Office of Research Services
First Floor
395 John Ireland Boulevard, Mail Stop 330
St. Paul, Minnesota 55155

ACKNOWLEDGMENTS

Funding for this project was provided by the Minnesota Department of Transportation. The authors wish to express their appreciation for the generous material donations provided by Rebarfab, Inc., Tilco Company, International Grating, Inc., Corrosion Proof Products/Hughes Brothers, Marshall Industries Composites, Inc., and Pultrall Inc.

TABLE OF CONTENTS

Appendix E: Crack Patterns
Appendix F: AE Figures

LIST OF TABLES

LIST OF FIGURES

EXECUTIVE SUMMARY

This report summarizes an experimental program that investigated the bond variability of glass-fiber-reinforced-polymer (GFRP) reinforcement in concrete. The variables in the study were manufacturer (Marshall Industries Composites, Inc. [M1] and Corrosion Proof Products/Hughes Brothers [M2]), bar size (No. 5 and 6), cover (2 and 3 bar diameters), and embedment length (10 through 47 in.). Tensile tests were also performed on the GFRP rebar for comparison to bond tests that exhibited bar failure.

Eighty-four inverted half-beam bond specimens were tested while monitoring load, loaded-end slip, free-end slip, cracking, and acoustic emissions on the embedded bar and concrete. Three to six replicate tests were conducted for each set of variables. The results of each test within a series were examined to investigate the relative variability with respect to the failure types.

The M1 rebar was observed to rely primarily on mechanical interlock to develop bond strength. This conclusion was based on investigations of the rebar surface condition, bar deformation geometry, slip curves, Acoustic Emission (AE) results, crack patterns and forensic investigations. Additionally, the ultimate loads for the bond tests with the M1 rebar were affected by changes in embedment lengths but did not vary for tests with 2 and $3d_b$ cover. The cover may not have had an influence because the majority of the tests failed with ultimate loads within two standard deviations of the tensile test average. A 15.0 in. development length was selected for these bars embedded with 2 or $3d_b$ cover. The corresponding $1/K_1$ value for this development length was 15.9. Overall the M1 rebar had coefficients of variation (COV) of 14.3 and 8.9% for bond tests that exhibited bar failure and tensile test bar failures, respectively. The bond tests that failed in concrete splitting had COVs from 5.2 to 5.9%.

The M2 rebar was observed to rely primarily on adhesion and friction to develop bond strength. This conclusion was based on investigations of the rebar surface condition, bar deformation geometry, slip curves, AE results, crack patterns and forensic investigations. Additionally, the ultimate loads for the bond tests with the M2 rebar were affected by changes in embedment lengths but did not vary for tests with 2 and $3d_b$ cover. A development length was determined by conducting a linear regression through the concrete splitting failures to the tensile test average and reported manufacturer's tensile strength (43.5 kips). The resulting development length was 31.5 in. with a corresponding $1/K_1$ value of 17.2. Overall the M2 rebar had a coefficient of variation (COV) of 2.9% for the tensile test bar failures and only one bond test exhibited a bar failure not within the grip system. The bond tests that failed in concrete splitting had COVs from 3.2 to 13.1%.

Neither bar was recommended for immediate use as reinforcement in bridge decks. The M1 rebar exhibited cracking and splitting along the outer coating of the bar which damaged bar deformations. Additionally these bars exhibited larger COVs for bar failures with average ultimate loads below the reported manufacturer's value. The M2 rebar exhibited a smaller COV for tensile test bar failures and a similar ultimate load average when compared to the manufacturer's reported strength. However, both GFRP rebar had 47.0 in. embedment length bond tests which exhibited bar failures with ultimate loads less than the tensile test average minus two standard deviations.

Chapter 1: Introduction

1.1 General

1.1.1 Corrosion Problem with Bridge Decks

The deterioration of reinforced concrete structures by corrosion of the steel reinforcement is a trillion dollar problem in the United States [1]. The corrosion is caused by chloride ions, which can be found in de-icing salts in northern climates and sea water along coastal areas. The primary concern is when corrosion reduces the reinforcement effective cross section and endangers the integrity of the structure. Additionally the products of corrosion take up more volume than the original material causing cracking, spalling and delamination of the concrete cover, which can also put the structure at risk [2].

1.1.2 Solutions to the Corrosion Problem

There are generally two methods to fighting the corrosion problem. The first method is protecting the steel reinforcement from corrosion. The most common protection method is epoxy coating the reinforcement which is frequently used in bridges and parking garages. Unfortunately there have been discoveries of premature corrosion of epoxy-coated rebar that have led engineers to search for other solutions [3]. Other methods of preventing corrosion include increased cover, zinc rebar coatings, polymer-modified cementious rebar coatings, zinc epoxy primers, cathodic protection and the use of corrosion-inhibiting admixtures in the concrete [2]. These methods have had varying success.

The second method of fighting corrosion is to use corrosion resistant reinforcement such as fiber-reinforced-polymer (FRP). Although currently more expensive than steel reinforcement, FRP rebar is quickly becoming a viable alternative.

1.2 Background on FRP Reinforcement

Fiber-reinforced-polymers are a manufactured material that can be designed for specific characteristics required by the engineer. FRP products are common in recreational equipment, such as fishing poles, skis, water craft, and in the military, products range from helmets to fighters. However, use of FRP products in the infrastructure has been limited because of their relative cost. Recently there has been an increasing interest in the use of FRP reinforcement in bridges and improved manufacturing technology has reduced FRP production costs. As a result,

these products have become an economical and advantageous alternative to steel reinforcement in corrosive environments.

There is a wide variety of currently available FRP reinforcement systems, including ropes for prestressing applications, grids for slab reinforcement and rods for conventionally reinforced members. The systems are assembled from the basic FRP bars made from commercially available fibers, such as carbon, aramid and glass. The bars are formed through a pultrusion process that pulls continuous fibers through a resin bath into a forming/curing die to form a generally smooth composite rod.

Glass-fiber-reinforced-polymer (GFRP) rebar is the least expensive of the three FRPs listed above and represent the most likely alternative to bridge deck reinforcement. A sample of five different GFRP reinforcing bars is shown in Figure 1.1 and are, top to bottom, from the following companies:

1) Tilco Company, Marshall, Arizona,
2) International Grating, Inc., Houston, Texas,
3) Corrosion Proof Products/Hughes Brothers, Tequesta, Florida,
4) Marshall Industries Composites, Inc., Jacksonville, Florida,
5) Pultrall Inc., Thetford Mines, Quebec.

The above bars have similar material compositions but significantly different surface deformation systems. External deformation systems can be formed from a variety of methods, but are generally one of the following three types.

1) Type 1, molded/cast bar deformations,
2) Type 2, exterior wound fibers that impress into the rods,
3) Type 3, exterior wound fibers that do not impress into the rods.

The Type 1 deformation system is currently available from only one GFRP rebar manufacturer, Marshall Industries Composites, Inc. Bars from this manufacturer are 70% (weight) E-glass fibers in a 10% recycled resin material. The bar deformations are formed from 3.5% ceramic fibers embedded in a 15% Urethane modified vinyl ester matrix and 1.5% corrosion inhibitor. The ceramic layer is added with a continuous molding process that creates the bar deformations which look similar to deformed steel rebar with significant rib face angle.

The Type 2 deformation system is available from many different GFRP manufacturers, including Tilco Company, International Grating, Inc., and Corrosion Products/Hughes Brothers.

The bar deformations are formed from tightly wound fibers that cause the bar to bulge between the wraps. The resulting rib face angles are less than typically observed in deformed steel rebar. In some cases, the bars may have additional sand grains or other particles attached for increased friction, as seen with the Tilco and Corrosion Proof Products/Hughes Brother bars. The GFRP rebar from International Grating included a light resin coat over the freshly deformed surface to provide additional protection to the wrapped fibers.

The Type 3 deformation system is also commonly available from GFRP manufacturers, including Pultrall Inc. This deformation system is similar to Type 2, but the exterior wound fibers do not impress into the bar. The wound fibers are the actual bar deformations attached to the bar surface. The Pultrall GFRP rebar also has attached particles with an overlaid resin material. The attached particles increase friction and the final resin layer provides additional protection to the deformation wraps.

Overall, GFRP reinforcement has significant advantages over normal steel reinforcement: high strength to weight ratio (10 to 15 times steel), excellent corrosion resistance, and excellent electromagnetic neutrality [4]. However, the disadvantages need to be carefully considered: questionable fatigue characteristics, higher cost (five times steel), low modulus of elasticity (resulting in excessive deflections), low failure strain, long-term strength that can be lower than short-term static strength, and unknown durability in concrete due to the alkali-silica reaction [4]. Additionally, there is a lack of manufacturing and testing standards for GFRP rebar. Its performance as a reinforcement is not sufficiently understood to warrant unconditional use in the infrastructure. Extensive research is required to understand its strengths and weaknesses. The benefit of this new material is the possible savings of billions of dollars in costly corrosion problems.

1.3 Background on Bond Mechanics

Reinforced concrete is a composite material that utilizes the compressive strength of concrete and the tensile strength of the reinforcement. An effective bond between concrete and reinforcement is critical in developing the composite action.

1.3.1 Bond Components

Reinforcement bonds with concrete through a complicated mechanism which can be influenced by many factors, including: 1) reinforcement properties (e.g. strength, surface

condition, modulus of elasticity [MOE], and Poisson's ratio), 2) concrete properties (e.g. compression and tensile strength, MOE, and Poisson's ratio), 3) confinement (e.g. concrete cover and additional reinforcement), 4) type of loading, and 5) time dependent effects [5].

There are typically three main components of the bonding mechanism: chemical adhesion, mechanical interlock and friction. The influence of each component on the ultimate bond strength varies with different types of reinforcement. Adhesion depends on the reinforcement material and its chemical reaction to concrete. Mechanical interlocking is related to the reinforcement geometry and surface deformations. Friction develops from surface roughness and its magnitude is related to the normal force acting on the plane of movement. Although the three main bond components are readily accepted as single elements, they interact and are difficult to separate when analyzing bond.

1.3.2 Measuring Bond

Quantitative measures of bond are typically determined in a global sense because of the difficulty in measuring the nonlinear distribution of bond stress along the bar. The nonlinearity of bond between reinforcement and concrete has been investigated by several researchers. Examples include **Grundhoffer's** [6] investigation of coated and uncoated steel rebar and **Benmokrane et al.** [7] and **Larralde's** [8] GFRP and steel rebar tests. In these studies, the bond stress was calculated from strain measured with gages inserted into steel rebar or mounted on GFRP rebar. Grundhoffer concluded that epoxy-coated rebar had different strain distributions than uncoated bars at low stress and near failure; the epoxy-coated rebar distributed the strain along greater lengths than the uncoated bars. Benmokrane concluded that GFRP rebar had a nonlinear distribution of bond stresses along the embedment length similar to uncoated steel rebar. Larralde found similar results in his tests with a maximum stress peak that shifted along the embedment length during loading. However, the strain gages mounted on the GFRP rebar may have influenced the bond stress distribution.

The most common approach to measuring bond is simply recording the ultimate load achieved during the bond test and then using this load to determine an ultimate bond strength. This value provides the ultimate bond strength from which one can determine bond stress in an average sense, but does not provide insight into the actual bond stress distribution nor the debonding process.

Some insight into the debonding process can be gained through slip measurements, which have been described in several ASTM test procedures [9, 10]. Slip is the relative movement between the reinforcement and the concrete, which results from material deformation (strain) and bond component failures. Slip is usually measured at the loaded end (LES) and the free end (FES) of the reinforcement. The LES includes the slip movement and bar elongation within the embedment length, which cannot be easily separated; measurement of LES does not include bar elongation outside the embedment length. FES provides a clearer indication of pure reinforcement movement, but does not reflect the nonlinearity of the bond along the embedment length early in loading.

Other non-destructive techniques can be used to evaluate and qualify the bond of rebar. These methods include vibration analysis, radar and acoustic emissions (AE).

1.3.3 Bond Equations

Various bond equations are available to describe and analyze a particular reinforcement bond mechanism. The simplest bond equation calculates an average bond stress (σ) from the test ultimate load. For a nominal round rebar,

$$\sigma = \frac{P_{ult}}{l \, \phi \, d_b}, \tag{1.1}$$

where σ is the average bond stress, P_{ult} is the test ultimate load, l is the embedment length, and d_b is the nominal reinforcement bar diameter.

From Eqn. (1.1) the reinforcement development length can be established as a function of the concrete and reinforcement properties. The development length is determined as the minimum length required to fully develop the reinforcement design tensile stress.

There is a significant difference between steel and GFRP reinforcement in terms of design tensile stress. Steel reinforcement development length equations are based on a design tensile stress at yield, f_y. Comparatively, GFRP reinforcement does not have a yield plateau, rather the behavior is typically linear elastic to failure. Consequently, the development length for use in design will be some portion of the GFRP ultimate strength, f_u. However, for the theoretical discussion of the development length equations, the GFRP reinforcement will use the ultimate strength term, f_u, substituted for the steel yield stress term, f_y. Finally, the development

length, as a function of the average bond stress, can be determined by setting the bond strength equal to the reinforcement design tensile strength in the following relationship,

$$\sigma \phi d_b l_d = A_b f_u, \tag{1.2}$$

where l_d is development length, A_b is the reinforcement bar area, $f_u$is the reinforcement design tensile strength.

Solving for the development length from Eqn. (1.2) with gives,

$$l_d \mid \frac{f_u A_b}{\sigma \phi d_b} \tag{1.3}$$

Empirical constants have been developed to replace the average bond stress in the development equation, Eqn. (1.3), and are ideally derived from tests of bars embedded at or near their development length. Additional development length equations with these empirical constants have been previously used in the American Concrete Institute (ACI) 318 Building Code [11] and are currently recommended by the ACI Committee 440 in the FRP Reinforcement State of the Art Report [5].

$$l_d \mid K_1 \frac{f_u A_b}{\sqrt{f'_c}}, \tag{1.4}$$

where K_1 is an empirical constant, f'_c is the concrete compressive strength.

The empirical constant, K_1, accounts for factors such as surface condition, confinement and bar properties, and can be calculated from Eqn. (1.4),

$$\frac{1}{K_1} \mid \frac{P_{ult}}{l_d \sqrt{f'_c}} \tag{1.5}$$

The constant $1/K_1$ is based upon the development length of a particular reinforcement and is valid for tests with embedment lengths close to the development length. When $1/K_1$ is calculated for a test with a much shorter embedment length relative to the development length, it will be erroneously large, because of the nonlinear distribution of bond stress. Conversely, if $1/K_1$ is calculated for a test with a much greater embedment than the development length (typically resulting in a bar tensile failure), the value for $1/K_1$ will be too small. However, Eqn. (1.5) is frequently referenced for GFRP rebar tests as a starting point for analysis and such results must be qualified when comparing $1/K_1$ values.

In addition to the previously discussed embedment length sensitivity for Eqn. (1.5), the equation also lacks individual consideration for reinforcement location, coating, size, lightweight

concrete, spacing or cover dimensions and transverse reinforcement. These factors are all inherent to the ultimate load, P_u, from which the empirical constant $1/K_1$ is derived. These factors have been separately accounted for in the 1995 ACI code equation (12-1) for steel reinforcement [11], which was based on research by **Orangun et al** [12],

$$\frac{l_d}{d_b} = \frac{3}{40}\frac{f_y}{\sqrt{f'_c}}\frac{\zeta\eta\nu\varsigma}{\left(\frac{c}{d_b} + \frac{K_{tr}}{d_b}\right)} \qquad (1.6)$$

where f_y is the steel reinforcement yield strength, ζ is the reinforcement factor, η is the coating factor, ν is the reinforcement size factor, ς is the lightweight concrete factor, c is the spacing or cover dimensions (inches), and K_{tr} is the transverse reinforcement index.

Equation (1.6) accounts for many of the factors that influence the bond components. Comparatively, for GFRP, Eqn. (1.5) does not account for these factors with its overall empirical constant, K_1. This constant is determined from bond tests, which can vary extensively and are outlined in the next section.

1.3.4 Bond Tests

There are many different types of tests for investigating bond and determining development lengths. Typically a test bar is embedded a desired length in a concrete specimen with the portion to be unbonded enclosed within PVC pipe or similar tubing to shield the reinforcement. Load, slip and strain measurements are typically recorded with attached instrumentation. The primary difference in the type of bond tests is the stress condition of the concrete specimen under loading.

Pullout tests, as shown in Fig. 1.2, require little material and have been used frequently to establish basic bond parameters. In these tests a bar is embedded in a concrete specimen, usually a standard concrete test cylinder. The specimen with bar is placed in a load frame that holds the specimen in place on the loaded end while the bar is pulled out. Although this type of test is economical and easily done, it places the concrete around the bar in compression, rather than tension which is usually the case for flexural members. Some researchers believe the tests can result in calculated bond strength that may be unconservative [3] and significantly different from a more realistic test where the concrete around the bar is in tension [13, 14].

A variation on the pullout test is the T-beam test that creates tension stress in the concrete around the rebar without using an entire beam. The T-beam, as shown in Fig. 1.3, moves the reaction forces, that would be on top of the specimen in the pullout bond test, down the specimen to create a tension zone in the concrete along the embedded test bar. Although more realistic than pullout tests, this test is not as desirable as a reinforcing bar in a beam under flexural loading, because there is no curvature in the specimen.

A number of variations of a simply-supported beam in four point bending provide realistic bond tests for rebar in tension. The notch beam bond test, as shown in Fig. 1.4, contains notches in the bottom tension face of the beam to isolate the test bar in the center constant moment region and to provide a place for slip instrumentation. Another variation is the splice beam bond test, as shown in Fig. 1.5, which includes splices of the test bar between the load points in the constant moment region. Finally, the hinge beam bond test, as shown in Fig. 1.6, consists of two separate rectangular beams connected at the top with a hinge mechanism and at the bottom with a longitudinal test bar.

A compromise between material usage and realistic stress development is the inverted half-beam test, as shown in Fig. 1.7, also refereed to as a beam-end test. This test, as the name implies, represents half of a simply-supported beam. The setup places the test bar in a concrete tension field with half the material required for a full length beam. The test procedure is established in ASTM A944: "Comparing Bond Strength of Steel Reinforcing Bars to Concrete Using Beam-End Specimen" [15].

1.3.5 Bond Failure Types

There are four types of failures that can occur in a bond test, and they are related to the confinement provided by the concrete cover or transverse reinforcement and the previously discussed bond components:

1) bar failure,
2) bar pullout,
3) concrete pullout,
4) concrete splitting.

As an embedded test rebar is pulled in tension, its bond mechanism will engage to prevent the bar from being pulled out of the concrete. With an adequate combination of

confinement and embedment length, a test bar will fail in tension at some point along its length before bond failure. Development of the full tensile strength of the bar during bond tests provides limited information on the required bar development length. This failure simply indicates that the upper limit of the reinforcement bonding mechanism has been exceeded. To determine the development length, which is the minimum length to reach the bar design strength, less confinement or embedment length are required to force one of the other three failures.

A bar pullout failure will occur if the confinement is sufficient, yet the bond strength cannot resist the load on the test bar. With this failure, there may be damage to the bar or concrete as the test bar slips through the concrete. A concrete pullout failure will occur if the bond strength is sufficient around the immediate area of the test bar, but the subsequent area of concrete is weak. The test bar pulls out of the concrete specimen with a cone of concrete attached to the bar.

The fourth type of failure, concrete splitting, will occur when there is successful bonding to the local concrete that causes cracking around the test bar. As the bar is loaded these cracks propagate to the surface and eventually there is sufficient cracking to release the embedded bar from the concrete.

1.4 Steel Rebar Bond Tests

A short review of some commonly referenced steel reinforcement bond research will provide a basis of general bond mechanics before GFRP research is reviewed. Highlighted in this section are references on epoxy-coated rebar which may have similar bond properties as GFRP rebar. Epoxy coated bars have a smoother surface than steel and the bar deformations are less defined due to the epoxy coating, which are similar to bar characteristics of GFPR rebar.

The current ACI development length equation, Eqn. (1.6), is based on a study by **Orangun et al.** [12] who investigated 62 splice beam bond tests. The authors conducted a nonlinear regression analysis on the data to develop the current equation. Their analysis accounted for the effects of length, cover, spacing, bar diameter, concrete strength, transverse reinforcement, and moment gradient on the strength of the lap splices. Additionally, they found the resulting equation to be valid for both splice and development length of reinforcement in concrete.

Lutz and Gergely at Cornell University [16] examined the bond mechanism of deformed steel bars in concrete based on results of pullout tests with different variables. They focused on the failure progression of bond with its initiation due to the difference between the concrete and steel axial strain. This difference in strain/elongation along the embedment length results in bar debonding and slipping. The initial bond resistance results from adhesion. Under low load the adhesion is broken and the bar begins to slip. This slip is resisted by mechanical interlocking of the deformation system on the bar surface. If the rib face angle is greater than 40 degrees, the concrete will crush under bearing of the deformations. Conversely, if the rib face angles were flatter, less than 30 degrees, the bar deformations will wedge between the concrete. Bars with shallower bar deformations will depend more on friction for continued resistance.

Failure progression can be further analyzed by considering slip versus load graphs for bond tests. These graphs provide a graphical description of the bond stiffness for a particular reinforcement. A slip criterion that is frequently referenced was developed by **Mathey and Watstein** with the National Bureau of Standards [13]. They conducted 18 notch beam and 18 pullout bond tests with high yield strength (100 ksi) deformed steel bar reinforcement. Two bar sizes, No. 4 and No. 8, were embedded at various lengths with 3.5 and 1.5 bar diameter covers, respectively. Additional steel longitudinal and shear reinforcement was used, and the beams were instrumented with dial gages on the ends to record FES and in notches to record LES.

Upon review of their LES and FES graphs, a common point of significant slope change at an LES of 0.01 in. and FES of 0.002 in. was identified. The authors recommended that bond stress associated with the lower of these slip values be identified as the "critical bond stress," essentially the design limit to prevent ultimate bond failure. The authors also considered the effect of different embedment lengths in their analysis and made another conclusion. They found that the loaded-end slip, at the points of significant slope change, were independent of the embedment lengths for a given bar size. The "critical bond stress" and the lack of embedment length effect on the LES limit have been investigated and validated by other researchers. In general, the "critical bond stress" limiting criterion of LES = 0.01 in. or FES = 0.002 in. is the standard for slip curve analysis of steel rebar bond.

Another investigation that closely examined slip graphs was **Johnston and Zia** at North Carolina State University at Raleigh [17]. They conducted 40 inverted half-beam bond tests with No. 6 and No.11 deformed steel rebar at various embedment lengths with clear concrete

cover of 1 in. The bars were normal mill scale, blast cleaned, or epoxy-coated. The specimen were reinforced with additional longitudinal steel and stirrups, and were instrumented with dial gages for recording FES and LES.

In reviewing the load versus slip behavior, they identified three phases in the bond failure for all types of bars. The first phase, below 10 to 20 ksi bar stress, had a low initial LES rate that gradually increased. This initial resistance was due to adhesion. The second phase, above 10 to 20 ksi bar stress, had linearly increasing LES with respect to the bar stress. Resistance was assumed to be provided by adhesion and mechanical interlock. The final phase was identified with a significant increase in LES related to splitting or reinforcement yielding. The No. 6 blast cleaned specimen had LES and FES between the normal mill and epoxy-coated rebar. However, No.11 blast cleaned specimen had less slip than the others up to 30 ksi bar stress and then had slightly more slip. The epoxy-coated specimen had generally greater slips at the peak load than the normal mil specimen. Overall, the authors concluded that the epoxy-coated bars had less slip resistance, but did not discuss the lack of any particular bond component.

An extensive epoxy-coated rebar investigation was conducted by **Grundhoffer** at the University of Minnesota [6]. Ninety-six inverted half-beam specimen with epoxy-coated and uncoated reinforcement were tested. Three bar sizes, No. 6, 8, and 11, were embedded at various lengths with two bar diameter covers. The specimen were additionally reinforced with open stirrups and auxiliary longitudinal reinforcement. The purpose of this reinforcement was to prevent specimen shear or flexural failure while not over-confining the test bar with the open stirrups. Six different concrete strengths were used in the investigation, ranging from 6650 psi to 13980 psi. Instrumentation for the tests included embedded strain gages in the reinforcement for analyzing strain distribution and LVDTs to measure LES and FES.

Based on the given data and sufficiently long embedment lengths, $1/K_1$ values were calculated for No. 6 coated and uncoated steel rebar: $1/K_{coated} = 32.8$ and $1/K_{uncoated} = 34.5$. These values are included in Table 1.1 which lists various researchers and their $1/K_1$ results for bond tests on deformed steel rebar with specific variables: type of bond test, confinement reinforcement, rebar size, and amount of cover.

Based on the slip graphs, the author noticed several differences with the epoxy-coated rebar. The load at first crack for each specimen was compared to the FES graphs and a difference between the coated and uncoated rebar was identified. After initial cracking, the

coated rebar had an increasing rate of FES, possibly due to the lack of adhesion and friction resistance. In comparison, the uncoated rebar continued at the same rate of FES; this was attributed to good friction resistance after splitting. Another difference was seen in the LES graphs when a secant stiffness analysis was done on the data. An LES of 0.004 in. was selected as the common transition point for all the tests and the LES rate of change before and after this point were measured. The transition point was defined as the point on the slip curve where there was a significant slope change. The coated rebar had a greater increase in LES rate of change, again related to the poor frictional resistance of the rebar during wedging.

In conclusion, the tests produced evidence that the epoxy-coated rebar had less bond strength due to poor friction resistance in the wedging action during splitting. Additionally, the epoxy coating smoothed the bar deformations and reduced the related rib area available for mechanical interlocking.

1.5 GFRP Rebar Bond Tests

There has been extensive and varied research on the many different types of GFRP rebar. Unfortunately, the lack of testing and manufacturing standards for GFRP rebar has limited the number of similar tests on similar types of bars that can be compared. Therefore, three criteria were used to select the most pertinent results for review:

1) Type of test. The focus was bond tests with the concrete in tension. Some eccentric pullout tests were included, but generally pullout test results were excluded.

2) Type of FRP. Only GFRP rebar bond test results were included out of the family of FRP reinforcement. All three types of bar deformations described in Section 1.2, were included in the review and the specific deformation system type was identified for each reviewed test:

   i) Type 1, molded/cast bar deformations,

   ii) Type 2, exterior wound fibers that impress into the rods,

   iii) Type 3, exterior wound fibers that do not impress into the rods.

3) Bar size. The bar sizes were generally limited to No. 3 through 8, which are common to bridge decks.

Tepfers et al. at Chalmers University of Technology, Sweden [18] conducted a series of pullout and splice beam bond tests with the Type 1 GFRP rebar from Marshall Industries Composites, Inc. Additionally, standard Swedish steel rebar, Ks600, were included in the tests

as controls for comparison. The pullout tests were done with central and eccentric positioned bars, and the spliced beam bond tests had an overlapped splice of the GFRP rebar. The bars tested were No. 4 and 5, embedded 3, 5, and 7 bar diameters (1.5 - 4.4 in.) in the pullout tests and spliced 15.7, 23.6, 31.5 in. in the 7.8 x 7.8 x 78.8 in. beams. The beams were reinforced with additional steel bars throughout and stirrups at the ends for shear. Various concrete strengths were tested with average compressive strengths measured at the time of the bond tests of 2900, 2300 and 3600 psi. The pullout and beam tests were instrumented with LVDTs for FES.

The 18 central pullout tests resulted in eight bar pullout failures and ten combination failures. Two of the bar pullout failures had concrete portions adhered to the bar. The other bar pullout failures resulted in the rebar deformations shearing off, which were unable to resist the concrete confinement. In reviewing all the failures with the variable embedment lengths and concrete strengths, the authors were unable to identify any trends in the relationship between the bond stress and these two variables. Additionally, when compared to the steel control rebar they found the GFRP rebar, with sufficient confinement, had the same bond stress relationship versus embedment length.

The 12 eccentric pullout test results were compared to similar tests done on the steel Ks600 rebar. The authors found that the GFRP rebar tests had less concrete cover cracking than the steel rebar tests of the same cover and size. They believe this could be attributed to the softer GFRP rebar not causing as much microcracking along the embedment length and limited wedging action.

The tensile overlap splice beam tests did not reveal significant bond mechanism information. However, it was noted that the GFRP rebar overlap splices had approximately 70% of the strength of similar steel rebar overlap splices.

Rizkalla at the University of Manitoba [19] conducted tensile and T-beam bond tests on No. 4 Type 1 GFRP rebar from Marshall Industries Composites, Inc. The 26 GFRP T-beam bond tests included 8 unconfined bars and 18 confined bars. The confined bars were embedded within the middle of the stem of the T-beam, while the unconfined bars had embedment lengths only in the top of the stem and did not continue through the flange of the T-beam. The T-beams had additional longitudinal and stirrup reinforcement throughout the specimen. Six epoxy-coated steel rebar were also tested for comparison. The unconfined rebar had embedment

lengths of 2.5 and 5 bar diameters (1.3 and 2.5 in., respectively). The confined bars had 2.5 to 25 bar diameter (1.3 to 12.5 in.) embedment lengths. The average concrete compressive strength for the tests was 6380 psi with a standard deviation of 137 psi. The test bars were instrumented with LVDTs for LES and FES.

An average $1/K_1$ value of 46.0 was calculated from the bond failures and is included in Table 1.2 which lists $1/K_1$ values from GFRP rebar bond researchers with specific variables: type of test, confinement reinforcement, rebar size and amount of cover. However, Rizkalla's results are questionable for comparison to other bond test results because of the type of bond test and short embedment lengths for the unconfined tests. The individual test results are tabulated in Table 1.3 which lists the bar size, concrete strength, cover, embedment length, ultimate load, failure mode and calculated values for the uniform bond stress and $1/K_1$ constant. The GFRP rebar with 2.5 and 5 bar diameter embedment lengths failed in bar pullout with the unconfined bar uniform bond stress averaging 1.60 ksi and the confined bar averaging 3.09 ksi. The tests with 10 bar diameter or greater embedment lengths resulted in bar tensile failures. The slip graphs were nearly linear to failure for both the LES and FES. The FES graphs transitioned to nonlinear curves at an average of approximately 0.02 in., which also corresponded to the peak load. This transition point represented the point of significant slope change on the FES curves.

In summary, the author calculated two bond parameters. First, the average bond stress for these GFRP rebar was found to be 3000 psi in confined concrete with a strength of 6380 psi. Second, the development length was determined to be approximately 7 in. for the confined No. 4 GFRP rebar. Conclusions were not drawn for bond performance for the unconfined bars because they failed in concrete pullout.

Daniali at Lamar University [14] conducted 30 notch beam bond tests with Type 2 GFRP rebar. The notches were positioned to align with the load points on the bottom of the beam for instrumentation. These beams were based on similar tests reported in the ACI Committee 208 report, "Test Procedure to Determine Relative Bond Value of Reinforcing Bars." The beams were made with a 28-day average concrete compressive strength 4000 psi (+/- 300 psi), and were additionally reinforced with stirrups on the ends where the test bar embedment lengths were measured and analyzed. GFRP rebar, sizes Nos. 4, 6, and 8, were embedded 16 to 30 bar diameters (8 - 30 in.) with concrete covers of 3, 2, and 1.75 bar diameters, respectively. The Type 2 GFRP rebar was made from 60 - 70% E-glass fibers (weight) in a vinyl ester resin matrix

with a deformed surface from additional fibers wrapped in a 45 degree helical pattern prior to the final heated polymerization of the resin. The beams were instrumented with dial gages for deflection and FES; additionally, strain gages were attached to the test bars at the notched locations.

The notch beam bond test results are given in Table 1.4 which lists the rebar size, concrete strength, cover, embedment length, ultimate load, failure mode and calculated values for the uniform bond stress and $1/K_1$ constant. Average $1/K_1$ values of 29.6 and 25.1 were calculated for the No. 6 and 8 bars, respectively, from the ultimate strains measured in the bar at the notches and the GFRP rebar properties. These values are included in the consolidated GFRP $1/K_1$ Table 1.2. The No. 4 bars all failed in tension and the $1/K_1$ was not calculated because it would be misleading. The authors observed that the GFRP rebar ribs on the surface were sheared off in the pullout failures. It could not be determined from the reference if the sheared bar deformations were just the fiber wrap or the actual bulged bar between the wraps. If the failure included the bulged bar portions, it could be classified more as a bar interlaminar failure, rather than a bond failure. Based on the beam test results, the authors recommended a 12 in. development length for the No. 4 GFRP rebar and an 18 in. development length for the No. 6 rebar. The development length for the No. 6 rebar was based on specimen with additional shear reinforcement. No recommendation was given for the No. 8 rebar.

Larralde et al. at California State University [20] conducted pullout and notched beam bond tests with FRP rebar of 0.25 and 0.33 in. diameter. Additional control tests were conducted with 0.37 in. steel rebar. Four pullout and nine beams were reinforced with 0.33 in. diameter GFRP rebar made of E-glass in a vinyl ester resin with a resin impregnated helically wrapped deformation strand. The specific type of deformation system, Type 2 or 3, could not be determined from the given information. Two bars were each embedded 2 and 4 in. in the pullout tests. Six beam tests had 2 in. embedment lengths and three beam tests had 4 in. embedment lengths. Concrete cover and additional reinforcement were not indicated in the reference. The cross section of the beams was only 4 in. by 4 in.; therefore, it is unlikely that any additional reinforcement was placed in the members along with the test bars. The average concrete compressive strength was 3100 psi. The beams were instrumented with LVDTs for FES at the ends and at a notch in the bottom of the beam for LES.

The GFRP test results are listed in Table 1.5 which lists the rebar size, concrete strength, cover, embedment length, ultimate load, failure mode and calculated values for the uniform bond stress and $1/K_1$ constant. The authors reported average $1/K_1$ factors of 13.7 and 35.7 for the 0.33 in. diameter GFRP and 0.37 in. diameter steel rebar, respectively. These values are included in the GFRP $1/K_1$ Table 1.2 and the steel $1/K_1$ values, Table 1.1 . However, the authors recommended that caution be used with these values because they were calculated from very short embedment lengths.

In addition, there was a noticeable difference in the $1/K_1$ values between the pullout and beam test results. Based on this observation, the authors recommend only using the $1/K_1$ values from the beam test results. In comparing the results of steel rebar with GFRP rebar, the consensus was that the GFRP deformation wraps did not provide as much mechanical interlock as conventional steel deformed rebar.

Makitani et al. at Kanto Gakuin University in Japan [21] tested FRP bars using hinge beam bond tests. The GFRP rebar were 0.39 in. diameter and embedded 10, 20, and 40 bar diameters (3.9 - 15.6 in.) on each side of the hinged beams with concrete cover of 3.5 bar diameters. The GFRP rebar were made from 60% glass fibers (volume) in a vinylon or plastic resin with a spiral wound Type 3 fiber deformation system. The specimen were cast with a design concrete compressive strength of 4300 psi and were reinforced with additional steel longitudinal rebar and stirrups. Concrete compressive tests were conducted at the time of the bond tests and the associated strength values were included in the test results. The beams were instrumented for FES on the ends with “high sensitive displacement meters.”

The hinge beam bond test results are listed in Table 1.6 which lists the bar size, concrete strength, cover, embedment length, ultimate load, failure mode and calculated values for the uniform bond stress and $1/K_1$ constant. The 20 and 40 bar diameter embedment (7.8 and 15.6 in.) length specimen failed in bar rupture and the 10 bar diameter embedment (3.9 in.) length specimen failed in pullout. Based on these failure modes, the $1/K_1$ value was only calculated for the 10 bar diameter tests. As shown in Table 1.6, a value of 49.4 was obtained for $1/K_1$, which must be carefully considered with the extremely short embedment length of 3.9 in. The authors also included the slip graph of the unit bond stress versus FES for the 10 bar diameter (3.9 in.) embedment test. The FES curve was linear up to approximately 0.002 in. and then became nonlinear to failure. In reviewing their results, the authors concluded that bond strength

increased with greater splices up to 40 bar diameters (15.6 in.), which they identify as the development length for FRP bars in general.

Tighiouart et al. at the University of Sherbrooke, Canada, [22, 7] conducted 62 hinge beam bond tests and 18 pullout tests with two types of GFRP bars and steel rebar as a control. The two GFRP rebar were identified as Type A and B. Type A GFRP rebar was supplied by Pultrall, Inc. and consisted of E-glass fibers in a thermosetting polyester matrix with a helical wrapped, sand coated, Type 3 deformation system. Type B GFRP rebar was supplied by International Grating and also consisted of E-glass fibers in a polyester resin with a Type 2 resin impregnated wrapped strand deformation system. The variables in the test included bar size, No. 4, 5, 6 and 8 with embedment lengths of 6, 10, and 16 bar diameters (3 - 16 in.). The bars, No. 4, 5, 6 and 8, had concrete clear covers of 2.7, 2.1, 1.6 and 1.1, respectively. The beams were cast with an average concrete compressive strength of 4500 psi and were fabricated with additional longitudinal steel rebar and stirrups. The beams and pullout test specimen were instrumented for FES on the ends with LVDTs. In the pullout specimen, strain gages were attached to the surface of the test bars within the embedment length to measure strain distribution.

The pullout tests focused on the strain distribution rather than determining bond strength parameters. The authors found that the pullout tests revealed a nonlinear strain distribution along the test bar embedment length, similar to steel rebar seen in other research. The hinge beam bond tests focused on bond strength parameters and the results are listed in Table 1.6 with the authors reported average $1/K_1$ value of 15.6 listed in the GFRP $1/K_1$ Table 1.2. Additionally, typical load versus slip curves were included from the No. 4 and 8 GFRP rebar. The FES curves had an initial linear portion followed by a nonlinear portion that reached a plateau near the peak load. The transition point of the FES curve was located at approximately 0.004 - 0.008 in.

In general, the authors found the GFRP rebar to have less bond strength than steel, which was attributed to the lack of mechanical interlock between the GFRP and concrete. The GFRP rebar lack certain deformation characteristics (high shear strength, high rigidity and deformation geometry) that help engage an effective mechanical interlock. Therefore, by default the GFRP rebar were primarily dependent on the less effective adhesion and friction components for bond strength. Comparatively, the steel rebar had stiff, homogenous, deformation systems that fully engaged a mechanical interlock which was very effective in developing bond strength.

Faza and GangaRao at the Constructed Facilities Center, West Virginia University [23] tested No. 3 and 8 FRP rebar in 12 inverted half-beam bond tests. The FRP rebar properties were not given, however it was inferred that they were GFRP rebar with an exterior wound fiber Type 2 or 3 deformation system. They were embedded 8 to 24 in. with 2.5 and 1 bar diameter clear cover. The specimen were cast with an average concrete compressive strength of 7500 psi and had additional longitudinal steel reinforcement and stirrups. The LES was measured with dial gages, although there was not any instrumentation indicated to account for bar elongation outside the embedment.

The inverted half-beam bond test results are listed in Table 1.7 with an average $1/K_1$ value of 15.5 for the No. 8 GFRP rebar specimen that failed in bond. This $1/K_1$ value is included in the GFRP $1/K_1$ Table 1.2. Typical slip graphs were included. Unfortunately, it could not be determined if the nonbonded region bar elongation was accounted for in the LES. The test setup figures showed only one dial gage on the rebar loaded-end for the LES measurement relative to the concrete face and the text did not discuss accounting for bar elongation in calculating LES. The LES slip graphs were labeled "Net Slip" and had transition points marked to identify the bar elongation and slip regions, approximately 0.006 - 0.013 in. Additional bond conclusions were limited due to the high number of bar tensile failures.

Ehsani et al. at the University of Arizona [3] developed a set of design recommendations for the bonding of GFRP rebar to concrete based on the tests of 48 inverted half-beams, 18 pullout and 36 hooked rebar half-beam bond tests. The hooked rebar were tested in the same inverted half-beam load frame as the straight bar. The difference with the hooked bars was that the free end extended out the top of the specimen due to the embedded hook. The GFRP rebar tested was E-glass with a polyester resin matrix and Type 2 helically-wrapped longitudinal fiber deformations. Bar sizes Nos. 3, 6 and 9 were embedded 3 to 30 in. with one to six bar diameters of clear concrete cover. The beams were additionally reinforced with steel stirrups. Target concrete strengths of 4000 and 8000 psi were used in the tests. LES and FES were measured on the inverted half-beam bond tests with dial gages.

The straight bar inverted half-beam bond tests for the No. 3 and 6 GFRP rebar are listed in Table 1.7 which lists the bar size, concrete strength, cover, embedment length, ultimate load, failure mode and calculated values for the uniform bond stress and $1/K_1$ constant. Based on extensive testing at various embedment lengths, with the majority of the tests resulting in bar

pullout or bar failure, the authors recommended conservative development length parameters. Overall they identified a minimum embedment length of 15 in. for all GFRP rebar. They recommended using Eqn. (1.5) with a $1/K_1$ value of 21.3 to calculate specific development lengths for different bars and concrete strengths and this value is listed in the GFRP $1/K_1$ Table 1.2. Two modification factors of 1.25 and 1.5 were included to account for top bar effect and insufficient cover (less than one bar diameter), respectively.

Similar to Mathey's steel rebar results [13], the researchers also found the limiting slip values that represent the significant slope changes on the LES and FES graphs to be independent of the embedment lengths for a given rebar size. They found this to be true up to slip limits of FES = 0.0025 in. and LES = 0.015 in. These values resulted in larger cracks than the Mathey steel slip criteria [13], but would not be a corrosion concern as with steel rebar because the GFRP rebar are corrosion resistant.

Retika at the University of Minnesota [24] conducted inverted half-beam tests to investigate the effects of thermal and mechanical cycling on GFRP rebar bond. The test specimen and load frame were the same as that used in Grundhoffer's tests [6]. The half-beams were cast with an average concrete compressive strength of 5630 psi and had auxiliary longitudinal steel reinforcement to prevent premature flexural failure. Additional stirrups were not included with the intent to replicate realistic deck reinforcement which lacks significant confinement forces. The concrete clear cover was limited to two bar diameters to ensure concrete splitting. Twelve of the tests were control specimen which were not subjected to thermal or mechanical cycling. The variables in the test included Type 1 No. 4 and No. 6 GFRP rebar from two different manufacturers, Hughes Brothers and Corrosion Proof Products and Polystructures, and No. 6 steel rebar. However, after testing had begun the author was informed by the No. 4 GFRP manufacturer that the bars were defective.

All of the specimen failed in concrete splitting and the results are recorded in Table 1.8 which lists the bar size, concrete strength, cover, embedment length, ultimate load, failure mode and calculated values for the uniform bond stress and $1/K_1$ constant. Although the embedment lengths were only 5.5 and 11 in. for the No. 4 and No. 6 rebar, respectively, the $1/K_1$ values were calculated and are listed in the GFRP $1/K_1$ Table 1.8. These results were valuable for comparison and review considering the lack of bond tests without stirrups, which is the realistic

reinforcement case for bridge decks. However, the manufacturer flaws in the No. 4 GFRP rebar were taken into account in the comparisons.

The FES graphs were reviewed and can be generally described as having linear slopes that rounded out to a plateau near the peak load with a transition point to nonlinear at approximately 0.001 in. The LES curves were almost entirely nonlinear with a limited linear portion in the beginning that changed to nonlinear at approximately 0.007 in.

In general the discussed GFRP results provided a basis for understanding the GFRP bond mechanism. Unfortunately, the difference in bars, lack of comparable test specimen and procedures must be qualified when comparing the results.

1.6 Acoustic Emissions Research

Nondestructive evaluation of materials can be accomplished through various methods, including vibration analysis, radar and acoustic emissions (AE). The AE method was chosen for this project as a qualitative tool to help understand the bonding mechanisms. This section provides a background on some of the previous research employing this method.

Ohtsu at Kumamoto University, Japan, [25] is a prolific Japanese researcher in the AE field. His article "The History and Development of Acoustic Emissions in Concrete Engineering," provides a starting point for reviewing AE techniques.

Ohtsu found pioneering work done by F. Kishinouye at the Earthquake Research Institute at Tokyo Imperial University and in B.H. Schofield's report on "Acoustic Emission under Applied Stress," in the 1950's. The Shofield report introduced the AE term and it has became the accepted acronym. The 1960's saw an increased interest in the applications of AE which led to international symposiums. However it was not until the 1970's that AE methods began to appear in concrete related research. Since then there has been ever increasing interest and research in applying AE techniques to evaluating concrete failures.

When concrete cracks, it releases stored strain energy in the form of elastic waves. These waves propagate through the concrete specimen and are detected by AE sensors that transform the stress wave into an electrical signal. The complicated AE wave generally includes physical waves which can be reflected or diffracted and are called P (longitudinal), S (shear), and surface (Rayleigh) waves. The measuring system for these waves includes the AE sensor, preamplifier, main amplifier and the filter. The outcome is a distinguishable AE signal that is recorded. This

signal is analyzed with analog methods to extract signal parameters and digital methods for quantitative analysis. The analog methods identify the stress waves recorded at the sensors as AE "hits" which can be used for source location of the original concrete crack. The source location is accomplished by using a known velocity for the stress waves and known location of the sensors. The details of this process will be further explained in Section 2.10.4. This is the basic outline of the AE technique that will be applied to help understand the bond mechanism of GFRP rebar.

Reinhardt et al. at the Stuttgart University, Germany, [26] has applied the AE technique to evaluate the bond deterioration of aramid bars in reinforced and prestressed concrete beams and pullout cubes. The concrete had an average 28-day compressive strength of 8410 psi measured on a 5.9 in. cube. The test rods, approximately 0.30 in. diameter, were aramid fibers in a vinyl ester resin with a sand-coated surface. The beams were 5.9 x 5.9 x 394 in., reinforced with one aramid rod. The cubes were 5.9 in. square and also reinforced with one aramid rod.

The beams and cubes were monitored with eleven and eight transducers, respectively, for three-dimensional source location. The accuracy of the source location of AE events was +/- 0.39 in. The AE events recorded for the beam tests were observed to originate at the bottom center tension face and propagated up the cross section as the cracks grew. Comparatively, the AE events recorded for the pullout tests were observed to originate at the top of the embedded bar and expanded across the bonded region.

Both tests successfully monitored concrete cracking during the test which helped qualify the debonding process. In conclusion, the authors believed that AE techniques provided a "sensitive means" for tracking the "process of bond deterioration" with the identification of concrete cracking.

Also at the University of Stuttgart, **Balzs et al.** [27] conducted a series of pullout tests under monotonic, cyclic and long-term loads. The tests were monitored with LVDTs for slip measurement and an AE system to record local damage around the embedded bars. The cubes in the test were 3.9 in. with a concrete strength of 5060 psi. The reinforcement was a standard steel deformed No. 5 rebar with only a 0.80 in. embedment length. Eight AE transducers were used to record three-dimensional source location. Primarily the AE system was used to detect failure of the steel and concrete interaction layer. This layer has been associated with the adhesive bond

component that fails at low loads. Identifying the failure of this component aided understanding the bond failure process.

Interestingly, the authors found similarity in the AE results and the bond stress versus slip graphs. The tests recorded the greatest AE amplitudes per interval matching the location of maximum bond stress, before they both decreased. Additionally, as the bar began to experience greater slip, the AE system recorded increasing activity with increasing number of peak amplitude threshold crossings. In summary, the AE system successfully identified the time and location of the maximum energy dissipation resulting from the debonding process.

The tests conducted at the Stuttgart University were on small specimen. Considering the heterogeneous nature of concrete it is necessary to challenge the accuracy of AE techniques on larger concrete specimen. **Hearn and Shield** at the University of Minnesota [28] investigated AE techniques on concrete specimen of moderate size. They tested three conventionally reinforced and two prestressed concrete beams under three point bending during cyclic loading. The conventionally reinforced beams were 12.0 x 8.0 x 96.0 in. long, with two No. 4 and one No. 5 standard deformed steel rebar. The prestressed beams were hollow-core floor members, 8.0 x 24.0 x 144 in. long, with two No. 4, 270 ksi, prestressing strands. The design concrete strengths were 6000 and 7000 psi for the conventional and prestressed beams, respectively. Four transducers were centered linearly on the bottom of each beam, paired as inner and outer arrays. The conventional beam transducer pairs were spaced 35.4 and 72.0 in. apart for the inner and outer arrays, respectively. The prestressed transducer pairs were spaced 35.8 and 107.9 in. apart for the inner and outer arrays, respectively.

The authors concluded that crack growth could be identified with an increase of AE activity. Furthermore this activity could accurately identify the location of the crack growth within several centimeters.

1.7 Objective and Scope

The objective of the bond study presented herein was to further the understanding of GFRP bond mechanisms in concrete. The focus of the study was to investigate the potential use of GFRP rebar reinforcement in bridge decks. The study exclusively focused on the bond of GFRP rebar to concrete and the determination of the variability of the results. Chapter 1 presented a review of the state of the art in bond tests. Chapter 2 outlines the GFRP rebar testing

program including discussion of the four variables investigated: manufacturer, bar size, cover and embedment length. Of the 84 tests conducted, 12 were part of a pilot study to verify procedures and initial specimen variables. Two sets of primary tests were conducted on 36 GFRP bars each to investigate two distinctly different GFRP rebar. The bars were of different size, had two and three bar diameter covers and variable embedment lengths. Chapter 3 presents and discusses the results. Information is given regarding the general bond mechanisms and variations of the results within each test series. Additional overall comparisons were made among the bars and with the results of other researchers. Chapter 4 draws conclusions for the results and lists recommendations for further investigation.

The results of this investigation provide insight regarding the bond performance and variability of two distinctly different GFRP rebar. Based on the evaluation of these results, the viability of the GFRP rebar for application as bridge deck reinforcement can be determined.

Chapter 2: Experimental Program

2.1 Introduction

This chapter outlines the details of the testing program. The objective of the investigation was to further the understanding of GFRP bond mechanisms in concrete, specifically in concrete bridge decks. In the case of bridge decks, the reinforcement is not confined within transverse reinforcement, and because GFRP reinforcement is not susceptible to corrosion, it may be possible to construct GFRP decks with reduced concrete cover. Because of the lack of data on development lengths of GFRP rebar under conditions of small cover and no transverse reinforcement, a pilot test was conducted to establish the specimen variables and test procedures to be used in the primary tests. The investigation developed in the following steps:

1) Select the general test variables and establish an identification system.
2) Select the type of bond test.
3) Determine the Pilot Test parameters and establish a testing matrix.
4) Determine the Primary Test parameters and establish a testing matrix.
5) Complete the final design of the concrete test specimen, determine all required materials and finalize the testing procedures.

These steps are described in detail in the following sections.

2.2 Select the General Variables and Establish an Identification System

The objective of the investigation was to further understanding of GFRP bond mechanisms in concrete, specifically in concrete bridge decks. Four variables were selected for investigation: manufacturer, bar size, cover, and embedment length. This section will discuss the selection of the variables.

The "manufacturer" variable was selected because of the wide variation in the type of GFRP rebar available. Nine GFRP manufacturers in the United States and Canada were contacted to donate rebar for testing. Five of the manufacturers responded by providing various quantities of bars. Each of the bars had different material compositions and deformation systems.

Initially, the focus of the investigation was on No. 6 rebar which could be considered as an average-to-large size bar for bridge deck reinforcement. Corrosion Proof/Hughes Brothers and International Grating No. 6 GFRP rebar were chosen as representative of the Type 2 helical

wrap surface deformation system. To provide information on a significantly different deformation system, the testing was expanded to include No. 5 GFRP rebar from Marshall Composites Industries which had the Type 1 molded/cast bar deformations system which emulated the appearance of a deformed steel bar. Ideally, a No. 6 bar would have been preferred to facilitate comparison of the results of the two types of bars, however Marshall Composites Industry did not have No. 6 rebar available at the time of testing.

The "cover" variable was initially selected to provide comparison of results with other researchers, many of whom tested only $2d_b$ covers or less. The testing was expanded to include $3d_b$ covers to investigate specimen with a wider range of covers practical for design of concrete bridge decks reinforced with GFRP rebar.

The "embedment length" variable was included to further understanding of the development length for a specific size GFRP rebar with a selected amount of bar cover. In general, the embedment lengths were chosen to approach the length required to fully develop the bars and exceed it with a few selected tests. The details of these calculations are discussed in the Pilot and Primary Parameters Sections (2.4 and 2.6).

Based on the number of general variables, an identification system was established to abbreviate each bond test title. A series of numbers and letters were selected to represent each GFRP bond test, such as "PM1-5-2-12.0" and "2M2-6-3-15.0". The first digit was "P" for the Pilot Test or a number for Primary Test (1 or 2). The next two characters identified the manufacturer. Bars from Marshall Industries Composites were labeled M1, bars from Corrosion Proof Products/Hughes Brothers were labeled M2 and bars from International Grating were labeled M3. The next three numbers identified the bar size, cover in terms of bar diameters, and embedment length in inches. For example, "PM1-5-2-12.0", identified a Pilot Test, M1 GFRP rebar, No. 5, 2 bar diameter cover with 12 in. embedment length.

2.3 Type of Bond Test Selected

The inverted half-beam bond test was selected for the testing program for its realistic tension field development in concrete around the test bar without using an entire beam. Additionally this type of bond test had been successfully used at the University of Minnesota by Grundhoffer [6] and Retika [24] for investigating epoxy-coated and GFRP rebar, respectively.

2.4 Pilot Test Parameters

The number of Pilot Tests and the calculation of the specimen variables are discussed in this section. The number of bond tests for the Pilot Study was based on the GFRP rebar available at the time, No. 4 and 5 from M1 and No. 4 and 6 from M3. Tests involving three different embedment lengths for each of the four bar types were initially planned for the Pilot Test. Ideally, the tests at three embedment lengths would provide information regarding the linearity of the GFRP rebar bond relationship with embedment length. In summary, the Pilot Study was to consist of 12 bars, embedded two per half-beam, for a total of six concrete specimen.

The three variables for the Pilot Test were the manufacturer, bar size and embedment length. Cover remained constant at $2d_b$ due to the limited number of tests in the Pilot Study. Additionally, this cover was the most probable and economical cover expected for bridge decks reinforced with GFRP rebar. Manufacturers M1 and M3 were selected for the Pilot Test because they had different deformation systems: Type 1 for the M1 bars and Type 2 for the M3 bars. Both manufacturers supplied two different bar sizes that resulted in four possible test bars: M1-4, M1-5, M3-4 and M3-6. Three lengths were selected for the M1-4 GFRP rebar and four lengths were selected for the M1-5 GFRP rebar. The extra embedment length for the M1-5 GFRP rebar was included because of the lack of comparable test results for bars of this size and deformation type. M3 GFRP rebar were selected because they were very similar to bars previously tested by Retika [24] at the University of Minnesota in terms of size and deformation type. Two lengths were selected for the M3-4 bars that matched Retika's [24] for direct comparison and three lengths were selected for the M3-6 bars.

The embedment lengths were determined by selecting a desired percentage of the bar's ultimate tensile strength, f_u, to be achieved in the test. Ideally, this percentage (less than 100%) would result in a concrete splitting failure and not bar fracture. The following percentages were targeted for each GFRP rebar test:

GFRP Rebar Test	% of Bar's Tensile Capacity
GFRP Rebar M1-4	65, 80 and 95%
GFRP Rebar M1-5	65, 75, 85 and 95%
GFRP Rebar M3-4	50 and 65%
GFRP Rebar M3-6	65, 80 and 95%

These percentages were used in Eqn. (1.4). Although this equation is based on fully developed reinforcement, it provided a starting point for determining the Pilot Test embedment lengths. The percentage of f_u listed above was used for f_u in the equation with the manufacturer reported tensile capacity (f_u) and cross-sectional area (A_b). The concrete strength used for the calculation was 4300 psi, which is the nominal concrete compressive strength used in Minnesota bridge decks. Although this was the strength ordered from a local batch plant, the average concrete compressive strength measured during the Pilot Test was 7580 psi. This increase in delivered strength over nominal strength is typical for concrete suppliers in Minnesota. Previous researcher's $1/K_1$ values were considered for use in Eqn. (1.4), but only Retika's [24] values were used because of the similarity in the type of bond test and confinement. These values provided the most reliable data for similar tests considering the continuity of using the same testing facility and procedures.

The $1/K_1$ value for each Pilot Test bar was based on Retika's $1/K_1$ values listed in Table 1.2. The PM1-4 GFRP rebar was significantly different from the GFRP rebar used by Retika; however, due to the lack of bond testing on this GFRP rebar type, Retika's results with a $1/K_1$ value of 28.3 provided an initial estimate for the $1/K_1$ value. Retika did not test No. 5 GFRP rebar, therefore her No. 4 and No. 6 $1/K_1$ values were averaged for the PM1-5 GFRP rebar; the average was 28.9. The M3-4 GFRP rebar was very similar in material composition and bar deformations to Retika's bars, but her original bars had reported manufacturing flaws. For the lack of a better value, Retika's $1/K_1$ value of 28.3 was used which provided the opportunity to verify her results. The PM3-6 GFRP rebar was also very similar in material composition and bar deformations to bars tested previously by Retika, therefore her corresponding $1/K_1$ value of 29.6 was used.

Based on the above analysis, calculations were made for embedment lengths that would achieve the desired percentage of the bar tensile capacity. The calculated embedment lengths were rounded to the nearest 1/2 in. to obtain the final Pilot Test embedment lengths which are shown in the Pilot Test matrix (Table 2.1).

2.5 Pilot Test Results

The Pilot Test successfully established the procedures for an effective bond test and provided valuable insight into the specimen variables for the primary test. All twelve specimen

in the Pilot Test failed in concrete splitting. The concrete had an average compressive strength of 7410 psi and split tensile strength of 605 psi. The test results are listed in Table 2.2. In this table, the tests are listed vertically with their associated ultimate loads, target $\%f_u$, resulting $\%f_u$, $1/K_1$ values and average $1/K_1$ values for each set of tests. The tests were grouped in sets based on manufacturer and bar size. Plots of embedment length versus ultimate load for the four different sets of bars are shown in Fig. 2.1. In this figure the Pilot Test results are shown with symbols and solid lines. The symbols with dashed lines represent the ultimate tensile strength of each set of bars. The M1 ultimate tensile strengths are from tensile testing (Appendix A) and the M3 ultimate tensile strengths are from the manufacturer data.

The Pilot Test $\%f_u$ were all below the desired target $\%f_u$ and the resulting $1/K_1$ values did not match the design $1/K_1$ values based on Retika's results, except for the M3-4 bars. The M3-4 bars, at 5.5 and 7.5 in. embedment lengths, did meet the target $\%f_u$ with 50 and 65%, and had similar ultimate loads compared to Retika's results for similar bars and embedment lengths. Additionally, the increased concrete compressive strength from the design value of 4300 psi to the average of 7580 psi should have resulted in a greater $\%f_u$. The differences could be attributed to the Pilot Test having greater embedment lengths than Retika's tests, effect of the nonlinear bond stress or simply the difference in GFRP rebar. Additionally, the $1/K_1$ values may be misleading because they were calculated from Eqn. (1.5) which is based on rebar development length. Neither Retika's nor the Pilot Test rebar were at the development length because they all failed in concrete splitting.

Figure 2.1 provides some insight into the relationship between load and embedment length for the Pilot Test bars. The three M1-4 bars had a nearly linear relationship, while conversely, the four M1-5 bars had scattered results with no clear relationship. Considering these results, it was apparent that additional tests were required to gain a comfortable understanding for this GFRP rebar type. The two M3-4 rebar results verified Retika's tests, but linearity could not be considered with only two tests. The M3-6 rebar did have a nonlinear increase in ultimate load with increasing embedment length.

2.6 Primary Test Parameters

The two Primary Test parameters discussed in this section are the number of tests and the calculation of the specimen variables. The number of tests for the primary investigation was

primarily based on space constraints. The structures lab at the University of Minnesota has limited space for constructing and storing specimen. Thirty-six inverted half-beam tests, from 18 concrete specimen, was the limit for the space constraints. Hence, it was decided that each testing series in the Primary Test would consist of 36 specimen. One series, 36 bond tests, would not sufficiently investigate the GFRP bond mechanism and three series, 108 bond tests, would be cost prohibitive. Two series and a limited Pilot Test was decided upon as providing the maximum research value for the minimum construction costs. In summary, 72 total bond tests, from two series of 18 concrete specimen each, were selected for the Primary Test.

The variables for the Primary Test included manufacturer, bar size, concrete cover and embedment length. The number of variables was limited by the desire to assess the GFRP rebar variability. Six repeats for the same set of variables were considered the minimum number of tests required for statistical significance in assessing variability. Additionally, to compare the two primary tests, one set of three tests from Primary Test 1 was repeated in Primary Test 2.

The two manufacturers initially considered for further testing were M1 and M3, due to their significantly different deformation systems. However, the M2 bars were substituted for the M3 bars to facilitate comparisons to Retika's results from the same manufacturer and because the required number of M2 test bars was readily available. Both the M2 and M3 bars had similar material composition and deformation systems that were significantly different than the M1 rebar.

As mentioned in Section 2.2, two GFRP rebar sizes, No. 5 and No. 6, were selected for the Primary Test. The No. 5 and No. 6 bars did not have clear relationships between their ultimate loads versus embedment lengths as shown in Fig. 2.1 compared to the No. 4 bars. The No. 5 bars from the M1 manufacturer were chosen to be tested in the first Primary Test with six repeats for each set of variables. The No. 6 bars from the M2 manufacturer were tested in the second Primary Test with six repeats for each set of variables. Three repeats of the No. 5 M1 rebar were tested again in the second Primary Test to establish a correlation of the results for the two series.

All of the Pilot Test specimen had exhibited concrete splitting failures which were the desired failure mode. With the Primary Tests, it was decided to include embedment lengths and/or confinement that would further approach or capture bar fracture. To bracket the rebar development length, tests were included with $3d_b$ concrete cover and rebar embedded the full

length of the concrete specimen, approximately 47 in. with $2d_b$ cover. The most economical design cover for bridge decks will be $2d_b$, however, there was some concern that $2d_b$ cover would not yield sufficient confinement and have a large impact on the development length of the bars. Hence $3d_b$ cover was also considered. The $3d_b$ cover tests extended the results of previous researcher investigations of cover, which had been limited to tests of $2d_b$ cover or less to $3d_b$.

Determination of the test embedment lengths was done with a procedure similar to that used for the Pilot Test. Three series of six repeats each at different embedment lengths for each of the two covers were selected for the first Primary Test. One of the chosen embedment lengths was 47 in., the full length of the specimen, with a $2d_b$ cover to ensure that full bar development was possible with a shallower cover. The other two embedment lengths for the specimen with $2d_b$ cover were chosen to achieve bar stresses of 70 and 85% of the bar tensile strength. The three embedment lengths chosen for the specimen with $3d_b$ cover were designed to achieve bar stresses of 55, 70 and 85% of the bar tensile strength. Equation (1.4) was used to calculate the embedment lengths with the desired percentage of bar tensile stress, manufacturer reported bar area and concrete compressive strength of 4300 psi. The tensile force (19.2 kips) used in the calculation was based on tensile test results performed at the University of Minnesota on the M1 rebar. The $1/K_1$ value (16.9) was based on the Pilot Test results on the M1 rebar. Equation (1.4) did not account for cover. Consequentially, the embedment lengths calculated for the tests with $3d_b$ cover were carefully considered. To compare the effect of the $3d_b$ cover to $2d_b$ cover, two series of specimen were cast with similar embedment lengths. The third series of specimen at $3d_b$ cover was cast with a shorter embedment because the increased cover was suspected to further increase confinement thereby reducing the required embedment lengths. Based on these considerations, and the above mentioned variables, the embedment lengths were calculated as 12.5, 15.0 and 47.0 in. for tests with $2d_b$ cover and 10.0, 12.5 and 15.0 in. for tests with $3d_b$ cover. These values are shown in the Primary Test 1 Matrix, Table 2.3, that lists each series vertically with their associated manufacturer, bar size, cover, embedment length and number of tests.

In the second Primary Test, three repeats of the M1-5-2-12.5 test were conducted to correlate results with the first Primary Test. The test, with $2d_b$ cover and 12.5 inch embedment length, was selected because it would likely result in a concrete splitting failure. Excluding these three correlation tests, Primary Test 2 consisted of 33 additional bond tests. Three of the tests

were conducted with the M2 bars at $2d_b$ cover and full embedment length, approximately 47 in. Only three tests were done at this embedment length and cover because bar tensile failures were almost guaranteed. The remaining 30 tests were divided into five series of six repeats each, again providing the minimum number of tests for statistical significance. The five series included three series with $2d_b$ cover and two series with $3d_b$ cover. The three tests with $2d_b$ cover were selected because this cover was the most probable and economical cover expected for bridge decks reinforced with GFRP rebar. The three embedment lengths for the specimen with $2d_b$ cover were chosen to achieve bar stresses of 60, 80 and 100% of the bar tensile strength. As for the case of the first Primary Test, the specimen with $3d_b$ cover were cast with similar covers to the shorter $2d_b$ embedment lengths to facilitate comparing the effects of cover. Equation (1.4) was used to calculate the embedment lengths for the $2d_b$ cover cases with the desired percentage of bar tensile stress, manufacturer reported bar area and concrete compressive strength of 4300 psi. The tensile capacity (30.0 kips) used in the calculation was based on tensile test results performed at the University of Minnesota on bars from the same M2 manufacturer, but an earlier batch. The batch of M2 bars used in the bond test were not yet tested prior to the embedment length calculations because of test equipment scheduling. The $1/K_1$ value (17.5) was based on the Pilot Test results on similar M3 bars. Based on these considerations, the embedment lengths for the tests with $2d_b$ cover were calculated as 15.0, 20.0 and 25.0 in. The $3d_b$ cover specimen were cast with corresponding embedment lengths of 15.0 and 20.0 in. These values are shown in the Primary Test 2 Matrix (Table 2.4) which lists each series vertically with their associated manufacturer, bar size, cover, embedment length and number of tests.

2.7 Specimen Design

The final specimen design was based on the inverted half-beam bond test set-up used for similar bond tests at the University of Minnesota. The individual half-beams were 48 in. long, 18 in. high and 12 in. wide, as depicted in elevation in Fig. 2.2 and cross section in Fig. 2.3. Two bars were embedded in each half-beam, one in the top portion and another in the bottom portion, as shown in Fig. 2.2. The Pilot Tests confirmed that each bar could be tested without influencing the other bar in the same specimen for future tests. Two PVC lifting ports were installed during the concrete pour at the third points for transporting the concrete specimen. PVC sleeves were positioned around the GFRP rebar to break the bond for the first 0.5 in. (lead

length) and beyond the end of the desired embedment length. The first 0.5 in. unbonded region had been successfully used at the University of Minnesota to prevent a conical pullout with similar tests. The lead length is identified with symbol "L_L" in diagrams and further calculations. The PVC sleeves were selected such that the GFRP rebar fit snugly into the sleeve. The sleeve sizes are listed in Table 2.5. The PVC sleeves were centered on the bar using masking tape wrapped around the bar and were sealed at the end with 100% silicon caulk.

The only additional reinforcement placed in the specimen were longitudinal bars to prevent flexural failure in the unbonded region of the specimen. The amount of longitudinal reinforcement was determined from a moment diagram, as shown in Fig. 2.4, for the case of the largest expected bar force at the end of shortest expected embedment length. The Pilot Test used two No. 5 steel rebar for the additional reinforcement. This reinforcement was changed to two No. 4 GFRP rebar for the Primary Tests. The additional reinforcement plan was changed from steel rebar to GFRP rebar to better simulate a GFRP reinforcement plan in a concrete bridge deck. Potentially, the steel rebar could have influenced the GFRP test bars in an inverted half-beam bond test. Specifically, the greatest concern was the difference in MOE values with the steel rebar having five to six times the MOE of the GFRP rebar [4].

2.8 Materials

2.8.1 Test Bars

The three bars selected for testing were from the manufacturers (code): Marshall Industries Composites, Inc. (M1), Hughes Brothers/Corrosion Proof Products (M2), and International Grating (M3). The test bars with manufacturer and size codes are shown in Figs. 2.5, 2.6, and 2.7 for the M1, M2, and M3 bars, respectively. Two different pairs of bars were used in the Pilot Test and Primary Tests as explained in Section 2.6

Details of the three types of GFRP rebar are described in the following paragraphs. A consolidated listing of the bar MOE, cross-sectional area and tensile strength is given in Table 2.6. This table lists the manufacturer reported values and experimentally determined values for the Primary Test bars. Additionally listed in the table are results from bars tested from Retika's study [24] and a second batch of M2 bars which were not used in the bond test. The procedure for experimentally determining the tensile strengths and cross-sectional areas of the bars are outlined in Appendix A and Appendix B, respectively.

The M1 GFRP bars were constructed of 70% (weight) E-glass fibers in a 10% recycled polyester resin material and had the most unique deformation system of the currently available GFRP rebar. The bars had a Type 1 deformation system with a ceramic coating which appeared similar to that of steel rebar with a rib face angle greater than 40 degrees. The deformations were formed from 3.5% ceramic fibers embedded in a 15% urethane modified vinyl ester matrix and a 1.5% corrosion inhibitor. The individual deformations (spaced at approximately 3 in.) were formed from a special molding process that was repeated along the bar length at approximately 9 in. lengths. At the mold joints, the pattern for the bar deformation system was interrupted and some bars appeared to be "missing" deformations at these points.

The second GFRP rebar tested was more typical of the bars currently available. The M2 bars were constructed with 76% (weight) E-glass Owens Corning Type 30-366-133 yield fibers in a 24% blended vinylester resin matrix. The manufacturer claimed this blended matrix was specially designed to protect the silica fibers from alkali attack. The rebar had a Type II deformation system formed from helically wrapped glass fibers with a pitch of approximately 1 in. This wrapped fiber system impressed into the bar core sufficiently to cause the bar to bulge between the wraps creating a deformation. The resulting rib face angles were less than 30 degrees. The number of deformations for this continuously wrapped system required counting the number of wraps across a plane along the length of the bar. The number of bar deformations within the embedment length per test was included in the results. The bars were coated with sand after the deformation system was formed to provide additional frictional resistance.

The third type of bar, from manufacturer M3, was similar to the M2 bars with a Type 2 deformation system that caused the bar to bulge between the wraps with a rib face angle less than 30 degrees. The M3 rebar were constructed of 70% (weight) E-glass fibers in a 30% polyester resin matrix. The deformation spacing was not as uniform as those of the M2 bars, but there was a similar manufacturer applied sand coating.

2.8.2 Concrete

The concrete ordered for each set of tests was delivered from a local ready-mix plant. The specified mix design was that used in bridge deck construction (i.e. Type 3Y33 Mn/DOT: 6% air entrainment, 3 in. slump with a nominal 28-day compressive strength of 4300 psi). Air content (ASTM C231) and slump (ASTM C143) tests were conducted during each construction

to verify the concrete properties. Values for these tests are in outlined in Appendix C. Test cylinders and modulus of rupture beams were made at the beginning, middle and end of each concrete pour. Compressive (ASTM C39) and split tensile strength (ASTM C496) tests were conducted at the beginning and end of the Pilot Test. In addition to these two tests, modulus of rupture (ASTM C78) and modulus of elasticity (ASTM C469) tests were conducted for the Primary Tests. The tests for the primary investigation were conducted at 28 days, at the beginning of the testing, 1/3 of the way through testing, 2/3 of the way through testing and at the end of the tests. The average values for the tests are shown in Tables 2.7, 2.8, and 2.9 for the Pilot, Primary 1 and Primary 2 test with the associated age. The average concrete compressive strengths measured, during the testing periods for the Pilot, Primary Test 1 and Primary Test 2 were 7580, 6450, and 6340 psi, respectively. A complete list of concrete testing data and procedures are given in Appendix C.

2.9 Specimen Construction

2.9.1 Formwork

The forms for the concrete specimen were fabricated from 0.5 in. thick plywood that was bolted together with 2 x 4 in. bracing to form the 48 x 18 x 12 in. half-beams. The plywood was sanded and covered with a form release agent, Noxcrete, prior to assembly. Care was taken to ensure that the form release agent did not come in contact with any reinforcement. The ends of the forms had holes to position the auxiliary longitudinal rebar and PVC sleeves as necessary. The rebar and PVC protruding through the holes were caulked to seal the form. The test bars extended approximately 18 in. beyond the concrete face on the loaded end to permit installation of a grip system and 2.5 in. on the free end to mount an FES LVDT bracket. The auxiliary rebar extended approximately 0.5 in. beyond the forms, which was sufficient for securing these bars within the forms for construction.

2.9.2 Casting

The specimen were cast on their side to eliminate the “top bar” effect associated with reinforcement having significant amounts of concrete beneath that may influence the results. The forms were positioned on the loading dock, as shown in Fig. 2.8 to ensure the pouring order did not influence the data. Four to six specimen were cast at one time. The concrete was placed in two lifts with a mechanical bucket and vibrated after each lift. Finally, the tops of the

specimen were float-finished smooth. The specimen for the Pilot Test, Primary Test 1 and Primary Test 2 were cast during the afternoon of 15 May 97, 17 Oct 97, and 27 Feb 98, respectively.

2.9.3 Concrete Curing and Stripping of Forms

All of the half-beam specimen, cylinders and modulus of rupture beams were cured and stored under the same conditions. Wet burlap and plastic sheets were placed over all the specimen, as shown in Fig. 2.9. The burlap was wetted for three days with the specimen in their original forms. On the third day, the forms were removed from all the specimen, they were repositioned and covered with soaked burlap and plastic. Again the burlap was wetted for four more days. Seven days after constructing the specimen, they were turned upright, moved into storage without wet burlap or plastic, and remained in the lab environment until testing.

2.10 Test Setup

2.10.1 Bond Test Frame

The inverted half-beam bond test was performed by loading the GFRP rebar in tension in a load frame as shown in Fig. 2.10. A 77 kip actuator mounted on a horizontal beam attached to a structural floor was used to apply the load. A computer data acquisition system recorded time, displacement and load throughout the test. The GFRP rebar was pulled in tension through a special grip system and the half-beam was held in position by three reactions, which are depicted in the shear and moment diagrams, Fig. 2.4, and pictorially in Fig. 1.7. Reaction 1 was provided by the concrete block with a full width plate that extended across the concrete specimen. Reaction 2 was provided by the tie down beam with roller that held the half-beam down and prevented it from lifting up when the GFRP rebar was pulled. Reaction 3 was provided by the end of the horizontal beam supporting the actuator. A 2.5 in. steel plate was placed between the half-beam end and the roller on the end of the horizontal beam to distribute the reaction across the compression region at the end face of the specimen. A hole was positioned in this plate to accommodate the free-end of the test bar located in the bottom of the specimen.

2.10.2 Grip System

The composite structure of the bars did not have sufficient transverse compressive strength for a standard wedge type grip system. To avoid transverse crushing of the bars, a

special grip was used based on research by Holte et al. [29]. An aluminum cylinder, made of T6061 material, was machined with a parabolic core to distribute the transverse stress and minimize local "pinching" pressure at the grip. The equations for the inside radius of the grips were

$$\text{No. 5 and 6 GFRP Rebar } r_x = 0.500 + 0.013(x^2) \quad (2.1)$$

$$\text{No. 4 GFRP Rebar } r_x = 0.350 + 0.020(x^2), \quad (2.2)$$

where r_x is the interior radius at position x (in.), x is the longitudinal position along the grip (in.).

The grip dimensions for use with the No. 5 and 6 GFRP rebar are shown in Fig. 2.11 and for the No. 4 GFRP rebar in Fig. 2.12. The grips were installed on the bars with the specimen standing on end and the test bar extending upward. The aluminum grip was positioned at the test bar tip and temporarily held in place with wood supports. The bottom of the grip was centered by wrapping masking tape around the test bar until it fit tightly in the grip. The top of the grip was centered with a PVC cap that fit around the grip and held the test bar in the center. The bottom of the grip was sealed around the bar with 5-minute epoxy. Once dry and sealed, the aluminum grip was filled with a two part resin, Sikadur 35. The resin was initially cast in three lifts, however this was changed to one lift to avoid a cold joint in the resin that may have caused early bar failures in the grip. Once the grips were installed, the specimen were repositioned and ready for testing.

The aluminum parabolic grips were attached to the actuator clevis by a steel connector. The steel connector for the No. 5 and 6 grips is shown in Fig. 2.13 and for the No. 4 grips in Fig. 2.14. The complete connection to the actuator clevis is shown in Fig. 2.15 for the No. 5 and 6 GFRP rebar test systems.

2.10.3 Slip Instrumentation

Bar movement and elongation were measured with Linear Variable Differential Transformers (LVDTs) and recorded at approximately two Hz with an OPTIM data acquisition system during the test. The loaded-end slip (LES) and unbonded region bar elongation were measured with two pairs of LVDTs on the loaded end. The first pair were 0.5 in. LVDTs, identified as LES1 and LES2, shown in Fig. 2.16. These LVDTs were held in a bracket, as shown in Fig. 2.17, left and right of the GFRP rebar (180 degrees apart). The LVDT bracket was positioned 2 in. from the front face of the concrete to allow for measurement and equipment

positioning; this length was identified as the "head length." The bar elongation outside the bonded region was measured with a second pair of 0.1 in. LVDTs, identified as LES3 and LES4 in Fig. 2.16. These LVDTs were held in a bracket (Fig. 2.18), above and below the test bar (180 degrees apart) normal to LES1 and LES2. This bracket was positioned 2 in. beyond the first LES LVDT bracket and this length was identified as the "gage length" (L_G). Finally, the free-end slip (FES) was measured with a pair of 0.1 in. LVDTs, identified as FES1 and FES2 in Fig. 2.19. These LVDTs were held in a bracket, as shown in Fig. 2.18, left and right of the test bar (180 degrees apart). After the half-beam was in position and the instrumentation installed, the head length (L_H), and gage length (L_G) were measured to within 0.03 inches.

With the given lengths, L_L, L_H, and L_G, and the LVDT results, the loaded end (LES) and free-end slips (FES) could be calculated. The LES is the slip and elongation of the bar within the embedment length relative to the load-end face of the concrete specimen. The LES does not include bar elongation outside the embedment length and this is accounted for in the following equations assuming a constant strain in the unbonded region. The FES is the pure slip of the reinforcement relative to the free-end face of the concrete.

$$LES = \frac{LES1 + LES2}{2} - \frac{LES3 + LES4}{2} \left(\frac{L_H + L_L}{L_G} \right) \tag{2.3}$$

$$FES = \frac{FES1 + FES2}{2}, \tag{2.4}$$

where *LES* is the loaded-end slip, *FES* is the free-end slip, L_H is the head length (approximately 2 in.), L_L is the lead length (approximately 0.5 in.), L_G is the gage length (approximately 2 in.).

2.10.4 Acoustic Emission Instrumentation

The goal of the acoustic emission (AE) instrumentation was to provide a qualitative approach to understanding the GFRP rebar bond mechanism. The AE sensors recorded stress waves above a set threshold that originated from concrete cracking or bar failure, called "hits." When two or more sensors would record "hits" that originated from the same source, an "event" source location would be recorded. To accurately determine the event locations, the system was calibrated for each test by determining the material wave velocities.

The stress wave velocities were determined from calibration tests as shown in Fig. 2.20. In these calibration tests the stress waves were initiated by breaking a glass rod or pencil lead at

known locations along the length of the material as shown on a concrete specimen in Fig. 2.20. The total length L between two sensors is divided into equal segments of X and the remaining portion (L-2X). The X segment is the distance from the from the glass rod or pencil lead break to the closet AE sensor. The glass rod or pencil lead breaks create quick jumps in surface displacements. The displacement jumps propagate along the surface of the specimen as Raleigh waves. Sensors positioned a known distance from the location of the break record these waves as "hits" at different times. The time difference between the sensors recording the hits is then used with the known source location to calculate the stress wave velocity:

$$V_{\text{stress wave}} = (L - 2X) / (\div t) , \tag{2.5}$$

where $V_{stress\ wave}$ is the stress wave velocity, $L - 2X$ is a known distance as shown in Fig. 2.20, $\div t$ is the time difference between the recording hits of the two sensors.

A minimum of five tests were conducted at multiple distances between the sensors for each material. The average stress wave velocity for these tests was then calculated for the concrete and GFRP rebar. Table 2.10 lists the stress wave velocities used throughout the study. These values were checked throughout each test to ensure they remained constant.

The sensors were attached to the concrete specimen or test bars with standard weight lubrication grease and held in position with duct tape. Various AE sensor positions were tried during the Pilot Test to determine the best combination of locations for obtaining information about the debonding process. Based on the results of the Pilot Test, five acoustic emission sensors were positioned as shown in Fig. 2.21 for the Primary Tests. AE Sensors were attached to each end of the GFRP test bar and on the top concrete surface at each end of the embedment length along the center line. A redundant AE sensor was positioned on the top concrete surface 6 - 8 in. beyond the embedment length. The two AE sensors on the GFRP rebar identified bar AE events and the three AE sensors along the embedment length on the concrete surface identified concrete cracking events.

2.11 Test Procedure

All of the tests were conducted according to the same basic procedure. The concrete specimen were placed into the test frame with the test bar centered on the actuator arm to ensure it was pulled straight. Any misalignment was recorded with the LES LVDTs as described in Appendix D. Initially the LES LVDT brackets were attached directly onto the GFRP rebar with

screws tightened onto the bar. After testing a number of M1 specimens, it was apparent the outer coating of the M1 bars was damaged by the screws and the bars would need protection. The initial protection method included application of tape directly to the bar under the screws. Both masking tape and duct tape were used for this protection system. Unfortunately neither tape sufficiently protected the outer coating of the M1 bars. In later tests the bars were wrapped with a nominal 5/8 or 3/4 in. rubber hose, slit for installation and covered with a nominal 1/16 in. thick aluminum strip to distribute the point loads from the screws. This rubber and aluminum protection system was successful in protecting the outer coating of the M1 bars and is discussed with each individual series in Section 3.2. After all instrumentation was installed and data acquisition systems activated, the test was run.

Each test started with tension load applied through the actuator to the GFRP rebar grip system at 0.05 in./min. This rate was successfully used by Retika [24] in similar tests and was based on ASTM A994, "Comparing Bond Strength of Steel Reinforcing Bars to Concrete Using Beam-End Specimen" and C234, "Comparing Concretes on the Basis of the Bond Developed with Reinforcing Steel." After application of one to two kips of load, the concrete specimen had positioned itself firmly within the load frame and the loading was continued until failure. As surface cracks developed, they were marked with a permanent marker on the specimen which had a pre-drawn grid system. The grid was drawn with a black marker. Each crack and associated load during the test was recorded on the specimen surface with a blue marker. Tests that failed in concrete splitting had additional cracks that occurred at ultimate load. These cracks were recorded on the specimen surface with a red marker.

After failure, the crack pattern was recorded and post test pictures were taken. The concrete specimen was then opened with a jack hammer to expose the test bar along the embedment length for inspection and photographs. The bar was then carefully removed and additional photographs were taken of the bar and exposed specimen. A careful investigation of the bar and the specimen was done to investigate fiber damage, concrete surface texture and other clues to the debonding process. The testing process culminated with an individual test report that documented the complete test and results. These reports were used to develop Data Tables 3.1 to 3.12 which are further explained in Section 3.2 of Chapter 3.

Chapter 3: Experimental Results and Discussion

3.1 Introduction

This chapter presents, discusses and compares the results of the two primary test series. The two primary tests consisted of a total of 72 bond tests divided into twelve series of 3, 6 or 9 tests as outlined in Section 2.6. The discussion of the results is divided into three major subsections. Section 3.2 provides a description of each series of tests, explains anomalies and summarizes results. Sections 3.3 and 3.4 present discussions of the two types of GFRP rebar tested and focuses on the within-test variability, effects of embedment length on ultimate load, effects of cover on ultimate load, bond parameters and general bond behavior. Section 3.5 presents a comparison of the two types of GFRP rebar.

3.2 Individual Series Results

3.2.1 General Data Table

General data tables (Tables 3.1 - 3.12) were developed for each of the twelve series to provide a consolidated list of test results for identifying trends and anomalies. Each data table is headed by the series name and average concrete compressive strength for the primary test associated with the series. The test results are listed vertically for each test with average values calculated in the final three columns. The first average value column is for all types of failures ("All"), the second average value column only considers specimen exhibiting concrete splitting failures ("Conc") and the third average value column only considers specimen exhibiting bar failures ("Bar"). The various test results are in numbered rows, with 28 rows of results for the M1 bars and 24 rows of results for the M2 bars. The first five and the last ten rows of results are similar for both bar types. The first five rows represent pre-test information. The last ten rows represent post-test results. The middle 6-17 and 6-13 rows for the M1 and M2 bars, respectively, were unique to each bar type because of the distinct bonding mechanisms associated with the different bar types. Data for these rows were taken from the individual slip graphs in Figures 3.1 through 3.24, crack patterns in Appendix E, and AE graphs in Appendix F.

The first row of the pre-test information is the test number within the primary test, 1 through 36. The second row is the specimen age in days. Testing was done in groups of three tests each and groups from the series were tested up to 60 days apart. This division was done to

account for the aging concrete during testing. Theoretically the concrete in the older specimen within a series should have been stronger and had the potential to increase the ultimate concrete splitting failure load compared to younger specimen. However, only the average modulus of rupture exhibited an increase in strength during the testing period. The concrete compressive strength, split tensile strength and modulus of elasticity (MOE) did not vary significantly over the same period. Therefore the effect of concrete strength was believed to be minimal. The concrete test results are discussed in Appendix C.

Row 3 in the data tables lists the number of bar deformations within the embedment length that were damaged or missing prior to the test relative to the possible number of bar deformations within the embedment length. Each bar deformation for the M1 bars represents a single deformation that wrapped circumferentially around the bar. The continuous deformation wraps for the M2 bars required counting the number of wraps across a plane along the length of the bar. However, a damaged deformation wrap for the M2 bars was less significant because the continuous wraps had already formed the bar surface deformation (i.e. the core bar bulged between the wraps).

Row 4 in the data tables lists the measured bar cover. The design bar cover is listed in the data table header. Relatively greater cover could increase bar confinement and the ultimate load for a concrete splitting failure compared to a specimen with less cover.

The final row in the pre-test data is Row 5 which identifies the type of protection applied to the GFRP rebar under the LVDT attachment brackets. Various bar protection methods were used to protect the bar from the screw attachment as shown in Fig. 2.16. Initially the screws were tightened directly onto the GFRP rebar and these tests are identified with "N" signifying "no protection" in the data tables. After testing began it was apparent that the outer coating of the M1 bars was easily damaged by the screws and the bars would need protection. The initial protection method included application of tape directly to the bar under the screws. Tests that used duct tape are identified with "D" and tests that used masking tape are identified with "M." Unfortunately neither tape sufficiently protected the outer coating of the M1 bars which were inspected by removing the tape after testing. In later tests, the bars were wrapped with a nominal 5/8 or 3/4 in. rubber hose, slit for installation, and covered with a nominal 1/16 in. thick aluminum strip to distribute the point loads from the screws. This rubber and aluminum protection system was successful in protecting the outer coating of the M1 bars and is identified

with “RA” in the data tables. The majority of the specimen in the first and all the specimen in the second Primary Tests used this protection system. When comparing tests within the M1 series, the different protection systems may have affected the bar failure ultimate loads.

The next rows in the data tables list the during-test data. There are twelve rows of these results for the M1 bars and eight rows of these results for the M2 bars. The rows are listed in order of occurrence, from the beginning of the loading to the ultimate failure load:

	M1 GFRP Rebar		**M2 GFRP Rebar**
Row	Result	Row	Result
6.	LES transition point	6.	LES transition point
7.	1st crack load	7.	1st crack load
8.	perpendicular cracking load	8.	FES transition point
9.	LES divergence point	9.	Concrete AE peak load
10.	Concrete AE peak load	10.	Bar AE peak load
11.	FES transition point		
12.	Bar AE peak load		

The data for these rows were taken from the slip graphs in Figures 3.1 through 3.24, crack patterns in Appendix E, and AE graphs in Appendix F. The following paragraphs discuss the slip graphs, crack patterns and AE graphs that provided the data for the individual rows of results listed above.

The FES and LES graphs are shown in Figures 3.1 through 3.24 with both slip graphs for an individual test shown together on a page. Each graph has the load in kips along the ordinate and the slip values in inches along the abscissa. The slip curves were developed from Eqns. (2.3) and (2.4) and the plotted curves were terminated at ultimate load. The purpose of the FES graphs was to illustrate pure slip (without bar elongation) relative to concrete versus the load. The purpose of the LES graphs was to illustrate bar slip and elongation within the embedment length versus the load.

Besides illustrating slip, the FES and LES graphs aided in identifying trends and anomalies to help understand the bond mechanisms of each bar. Transition and divergence points were two of the trends identified on the LES graphs and examples of these are shown in Fig. 3.25 (M1-5-3-15.0-3) and Fig. 3.26 (M2-6-2-20.0-5) for the M1 and M2 bars, respectively. Similarly sample FES graphs are shown in Fig. 3.27 (M1-5-3-15.0-3) and Fig. 3.28 (M2-6-2-20.0-5) for the M1 and M2 bars, respectively. The transition points represented a change in

stiffness for the specimen: defined as the relative rate of slip versus loading. Initially the specimen exhibited linear stiffness with linear slip rates versus load. At transition points the specimen stiffness changed significantly and the linear slip curves changed to nonlinear or exhibited bilinear behavior. Hence, transition points were selected on the slip graphs for both types of GFRP rebar by placing a straight edge along the initial slip curve and manually selecting the point where the curve changed to nonlinear or exhibited bilinear behavior. The FES transition points were easier to identify because these curves consisted of a clear linear portion that changed slope significantly before failure. The transition points were recorded to the nearest 0.1 kips and 0.001 in. on LES curves and 0.0001 in. on the FES curves. Additionally, the loads associated with the FES transition points were noted on the LES graphs and the associated LES was recorded for comparison. Finally, a regression analysis was done to verify the linearity of the selected portion of the slip curves and all the R^2 values were above 0.9.

Divergence points observed on the LES graphs also represented a change in specimen stiffness, but a much more severe and widely varied change than represented by the transition points. Specifically, slip curves for a particular series would significantly "diverge" from each other with inconsistent and unpredictable rates of slip. This divergence was only observed in the LES curves for the M1 bars. The divergence points were identified on the individual LES curves; however, these points were easier to distinguish on graphs where the entire series of tests were plotted together. The divergence points were manually selected and recorded to the nearest 0.1 kips and 0.001 in. A selected divergence point for a typical M1 bar is shown in Fig. 3.25 (M1-5-3-15.0-3). These divergence points may have been caused by a shifting of the LES LVDT bracket due to a sudden change in strain along the outer coating of the M1 rebar. This sudden change in strain was probably related to bond behavior along the embedment length

The acoustic emission (AE) results provided qualitative information about the bonding mechanisms of each GFRP rebar type as well as some quantifiable information. Six graphs were developed from the AE data for each test and are included in Appendix F. A typical set of six AE graphs are shown in Figs. 3.29 and 3.30 for the M1 (M1-5-3-10.0-1) and M2 (M2-6-2-15.0-1) bars, respectively. The graphs in the examples are labeled with a letter and number for identification. The letter indicates the sensor type with "C" for concrete sensor graphs and "B" for bar sensor graphs. The number, from 1 to 3, indicates the row for the graph. The three graphs on the left are C1, C2 and C3, and the three graphs on the right are B1, B2 and B3. The

concrete sensor graphs (C) represent data collected from AE sensors placed at the beginning and end of the embedment length and a third point six to eight inches beyond the end of the embedment. The bar sensor graphs (B) represent data collected from AE sensors placed on the bar at the loaded and free end.

The top row of the graphs, C1 and B1, are "event" graphs with each symbol on these graphs representing an AE event plotted with respect to location and load. An AE event was defined in Section 2.10.4. The abscissa for the C1 graphs is the location of the event along the specimen centerline. The embedment length is identified in the figure label with the fourth set of numbers in the test code as discussed in Section 2.2 (e.g. M1-5-3-10.0-1 is for a test with a 10.0 in. embedment length). The abscissa for the B1 graphs is the location of the event along the bar. The embedded portion of the bar was between the two vertical lines identified on the B1 and B2 graphs. The ordinates for the C1 and B1 graphs are load in kips. The maximum ultimate loads (as given by the ordinates in the graphs) was 24 and 50 kips for the M1 and M2 rebar, respectively.

The middle row of graphs, C2 and B2, displays the number of cumulative events observed to occur during the tests within one inch increment lengths along the embedment length. The abscissa for the C2 graphs is given in one inch increments along the specimen center line with the embedment length identified as in the C1 graphs. The abscissa for the B2 graphs is given in one inch increments along the bar with the embedment length identified between the superimposed lines as in the B1 graphs. The ordinates for the C2 and B2 graphs are the cumulative number of events for the associated one inch increments. The maximum values for the ordinates were dependent on the amount of AE activity for a given test. The purpose of these graphs was to identify patterns in the distribution of events along the embedment length for the concrete and bar sensors. There were four types of patterns observed in the C2 graphs: decreasing, uniform/decreasing, increasing/decreasing and uniform. The decreasing pattern displayed a decreasing distribution of concrete AE events along the embedment length. The uniform/decreasing pattern displayed a uniform distribution of concrete AE events for several inches and then decreased along the embedment length. The increasing/decreasing pattern displayed an increasing distribution of concrete AE events for several inches and then decreased along the embedment length. The uniform distribution pattern displayed a generally uniform amount of concrete AE events along the embedment length. These patterns are shown in Figs.

3.31 and 3.32 for the M1 and M2 bars, respectively. Similar types of patterns were observed in the B2 graphs. These patterns are shown in Figs. 3.33 and 3.34 for the M1 and M2 bars, respectively.

The third row of graphs, C3 and B3, displays the number of cumulative events that occurred during one kip load increments during the tests for the concrete and bar sensors, respectively. The abscissas for the C3 and B3 graphs were the one kip increments up to the maximum loads for each bar. The ordinates for the C3 and B3 graphs were the total number of events for the associated one kip increments. The maximum values for the ordinates were dependent on the amount of AE activity for a given test. The purpose of these graphs was to identify the one kip load increment during which the largest number of AE events occurred. Two different peaks were observed for the M1 bars in the C3 graphs: during load peak (labeled "mid-load peak") and near ultimate load peak (labeled "ult load peak"). Examples of these peaks for the concrete sensors for the M1 bars are shown in Fig. 3.35. Only the "ult load peak" pattern was observed for the M2 bars with an example shown in Fig. 3.36. Both types of bars primarily exhibited the "ult load peak" pattern for the bar sensors in the B3 graphs. Examples of these peaks for the bar AE events in the B3 graphs are shown in Figs. 3.37 and 3.38 for the M1 and M2 bars, respectively.

The crack patterns for each test are given in Appendix E. Samples of the crack patterns are shown in Figs. 3.39 and 3.40 for the M1 (M1-5-3-10.0-6) and M2 (M2-6-3-15.0-6) bars, respectively. Each test crack pattern is displayed on a single page with six boxes of information. The bottom left corner box contains information identifying the specific test for the crack pattern and the bottom right corner box contains the drawing key. The remaining four boxes are the top, front and sides of the concrete specimen as if these elements were folded out from their 3-dimensional positions. The load associated with each crack were recorded and specifically the load for the first crack was identified. The first crack always formed on the top of the specimen orientated along the rebar centerline, near the beginning of the embedment length.

Distinct cracking patterns were associated with the two different GFRP rebar. Specifically, the M1 bars developed more cracking perpendicular to the embedment length along the top of the specimen than the M2 bars. The location and load of the first perpendicular cracks for each M1 bar test were recorded in the data tables (Tables 3.1 - 3.12) to the nearest 0.1 in. and 0.1 kips, respectively. Finally, the amount of cracking on the front face of the concrete specimen

was considered “fully developed” if the cracking extended from the embedded test bar down the front and across to the sides as shown in Figs. 3.39 and 3.40 for the M1 (M1-5-3-10.0-6) and M2 (M2-6-3-15.0-6) bars, respectively.

The AE results were carefully analyzed for the M1 rebar because of the significant perpendicular cracking in the concrete specimen during the bond tests. This type of cracking could have potentially isolated the initial concrete AE sensor along the embedment length. Two areas were checked to verify that this sensor was not significantly isolated. First, the pattern of hits on the concrete AE sensors were similar and this indicated that all the sensors remained active. Second, the concrete AE sensor near the loaded end did not exhibit any significant drop-off in activity during the testing.

The remaining ten rows of post-test results in the data tables were reported for both types of bars and some are described in detail below. These rows include the ultimate load recorded to the nearest 0.1 kips; the failure type; AE patterns and peaks for the C2, B2, C3 and B3 graphs; flexural stress on the extreme fibers at the LES LVDTs relative to the ultimate bar stress; bar modulus of elasticity (MOE) as measured during the tests; mean bond stress from Eqn. (1.1); and the amount of bar deformation damage observed after the test.

The seven different failure types seen during the primary bond tests were:

1) Concrete splitting failures, identified by “C”, as shown in Fig. 3.41,
2) Bar failures inside the embedment that resulted in the bar breaking into separate strands resembling “spaghetti”, identified by “IA”, as shown in Fig. 3.42,
3) Bar “spaghetti” failures outside the embedment, identified by “IB”, as shown in Fig. 3.43,
4) Bar “spaghetti” failures both inside and outside the embedment, identified by “IC”, as shown in Fig. 3.44,
5) Bar tensile failures inside the embedment with a complete “fracture” of the bar, identified by “IIA”. For M1 GFRP rebar this usually occurred at a coating mold joint as shown in Fig. 3.45,
6) Bar “fracture” failures outside the embedment, identified by “IIB”, as shown in Fig. 3.46,
7) Bar tensile failures within the grip system, identified as “III”, as shown in Fig. 3.47.

The four rows in the data table after the failure type are associated with the AE graphs. The following code was used to identify the pattern or peaks in the AE graphs, associated with the bars:

1) The distribution patterns in the AE C2 (concrete sensors) graphs were identified as "D" for decreasing, "UD" for uniform/decreasing, and "U" for uniform, as shown in Figs. 3.31 and 3.32 for the M1 and M2 bars, respectively.
2) The distribution patterns in the AE B2 (bar sensors) graphs were identified as "D" for decreasing, "UD" for uniform/decreasing, "ID" for increasing/decreasing, and "U" for uniform, as shown in Figs. 3.33 and 3.34 for the M1 and M2 bars, respectively.
3) The AE event peaks in the AE C3 (concrete sensors) graphs were identified as "M" for mid-load peak or "U" for ultimate load peak, as shown in Figs. 3.35 and 3.36 for the M1 and M2 bars, respectively.
4) The AE event peaks in the AE B3 (bar sensors) graphs were identified as "M" for mid-load peak or "U" for ultimate load peak, as shown in Figs. 3.37 and 3.38 for the M1 and M2 bars, respectively.
5) In all four rows of AE results an "X" identified that there was insufficient data to determine a pattern or peak for the AE graphs.

Flexural stress (f_b) was imposed on the test bars from the inverted half-beam setup and from any misalignment in the grips. Although the f_b value was not calculated along the embedment length, it was calculated at ultimate load for each test at the location of the LES LVDTs as discussed in Appendix D. Furthermore, the values shown in the data tables are for "relative induced flexural stress" which was the induced flexural stress at ultimate load (f_b) divided by the ultimate stress ($\omega_{ult} = P_u/A_{nominal}$). These values were calculated to permit comparison among the tests.

The modulus of elasticity (MOE) was calculated for each bar from the LES3 and LES4 LVDTs that recorded bar elongation outside the embedment length. Details of this instrumentation was given in Section 2.10.3. The stress-strain curves calculated from the LVDT results were usually linear to failure. However, some curves were cut off before failure because of LVDT malfunction. Overall the calculated MOEs were similar to the manufacturer's reported values.

Mean bond stress (σ) was calculated from Eqn. (1.1) for each test, regardless of the type of failure. The ultimate failure load (kips), embedment length (in.) and nominal bar diameter (in.) were used in the equation for determining the mean bond stress.

Finally, the last row in the data tables lists the bar deformations damaged during the test relative to the number of bar deformations available prior to the test. The number of bar deformations available was taken as the total bar deformations within the embedment length minus those damaged before the test, as recorded in row three of the data tables. The bar deformation damage values were obtained by examining the bars that were carefully removed from the concrete specimen after the tests. Additionally, close examinations were done on the exposed embedment length areas as shown in Figs. 3.48 and 3.49 for the M1 and M2 rebar respectively.

3.2.2 Results: Manufacturer 1, No. 5 Rebar, $3d_b$ Cover, 15.0 in. Embedment

The results for this series of tests are shown in Table 3.1. The average ultimate load for the 1M1-5-3-15.0 series was 19.0 kips with a standard deviation of 0.8 kips. The tests exhibited Type IB "spaghetti" bar tensile failures outside the embedment length. The tests were designed to have concrete splitting failures at 85% of f_u, 16.3 kips. The embedment lengths for this series were based on the Pilot Test results while recognizing that the $3d_b$ cover may result in greater ultimate loads. Details of the test design are discussed in Section 2.6.

The effect of several results on the ultimate load were investigated: pre-test deformation damage, measured cover, LVDT bracket attachment, bar failure location and relative induced flexural stress (f_b/ω_{ult}). Because all the tests exhibited the same type of bar failure, it is unlikely that the pre-test bar deformation damage, measured cover and bar failure location had an effect on the variability in the ultimate loads. Each bar developed sufficient bond within the embedment length, regardless of the deformation damage or confinement, to produce bar failure. However, the LVDT bracket attachment, located outside the embedment length, may have influenced the ultimate loads.

The bars in Tests 1 through 3 had no protection under the LVDT bracket attachment and their average ultimate load was 18.7 kips. Comparatively, the bar in Test 4 had duct tape protection and an ultimate load of 18.2 kips. The drop in ultimate load was not significant. Therefore the two different systems probably had the same limited effect protecting the outer

coating of the M1 bars. The bars in Test 5 and 6 had rubber and aluminum protection under the LVDT bracket attachment and their average ultimate load was 19.9 kips. It is possible that the superior bar protection contributed to the greater ultimate load.

The average relative induced flexural stress at the LES LVDTs was 0.09 and Test 6 had the largest value at 0.12. This test also exhibited the greatest ultimate load for the series; therefore, the relative induced flexural stress did not appear to influence the ultimate loads.

The FES graphs, as shown in Fig. 3.1, were similar and their transition points were included in the data table with an average 17.3 kips at an average FES of 0.0005 in. The LES graphs, as shown Fig. 3.2, were also similar, except that Test 1 had a different slip curve with less slope and some erratic movements during loading. The erratic movements consisted of jumps in slip without changes in load. These changes in slip may have resulted from improper LVDT attachment for this first test and therefore the LES divergence and transition point results were excluded from the data table. The remaining five tests had comparable LES curves up to their divergence points at an average of 12.7 kips and 0.026 in. LES. The LES transition point was at an average of 7.6 kips and LES of 0.009 in.

The crack patterns, as shown in Figs. E.2 through E.7, were generally similar with the first crack appearing at an average load of 10.2 kips. Additionally the tests had extensive perpendicular cracking with significant cracking across the concrete specimen front face. The fully developed cracks extended from the embedded bar down the loaded face and to the sides of the specimen.

The AE graphs are shown in Figs. F.2 through F.7. All the tests had decreasing or uniform/decreasing distribution patterns in the C2 graphs, except for Test 5 with insufficient concrete AE data to draw any specific conclusions. The tests had similar distribution of events in the C3 graphs with the largest number of concrete AE events beginning at an average load of 12 kips. Regarding the bar AE events, Tests 2 had a uniform distribution in the B2 graph and the remaining tests had decreasing or uniform/decreasing distributions on the same graphs. In general the largest number of bar AE events occurred at a location before the embedment length at a mold joint. All the tests had the largest number of bar AE events recorded at a load close to the ultimate load.

In summary, this series had bar failures that resulted from sufficient confinement ($3d_b$ cover) and embedment length (15.0 in.). Additionally, the LVDT bracket attachments may have

influenced the ultimate loads. However, the overall average ultimate load of 19.0 kips compared favorably with the tensile test average of 19.2 kips but was significantly less than the manufacturer reported capacity of 29.2 kips. In reviewing the other results, the concrete AE events appeared to be related to the perpendicular cracking and similarly the bar AE events appeared to be related to the location of the bar failure.

3.2.3 Results: Manufacturer 1, No. 5 Rebar, $3d_b$ Cover, 12.5 in. Embedment

The results for this series of tests are shown in Table 3.2. The average ultimate load for the 1M1-5-3-12.5 series was 19.0 kips with a standard deviation of 1.3 kips. Five of the tests exhibited concrete splitting failures. The other test, Test 4, exhibited a Type IIA bar failure at a mold joint inside the embedment with an ultimate load of 17.7 kips. The average ultimate load for the specimen with concrete splitting failures was 19.2 kips with a standard deviation of 1.3 kips. The embedment lengths for this series were based on the Pilot Test results while recognizing that the $3d_b$ cover may result in greater ultimate loads. Details of the test design are discussed in Section 2.6.

The effect of several results on the ultimate load were investigated: pre-test deformation damage, measured cover, LVDT bracket attachment and relative induced flexural stress (f_b/ω_{ult}). The ultimate load in Test 4 was probably not related to any of these effects because the test had zero pre-test deformation damage, average cover, rubber/aluminum bar protection under the LVDT bracket and less than average relative induced flexural stress. However the test still resulted in a bar failure with the lowest ultimate load in the series. The other five tests that failed in concrete splitting had similar pre-test deformation damage and measured cover, thereby eliminating these factors as possibly influencing the ultimate loads. Additionally the relative induced flexural stress did not appear to influence the ultimate loads because Test 1 had the largest value and the second largest ultimate load.

The FES graphs, as shown in Fig. 3.3, with the exception of Test 6 had the same general slope and shape with a transition point at an average 15.5 kips and 0.0006 in. The Test 6 FES curve had a transition point closer to its ultimate load than the other tests in the series. This indicates that the bar did not slip until near failure. The LES graphs, as shown in Fig. 3.4., with the exception of Test 6 were similarly shaped with a transition point at an average 7.3 kips and 0.008 in. and a divergence point at an average 12.9 kips and 0.025 in. The Test 6 LES curve did

not diverge. It continued nonlinearly to failure which is probably related to the greater transition load for the FES curve.

The crack patterns, as shown in Figs. E.8 through E.13, were generally similar with the first crack appearing at an average load of 10.4 kips. Generally there was significant perpendicular cracking and fully developed cracks across the concrete specimen front face. The front face cracking extended down from the embedded bar and across to the sides in the shape of an inverted letter "V". However, the specimen in Test 4, that exhibited a bar failure, did not have as much cracking as the specimen that displayed concrete splitting failures. This was expected because the test had a bar failure at a lower ultimate load, and therefore the specimen did not develop as much cracking as the concrete splitting failures with greater ultimate loads.

The AE graphs are shown in Figs. F.8 through F.13. All the tests had a decreasing distribution pattern in the C2 graphs, except for Test 6 with insufficient concrete AE data to determine any pattern. Additionally, the tests had similar event distribution in the C3 graphs, except for Test 2, with the largest number of concrete AE events beginning at an average load of 13 kips. Test 2 had the largest number of concrete AE events beginning near the ultimate load at 17 kips. Regarding the bar AE events in the B2 graphs, Tests 3 and 6 had a uniform distribution pattern, Test 1 had a increasing/decreasing distribution pattern, Test 2 had a decreasing distribution pattern and Tests 4 and 5 had insufficient bar AE data for analysis. Additionally, Tests 2 and 3 had the largest number of bar AE events recorded at the mold joint located before the embedment which indicates a potential weak point. Tests 1 through 3 had the largest number of bar AE events recorded near the ultimate load. Test 6 had the largest number of bar AE events beginning at 15 kips and Tests 4 and 5 had insufficient data for analysis.

In summary, this series of tests had one bar fracture failure inside the embedment length at a low load and five concrete splitting failures with loads that may have been approaching bar failure. The unique bar failure was not related to a lack of LVDT bracket bar protection nor excess pre-test deformation damage. Therefore the bar failure should be considered part of the M1 bar variability. Additionally, the bar failure ultimate load of 17.7 kips was less than both the tensile test average of 19.2 kips and the manufacturer reported capacity of 29.2 kips. However, the concrete splitting failures had an average ultimate load of 19.2 kips that matched the tensile test average. Considering this, the $3d_b$ cover and 12.5 in. embedment length may be near the development length required for these bars.

3.2.4 Results: Manufacturer 1, No. 5 Rebar, $3d_b$ Cover, 10.0 in. Embedment

The results for this series of tests are shown in Table 3.3. The average ultimate load for the 1M1-5-3-10.0 series was 17.5 kips with a standard deviation of 1.7 kips. There were four Type I "spaghetti" bar tensile failures outside or both inside and outside the embedment length. The average ultimate load for the four bar failures was 18.0 kips with a standard deviation of 1.9 kips. The two concrete splitting failures had ultimate loads of 16.0 and 17.3 kips with an average of 16.7 kips. The embedment lengths for this series were based on the Pilot Test results and recognizing that the $3d_b$ cover may result in greater ultimate loads. Details of the test design are discussed in Section 2.6.

The effect of several results on the ultimate load were investigated: pre-test deformation damage, measured cover, LVDT bracket attachment, bar failure location and relative induced flexural stress (f_b/ω_{ult}). The two specimen that failed in concrete splitting, Tests 1 and 6, had similar amounts of pre-test deformation damage and cover, but different LVDT bracket attachments. The concrete splitting failure of Test 1 which had a lack of bar protection indicates that the LVDT bracket attachment probably did not influence the failure type. The four bar failures could not be clearly related to the LVDT bracket attachment because Test 4 with the rubber/aluminum bar protection had an ultimate load of 16.8 kips which was less than the ultimate loads of Tests 2 and 3 with masking tape bar protection. However, Test 5 with the rubber/aluminum bar protection had the greatest ultimate load in the series.

The tests that exhibited bar failures had failure locations either outside or both inside and outside the embedment length. There did not appear to be any correlation between the bar failure location and the ultimate load values. The average relative induced flexural stress at the LES LVDTs was 0.11. Test 6 had the largest relative induced flexural stress of 0.20 and a slightly below average ultimate load. Comparatively, Test 3 had the smallest relative induced flexural stress of 0.07 and nearly the same ultimate load as Test 6. Therefore, the relative induced flexural stress did not appear to influence the ultimate loads.

The FES graphs, as shown in Fig. 3.5, were generally similar, except for Tests 1 and 3 which had steeper initial slopes and Test 2 with smaller slope after approximately 10 kips. The LES graphs, as shown in Fig. 3.6, were also generally similar for all six tests with a transition point at an average 7.4 kips and 0.009 in. and a divergence point at an average 13.1 kips and

0.025 LES in. However, the LES curves for Tests 4, 5 and 6 continued along their initial slopes to greater ultimate loads than the other three tests. The differences in the FES and LES curves may be related to the LVDT bracket attachments. Specifically, the LES curves for Tests 1, 2 and 3 may have been influenced by the LVDT bracket that damaged the outer coating of the rebar at the LES LVDT location.

The crack patterns, as shown in Figs. E.14 through E.19, were generally similar with the first crack appearing at an average load of 9.7 kips. Additionally, the tests had fully developed cracking across the front face of the specimen with cracks extending down from the embedded bar and across to each side. Overall the extent of cracking in the tests that failed in concrete splitting was more extensive than the tests that exhibited bar failures. Although much of this difference was observed in the cracking at the ultimate load for the tests that failed in concrete splitting.

The AE graphs are shown in Figs. F.14 through F.19. All the tests had decreasing or uniform/decreasing distribution patterns in the C2 graphs, except for Test 2 with insufficient concrete AE data to analyze. Tests 1, 3, 4 and 5 had the largest number of concrete AE events beginning at an average load of 11 kips as shown in the C3 graphs. Comparatively, Test 6 had the largest number of concrete AE events near the ultimate load (17 kips) in the C3 graph and Test 2 had insufficient concrete AE data to analyze. Regarding the bar AE events in the B2 graphs, Tests 1 and 5 had a uniform/decreasing distribution pattern in the B2 graphs, Test 2 had a increasing/decreasing distribution, Test 3 had a decreasing distribution and Tests 4 and 6 had insufficient bar AE data for analysis. Tests 1, 2 and 5 had the largest number of bar AE events near the ultimate load, Test 3 had the largest number beginning at 14 kips and Tests 4 and 6 had insufficient bar AE data for analysis.

In summary this series had two tests that failed in concrete splitting. The ultimate loads for the two tests were unaffected by the pre-test deformation damage, measured cover and LVDT bracket attachment type. There were four bar failures that may have been influenced by the LVDT bracket attachment; however, Test 4 with the rubber/aluminum protection had the lowest ultimate load for a bar failure. Finally, the average ultimate load for the four bar failures was 18.0 kips which was less than the tensile test average of 19.2 kips and the manufacturer capacity of 29.2 kips.

3.2.5 Results: Manufacturer 1, No. 5 Rebar, $2d_b$ Cover, 47.0 in. Embedment

The results for this series of tests are shown in Table 3.4. The average ultimate load for the 1M1-5-2-47.0 series was 17.8 kips with a standard deviation of 4.0 kip . The tests exhibited Type I "spaghetti" bar tensile failures with three tests failing outside the embedment length and three tests failing both inside and outside the embedment length. Bar failures were expected, because these bars were fully embedded over the entire length of the concrete half-beam.

The effect of several results on the ultimate load were investigated: pre-test deformation damage, measured cover, LVDT bracket attachment, bar failure location and relative induced flexural stress (f_b/ω_{ult}). Because the tests all exhibited bar failures the pre-test bar deformation damage and measured cover probably did not affect the variations in the ultimate loads. Each bar developed sufficient bond within the embedment length, regardless of the deformation damage or confinement factors, to cause a bar failure.

The LVDT bracket attachment, located outside the embedment length, may have influenced the ultimate loads. The average ultimate load for the first three tests with either masking tape or duct tape bar protection was 16.0 kips which was less than the average of 17.3 kips for the second three tests with rubber/aluminum bar protection. However, Test 2 (with masking tape protection) had an ultimate load of 21.9 kips which was greater than that measured in Tests 4 and 5 (with rubber/aluminum protection). This contradictory result shows that the variation in bar strength may have had more influence than the effects of the LVDT bracket attachments on the ultimate loads.

Tests 1, 3 and 4 exhibited spaghetti bar failures outside the embedment length and the other three tests exhibited the same bar failure both inside and outside the embedment length. The average ultimate load for tests that exhibited bar failures both inside and outside the embedment length was 19.6 kips and the average ultimate load for the other three tests was 15.9 kips. However, Test 5 had the second lowest ultimate load (14.3 kips) and failed both inside and outside the embedment length. It was inconclusive for these tests whether the failure location effected the ultimate loads.

The average relative induced flexural stress at the LES LVDTs was 0.10. Test 1 had the lowest relative induced flexural stress (0.06) and a below average ultimate load and conversely Test 5 had the greatest relative induced flexural stress (0.14) and the second lowest ultimate

load. Therefore, it was inconclusive for these tests whether the relative induced flexural stress influenced the ultimate loads.

The FES curves for this series, as shown in Fig. 3.7, were nearly vertical along the ordinate except for Tests 1 and 2. Test 1 had some minor slip initially in the positioning of the specimen and then exhibited a nearly vertical FES curve. However, only Test 2 exhibited some FES during loading. The LES graphs, as shown in Fig. 3.8, were also similar with a transition point at an average 7.3 kips and 0.010 in. and a divergence point at an average 12.4 kips and 0.026 in. Test 2 exhibited more LES than the other tests in the series which is related to a greater ultimate load and possibly the linear FES curve.

The crack patterns, as shown in Figs. E.20 through E.25, were generally similar with the first crack appearing at an average load of 9.8 kips. The amount of cracking appeared related to the magnitude of the ultimate loads. Generally the bars with greater ultimate loads had more perpendicular cracking farther along the embedment and more front face cracking than tests with lower ultimate loads.

The AE graphs are shown in Figs. F.20 through F.25. Tests 1, 4, 5 and 6 exhibited a uniform/decreasing pattern in the C2 graphs, Test 2 had a uniform distribution, and Test 3 had insufficient concrete AE data for analysis. In general the largest number of concrete AE events occurred at an average of 15 kips as shown in the C3 graphs. Regarding the bar AE events in the B2 graphs, Test 5 had a uniform distribution pattern, Test 4 had a decreasing distribution pattern, Test 6 had a uniform/decreasing distribution pattern and Tests 1 through 3 had insufficient data for analysis. The spike of bar AE events in Test 6 at approximately 25 in. was the location of a mold joint within the embedment length, but was not a source of overall bar failure. Tests 4 through 6 had the largest number of bar AE events occurring near the ultimate load as shown in the B3 graphs.

In summary, the purpose of this series was to investigate excessive embedment lengths with a reasonable amount of confinement from $2d_b$ bar cover. The tests with rubber/aluminum bar protection had an average ultimate load of 18.5 kips that was below the tensile test average of 19.2 kips and the manufacturer reported capacity of 29.2 kips. There were two tests with low loads, 12.9 and 14.3 kips, that should be considered part of the bar variability because they did not have any unique test characteristics that could explain their low values. Overall the LVDT

attachment effects were not conclusive because a test with only tape protection had a greater ultimate load than two tests with the rubber/aluminum protection.

3.2.6 Results: Manufacturer 1, No. 5 Rebar, $2d_b$ Cover, 15.0 in. Embedment

The results for this series of tests are shown in Table 3.5. The average ultimate load for the 1M1-5-2-15.0 series was 17.9 kips with a standard deviation of 3.1 kips. Five of the specimen exhibited bar failures and one specimen failed in concrete splitting. The specimen that exhibited Type I "spaghetti" tensile failures inside and outside the embedment had an average ultimate load of 17.0 kips and a standard deviation of 2.4 kips. The one specimen that failed in concrete splitting had an ultimate load of 22.5 kips. The tests were designed to have concrete splitting failures at 85% of f_u, 16.3 kips. This design load was based on the Pilot Test results with $2d_b$ cover and assumed a uniform bond strength distribution for embedment lengths near the development length. Details of the test design are discussed in Section 2.6.

The effect of several results on the ultimate load were investigated: pre-test deformation damage, measured cover, LVDT bracket attachment, bar failure location and relative induced flexural stress (f_b/ω_{ult}). Test 3 which failed in concrete splitting had slightly more pre-test deformation damage, average cover and only the duct tape LVDT bracket protection system. Because it exhibited the largest ultimate load, it did not appear to be influenced by these issues. Overall, the bar protection under the LVDT bracket did not appear to influence the ultimate loads for the five bar failures. The average for Tests 1 and 2 with the bar protected with duct tape was 16.9 kips and this was only slightly below the average ultimate load for Tests 4 through 6 at 17.1 kips with bars protected with the rubber/aluminum combination. However, Test 1 (with duct tape) had the highest ultimate load of the specimen that exhibited bar failures at 20.0 kips and Test 2 (with duct tape) had the lowest ultimate load at 13.7 kips.

The bar failure location did not appear to influence the ultimate loads for the tests because there were failures both inside and outside the embedment length. The average relative induced flexural stress at the LES LVDTs was 0.11. Test 6 had relative induced flexural stress of 0.20 and the second largest ultimate load for the series. Comparatively, Test 3 had the lowest relative induced flexural stress of 0.11 and the lowest ultimate load for the series. Therefore, the relative induced flexural stress did not appear to influence the ultimate loads.

The FES graphs, as shown in Fig. 3.9, were similar in shape and the transition point was at an average 17.1 kips and 0.0005 in. The LES graphs, as shown in Fig. 3.10, were also similar in shape with a transition point at an average 8.2 kips and 0.011 in. and a divergence at an average 11.6 kips and 0.021 in. The Test 6 LES curve was more erratic after the divergence point but this test did not have any other significant results that correlated to the erratic slip or realignment of the LVDT bracket.

The crack patterns, as shown in Figs. E.26 through E.31, were generally similar with the first crack appearing at an average load of 10.2 kips. The extent of the cracking appeared related to the magnitude of the ultimate loads. Typically tests with greater ultimate loads had more extensive cracking. Specifically Test 3 that failed in concrete splitting with the largest ultimate load had the most extensive cracking.

The AE graphs are shown in Figs. F.26 through F.31. There was varying distribution patterns of concrete AE events in the C2 graphs: Tests 1, 2 and 6 had uniform/decreasing distribution patterns, Test 4 had a decreasing distribution pattern, Test 3 had a uniform distribution pattern and Test 5 had insufficient data for analysis. The largest number of concrete AE events occurred close to the ultimate load at an average load of 17 kips for Tests 2, 3 and 4 as shown in the C3 graphs. Comparatively, the largest number of concrete AE events occurred during the load at an average load of 13 kips for Tests 1, 4, and 5. Regarding the bar AE events, Tests 2 and 6 had limited results. Tests 1 and 5 had decreasing distribution patterns on the B2 graphs, Test 3 had an increasing/decreasing distribution pattern and Test 4 had a uniform/decreasing distribution pattern on the B2 graph. In general, the tests displayed the largest number of bar AE events near the ultimate load as shown in the B3 graphs.

In summary, this series had five tests with bar failures and one test that failed in concrete splitting. The tests that exhibited bar failures were probably not influenced by the LVDT bracket attachment because Test 1 (with duct tape) had the largest ultimate load and Test 3 (with duct tape) failed in concrete splitting. The concrete splitting failure had an ultimate load of 22.5 kips which exceeded the tensile test average of 19.2 kips, while the average ultimate load for tests exhibiting bar failures was 16.4. Neither value approached the manufacturer reported capacity of 29.2 kips.

3.2.7 Results: Manufacturer 1, No. 5 Rebar, $2d_b$ Cover, 12.5 in. Embedment

The results for this series of tests are shown in Table 3.6. The M1-5-2-12.5 specimen were tested in both primary tests with six repeats in the first primary test and three repeats in the second primary test. The individual tests are identified with a "1-#" for the first primary tests and a "2-#" for the second primary tests. The average ultimate load for all nine tests was 16.4 kips with a standard deviation of 2.9 kips. Three of the first primary tests exhibited concrete splitting failures with an average ultimate load of 17.4 kips and the other three exhibited bar failures with an average ultimate load of 14.4 kips. The tests exhibiting the bar failures were one Type IIA "fracture" tensile failure and two Type I "spaghetti" tensile failures. All three tests in the second primary test exhibited concrete splitting failures with an average ultimate load of 17.4 kips. The overall average ultimate load for the six concrete splitting failures was 17.4 kips. The tests were designed to have concrete splitting failures at 70% of f_u, 13.4 kips, as discussed in Section 2.6. This design load was based on the Pilot Test results with $2d_b$ cover and assumed a uniform bond strength distribution for embedment lengths near the development length. The unexpected increase in ultimate load between the Pilot Test and Primary Test is difficult to explain because both tests had similar concrete strengths, covers, and embedment lengths.

The three specimen exhibiting bar failures in the first primary test included one test, 1-1, that was unique to all the other tests with an ultimate load of only 9.1 kips. The test also exhibited a Type IIA bar "fracture" failure outside the embedment length near the location of the LVDT bracket attachment. The only other similar test was 1M1-5-3-12.5-4 that exhibited a similar bar failure inside the embedment length, but with a greater ultimate load of 17.7 kips.

The effect of several results on the ultimate load were investigated: pre-test deformation damage, measured cover, LVDT bracket attachment and relative induced flexural stress (f_b/ω_{ult}). The two tests, excluding the previously discussed Test 1-1, resulting in bar failures were probably not dependent on the type of bar protection for the LVDT bracket attachment because Test 1-3 with duct tape protection had an ultimate load of 17.9 kips that was greater than Test 1-4 with the rubber/aluminum bar protection and an ultimate load of 16.1 kips. Additionally there did not appear to be any correlation between the pre-test bar deformation damage and cover compared to the test ultimate loads.

The average relative induced flexural stress at the LES LVDTs was 0.13. Test 1-1 had the largest relative induced flexural stress of 0.18, which may have influence the failure of that test. Test 2-3 had the next largest relative induced flexural stress of 0.16 and a slightly below average ultimate load. Therefore, it was inconclusive whether the relative induced flexural stress influenced the ultimate loads.

The FES graphs, as shown in Fig. 3.11, were similar for seven of the nine tests with the slip curves for Test 1-3 and 2-1 not recorded due to LVDT malfunction. The FES transition point was at an average 13.5 kips and 0.0005 in. The LES graphs, as shown in Fig. 3.12, were also similar for six of the nine tests with Tests 1-1 and 1-2 having different curves and no curve for Test 2-1 due to LVDT malfunction. Test 1-1, as previously discussed, had an LES curve that diverged at approximately 5 kips and continued to failure at 9.1 kips. Test 1-2 experienced erratic movements, possibly caused by the LVDTs being accidentally bumped, that resulted in negative LES values early in the test and less slope during the test. The remaining six curves had similar shapes with a transition point at an average 7.6 kips and 0.010 in. and a divergence point at an average 12.4 kips and 0.022 in.

The crack patterns, as shown in Figs. E.32 through E.40, were similar with the first crack appearing at an average load of 10.1 kips. Generally tests failing in concrete splitting had more perpendicular cracking that was farther along the embedment length than specimen exhibiting bar failures. Additionally, Test 1-1 did not have any cracking due to bar failure at a low ultimate load.

The AE graphs are shown in Figs. F.32 through F.40. There was a variation in the distribution patterns displayed in the C2 graphs: Test 1-1 had a decreasing distribution, Tests 1-2, 1-3, 1-5, 1-6, 2-1 and 2-3 had uniform/decreasing distributions, Tests 1-4 had a uniform distribution and Test 2-2 had insufficient data for analysis. Overall, the tests exhibited a peak of concrete AE events in the C3 graphs at an average load of 13 kips. Regarding the bar AE events in the B2 graphs, Tests 1-3 and 2-1 had uniform distribution patterns, Tests 1-6 had a uniform/decreasing distribution, Test 1-5 had a decreasing distribution pattern, Test 1-4 had an increasing/decreasing pattern and Tests 1-1, 1-2, 2-2, and 2-3 had insufficient bar AE data for analysis. All the tests had the largest number of bar AE events occurring near the ultimate load.

In summary this series successfully bridged the two primary tests with nearly identical concrete splitting failure results with similar average concrete compressive strengths, 6450 and

6340 psi, for the first and second primary tests, respectively. The three bar failures had a low overall average ultimate load of 15.5 kips which was significantly below the tensile test average of 19.2 kips and the manufacturer reported capacity of 29.2 kips. There was no clear cause for the low average, such as LVDT bracket attachment.

3.2.8 Results: Manufacturer 2, No. 6 Rebar, $3d_b$ Cover, 20.0 in. Embedment

The results for this series of tests are shown in Table 3.7. The average ultimate load for the 2M2-6-3-20.0 series was 35.9 kips with a standard deviation of 3.5 kips. The first four tests exhibited concrete splitting failures with an average ultimate load of 34.1 kips and the other two tests exhibited Type III bar failures in the grips with an average ultimate load of 39.5 kips. Because the rebar failed within the grip system the ultimate load does not accurately represent the tensile capacity of the bars. The embedment lengths for this series were based on the Pilot Test results while recognizing that the $3d_b$ cover may result in greater ultimate loads. Details of the test design are discussed in Section 2.6.

The effect of several results on the ultimate load were investigated: pre-test deformation damage, measured cover and relative induced flexural stress (f_b/ω_{ult}). Test 6 had a damaged deformation wrap prior to the test and still had an above average ultimate load. The measured concrete covers were similar for all six tests, thereby eliminating this factor as possibly influencing the ultimate loads. The average relative induced flexural stress at the LES LVDTs was 0.07. Test 5 with the largest ultimate load had an average relative induced flexural stress of 0.07 and Test 6 had an above average ultimate load and the lowest relative induced flexural stress. Therefore, the relative induced flexural stress did not appear to influence the ultimate loads.

The FES curves, as shown in Fig. 3.13, were similar with a transition point at an average 25.9 kips and 0.0004 in. The LES graphs, as shown in Fig. 3.14, were also similar with a transition point at an average 9.0 kips and 0.011 in. However, Test 5 did exhibit the greatest ultimate load and the associated FES and LES curves were higher on the graphs than the other tests in the series.

The crack patterns, as shown in Figs. E.41 through E.46, were generally similar. However, the average load of the first crack appearing on Tests 1 through 3 was 10.7 kips and the average load for Tests 4 through 6 was 26.2 kips. The difference did not appear related to

any of the other results and should be considered part of the concrete splitting test variability. The overall crack patterns appeared to be related to the type of failure. Tests 1, 3 and 4 which failed in concrete splitting had similar cracking along the embedment length with some minor perpendicular cracking. Additionally the tests had fully developed front face cracking that extended down the middle of specimen and out to the sides resembling an inverted "Y". However, Test 2, which also exhibited a concrete splitting failure, had limited perpendicular and front face cracking which was different than the other tests that failed in concrete splitting. Comparatively, Tests 5 and 6 which exhibited bar failures had limited cracking along the top and front of the specimen.

The AE graphs are shown in Figs. F.41 through F.46. Tests 1 and 4 had uniform distribution patterns of concrete AE events in the C2 graph and Tests 2 and 3 had uniform/decreasing distributions in the same graph. Tests 5 and 6 had insufficient concrete AE data for analysis. The largest number of concrete AE events occurred near the ultimate load as shown in the C3 graphs. Regarding the bar AE events in the B2 graphs, Test 2 had a decreasing distribution pattern, Test 3 had a uniform/decreasing distribution pattern, Test 5 had a uniform distribution pattern and Tests 1, 4 and 6 had insufficient AE bar data for analysis. The largest number of bar AE events occurred near the ultimate load as shown in the B3 graphs.

In summary this series had four similar concrete and two similar bar failures. Two of the four tests failing in concrete splitting had AE event distributions that may indicate a more uniform stress distribution. The two tests exhibiting bar failures had an average ultimate load of 39.5 kips which was less than the tensile test average and the manufacturer reported capacity of 43.5 kips. The lower average ultimate load from the bond tests was reasonable considering the bars failed in the grip system preventing them from achieving their true ultimate tensile capacity.

3.2.9 Results: Manufacturer 2, No. 6 Rebar, 3d_b Cover, 15.0 in. Embedment

The results for this series of tests are shown in Table 3.8. The average ultimate load for the 2M2-6-3-15.0 series was 29.2 kips with a standard deviation of 3.2 kips. The embedment lengths for this series were based on the Pilot Test results while recognizing that the 3d_b cover may result in greater ultimate loads. Details of the test design are discussed in Section 2.6.

Although the tests all exhibited concrete splitting failures, Test 3 had a unique cracking pattern that would indicate a different type of failure. The concrete specimen developed

cracking during loading on the sides as shown in Fig. 3.50 and at the end of the embedment length as shown in Fig. 3.51. Typically these cracks along the side and at the end of embedment length would appear at failure as part of a concrete splitting. However, these cracks appeared prior to failure and may indicate that the concrete specimen had a failure independent of the any of the typical bond failure modes.

The effect of several results on the ultimate load were investigated: pre-test deformation damage, measured cover and relative induced flexural stress (f_b/ω_{ult}). The pre-test deformation damage and measured covers were similar for all the tests, thereby eliminating these factors as possibly influencing the ultimate loads. The average relative induced flexural stress at the LES LVDTs was 0.11. Test 2 had the largest relative induced flexural stress of 0.11 and a below average ultimate load. However, Test 4 had the next largest relative induced flexural stress of 0.11 and the greatest ultimate load for the series. Therefore, it was inconclusive whether the relative induced flexural stress influenced the ultimate loads.

The FES graphs, as shown in Fig. 3.15 were similarly shaped for five tests with reliable LVDT data. The FES transition point was observed at an average load 21.4 kips and slip of 0.0005 in. Test 3 had an LVDT malfunction and only the ultimate load is indicated on the graph with a dashed horizontal line. The LES graphs, as shown in Fig. 3.16, were also similarly shaped for the four tests with reliable LVDT data. Test 1 in addition to Test 3 had an LVDT malfunction and only their ultimate loads are indicated on the graphs with a dashed horizontal line. The LES transition point was at an average 6.2 kips and 0.005 in.

The crack patterns, as shown in Figs. E.47 through E.52, were generally similar with the first crack appearing at an average load of 18.6 kips. Cracking occurred primarily along the embedment length with some perpendicular cracking. The front face of each concrete specimen had fully developed cracks that extend down the middle of the specimen and then branched out to each edge as an inverted “Y”.

The AE graphs are shown in Figs. F.47 through F.52. Tests 1 and 3 exhibited uniform/decreasing distribution patterns of concrete AE events in the C2 graphs and Tests 5 and 6 had uniform distribution patterns in the same graph. Tests 2 and 4 had insufficient AE data for concrete or bar event analysis. Additionally, Test 3 exhibited a large number of concrete AE events near the location of the perpendicular cracking as previously discussed. The largest number of concrete AE events occurred near the ultimate load as shown in the C3 graphs.

Regarding the bar AE events on the B2 graphs, Tests 1 and 6 displayed a uniform distribution pattern and Test 3 had an increasing distribution pattern. In addition to Tests 2 and 4, Test 5 had insufficient bar AE data for analysis. Additionally, Test 3 exhibited a large number of bar AE events near the location of the perpendicular cracking similar to the concrete sensors. The largest number of bar AE events occurred near the ultimate load for Tests 3 and 6 and began at 25 kips for Test 1.

In summary all of the specimen in this series failed in concrete splitting with Test 3 exhibiting a unique perpendicular crack during the loading that appeared to fracture the entire concrete half-beam. Additionally, the concrete and bar AE sensors both had a large number of events occurring near the location of this unique perpendicular crack. Unfortunately, the LVDTs malfunctioned for Test 3 and additional information was unavailable for comparison.

3.2.10 Results: Manufacturer 2, No. 6 Rebar, $2d_b$ Cover, 47.0 in. Embedment

The results for this three test series are shown in Table 3.8. The average ultimate load for the 2M2-6-2-47.0 series was 38.4 kips with a standard deviation of 6.3 kips. All three tests had bar failures with two of the tests exhibiting Type III bar failures within the grip system and the third test exhibiting a Type IA "spaghetti" tensile failure outside the embedment length. The test was designed for bar failures with the fully embedded bars.

The effect of several results on the ultimate load were investigated: pre-test deformation damage, measured cover and relative induced flexural stress (f_b/ω_{ult}). The tests had zero pre-test deformation damage and similar measured cover values, thereby eliminating these factors as possibly influencing the ultimate load. The average relative induced flexural stress at the LES LVDTs was 0.11. Values were only recorded for Tests 1 and 2 because the LVDTs malfunctioned for Test 3. Test 2 had the largest relative induced flexural stress of 0.12 and the greatest ultimate load for the series. It did not appear that the relative induced flexural stress influenced the ultimate loads.

The FES graphs, as shown in Fig. 3.17, included only a dashed horizontal line for the ultimate load for Test 3 because of an LVDT malfunction. The other two tests had generally vertical FES curves indicating zero slip to ultimate load without any transition points. The LES graphs, as shown in Fig. 3.18, also displayed only a dashed horizontal line for Test 3. Tests 1 and 2 had similar slip curves for the majority of the loading and a transition point at an average

12.6 kips and 0.011 in. Near the ultimate load, Test 2 had erratic slip movements caused by grounding noise in the LVDT system late in the test.

The crack patterns, as shown in Figs. E.53 through E.55, were generally similar with the first crack appearing along the embedment length at an average load of 16.8 kips. Tests 1 and 3 had similar crack patterns probably related to their close ultimate loads. Test 2 had a greater ultimate load but less cracking on the top and nearly none on the front face of the concrete specimen. This significant difference is difficult to explain because the specimen ages and covers were similar for the different tests. Therefore, the results should be considered due to concrete variability.

The AE graphs are shown in Figs. F.52 through F.54. Test 1 had a uniform distribution pattern of concrete AE events in the C2 graph and Test 2 had a decreasing distribution pattern. Both tests had the largest number of concrete AE events occurring near the ultimate load as shown in the C3 graphs. Test 3 had insufficient data for analysis. All the tests displayed a generally uniform distribution of bar AE events in the B2 graphs and the largest number of bar AE events was observed near the ultimate load as shown in the B3 graphs.

In summary this series had considerable variability in the ultimate load for the three fully embedded bars. The average ultimate load was 38.4 kips which was less than the tensile test average and the manufacturer capacity of 43.5 kips. The lower average was expected because two tests exhibited bar failures within the grip and those ultimate loads do not accurately reflected the rebar ultimate tensile capacity. However, the third test, which did not fail within the grips, was still below the tensile test average (ultimate load of 35.5 kips). Additionally, this test had LVDT and AE malfunctions that limit additional test analysis. Therefore, it is inconclusive whether the third test should be considered part of the rebar variability.

3.2.11 Results: Manufacturer 2, No. 6 Rebar, 2d_b Cover, 25.0 in. Embedment

The results for this series of tests are shown in Table 3.10. The average ultimate load for the 2M2-6-2-25.0 series was 37.5 kips with a standard deviation of 3.4 kips. Four of the tests exhibited concrete splitting failures with an average ultimate load of 36.0 kips and the other two tests exhibited Type III bar failures in the grip with an average ultimate load of 40.5 kips. The test was designed for 100% f_u that should have resulted in all bar failures. Although the cover did not change from the Pilot Test, rebar used in the Pilot Test was from a different manufacturer

(M3), and the estimated tensile strength of the M2 rebar was based on tensile tests of M2 bars from a different batch (30.0 kips as compared to 43.5 kips). In addition, the concrete strength differed considerably. As result, the embedment lengths calculated were approximately 10% less than required to achieve 100% f_u. The details of the design are discussed in Section 2.6

The effect of several results on the ultimate load were investigated: pre-test deformation damage, measured cover and relative induced flexural stress (f_b/ω_{ult}). There was no pre-test deformation damage and the measured cover was similar for all six tests. The average relative induced flexural stress at the LES LVDTs was 0.09. Test 5 had above average relative induced flexural stress and the second greatest ultimate load for the series. Comparatively, Test 3 had the lowest relative induced flexural stress and the lowest ultimate load for the series. Therefore, it did not appear that the relative induced flexural stress influenced the ultimate loads.

The FES graphs, as shown in Fig. 3.19, had similar initial slopes and a transition point at an average slip of 0.0004 in. and 34.4 kips. The LES graphs, as shown in Fig. 3.20, were similarly shaped with a transition point at an average 8.1 kips and 0.007 in. However, Test 6 had a unique slip change at approximately 22 kips with a drop in load and an increase in slip unlike the other slip curves. Additionally, Test 1 had some erratic slip near the peak load that was related to electric noise in the LVDT system.

The crack patterns, as shown in Figs. E.56 through E.61, were generally similar with the first crack appearing at an average load of 16.5 kips. Test 6 had a set of perpendicular cracking at approximately 22 kips that may have corresponded to the LES curve change as discussed above. Additionally it appeared that the amount of cracking was related to the type of failure. The concrete splitting failures had cracking along the embedment length with some perpendicular cracking and cracking across the front face of the concrete specimen that resembled an inverted "T". Comparatively, the two specimen exhibiting bar failures had less cracking on the concrete specimen top and front face.

The AE graphs are shown in Figs. F.56 through F.61. There were varying patterns observed with the concrete AE sensors as shown in the C2 graphs: Tests 1, 3 and 4 had uniform/decreasing distributions, Tests 5 had a uniform distribution, and Tests 2 and 6 had insufficient data for analysis. The tests with sufficient data had the largest number of concrete AE events near the ultimate load as shown in the C3 graphs. Regarding the bar AE data as shown in the B2 graph, Tests 1 and 2 had a uniform distribution pattern, Tests 3, 5 and 6 had a

increasing/decreasing distribution pattern and Test 4 had insufficient data for analysis. The largest number of bar AE events occurred near the ultimate load for all the tests except Test 3 which had a peak during the loading. Test 6 did have a group of bar AE events at approximately 22 kips, which was possibly related to the previously discussed cracking at that location.

In summary, this series had four tests which failed in concrete splitting and two tests which exhibited bar failures. The bar failure average of 40.5 kips was slightly below the tensile test average and the manufacturer reported capacity of 43.5 kips. However, the lower average was expected due to the failures within the grip system. Finally, the erratic LES for Test 6 at approximately 22 kips correlated with a perpendicular crack at that load and with AE events.

3.2.12 Results: Manufacturer 2, No. 6 Rebar, $2d_b$ Cover, 20.0 in. Embedment

The results for this series of tests are shown in Table 3.11. The average ultimate load for the 2M2-6-2-20.0 series was 36.0 kips with a standard deviation of 3.4 kips. Five of the specimen failed in concrete splitting and the other test exhibited a bar failure. The average ultimate load for the concrete failures was 35.0 kips with a standard deviation of 2.8 kips. Test 5 exhibited a Type III bar failure in the grip system with an ultimate load of 40.8 kips. The average concrete splitting failure ultimate load compared favorably with the design load of 34.8 kips based on a target stress of 80% f_u for specimen with $2d_b$ cover. The details of the design are discussed in Section 2.6

The effect of several results on the ultimate load were investigated: pre-test deformation damage, measured cover and relative induced flexural stress (f_b/ω_{ult}). Test 4 had one deformation wrap that was damaged before the test but this did not appear to influence the ultimate load. The measured cover varied for each test with Tests 1, 2, 5 and 6 having 1.50 in., Test 3 having 1.63 in. and Test 4 having 1.44 in. cover. Test 3 had a greater ultimate load than Test 4, but less than that of Test 6. Therefore the difference in covers did not appear to consistently affect the ultimate loads. The average relative induced flexural stress at the LES LVDTs was 0.08. Test 5 had the second largest relative induced flexural stress of 0.09 and the greatest ultimate load for the series. Therefore, it did not appear that the relative induced flexural stress influenced the ultimate loads.

The FES graphs, as shown in Fig. 3.21, had similar initial slopes for all the tests. Test 1 had an LVDT malfunction and only the ultimate load is shown with a dashed horizontal line on

the FES and LES graphs. The FES transition point was at an average 31.8 kips and 0.0006 in. The LES graphs, as shown in Fig. 3.22, were also similar for the tests except for Test 1 as previously discussed and Test 3 with a slightly lower initial slope. The LES transition point was at an average 8.8 kips and 0.007 in.

The crack patterns, as shown in Figs. E.62 through E.67, were generally similar with the first crack appearing at an average load of 15.8 kips. The typical pattern consisted of top cracks that generally followed the embedment length with some perpendicular cracking. Additionally the tests that exhibited bar failures had slightly less cracking but not enough to completely distinguish them from the tests that failed in concrete splitting.

The AE graphs are shown in Figs. F.62 through F.67. There were varying patterns observed with the concrete AE sensors as shown in the C2 graphs: Test 1 had an increasing/decreasing distribution, Tests 3 and 4 had uniform distributions, Tests 5 and 6 had uniform/decreasing distributions, and Test 2 had insufficient data for analysis. The tests with sufficient data had the largest number of concrete AE events near the ultimate load as shown in the C3 graphs. Regarding the bar AE data as shown in the B2 graph, Tests 1 and 3 had an increasing/decreasing distribution pattern, Tests 2, 4 and 6 had a uniform/decreasing distribution pattern and Test 5 had a decreasing pattern. The largest number of bar AE events occurred near the ultimate load for all the tests except Test 5 which had a peak during the loading at approximately 29 kips. This tests also exhibited the only bar failure within the series.

In summary this series had five tests that failed in concrete splitting and one test that exhibited a bar failure at an ultimate load of 40.8 kips that was close to the tensile test average and manufacturer reported capacity of 43.5 kips. The test that exhibited the bar failure also had corresponding AE data that indicated a local bar failure during loading. The slightly lower ultimate load was reasonable considering the failure occurred within the grip.

3.2.13 Results: Manufacturer 2, No. 6 Rebar, 2d_b Cover, 15.0 in. Embedment

The results for this series of tests are shown in Table 3.12. The average ultimate load for the 2M2-6-2-15.0 series was 27.2 kips with a standard deviation of 1.7 kips. All six tests failed in concrete splitting which compared favorably with the design load of 26.1 kips based on a target stress of 60% f_u for specimen with 2d_b cover. Details of the test design are discussed in Section 2.6.

The effect of several results on the ultimate load were investigated: pre-test deformation damage, measured cover and relative induced flexural stress (f_b/ω_{ult}). There was only one specimen that had pre-test deformation damage and it was associated with just a single occurrence. Test 4 had slightly less than average measured cover and Test 6 had more than average cover, but it did not appear to affect the ultimate loads. The average relative induced flexural stress at the LES LVDTs was 0.08. Test 6 had the largest relative induced flexural stress and an above average ultimate load. Therefore, it did not appear that the relative induced flexural stress influenced the ultimate loads.

The FES graphs, as shown in Fig. 3.23, were very similar with the exception of Test 1 having a transition point at a significantly lower load than the other five tests. Additionally, Test 4 had a lower ultimate load but a generally similar FES curve. Overall the FES transition point occurred at an average of 19.1 kips and 0.0005 in. The LES graphs, as shown in Fig. 3.24, were also nearly identical for all six tests with a transition point at an average of 9.4 kips and 0.010 in.

The crack patterns, as shown in Figs. E.68 through E.73, were generally similar with the first crack appearing at an average load of 18.5 kips. The typical pattern had a line of cracks along the embedment length with some perpendicular cracking, except for Test 5 that had no perpendicular cracking. All the tests had some cracking on the front face of the concrete specimen with a crack extending down from the embedded bar and branching out to the edges as an inverted "Y".

The AE graphs are shown in Figs. F.68 through F.73. There were varying patterns observed with the concrete AE sensors as shown in the C2 graph: Test 1 had a uniform distribution, Tests 2, 4 and 6 had uniform/decreasing distributions, Test 5 had an increasing/decreasing distribution and Test 3 had insufficient data for analysis. The tests with sufficient data had the largest number of concrete AE events near the ultimate load as shown in the C3 graphs. Regarding the bar AE data as shown in the B2 graph, Test 1 had a uniform distribution pattern, Test 2 had an increasing/decreasing distribution pattern, Test 5 had an increasing pattern and Tests 3, 4 and 6 had insufficient data for analysis. The largest number of bar AE events occurred near the ultimate load for all the tests.

Overall this series had similar results with all the tests failing in concrete splitting. Test 5 had a different crack pattern than the other tests but similar failure load, slip curves and AE results. The different crack pattern was possibly related to a local variation in concrete strength.

3.3 M1 GFRP Rebar Discussion

3.3.1 Overall Results

Primary Test results for the M1 rebar bond tests are plotted in Fig. 3.52 which shows the relationship between embedment length and ultimate load. The tests that exhibited bar failures are shown without reference to cover because there was sufficient confinement to contribute to a bar failure regardless of the amount of cover. Each test that failed in concrete splitting is shown with a symbol corresponding to the associated cover. The average values for each embedment length are connected by lines for $2d_b$ (dash) and $3d_b$ (solid) cover. Additionally, the four Pilot Test results for the No. 6 M1 bars with $2d_b$ cover, that failed in concrete splitting, are also included. The average tensile test ultimate load of 19.2 kips and the manufacturer capacity of 29.2 kips are shown with horizontal dash-dot lines. The dash-dot-dot lines represent the average tensile test value (19.2 kips) +/- two standard deviations (1.7 kips). All the failure loads for the tensile tests were between these values with a range of 15.8 to 21.1 kips.

As shown in Fig. 3.52 the majority of the ultimate loads for the bond tests were within +/- two standard deviations of the tensile test average failure load. There were four tests which exhibited bar failures which were not within the two standard deviation values. Of particular interest are the results for the fully embedded bars (47.0 in.) which exhibited bar failures, but with a large scatter of ultimate loads and two tests below the two standard deviation value. As discussed in Section 3.2.5 there were not any specific results to explain the low ultimate loads in the 47.0 in. embedment length series. Further analysis of this series is given in Section 3.3.2 which examines the variability of bond tests which exhibited bar failures. The other two tests below the two standard deviation value were tests 1M1-5-2-12.5-1 and 1M1-5-2-15.0-2. The first test failed at an ultimate load of 9.1 kips and should be considered part of the rebar variability because it exhibited a Type IIB failure (fracture outside the embedment length) which will be further discussed in Section 3.3.2. The second test had only duct tape protection under the LVDT bracket and this may have influenced the ultimate load as discussed in Section 3.2.6 for the 15.0 in. embedment length series. The remaining tests, which where within the two standard deviation limits, could have exhibit bar failures based on their failure loads and the tensile test average failure load.

The Pilot Test results shown in Fig. 3.52 should be compared carefully to the Primary Test results because of the difference in concrete compressive strengths. The average compressive strength for the Pilot Test was 7580 psi (range of 7160 to 8420 psi) compared to the Primary Test 1 average of 6450 psi (range of 5860 to 7160 psi). This difference would hypothetically result in greater ultimate loads for the Pilot Test specimens compared to similar embedment lengths for the Primary Test specimens. However, this effect was not consistently observed.

The M1 results are tabulated in Table 3.13 which lists each series with corresponding cover, embedment length, target $\%f_u$ (Section 2.6), average ultimate load for tests which failed in concrete splitting, the actual $\%f_u$, and the average ultimate load for tests which exhibited bar failures. In general, the series exhibited greater average ultimate loads than design as shown with the $\%f_u$ values in Table 3.13. The design embedment lengths for the series were calculated using Eqn. (1.4) with actual tensile test results for the M1 rebar, a $1/K_1$ averaged from the Pilot Test and a target concrete compressive strength of 4300 psi. The actual concrete compressive strength of the Primary Tests was 6450 psi. As a result the design embedment lengths were longer than required to achieve the desired $\%f_u$. Therefore, the relatively stronger concrete resulted in increased ultimate loads for tests that failed in concrete splitting and the actual $\%f_u$ exceeded the target $\%f_u$ for every series.

3.3.2 Variability

The variability of the M1 GFRP rebar bond tests was analyzed separately for tests that exhibited bar and concrete failures. Additionally, the hypothesis that increasing embedment lengths should cause an increase in the percentage of tests exhibiting bar failures was examined.

3.3.2.1 Variability of Bar Failures

There were twenty-five M1 rebar bond tests that exhibited bar failures as shown in Table 3.14. This table lists the individual bar failures with the associated type of bar protection for the LVDT attachment, failure type, relative induced flexural stress (f_b/ω_{ult}) and ultimate load. The notation for the LVDT attachment and failure type were outlined in Section 3.2.1. The f_b calculations were discussed in Section 3.2.1 and are outlined in Appendix D. The relative induced flexural stress value was not available for test 1M1-5-3-15.0-1 because the LVDTs malfunctioned. Average and standard deviation values of selected tests are given at the bottom

of the table. The first values were obtained from using all twenty-five bond tests that exhibited bar failures. The next values were obtained from ten tests selected from the bond tests that exhibited bar failures. The selected tests were chosen for factors discussed below. The third values were obtained from tensile tests conducted on the M1 rebar, as discussed in Appendix A. The final values were those reported by the manufacturer for tensile strength and standard deviation.

The average ultimate bar failure load for the twenty-five bar failures was 17.5 kips with a standard deviation of 2.9 kips. This average was less than the average tensile test ultimate load of 19.2 kips with a standard deviation of 1.7 kips and the manufacturer reported capacity of 29.4 kips with a standard deviation of 0.5 kips. The results were further analyzed for factors that would account for the difference and the following criteria were used to eliminate tests from inclusion:

1) type of bar failure observed (specifically bar fracture),
2) bars with damage associated with the LVDT bracket attachment,
3) bars with large amounts of relative induced flexural stress (f_b/ω_{ult}).

The first factor considered was the type of bar failure observed. There were two Type IA "spaghetti" failures inside the embedment length, fourteen Type IB "spaghetti" failures outside the embedment length, seven Type IC "spaghetti" failures both inside and outside the embedment length and two Type II "fracture" failures. Of the two Type II "fracture" failures, one occurred inside and one occurred outside the embedment length. These two unique Type II failures occurred at production mold joints on the M1 bars and represent possible local defects. However, there was a large difference in the ultimate loads between the Type IIA failure inside the embedment length (17.7 kips) and the Type IIB failure outside the embedment length (9.1 kips). These tests were excluded from the selected bar failure average because they represented anomalies.

The second factor considered was the impact of the LVDT bracket attachments, discussed in Sections 3.2.2 through 3.2.13 for each series individually. Without the rubber/aluminum protection system the outer coatings of the M1 bars were cracked due to the LVDT bracket screws. This cracking reduced the integrity of the bar and probably caused a reduction in the bar tensile capacity. To eliminate this influence, only tests with the rubber/aluminum protection were included in the selected bar failure average.

The third factor considered was the relative induced flexural stress (f_b/ω_{ult}) value as discussed in Section 3.2.1 and outlined in Appendix D. The effect of this stress was examined in Fig. 3.53 which shows a plot of the relative induced flexural stress versus ultimate load. As evident from this figure, increased relative induced flexural stress corresponded to a slight decrease in ultimate load. Therefore tests with excessive amounts of relative induced flexural stress, (i.e. greater than +/- two standard deviations) were excluded from the selected test average ultimate load. Based on this criteria, the ultimate load for test 1M1-5-2-15.0-6 was excluded from the average for the selected bar failures. Regarding the tensile tests, limited tests were instrumented with LVDTs and an accurate estimate of the f_b could not be calculated and compared to the bond tests which exhibited bar failure.

The selected average bar ultimate load was calculated after elimination of tests based on the three factors discussed above. The average for the selected tests was 18.2 kips with a standard deviation of 2.6 kips. This average was within approximately 5% of the tensile test average failure load, but was significantly less (38%) than the manufacturers reported tensile strength.

3.3.2.2 Variability of Concrete Splitting Failures

There were fourteen M1 bar bond tests that exhibited concrete splitting failures as shown in Table 3.15 including the three replicate specimen (2M1-5-2-12.5 series) tested as part of Primary Test 2. The table lists the individual concrete splitting failures with their associated ultimate loads. Additionally, average ultimate loads, standard deviations and coefficient of variation (COV) were calculated for each series. The COV is the standard deviation expressed as a percentage of the average ultimate load of each respective series. The COV ranged from 5.2 to 5.9%. The largest COV (5.9%) was observed in the 1M1-5-3-12.5 series.

3.3.2.3 Examination of Increasing Bar Failure Hypothesis

The hypothesis of increased embedment lengths increasing the likelihood of bar failures was examined using Fig. 3.54. In this figure the percentage of bar failures is plotted relative to the embedment length. The expected trend was an increase in tests that exhibited bar failures with increasing embedment lengths for the same amount of cover. This expected trend held true for tests with $2d_b$ cover. However, the trend was not observed for tests with $3d_b$ cover. There was a decrease in the percentage of bar failures with an increase in embedment length from 10.0

to 12.5 in. Both series were scrutinized, but there were not specific results to explain to the unexpected decrease in percentage of bar failures for the embedment length increase from 10.0 to 12.5 in. However, because the majority of the M1 bond tests had ultimate strengths within two standard deviations of the tensile test average failure load, a large percentage of bar failures could be expected for all series.

3.3.3 Effect of Embedment Length on Ultimate Load

Figure 3.52 was used to examine the effect of embedment length on the ultimate load for the M1 bars in the Primary Test. In general there was an increase in average ultimate load with increasing embedment length for tests that failed in concrete splitting. The average ultimate load for tests that failed in concrete splitting with $3d_b$ cover increased from 16.7 kips for 10.0 in. embedment length to 18.8 kips for 12.5 in. embedment length. Similarly, the average ultimate load for tests that failed in concrete splitting with $2d_b$ cover increased from 17.4 kips for 12.5 in. embedment length to 22.5 kips for one test at 15.0 in. embedment length. From these results it is probable that any increase in embedment length over 15 in. will result in a bar failure. However, the scatter of ultimate loads at 47.0 in. embedment length should be considered when examining the effect of embedment length on the ultimate load. These scattered failure loads indicate that the M1 bars have considerable variability in tensile strength which was not evident in the pure tensile test results.

The effect of cover, which will be discussed in the following section, can be seen in Fig. 3.52 by comparing the slopes of the average value lines. The average value line for tests with $2d_b$ cover appeared to be slightly steeper than those tests with $3d_b$ cover. However, their similarity indicates that the difference between 2 and $3d_b$ cover is minimal for the tests which exhibited ultimate loads within two standard deviations of the tensile test average failure load.

3.3.4 Effect of Cover on Ultimate Load

The analysis of the effect of cover on ultimate load focused on the concrete splitting failures. Figure 3.55 shows the relationship between the ultimate load for bond tests that failed in concrete splitting with 12.5 in. embedment length versus cover. This was the only embedment length which was common for 2 and $3d_b$ cover. The $2d_b$ cover tests had an average ultimate load of 17.4 kips for six tests. Comparatively, the $3d_b$ cover tests with the same embedment length had an average ultimate load of 18.8 kips for five tests. Therefore the influence on the ultimate

load for tests that failed in concrete splitting was an increase of 1.2 kips for an increase in cover from 2 to 3 bar diameters. This was expected because greater cover at similar embedment lengths should require greater load to cause a concrete splitting failure. However, this increase was insignificant when compared to the test COV for these series. The 1.2 kip increase was 6.4% of the average ultimate load for the $3d_b$ cover tests and was comparable to the 5.9% COV for the same tests. The minimal difference may have resulted from the majority of the tests at 12.5 in. embedment length falling between the tensile test average +/- two standard deviations. A more significant difference may have been found with shorter embedment lengths which hypothetically would have resulted in lower ultimate loads and greater percentage of concrete splitting failures.

3.3.5 Mean Bond Stress

The mean bond stress was examined for the M1 bars, regardless of the type of failure. The mean bond stress values were calculated for each test using Eqn. (1.1). Figure 3.56 shows the relationship between the mean bond stress for each test versus embedment length. The bar and concrete failures are shown with different symbols. Additionally, for the tests that failed in concrete splitting the results are shown with different symbols for different covers. The average values for each embedment length were calculated and are shown with a short horizontal line. The averages do not account for different covers, because cover did not appear to significantly influence the ultimate loads for these tests as discussed in Section 3.3.4. Additionally, the average for the fully embedded bars must be qualified because those bars were embedded significantly beyond the development length and theoretically the majority of the embedment length was probably under minimal bond stress. There was a pattern of decreasing mean bond stress with increasing embedment length. This pattern was expected because the distribution of bond stress was not uniform and further embedment length decreased the average values.

3.3.6 Development Length and $1/K_1$ Value

Based on the overall results, the M1 bars appeared to have a development length of 15.0 in. This was primarily based on the observation that eleven of the twelve tests at this embedment length exhibited bar failure. These results can also be seen in Fig. 3.52 as the ultimate loads for tests with 15.0 in. embedment length were at or near the tensile test average failure load. The eleven tests that exhibited bar failure had 2 and 3 bar diameter covers which indicates that both

these covers provided sufficient confinement in conjunction with the embedment length to result in a bar failure. The minimal effect of cover was also discussed in Section 3.3.3 and 3.3.4.

Based on the 15.0 in. embedment length, a tensile test average failure load of 19.2 kips and an average concrete compressive strength during Primary Test 1 of 6450 psi, a $1/K_1$ value of 15.9 was calculated using Eqn. (1.5). Although $1/K_1$ values have been proposed by other researchers for GFRP reinforcement (see Chapter 1 and Table 1.2), specific comparisons were avoided because their values were based on significantly different bars and types of tests. The calculated $1/K_1$ value for this test series was unique to the M1 rebar and the inverted half-beam setup for specimens without additional confinement reinforcement. There were not any other similar bars or test setups to facilitate a comparison.

3.3.7 Bond Behavior

The bond behavior of the M1 rebar was analyzed by hypothesizing the debonding sequence of the bars. This section outlines a debonding sequence for the M1 GFRP rebar as surmised from the test results. The debonding sequence is presented in three consecutive phases that were developed from selected M1 bond test results observed in Primary Test 1 and the replicate tests in Primary Test 2. The selected test results are shown in Table 3.16 which were taken for each series from Tables 3.1 through 3.12. The top row of this table identifies the series in each column and the failure type with the form "#/#/#." The first number in this sequence is the total number of bond tests in the series. The second and third numbers represent the number of bond tests exhibiting concrete splitting and bar failures, respectively. The selected results for the mechanism analysis are shown vertically with the associated average values for each series. Following the individual series results is the average and standard deviation across the five series for each of the results. The final column lists the results for the fully embedded M1 bars. This data was not included in the overall averages because the fully embedded tests investigated an embedment length beyond the development length.

The results in Table 3.16 are listed in the order of occurrence during the test. The first result is the LES transition point. This point is defined on the LES curves as the transition point from the initial linear to the nonlinear portion of the curve. The second result is the load at which the first crack appeared. The next three results occurred at approximately the same load during the test: the load and location of the first significant perpendicular crack, the load

increment that had the largest number of concrete AE events, and the load and location of the LES curve divergence. The next two results are the load and slip of the FES transition point and the beginning load (+/- 1 kips) for the peak bar AE events. The final result listed is the ultimate load.

The average values were considered for the selected results because they generally represented "during loading" activity. Based on these results, the bond behavior of the M1 GFRP rebar is discussed with a hypothesized general debonding sequence in the following three consecutive phases. Each phase is in italics and is followed by discussion and supporting evidence.

1) *Initial Bond Phase.* Bond stress began developing along the embedment length with a non-uniform distribution as the bar was loaded. This was a reasonable assumption based on research by Grundhoffer [6] on steel rebar with a deformation system that was found to rely on mechanical interlock for bond strength. In his investigation the strain distribution was measured with gages inserted into the steel rebar. In general, he found the bond stress peaked near the beginning of the embedment and decreased non-uniformly along the embedment length.

In the M1 tests reported herein, the concrete AE results provided evidence of a non-uniform bond stress distribution. The distribution of concrete AE events in the C2 graphs was non-uniform and typically decreased along the embedment length. Although these graphs are an end-state for each test they correlated with specific distributions of events in the C1 graphs as shown in Appendix F. For example, the uniform/decreasing distribution in the C2 graphs corresponded to concrete AE events on the C1 graphs which were observed primarily near the beginning of the embedment at low loads. The concrete AE events on the C1 graphs extended their distribution further along the embedment length with increasing load. In general, a uniform/decreasing distribution pattern was observed in 92% of the C2 graphs for tests that failed in concrete splitting. The remaining tests that failed in concrete splitting exhibited decreasing distributions of concrete AE events in the C2 graphs. The generally decreasing distributions indicates a non-uniform distribution of AE events that corresponded to a non-uniform bond stress.

The bond component adhesion would typically engage in the initial bond phase as proposed by Lutz et al. [16]. However, it appears the M1 rebar never developed significant adhesion as part of the bond mechanism. This theory was based on a close investigation of the

bars after testing that revealed a lack of concrete particles adhering to the M1 rebar and a lack of bar particles adhering to the concrete. Although some of these particles may have scraped off during loading, the bars were smooth to the touch both before and after the bond tests.

2) *Sustained bond phase.* With the lack of the adhesion bond component, the M1 bars relied on mechanical interlock for bond strength. The effectiveness of the mechanical interlock was investigated by Lutz et al. [16] who concluded steel rebar with rib face angles greater than 40 degrees rely on mechanical interlock for primary bond capacity and have a linear LES curve. The M1 GFRP rebar had distinct bar deformations with rib face angles greater than 40 degrees and probably developed mechanical interlock. Post-test examinations revealed that the embedded M1 rebar caused impressions in the surrounding concrete as shown in Fig. 3.48. In this figure the M1 rebar had been removed from the embedded portion and the impressions from the bar deformations are clearly shown. Additionally, the post-test examinations revealed that 37% of the deformations along the embedment sheared off the M1 rebar.

Lutz et al. [16] also concluded that generally linear LES curves result from rebar deformation systems which rely on mechanical interlock for bond strength. The initial portion of the LES curves for the M1 rebar were generally linear as shown in Figs. 3.2, 3.4, 3.6, 3.8, 3.10 and 3.12. However, the M1 rebar did exhibit a transition from linear to generally non-linear at an average load of 7.6 kips and slip of 0.009 in. which indicates the bond behavior changed. Shortly after this change, cracking began to appear on the surface of the specimen at an average load of 10.0 kips with a standard deviation of 0.4 kips.

Mechanical interlock continued to develop along the embedment length and resulted in an increase in the cracking observed on the specimen. The crack expanded perpendicularly and further along the embedment length. Perpendicular cracking initiated at an average load of 11.2 kips with a standard deviation of 0.7 kips ranging in location from 1.5 to 3.8 in. along the embedment length. Two other results, concrete AE event peaks and LES curve divergence, were related to the perpendicular cracking observed in the M1 bond tests. The concrete AE sensors detected an increasing number of events up to this perpendicular cracking load with the largest number of events occurring between 12 and 14 kips as shown in the C3 graphs. This particular pattern was observed in 67% of the tests that failed in concrete splitting. In addition to the AE results, the perpendicular cracking caused the LES curves to diverge at an average load of 12.6 kips and an average LES of 0.024 in. as shown in a typical M1 (M1-5-3-15.0-3) LES curve in

Fig. 3.25. This divergence may have resulted from a shift in the LVDT brackets due to a change in strain along the outer coating of the M1 rebar.

3) *Bond Failure Phase.* Near ultimate load the FES curves changed from linear to nonlinear as shown for a typical M1 (M1-5-3-15.0-3) FES curve in Fig. 3.27. The corresponding load at this point on the FES graph was dependent on the embedment length and amount of cover as shown in Table 3.17. The table lists the five M1 series in terms of cover and embedment length with their associated average FES transition loads. The amount of slip at this point was independent of the embedment length and occurred at an average of 0.0005 in. Based on these observations, it is apparent that there is an ultimate slip independent of embedment length that identifies an impending bond failure.

An increase of bar AE events also warned of an impending failure; 89% of the tests which failed in concrete splitting exhibited the maximum number of bar AE events in the one kip interval prior to the ultimate load. These results were taken from the number of bar AE events versus load graphs (B3) as shown in a typical AE graph for M1 (M1-5-3-10.0-1) bars in Fig. 3.29. Finally, the ultimate load was achieved for each test and the average results for the series are shown in Table 3.13.

3.4 M2 GFRP Rebar Discussion

Primary Test results for the M2 rebar bond tests are plotted in Fig. 3.57 which shows the relationship between embedment length and ultimate load for the M2 rebar. The tests that exhibited bar failures are shown without reference to cover because there was sufficient confinement to contribute to a bar failure regardless of the amount of cover. Each test that failed in concrete splitting is shown with a symbol corresponding to an associated cover. The average values for each embedment length are connected by lines for $2d_b$ (dash) and $3d_b$ (solid) cover. The average tensile test ultimate load and the manufacturer capacity of 43.5 kips are shown with horizontal dash-dot lines for the M2 rebar tested in Primary Test 2. The dash-dot-dot lines represent the average tensile test value and +/- two standard deviations (1.3 kips). All the failure loads for the tensile tests were between these values with a range of 41.9 to 45.0 kips. Additionally, results from two other tests are included in Fig. 3.57 for comparison: the three Pilot Test results for the No. 6 M3 bars with $2d_b$ cover that failed in concrete splitting and three similar bond tests from Retika for rebar from the M2 manufacturer with $2d_b$ cover [24]. The

manufacturer reported tensile strength for the M3 rebar tested in the Pilot Test and the tensile test average for Retika's M2 bars are shown with dashed lines bracketed with the appropriate symbols.

In Fig. 3.57 the majority of the tests were below the two standard deviation line. At these load levels the bond tests should have all failed in concrete splitting, which the majority of them did. Of the eight tests that exhibited bar failures, four were below the two standard deviation line and one was within one kip of the tensile test average minus two standard deviations (2M2-6-2-20.0-5 at 40.8 kips). Three of the four tests below the two standard deviation line exhibited bar failures within the grip and therefore their true ultimate loads were never achieved. Test 2M2-6-2-47.0-3 was the remaining test below the two standard deviation line and it exhibited a spaghetti bar failure within the embedment length at 35.5 kips. This failure at the 47.0 in. embedment length was closely examined; however, it was difficult to analyze because the LVDT and AE equipment malfunctioned. Therefore, the low failure load of 2M2-6-2-47.0-3 should be carefully considered when determining the variability of the M2 rebar.

Comparison of Retika's and the Pilot Tests results to the M2 Primary Tests must be done with caution because of the differences in concrete strength and rebar tensile capacity. As shown in Fig. 3.57, Retika's results (for her batch of M2 bars with a tensile capacity of 33.1 kips) with an f'_c of 5600 psi appeared to be comparable to the M2 rebar tested in Primary Test 2. Retika's results appear to be an extension of the dashed line connecting the average values of the specimen with $2d_b$ cover. However, because Retika's bars were from a different production batch of M2 bars, the bars might be expected to have different bond characteristics from the Primary Test 2 series (the ultimate tensile strength was quite a bit different between the two batches). Therefore, substantial comparisons should not be made concerning these results. For the Pilot Test results, similar bars from a different manufacturer were used (M3) and the Pilot Test f'_c was 7580 psi. As with Retika's results, substantial comparisons should be avoided because of these differences.

The M2 results are tabulated in Table 3.18 which lists each series with corresponding cover, embedment lengths, target $\%f_u$ (Section 2.6), average ultimate load for tests which failed in concrete splitting, the actual $\%f_u$, and average ultimate load for tests which exhibited bar failures. In general the series exhibited average ultimate loads comparable to the design $\%f_u$ as shown in Table 3.13. The embedment lengths for the series were designed using Eqn. (1.4) with

a tensile test average (30.0 kips) for a different batch of M2 bars than examined in the bond tests, a $1/K_1$ average from the Pilot Test and a concrete compressive strength of 4300 psi. The tensile strength average from an earlier (Retika's) batch of M2 bars was used for designing the M2 Primary Test embedment lengths because the tensile strength was not assumed to vary with the new batch of M2 bars. However, the actual tensile test average, as tested later, for Primary Test M2 bars was 43.5 kips. The effect of the increased actual tensile strength on the design embedment length was counteracted by the actual average concrete compressive strength of 6340 psi compared with the concrete design strength of 4300 psi. (i.e. increased f_u increased required embedment lengths and the increased f'_c decreased the required embedment lengths). The off-setting concrete strength and bar tensile capacity resulted in achievement of near design ultimate loads and $\%f_u$ during Primary Test 2. One test series with 25.0 in. embedment length and $2d_b$ cover failed to achieve the target $\%f_u$. Assuming linear bond characteristics, this series should have resulted in all bar failures, but only two of the six tests exhibited bar failures. Therefore, the relationship between ultimate load and embedment length is probably nonlinear as the embedment length approaches the development length. However, this nonlinearity is not represented in the development length Eqn. (1.4) which uses the $1/K_1$ empirical constant.

3.4.1 Variability

The variability of the M2 GFRP rebar bond tests was analyzed separately for tests that exhibited bar and concrete failures. Additionally, the hypothesis that increasing embedment lengths should cause an increase in the percentage of tests exhibiting bar failures was examined.

3.4.1.1 Variability of Bar Failures

There were eight M2 rebar bond tests that exhibited bar failures as shown in Table 3.19. This table lists the individual bar failures, failure type, relative induced flexural stress (f_b/ω_{dlt}) and ultimate load. The notation for the failure type was outlined in Section 3.2.1. The f_b calculations were discussed in Section 3.2.1 and are outlined in Appendix D. The relative induced flexural stress was not available for test 2M2-6-2-47.0-3 because the LVDTs malfunctioned. Average and standard deviation values are given at the bottom of the table. The first value is for the only test (2M2-6-2-47.0-3) which did not exhibit a bar failure within the grips. The next values were obtained from the tensile tests done on the M2 rebar, as discussed in Appendix A. The final value is the manufacturer reported tensile strength.

During the bond tests, there were seven Type III bar tensile failures that occurred within the grips and one Type IA "spaghetti" bar tensile failure that occurred within the embedment length. The relative induced flexural stress (f_b/ω_{ult}) was considered to possibly influence the ultimate loads, but Fig. 3.58 shows as the relative induced flexural stress increased the ultimate load also increased. This relationship was unexpected, because greater relative flexural stress should have caused a decrease in ultimate load. Additionally, the average relative induced flexural stress was 0.09 and the bond test values were all within two standard deviations of this value. Therefore, the relative induced flexural stress was not related to a decrease in ultimate load.

Based on the type of bar failures, it would be misleading to calculate the average ultimate load for the eight bar failures with seven failures within the grips. The only test to exhibit a bar failure not within the grips was 2M2-6-2-47.0-3 with an ultimate load of 35.5 kips. This load was below the tensile test average minus two standard deviations. As previously discussed, further analysis of this test was not possible because the LVDT and AE equipment malfunctioned. Comparatively, the tensile test average only included tests with failures that did not occur within the grips. However, the average for the bond tests which exhibited bar failures within the grips was 40.1 kips, which is comparable to the tensile test average and manufacturer's reported tensile strength of 43.5 kips.

3.4.1.2 Variability of Concrete Splitting Failures

There were twenty-five M2 bar bond tests that exhibited concrete splitting failures as shown in Table 3.20. This table lists the individual concrete splitting failures with their associated ultimate loads. Additionally, average ultimate loads, standard deviations and coefficients of variation (COVs) were calculated for each series. The COV is the standard deviation expressed as a percentage of the average ultimate load of each respective series. The COV ranged from 3.2 to 13.1%. The largest COV (13.1%) was observed in the 2M2-6-2-25.0 series. This larger COV may have been caused by the longer embedment length which allowed for a greater occurrence of bar variation that could have influenced the variation in ultimate loads.

3.4.1.3 Examination of Increasing Bar Failure Hypothesis

The hypothesis of increasing embedment length increasing the percentage of bar failures was examined using Fig. 3.59. In this figure the percentage of bar failures is plotted relative to the embedment length. The expected trend was an increase in tests that exhibited bar failures with increasing embedment lengths for the same amount of cover. This expected trend held true for the case of both the 2 and $3d_b$ covers.

3.4.2 Effects of Embedment Length on Ultimate Load

Figure 3.57 was used to examine the effect of embedment length on the ultimate load. In general, there was an increase in average ultimate load with increasing embedment length for tests that failed in concrete splitting. The average ultimate load for tests that failed in concrete splitting with $3d_b$ cover increased from 29.2 kips for 15.0 in. embedment length to 34.1 kips for 20.0 in. embedment length. Similarly, the average ultimate load for tests that failed in concrete splitting with $2d_b$ cover increased from 27.2 to 35.0 to 36.0 kips for 15.0, 20.0 and 25.0 in. embedment lengths, respectively. Additionally, the majority of the ultimate loads for the M2 bar bond tests were not within the tensile test average failure load +/- two standard deviations. Therefore, it appears Primary Test 2 embedment lengths only approached the development length for these bars.

The effect of cover, which will be discussed in the following section, can be seen in Fig. 3.57 by comparing the slopes of the average value lines between 15.0 and 20.0 in. embedment length. The average value line for tests with $2d_b$ cover appeared to be slightly steeper than those tests with $3d_b$ cover. Their similarity indicates that the difference between 2 and $3d_b$ cover was minimal. However, the average value line for the $3d_b$ cover flattened considerably after 20.0 in. embedment length.

3.4.3 Effects of Cover on Ultimate Load

The analysis of the effect of cover on the ultimate load focused on the concrete splitting failures. Figure 3.60 shows the relationship between the ultimate load for each bond test that failed in concrete splitting versus cover. Two embedment lengths, 15.0 and 20.0 in., had common bar covers with tests at both 2 and $3d_b$ cover. The tests with 15.0 in. embedment length had average ultimate loads of 27.2 and 29.2 kips for 2 and $3d_b$ cover, respectively. Comparatively, tests with 20.0 in. embedment length had average ultimate loads of 35.0 and 34.1

kips for 2 and $3d_b$ cover, respectively. The slight decrease in ultimate load indicates that 2 and $3d_b$ cover may not significantly influence the ultimate load for these bars. In comparison, the effect of cover on ultimate load was insignificant when compared to the COV for both series. The 15.0 in. embedment lengths exhibited a 2.0 kip increase in ultimate load from 2 to $3d_b$ cover which was 6.8% of the average ultimate load for the $3d_b$ cover tests. However, this percentage of increase was less than the 10.9% COV for the same series. Similarly, the 20.0 in. embedment lengths exhibited a 0.9 kip decrease in ultimate load from 2 to $3d_b$ cover which was 2.6% of the average ultimate load for the $3d_b$ cover tests. Again, this percentage of decrease was less than the 3.2% COV for the same series.

3.4.4 Mean Bond Stress

The mean bond stress was examined for the M2 bars, regardless of the type of failure. The mean bond stress was calculated for each test using Eqn. (1.1). Figure 3.61 shows the relationship between the mean bond stress for each test versus embedment length. The bar and concrete failures are shown with different symbols. Additionally, the associated covers for the tests that failed in concrete splitting are shown with different symbols. The average values for each embedment length were calculated and are shown with a short horizontal line. The averages do not account for different covers, because cover was not shown to significantly influence the ultimate loads as discussed in Section 3.3.4. Additionally, the average for the fully embedded bars must be carefully considered because those bars were embedded beyond the development length and theoretically a portion of the embedment length should have been without bond stress.

Regarding the average bond stress values for the M2 rebar in Primary Test 2, there was little change between 15.0 and 20.0 in. embedment lengths and then a decrease between the 25.0 and 47.0 in. embedment lengths. The limited change was expected because the M2 rebar were believed to rely on adhesion and friction which result in a more uniform bond stress over greater embedment lengths.

3.4.5 Development Lengths and $1/K_1$ Values

Based on the overall results, a specific development length was not clearly observed. The majority of tests exhibited concrete splitting failures. A specific embedment length (except the fully embedded bars) did not result in a majority of the tests exhibiting bar failures within a

series. However, a linear regression through the concrete splitting failures provides a minimum estimate of the development length for comparison. The linear regression through the concrete splitting failures intercepted the tensile test average and manufacturer's reported tensile strength (43.5 kips) at a 31.5 in. embedment length.

An upper bound $1/K_1$ value of 17.2 was calculated from Eqn. (1.5) based on the 31.5 in. embedment length, a tensile test average failure load of 43.5 kips, and an average concrete compressive strength during Primary Test 2 of 6340 psi. This value compares favorably to some of the other researcher's [22, 23] values for GFRP rebars as shown in Table 1.2. Specific variations between the values could have resulted from confinement reinforcement which would increase the $1/K_1$ value, differences between the GFRP rebar tested, type of test, and amount of cover or confinement reinforcement.

3.4.6 Bond Behavior

The bond behavior of the M2 rebar was analyzed by hypothesizing the debonding sequence of the bars. This section outlines a hypothesized debonding sequence for the M2 GFRP rebar as surmised from the test results. The debonding sequence is presented in three consecutive phases that were developed from selected M2 bond test results observed in Primary Test 2. The selected test results are shown in Table 3.21 which were taken for each series from Tables 3.1 through 3.12. The top row of this table identifies the series columns and the failure type with the form "#/#/#." The first number in this sequence is the total number of bond tests in the series. The second and third numbers represent the number of bond tests exhibiting concrete splitting and bar failures, respectively. The selected results for the mechanism analysis are shown vertically with the associated average values for each series. Following the individual series results is the average and standard deviation across the five series for each of the results. The final column lists the results for the fully embedded M2 bars. This data was not included in the overall averages because the fully embedded tests investigated an embedment length significantly the development length.

The results are listed in Table 3.21 in order of occurrence during the test. The first result is the LES transition point. This point is defined on the LES curve as the transition point from the initial linear to the nonlinear portion of the curve. The second result is the load at which the first crack appeared and the third result is the load and slip associated with the FES transition

point. The next two results are the average loads at which the largest number of events for the AE concrete and bar sensors were recorded, both of which were observed near the ultimate load. The final result listed is the ultimate load.

The average values were considered for the selected results because they generally represented the "during loading" activity. Based on these results, the bond behavior of the M2 GFRP rebar is discussed with a hypothesized general debonding sequence in the following three phases. The general action in each phase is in italics followed by discussion and supporting evidence from the Primary Tests.

1) *Initial Bond Phase.* Bond stress began developing along the embedment length with a more uniform distribution as the bar was loaded. Evidence of this was observed in the distribution of concrete AE events in the C2 graphs. Although these graphs are an end-state for each test they generally correlated with similar distributions of events in the C1 graphs as shown in Appendix F. For example, the uniform distribution in the C2 graphs corresponded to concrete AE events on the C1 graphs which were observed along the entire embedment length at various loads. A uniform distribution pattern was observed in 42% of the C2 graphs for tests that failed in concrete splitting. The remaining tests that failed in concrete splitting exhibited uniform/decreasing (53%) and increasing/decreasing (11%) distribution patterns of the concrete AE events in the C2 graphs. The limited percentage of uniform patterns may have resulted from cracking on the face of the specimen. This face cracking may have been recorded as concrete AE events near the beginning of the embedment length. However, in general these types of distribution patterns correspond to a more uniform bond stress distribution.

The bond component adhesion appears to have successfully engaged along the embedment length for the M2 rebar. Evidence of this bond component was observed in the forensic examination of the bars after the tests which showed concrete particles adhering to the rebar surface. However, at the loss of adhesion the M2 rebar was probably unsuccessful in developing mechanical interlock for bond strength because the rebar had rib face angles less than 30 degrees. Research by Lutz et al. [16] indicated that this configuration was not effective for mechanical interlock and the resulting LES curves were generally non-linear. Corresponding to this theory were the generally non-linear LES curves for M2 rebar shown in Figs. 3.14, 3.16, 3.18, 3.20, 3.22, and 3.24.

2) *Sustained Bond Phase.* Continued bond was accomplished through friction. This component was fairly effective because the adhesion component successfully bonded the bar with the concrete and the M2 rebar surface had a rough sand coated surface. The transition point in the LES curve, as shown in Fig. 3.26 for a typical M2 (M2-6-20.0-5) bond test, may have indicated the transition from adhesion to friction. The transition point occurred at an average load of 8.3 kips. Additionally, the friction component probably contributed to the more uniform concrete AE patterns in the C2 graphs as discussed above.

Eventually the continued loading resulted in cracks which appeared on the surface at an average load of 17.6 kips. The lack of significant perpendicular cracking indicated a more uniform bond stress distribution that relied on greater portions of the embedment length to develop bond strength.

3) *Bond Failure Phase*. Near ultimate load, the FES curve changed from linear to nonlinear as shown for a typical M2 (M2-6-20.0-5) FES curve in Fig. 3.28. This transition point was observed at a slip value of 0.0005 in. regardless of the embedment length, except for the fully embedded bars. This value identifies the ultimate slip that indicates an impending bond failure. However, the corresponding load at this point on the FES graph was dependent on the embedment length as shown in Table 3.22 which lists the five M2 series (not including the fully embedded bars).

An increase in AE events also warned of an impending failure. The largest number of bar and concrete AE events typically occurred within the one kip interval prior to the ultimate load. This pattern was observed for all the tests as shown in the C3 graphs and all but three of the tests as shown in the B3 graphs. Finally, the ultimate load was achieved for each test and the average results for the series are shown in Table 3.18.

3.5 GFRP Rebar Comparison

3.5.1 General Differences

The two GFRP rebar had distinct differences that should be noted before any comparisons are made:

1) Size: the M1 rebar tested was a No. 5 with a nominal cross-sectional area of 0.27 in.^{2} and the M2 rebar tested was a No. 6 with a nominal cross-sectional area of 0.44 in.^{2} The average cross-sectional difference between the rebar was observed to be 0.169

in.^{2} as determined with the Volume Displacement Method discussed in Appendix B. However, some results were normalized to account for the size to facilitate comparisons. Regardless of the normalization, the tensile strength of GFRP rebar has been observed to be affected by a "shear lag" phenomenon [3]. This phenomenon has been associated with a variation between the tensile force resistance of the core fibers and those on the surface in contact with the concrete. Therefore, care must be taken in making specific comparisons with regard to bar size.

2) Composite Structure: the M1 rebar tested was 70% (by weight) fibers and the M2 rebar tested was 76% (by weight) fibers. Although this was only a 6% difference in fiber content, it could account for a higher tensile stress capacity in the M2 rebar.
3) Deformation System: the M1 rebar tested had a smooth ceramic molded deformation system and the M2 rebar tested had a fiber wound and sand coated deformation system.

3.5.2 Bond Behavior Comparison

The most significant difference between the two GFRP rebar types was the general bond mechanisms as observed in the analysis of the bond behavior. The M1 rebar relied primarily on mechanical interlock without significant adhesion or friction resistance to develop bond along incremental portions of the embedment length. Comparatively, the M2 rebar relied primarily on friction, enhanced with adhesion, for bond resistance developed along greater portions of the embedment length. Additionally, the M2 rebar did not develop any significant mechanical interlock. The bond mechanisms for each rebar were based on analysis of the rebar surface condition, deformation geometry, slip curves, AE results, crack patterns and forensic investigations, each of these areas are discussed below.

The rebar surface condition established the initial bond phase for each GFRP rebar. The M1 rebar had a smooth ceramic outer coating and the M2 rebar had a rough sand coated surface. The smooth nature of the M1 rebar probably had difficulty developing friction. Comparatively, the M2 rebar developed greater frictional resistance which was enhanced by adhesion. Forensic examinations of the specimen revealed that concrete particles adhered to the M2 rebar, increasing the surface roughness and frictional resistance. Comparatively, the M1 rebar remained smooth. Additionally, there was significant cracking in the outer ceramic coating of

the M1 rebar and an average of 37% of the M1 ceramic deformations sheared off. Based on this analysis the M1 rebar appeared to rely primarily on mechanical interlock to develop bond strength and the M2 rebar appeared to rely on adhesion and friction.

The successful bearing on the surrounding concrete through mechanical interlock is based on the rib face angle of the bar deformations. Research by Lutz et al. [16] concluded that rib face angles greater than 40 degrees rely primarily on mechanical interlock for bond, whereas rib face angles less than 30 degrees rely primarily on adhesions and friction for bond. The M1 rebar had distinct bar deformations which developed bearing and mechanical interlock with the surrounding concrete. The M2 rebar had less distinct bar deformations with a wrapped deformation system which indented the core bar slightly and were less effective in developing bearing and mechanical interlock with the surrounding concrete.

A comparison of the slip curves also provided insight into the two GFRP rebar bond mechanism. Selected FES and LES curves for the M1 and M2 rebar were plotted versus bond stress per unit length in Figs. 3.62 and 3.63, respectively. The tests shown bracket the other tests for each GFRP rebar by representing the maximum and minimum curves with the majority of the remaining curves between. Regarding the LES curves, Lutz et al. [16] concluded that rebar which developed mechanical interlock would exhibit a more linear LES curve than rebar which rely on adhesion and friction for bond strength. Although not clearly seen in Fig. 3.63, the LES curves for the M1 rebar (Figs. 3.2, 3.4, 3.6, 3.8, 3.10, and 3.12) were steeper and generally more linear when compared to the LES curves for the M2 rebar (Figs. 3.14, 3.16, 3.18, 3.20, 3.22, and 3.24).

The bearing by the M1 rebar on the surrounding concrete resulted in a difference in cracking and associated concrete AE activity when compared to the M2 rebar. The mechanical interlock of the M1 rebar developed bond stress over a shorter portion of the embedment length. This stress resulted in a greater initial peak of stress in the concrete near the loaded end, causing earlier concrete cracking for the M1 rebar. Cracking was first observed at 10.0 kips for the M1 rebar, compared to 17.6 kips for the M2 rebar. Continued perpendicular cracking for the M1 rebar also indicated that incremental bonding occurred for these rebar. Perpendicular cracking was not observed for the M2 rebar. The concrete AE results were consistent with these cracking observations. The M2 rebar exhibited a more uniform distribution of concrete AE events which were observed in the AE C2 graphs. The M1 rebar exhibited a uniform/decreasing distribution

pattern of concrete AE events along the embedment length in 92% of the C2 graphs for tests that failed in concrete splitting. Comparatively, the M2 rebar exhibited the same distribution in only 53% of the C2 graphs and a uniform distribution pattern in 42% of the C2 graphs for tests that failed in concrete splitting. The overall results for the concrete AE event distribution are shown in Table 3.23. Based on these results it appears that the M2 rebar specimens had a greater portion of the embedment length under load. Hence, these bars had a more uniform bond stress which is associated with the adhesion and friction bond components.

Although the two rebar appeared to develop bond strength with two distinctly different systems, they did have some similarities in the FES graphs. In Fig. 3.62 the two FES curves for the GFRP rebar are displayed. There appears to be an overlap region and a common slip value where the curves transitioned from linear to nonlinear. This common transition point is shown on Fig. 3.62 with a vertical dashed line. The M1 and M2 rebar transitioned at the same average value of 0.0005 in. The averages do not include fully embedded bars which had generally vertical slip graphs and no transition points. The similar slip value for the FES transition points implies the bars had a similar ultimate slip value where the tests failed regardless of embedment length and load. This common FES slip value was similar to Retika's [24] value of 0.001 in. and significantly below Mathey's [13] slip criteria value of 0.0025 in. Mathey's value is for steel rebar and was determined from significantly different tests. However, the larger value indicates that steel rebar can sustain significantly more FES before bond failure.

3.5.3 Variability Comparison

As with the individual bars, the variability relative to failure type and failure rates were compared separately for the individual failure mechanisms (bar failure versus concrete splitting). Table 3.24 compares the coefficient of variations (COV) for tests that exhibited bar failures for each GFRP rebar. It is difficult to compare the bond test bar failure COVs because the M2 bars had only one test which exhibited a bar failure outside of the grip system. The M1 bars had COVs of 14.3 and 8.9% for the bond and tensile test bar failures, respectively. The M2 bars had a COV of 2.9% for the tensile test bar failures. These average COVs are based on the results excluding the unique failures (i.e. bar defects, LVDT bracket attachment effects, relative induced flexural stress, and grip failures with each bar in Sections 3.3 and 3.4 for the M1 and M2 rebar,

respectively). Table 3.25 compares the COVs for tests that failed in concrete splitting for each GFRP rebar. The M2 bar series had larger COVs (3.2 to 13.1%) than the M1 bars (5.2 to 5.9%).

The variation in ultimate loads from bond test bar failures and the tensile tests was directly related to the rebar quality. In addition to the large COVs observed for the M1 rebar, the difference between the manufacturer's reported tensile strength and the average tensile strength tested was a concern. Some of the difference may be related to testing procedures and setups, such as grip systems, which probably varied between the results reported here and the manufacturer reported values. However, such differences are unlikely to account for the large discrepancy which is more likely related to the quality and variability of the M1 rebar. Comparatively, the M2 rebar had a lower COV and, more importantly, the manufacturer's and tensile test averages were similar. This similarity validates the testing procedures and setups used to test both bars. However, both bars exhibited at least one low ultimate load for a bond test bar failure with a fully embedded bar. These failures are a concern because they failed in a test that simulates actual loading of a flexural member rather than a pure tensile test. Overall, it is critical to establish a reliable tensile strength in reinforcement to facilitate design with a reasonable expectation of material performance.

The variation in ultimate loads for the bond tests that failed in concrete splitting was related to the rebar quality, concrete variation and the ability to reproduce the testing procedures and setup for each test. However, it is difficult to compare the results because the M1 bars exhibited the majority of the failures within two standard deviations of the tensile test average and conversely the M2 bars exhibited the majority of the failures below the two standard deviation limit. Therefore, the majority of the M1 concrete splitting failures may have been on the verge of exhibiting a bar failure with a relatively lower COV. The M2 bars were definitely in the zone of loads for predominately concrete splitting failures. Hence, the M2 bars were subject to the greater combined variations in the bar and concrete.

3.5.4 Development Length and $1/K_1$ Comparison

The development length was difficult to compare for these tests at 2 or $3d_b$ cover and a concrete strength of approximately 6400 psi (average of the two Primary Tests). The No. 5 M1 rebar required 15.0 in. to fully develop the tensile capacity (19.2 kips) compared to 31.5 in.

(estimated through linear regression) for the M2 rebar to fully develop its tensile capacity (43.5 kips). The large difference in tensile capacity obviously affects the required development length.

The $1/K_1$ empirical constant, which was determined from the development length for each GFRP rebar, provides a normalized variable for comparison. The $1/K_1$ values were similar with 15.9 and 17.2 for the M1 and M2 rebar, respectively. This was unexpected because the $1/K_1$ constant accounts for bar surface conditions, bar properties and confinement. Considering these values the M2 rebar would require slightly less development length for a similar size GFRP rebar with similar confinement and concrete strength.

3.5.5 Recommendation

Considering all the previously discussed issues for each bar, neither is unconditionally recommended for immediate use as bridge deck reinforcement. The M1 rebar developed bond strength with mechanical interlock, which appeared effective but susceptible to degradation when the outer coating cracked. Additionally, the M1 rebar had a larger COV for bar failures with two unique fracture failures during the bond tests associated with mold joints along the rebar. Comparatively, the M2 rebar developed bond strength with adhesion and friction. However, the M2 rebar exhibited larger COVs relative to concrete splitting failures and both bars exhibited at least one unexpectedly low ultimate load for a fully embedded bar.

Chapter 4: Conclusions

4.1 General

The results of this study furthered the understanding of GFRP rebar bond mechanisms for two significantly different GFRP rebar. The following summarizes the findings, recommendations and needs for future research.

4.2 Conclusions

The two GFRP rebar included in the study differed in size, composite structure and deformation system. Considering the rebar surface condition, deformation geometry, slip curves, AE results, crack patterns and forensic investigations, two distinctly different bond behaviors were observed.

The M1 rebar relied primarily on mechanical interlock to develop bond strength. This bond mechanism for the M1 rebar was postulated by observing the distinct bar deformations which imprinted into the surrounding concrete and lack of concrete particles found adhered to the smooth rebar surface in the forensic investigations. The distinct bar deformations developed bearing on the surrounding concrete that led to a generally linear initial LES curve, lower loads for initial cracking, significant perpendicular cracking and unique AE patterns. This type of bond development corresponded to an incremental and less uniform bond behavior along the embedment length. It was observed that for these bond tests that the ultimate load for the M1 rebar was affected by embedment length changes but did not significantly vary for tests with 2 and $3d_b$ cover. The lack of influence from cover was unexpected for the M1 rebar which relied on mechanical interlock for bond strength. However, the majority of the M1 bond tests achieved ultimate loads within two standard deviations of the tensile test average. Hence, these results may not clearly define the effect of cover on ultimate load for the M1 bars. Finally, a development length of 15.0 in. was selected for No. 5 M1 rebar with 2 or $3d_b$ cover at a concrete compressive strength of 6450 psi. A corresponding $1/K_1$ value for the 15.0 in. development length was found to be 15.9.

The M2 rebar relied primarily on adhesion and friction to develop bond strength. These bond mechanisms were postulated based on the rough surface condition of the bar, shallow indented bar deformations from wrapped fibers, and the identification of concrete particles found adhered to the rebar in the forensic investigations. This type of bond development, with a more

uniform bond stress over a greater portion of the embedment length, corresponded to generally nonlinear initial LES curves, higher loads for initial cracking, lack of perpendicular cracking and unique AE patterns. The ultimate load for the M2 bond tests was affected by embedment length changes but did not significantly vary for tests with 2 and $3d_b$ cover. Finally, a development length was selected by conducting a linear regression through the concrete splitting failures to the tensile test average and reported manufacturer's tensile strength of 43.5 kips. The resulting development length was 31.5 in. for No. 6 M2 rebar with 2 or $3d_b$ cover at a concrete compressive strength of 6340 psi. A corresponding $1/K_1$ value for this length was found to be 17.2.

Regarding the variability of the bars, the M1 rebar had a greater variation than the M2 rebar in ultimate loads for tensile test bar failures. However, both the M1 and M2 rebar had bond tests for bars embedded 47.0 in. which exhibited a bar failure at an ultimate load less than the tensile test average minus two standard deviations. These failures should be considered part of the individual rebar variability. Regarding the variability for bond tests which failed in concrete splitting, the M2 rebar had a greater variation in ultimate loads than the M1 rebar. The difference in variation may be related to the different bond mechanisms or the longer embedment lengths investigated for the M2 rebar which would have resulted in a greater influence by concrete variations.

Based on the overall results, neither GFRP rebar is unconditionally recommended for immediate use as reinforcement in bridge decks. The primary concerns for the M1 GFRP rebar were the cracking of the outer coating which influences the bar deformations and the large COV for bar failures with an average significantly below the reported manufacturer's value. The M1 rebar exhibited two bar fractures and several bar failures in the bond tests with ultimate loads significantly below the tensile test average minus two standard deviations. Two of these bar failures below the two standard deviation limit were fully embedded bars. The M2 rebar did have a slightly larger value than the M1 rebar for the $1/K_1$ empirical constant (17.2 compared to 15.9) which indicates that the M2 rebar requires less development length for similar size rebar in similar confinement and concrete strength conditions. Finally, both bars exhibited at least one unexpectedly low ultimate load for a fully embedded bar.

4.3 Recommendations for Future Research

There are still a number of unresolved issues regarding the bond mechanism of GFRP rebar. Unfortunately, the number of issues is multiplied by the many different types of GFRP currently available which should be individually tested to understand their bond mechanisms and properties. For example, the M1 and M2 rebar were significantly different in many aspects and therefore yielded different results.

1) Bond and tensile tests need to be standardized and specifically designed for FRP rebar which would facilitate for comparison of research results. Currently, the large variation in testing procedures limits comparisons.
2) The long term durability and vulnerability of the GFRP rebar is unknown at this time. Specific studies need to address these concerns prior to application of the GFRP rebar as reinforcement in bridge decks.
3) The effect of bridge deck cracking on GFRP reinforcement needs to be investigated. These effects could result in durability and local strain problems which are also not fully understood at this time.
4) Additional tests and investigations are needed to establish a reliable grip system for the M2 rebar because bar failures must be avoided in the grip to facilitate accurate testing.

REFERENCES

1. Bedard, Claude, "Composite Reinforcing Bars: Assessing Their Use in Construction," *Concrete International*, Jan. 1992, pp. 55-59.
2. Emmons, Peter H., and Alexander M. Vaysburd, "Corrosion Protection in Concrete Repair: Myth and Reality," *Concrete International*, Mar. 1997, pp. 47-56.
3. Ehsani, M. R., H. Saadatmanesh, and S. Tao, "Design Recommendations for Bond of GFRP Rebar to Concrete," *Journal of Structural Engineering*, Mar. 1996, pp. 247-254.
4. Erki, M.A., and S.H. Rizkalla, "FRP Reinforcement for Concrete Structures," *ACI Compilation: Fiber Reinforced Plastic Reinforcement*, 1997, pp. 3-8.
5. *State of the Art Report: FRP Reinforcement, 440R-32*, American Concrete Institute, Detroit, MI, 1996.
6. Grundhoffer, T.M., "Bond Behavior of Uncoated and Epoxy-Coated Reinforcement in Concrete," University of Minnesota, Masters Thesis, 1992.
7. Benmokrane, B., B. Tighiouart, and O. Chaallal, "Bond Strength and Load Distribution of Composite GFRP Reinforcing Bars in Concrete," *ACI Materials Journal*, May-June 1996, pp. 246-253.
8. Larralde, J., J. Burdette, and B. Harris, "Bond Stress Distribution of RP Bars in Concrete," *38th International SAMPE Symposium*, May 1993, pp. 1775-1788.
9. *Standard Test Method for Comparing Concretes on the Basis of the Bond Developed with Reinforcing Steel*, *C234-91a*, American Society for Testing and Materials, Philadelphia, PA, 1991.
10. *Standard Specification for Epoxy-Coated Seven-Wire Prestressing Steel Strand, A882-96*, American Society for Testing and Materials, Philadelphia, PA, 1996.
11. *Building Code and Commentary, 318*, American Concrete Institute, Detroit, MI, 1995.
12. Orangun, C.O., J.O. Jirsa, and J.E. Breen, "A Reevaluation of Test Data on Development Length and Splices," *ACI Journal*, Mar. 1977, pp. 114-122.
13. Mathey, Robert G., and David Watstein, "Investigation of Bond in Beam and Pull-Out Specimens with High-Yield-Strength Deformed Bars," *Journal of the American Concrete Institute*, Mar. 1961, pp. 1071-1090.
14. Daniali, S., "Development Length for Fibre-Reinforced Plastic Bars," *Advanced Composite*

Materials in Bridges and Structures, edited by K.W. Neale and P. Labossiere, 1992, pp. 179-188.

15. *Standard Test Method for Comparing Bond Strength of Steel Reinforcing Bars to Concrete Using Beam-End Specimens*, *A944-95*, American Society for Testing and Materials, Philadelphia, PA, 1995.
16. Lutz, Leroy, and Peter Gergely, "Mechanics of Bond and Slip of Deformed Bars in Concrete," *ACI Journal*, Nov. 1967, pp. 711-721.
17. Johnston, David, and Paul Zia, "Bond Characteristics of Epoxy-Coated Reinforcing Bars," *Report No. FHWA-NC-82-002, Federal Highway Administration*, Washington D.C., 1982.
18. Tepfers, Ralejs, and Mats Karlsson, "Pull-Out and Tensile Reinforcement Splice Tests Using FRP C-Bars™," *Non-Metallic (FRP) Reinforcement for Concrete Structures*, *Proceedings of the Third International Symposium,* Vol. 2, Oct.1997, pp. 357-364.
19. Rizkalla, Sami, "Material Properties of C-Bar™ Reinforcing Rods," Research Report, unpublished, 1997.
20. Larralde, J., J. Mueller-Rochholz, T. Schneider, and J. Willmann, "Bond Strength of Steel, AFRP and GFRP Bars in Concrete," *Second International Conference on Composites in Infrastructure*, edited by H. Saadatmanesh and M.R. Ehsani, 1998, pp. 92-101.
21. Makitani, E., I. Irisawa, and N. Nishiura, "Investigation of Bond in Concrete Member with Fiber Reinforced Plastic Bars," *Fiber-Reinforced-Plastic Reinforcement for Concrete Structures - Int'l Symposium*, 1993, pp. 315-323.
22. Tighiouart, B., B. Benmokrane, and D. Gao, "Investigation of the Bond of Fiber Reinforced Polymer (FRP) Rebar in Concrete," *Second International Conference on Composites in Infrastructure*, edited by H. Saadatmanesh and M.R. Ehsani, 1998, pp. 102-112.
23. Faza, Salem S., and Hota V.S. GangaRao. "Bending and Bond Behavior of Concrete Beams Reinforced with Plastic Rebar," *Transportation Record 1290*. Washington D.C., 1990, pp. 185-193.
24. Retika, Annie C., "Thermal and Mechanical Fatigue Effects On GFRP Rebar-Concrete Bond," University of Minnesota, Masters Thesis, 1996.
25. Ohtsu, M., "The History and Development of Acoustic Emission in Concrete Engineering," *Magazine of Concrete Research*, 48, No. 177, Dec. 96, pp. 321-330.

26. Reinhardt, Hans W., Liane Gollas, Bernd Weiler, Christian Grosse, and Klaus Eberle, "Non-Destructive Assessment of Bond Deterioration of Aramid in Reinforced and Prestressed Concrete," *Non-Metallic (FRP) Reinforcement for Concrete Structures*, Volume 2, Oct. 1997, pp. 397-404.
27. Balazs, G.L., C.U. Grosse, R. Koch, and H.W. Reinhardt, "Damage Accumulation on Deformed Steel Bar to Concrete Interaction Detected by Acoustic Emission Technique," *Magazine of Concrete Research*, Vol. 48, No. 177, Dec. 1996, pp. 311-320.
28. Hearn, Stephen, and Carol K. Shield, "Acoustic Emission Monitoring as a Nondestructive Testing Technique in Reinforced Concrete," *ACI Materials Journal*, November-December 1997, pp. 510-519.
29. Holte, L.E., C.W. Dolan, and R.J. Schmidt, "Epoxy Socketed Anchors for Non-Metallic Prestressing Tendons," *Fiber-Reinforced-Plastic Reinforcement for Concrete Structures - International Symposium*, 1993, pp. 318-400.

TABLES

Table 1.1 Steel $1/K_1$ Values

Researcher	Type of Tests	Confinement Reinforcement	Size	Cover ($\#d_b$)	$1/K_1$
Grundhoffer [6]	inverted half-beams	no	No. 6 No. 8 No.11	2.0	coated 32.8 uncoated 34.5
Larralde [20]	notch beams	yes	No.3	unk	35.7
Retika [24]	inverted half-beams	no	No. 6	2.0	39.8*

* short embedment lengths

Table 1.2 GFRP $1/K_1$ Values

Researcher	Type of Tests	Confinement Reinforcement	Size	Cover ($\#d_b$)	$1/K_1$
Rizkalla [19]	T-beams	yes	No. 4	n.a.	46.0
Daniali [14]	notch beams	yes	No. 6 No. 8	2.0 1.8	29.6 25.1
Larralde [20]	notch beams	no	No.3	unk	13.7
Makitani [21]	hinge beams	yes	0.39 in.	3.5	49.4
Tighiouart [22]	hinge beams	yes	No. 4 No. 5 No. 6 No. 8	2.7 2.1 1.6 1.1	15.6 for all
Faza [23]	inverted half-beams	yes	No. 8	1.0	15.5
Ehsani [3]	inverted half-beams	yes	No.3 No. 6 No. 9	1 - 6	21.3 for all
Retika [19]	inverted half-beams	no	No. 4 No. 6	2.0 2.0	28.3* 29.6*

*short embedment lengths

Table 1.3 T-Beams with Additional Reinforcement
(Rizkalla [19])

Ref	Id	Size	f'_c (psi)	Cover/ Confinement	Embed. (in.)	P_{ult} (kips)	ω_{bond} (psi)	$1/K_1$	Failure Mode
[19]	1	No. 4	6380	unconfined	1.3	2.8	1407	27.6	bond failure
	2	No. 4	6380	unconfined	1.3	3.3	1682	33.0	bond failure
	3	No. 4	6380	unconfined	1.3	3.1	1552	30.5	bond failure
	4	No. 4	6380	unconfined	1.3	3.0	1494	29.3	bond failure
	5	No. 4	6380	unconfined	2.5	7.2	1813	35.6	bond failure
	6	No. 4	6380	unconfined	2.5	6.8	1726	33.9	bond failure
	7	No. 4	6380	unconfined	2.5	5.7	1436	28.2	bond failure
	8	No. 4	6380	unconfined	2.5	6.9	1740	34.2	bond failure
	9	No. 4	6380	confined	1.6	6.0	2436	47.8	bond failure
	10	No. 4	6380	confined	1.6	7.5	3074	60.4	bond failure
	11	No. 4	6380	confined	1.6	7.8	3176	62.4	bond failure
	12	No. 4	6380	confined	1.6	7.9	3219	63.2	bond failure
	13	No. 4	6380	confined	2.5	12.8	3234	63.5	bond failure
	14	No. 4	6380	confined	2.5	11.6	2929	57.5	bond failure
	15	No. 4	6380	confined	2.5	11.5	2915	57.2	bond failure
	16	No. 4	6380	confined	2.5	14.6	3683	72.3	bond failure
	17	No. 4	6380	confined	5.0	17.5	2233	n.a.	bar failure
	18	No. 4	6380	confined	5.0	16.6	2117	n.a.	bar failure
	19	No. 4	6380	confined	5.0	17.2	2190	n.a.	bar failure
	20	No. 4	6380	confined	5.0	16.1	2045	n.a.	bar failure
	21	No. 4	6380	confined	7.5	17.0	1450	n.a.	bar failure
	22	No. 4	6380	confined	7.5	16.2	1378	n.a.	bar failure
	23	No. 4	6380	confined	10.0	17.3	1102	n.a.	bar failure
	24	No. 4	6380	confined	10.0	18.0	1146	n.a.	bar failure
	25	No. 4	6380	confined	12.5	17.7	899	n.a.	bar failure
	26	No. 4	6380	confined	12.5	16.5	841	n.a.	bar failure

Table 1.4 Notch Beams with Additional Reinforcement
(Daniali [14])

Ref	Id	Size	f'$_c$	Cover (#d_b)	Embed (in.)	P_{ult} (kips)	ω_{bond} (ksi)	$1/K_I$	Failure Mode
[14]	T4-1	No. 4	4000	3.0	8.0	20.6	>1640	n.a.	rebar failure
	T4-2	No. 4	4000	3.0	8.0	20.6	>1640	n.a.	rebar failure
	T4-3	No. 4	4000	3.0	8.0	20.6	>1640	n.a.	rebar failure
	T4-4	No. 4	4000	3.0	24.0	20.6	>550	n.a.	rebar failure
	T4-5	No. 4	4000	3.0	24.0	20.6	>550	n.a.	rebar failure
	T4-6	No. 4	4000	3.0	24.0	20.6	>550	n.a.	rebar failure
	T4-7	No. 4	4000	3.0	16.0	20.6	>820	n.a.	rebar failure
	T4-8	No. 4	4000	3.0	16.0	20.6	>820	n.a.	rebar failure
	T4-9	No. 4	4000	3.0	16.0	20.6	>820	n.a.	rebar failure
	T6-1	No. 6	4000	2.0	12.0	26.2	1050	34.5	rebar pullout
	T6-2	No. 6	4000	2.0	12.0	26.2	1050	34.5	rebar pullout
	T6-3	No. 6	4000	2.0	12.0	26.2	1050	34.5	rebar pullout
	T6-4	No. 6	4000	2.0	18.0	26.2	700	23.0	cover splitting
	T6-6	No. 6	4000	2.0	18.0	26.2	700	23.0	cover splitting
	T6-7	No. 6	4000	2.0	18.0	33.0	778	n.a.	rebar failure
	T6-8	No. 6	4000	2.0	24.0	33.0	584	n.a.	rebar failure
	T6-9	No. 6	4000	2.0	24.0	33.0	584	n.a.	rebar failure
	T6-4*	No. 6	4000	2.0	18.0	33.0	778	29.0	rebar pullout
	T6-5*	No. 6	4000	2.0	18.0	33.0	778	29.0	rebar pullout
	T6-6*	No. 6	4000	2.0	18.0	33.0	778	29.0	rebar pullout
	T8-1	No. 8	4000	1.8	20.0	40.3	970	31.9	rebar pullout
	T8-2	No. 8	4000	1.8	20.0	33.2	798	26.3	rebar pullout
	T8-3	No. 8	4000	1.8	20.0	40.3	970	31.9	rebar pullout
	T8-4	No. 8	4000	1.8	25.0	42.7	820	27.0	rebar pullout
	T8-5	No. 8	4000	1.8	25.0	42.7	820	27.0	rebar pullout
	T8-6	No. 8	4000	1.8	25.0	37.9	730	24.0	rebar pullout
	T8-7	No. 8	4000	1.8	30.0	33.2	532	17.5	rebar pullout
	T8-8	No. 8	4000	1.8	30.0	37.9	608	20.0	cover splitting
	T8-9	No. 8	4000	1.8	30.0	37.9	608	20.0	cover splitting

Table 1.5 Notch Beams without Additional Reinforcement
(Larralde [20])

Ref	Id	Size	f'_c	Cover ($\#d_b$)	Embed (in.)	P_{ult} (kips)	ω_{bond} (ksi)	$1/K_1$	Failure Mode
[20]	GFRP1	0.33 in.	4235	unk	2.0	8.2	unk	13.7*	unk
	GFRP2	0.33 in.	4695	unk	2.0	8.8	unk		unk
	GFRP3	0.33 in.	4695	unk	2.0	10.2	unk		unk
	GFRP4	0.33 in.	5345	unk	2.0	7.9	unk		unk
	GFRP5	0.33 in.	5345	unk	2.0	8.3	unk		unk
	GFRP6	0.33 in.	5345	unk	2.0	9.9	unk		unk
	GFRP7	0.33 in.	4020	unk	4.0	12.9	unk		unk
	GFRP8	0.33 in.	4020	unk	4.0	15.4	unk		unk
	GFRP9	0.33 in.	4480	unk	4.0	16.2	unk		unk

* $1/K_1$ value was given in the reference for all test results

Table 1.6 Hinge Beams with Additional Reinforcement
(Makitani [21] and Tighiouart [22])

Ref	Id	Size	f'_c (psi	Cover ($\#d_b$)	Embed (in.)	P_{ult} (kips)	ω_{bond} (psi)	$1/K_1$	Failure Mode
[21]	G1D40	0.39 in.	4480	3.5	15.6	21.8	114	n.a.	rebar failure
	G1D20	0.39 in.	3770	3.5	7.8	19.1	200	n.a.	rebar failure
	G1D10	0.39 in.	4280	3.5	3.9	12.6	264	49.4	rebar pullout
[22]	A4	No. 4	4500	2.7	5.0	7.8	1537	15.6*	rebar pullout
	B4	No. 4	4500	2.7	5.0	9.1	1784		rebar pullout
	A5	No. 5	4500	2.1	6.3	3.5	1059		rebar pullout
	B5	No. 5	4500	2.1	6.3	5.1	1566		rebar pullout
	A6	No. 6	4500	1.6	7.5	2.2	957		rebar pullout
	A8	No. 8	4500	1.1	10.0	1.2	928		rebar pullout
	B8	No. 8	4500	1.1	10.0	1.4	1073		rebar pullout
	A4	No. 4	4500	2.7	8.0	6.4	1262		rebar pullout
	A6	No. 6	4500	1.6	12.0	1.7	769		rebar pullout
	A8	No. 8	4500	1.1	16.0	0.9	740		rebar pullout
	A4	No. 4	4500	2.7	3.0	8.3	1639		rebar pullout
	A5	No. 5	4500	2.1	3.8	5.0	1537		rebar pullout
	A6	No. 6	4500	1.6	4.5	2.3	1030		rebar pullout
	A8	No. 8	4500	1.1	6.0	1.3	1015		rebar pullout

* $1/K_1$ value was given in the reference for all tests

Table 1.7 Inverted Half-Beams with Additional Reinforcement
(Faza [23] and Ehsani [3])

Ref	Id	Size	f'_c	Cover ($\#d_b$)	Embed (in.)	P_{ult} (kips)	ω_{bond} (ksi)	$1/K_1$	Failure Mode
[23]	B0.1.1	No. 8	7500	1.0	16.0	22.5	450	16.2	rebar pullout
	B0.1.2	No. 8	7500	1.0	16.0	24.0	480	17.3	rebar pullout
	B0.1.3	No. 8	7500	1.0	24.0	29.0	387	14.0	rebar pullout
	B0.1.4	No. 8	7500	1.0	24.0	30.0	400	14.4	rebar pullout
	B0.2.1	No.3	7500	2.5	16.0	unk	unk	n.a.	failure in grip
	B0.2.2	No.3	7500	2.5	16.0	unk	unk	n.a.	failure in grip
	B0.2.3	No.3	7500	2.5	24.0	11.0	>389	n.a.	rebar failure
	B0.2.4	No.3	7500	2.5	24.0	10.9	>389	n.a.	rebar failure
	B0.H1	No.3	7500	2.5	12.0	8.2	>580	n.a.	rebar failure
	B0.H2	No.3	7500	2.5	12.0	8.1	>573	n.a.	rebar failure
	B0.H3	No.3	7500	2.5	8.0	9.4	>997	n.a.	rebar failure
	B0.H4	No.3	7500	2.5	8.0	8.0	>849	n.a.	rebar failure
[3]	43B4B2	No.3	4321	2.0	4.0	7.9	1668	21.3*	rebar failure
	83B4B4	No.3	7105	4.0	4.0	8.3	1755		rebar failure
	43B6B4	No.3	5075	4.0	6.0	10.1	1436		rebar failure
	83B6B4	No.3	7105	4.0	6.0	9.5	1349		rebar failure
	43B8B6	No.3	5075	6.0	8.0	10.7	1131		rebar failure
	83B8B8	No.3	7105	8.0	8.0	8.5	899		rebar failure
	43B8T6	No.3	5075	6.0	8.0	9.0	957		rebar failure
	83B8T6	No.3	7105	6.0	8.0	9.6	1015		rebar failure
	43B1.5T1	No.3	4002	1.0	1.5	5.3	2987		concrete splitting
	43B1.5T2	No.3	4002	2.0	1.5	6.5	3698		rebar pullout
	43B3T2	No.3	4002	2.0	3.0	7.1	2001		rebar failure
	43B4T2	No.3	4321	2.0	4.0	8.6	1827		rebar failure
	83B4T2	No.3	7105	2.0	4.0	9.0	1900		rebar failure
	43B6T4	No.3	5075	4.0	6.0	9.1	1291		rebar failure
	83B6T4	No.3	7105	4.0	6.0	8.4	1189		rebar failure

* $1/K_1$ value was given in the reference for all test results

Table 1.7 Inverted Half Beams with Additional Reinforcement continued

Ref	Id	Size	f'_c	Cover ($\#d_b$)	Embed. (in.)	P_{ult} (kips)	ω_{bond} (psi)	$1/K_1$	Failure Mode
[3]	46B3B1	No. 6	4002	1.0	3.0	13.7	1943	21.3*	concrete splitting
	46B3B2	No. 6	4002	2.0	3.0	17.5	2480		rebar pullout
	46B6B2	No. 6	4002	2.0	6.0	19.1	1349		rebar pullout
	46B12B2	No. 6	5684	2.0	12.0	23.0	812		rebar pullout
	86B12B2	No. 6	6917	2.0	12.0	23.4	827		rebar pullout
	46B16B4	No. 6	5684	4.0	16.0	29.5	783		rebar pullout
	86B16B4	No. 6	6917	4.0	16.0	28.4	754		rebar pullout
	46B18B6	No. 6	5684	6.0	18.0	31.4	740		rebar failure
	86B18B6	No. 6	6917	6.0	18.0	30.1	711		rebar failure
	46B3T1	No. 6	4002	1.0	3.0	11.0	1552		concrete splitting
	46B3T2	No. 6	4002	2.0	3.0	14.6	2059		rebar pullout
	46B6T2	No. 6	4002	2.0	6.0	15.6	1102		rebar pullout
	46B12T2	No. 6	5684	2.0	12.0	21.3	754		rebar pullout
	86B12T2	No. 6	6917	2.0	12.0	22.5	798		rebar pullout
	46B16T4	No. 6	5684	4.0	16.0	27.9	740		rebar pullout
	86B16T4	No. 6	6917	4.0	16.0	27.3	725		rebar pullout
	46B8T6	No. 6	5684	6.0	8.0	14.2	754		rebar failure
	86B18T6	No. 6	6917	6.0	18.0	29.5	696		rebar failure

* $1/K_1$ value was given in the reference for all test results

Table 1.8 Inverted Half Beams without Additional Reinforcement
(Retika [24])

Ref	Id	Size	f'_c	Cover ($\#d_b$)	Embed (in.)	P_{ult} (kips)	ω_{bond} (psi)	$1/K_1$	Failure Mode
[24]	CG6AM1	No. 6	5630	2.0	10.0	23.4	991	31.1	concrete splitting
	CG6BM1	No. 6	5630	2.0	10.0	22.4	951	29.9	concrete splitting
	CG6BM1	No. 6	5630	2.0	10.0	21.9	929	29.2	concrete splitting
	CG6AM2	No. 6	5630	2.0	10.0	24.8	1051	33.0	concrete splitting
	CG6BM2	No. 6	5630	2.0	10.0	19.5	826	25.9	concrete splitting
	CG6CM2	No. 6	5630	2.0	10.0	21.2	898	28.2	concrete splitting
	CG4AM1	No. 4	5630	2.0	5.5	11.5	890	28.0	concrete splitting
	CG4BM1	No. 4	5630	2.0	5.5	12.9	998	31.3	concrete splitting
	CG4CM1	No. 4	5630	2.0	5.5	10.5	813	25.5	concrete splitting

Table 1.9 GFRP Development Lengths

Researcher	Type of Tests	Confinement Steel	Bar Dia.	Development Length
Rizkalla [19]	tee-beams	yes	No. 4	40 d_b
Daniali [14]	beams	yes	No. 4 No. 6 No. 8	No. 6: 18 in
Makitani [21]	hinge-beams	yes	No. 3 No. 5	40 d_b
Ehsani [3]	inverted half-beams	yes	No. 3 No. 6 No. 9	minimum 15 in.

Table 2.1 Pilot Test Matrix

Test Identification	Bar Type	Bar Size	Cover (d_b)	Embedment (inches)	Number of Tests
PM1-4-2- 7.5	M1	4	2	7.5	1
PM1-4-2- 9.0	M1	4	2	9.0	1
PM1-4-2-10.5	M1	4	2	10.5	1
PM1-5-2-10.5	M1	5	2	10.5	1
PM1-5-2-12.0	M1	5	2	12.0	1
PM1-5-2-13.5	M1	5	2	13.5	1
PM1-5-2-15.0	M1	5	2	15.0	1
PM3-4-2- 5.5	M3	4	2	5.5	1
PM3-4-2- 7.5	M3	4	2	7.5	1
PM3-6-2-14.0	M3	6	2	14.0	1
PM3-6-2-17.0	M3	6	2	17.0	1
PM3-6-2-20.0	M3	6	2	20.0	1

Table 2.2 Pilot Test Results

Test Identification	P_{ult}	Target % f_u	Tested % f_u	$1/K_1$	Avg. $1/K_1$
PM1-4-2- 7.5	12.1	65	60	18.8	avg.
PM1-4-2- 9.0	13.2	80	66	17.0	17.5
PM1-4-2-10.5	14.8	95	74	16.6	
PM1-5-2-10.5	16.7	65	57	18.5	
PM1-5-2-12.0	16.6	75	57	16.1	avg.
PM1-5-2-13.5	21.5	85	73	18.5	16.9
PM1-5-2-15.0	18.9	95	64	14.6	
PM3-4-2- 5.5	10.8	50	50	22.7	avg.
PM3-4-2- 7.5	12.9	65	60	20.0	21.4
PM3-6-2-14.0	21.0	65	53	17.4	avg.
PM3-6-2-17.0	27.3	80	69	18.7	17.5
PM3-6-2-20.0	28.1	95	71	16.3	

Table 2.3 Primary Test 1 Matrix

Test Identification	Bar Type	Bar Size	Cover (d_b)	Embedment (inches)	Number of Tests
M1-5-2-47.0	M1	5	2	47.0	6
M1-5-2-15.0	M1	5	2	15.0	6
M1-5-2-12.5	M1	5	2	12.5	6
M1-5-3-15.0	M1	5	3	15.0	6
M1-5-3-12.5	M1	5	3	12.5	6
M1-5-3-10.0	M1	5	3	10.0	6

Table 2.4 Primary Test 2 Matrix

Test Identification	Bar Type	Bar Size	Cover (d_b)	Embedment (inches)	Number of Tests
M1-5-2-12.5	M1	5	2	12.5	3
M2-6-2-47.0	M2	6	2	47.0	3
M2-6-2-25.0	M2	6	2	25.0	6
M2-6-2-20.0	M2	6	2	20.0	6
M2-6-2-15.0	M2	6	2	15.0	6
M2-6-3-20.0	M2	6	3	20.0	6
M2-6-3-15.0	M2	6	3	15.0	6

Table 2.5 PVC Sleeve Size Details

GFRP Rebar Size	PVC Tube Label	Inside Diameter (in.)
No. 4	1/2 in. 600 psi	0.63
No. 5	3/4 in. 480 psi	0.91
No. 6	3/4 in. 300 psi	0.93

Table 2.6 GFRP Rebar Property Comparisons

Bar Code	Manufacturer Reported				Tested	
	MOE (ksi)	Cross-Sectional Area (in^2)	Ultimate Tensile Strength (ksi)	Ultimate Tensile Strength (kips)	Cross-Sectional Area[1] (in^2)	Ultimate Tensile Strength[2] (kips)
M1-4	6090	0.175	112	19.6	X[3]	16.4
M1-5	6090	0.273	108	29.4	0.302	19.2
M2-4	5800	0.20[6]	110	22.0	X[3]	X[3]
M2-6	5800	0.458	95	43.5	0.471	43.5
M2-6[4]	5800	0.458	95	43.5	X[3]	33.1
M2-6[5]	5800	0.458	95	43.5	X[3]	46.5
M3-4	7210	0.20[6]	107	21.4	X[3]	X[3]
M3-6	7210	0.44[6]	90	39.6	X[3]	X[3]

Notes:
1) Cross-sectional area from the volume displacement method outlined in Appendix B.
2) Ultimate tensile strength based only on failures outside of the grips.
3) Rebar was not tested.
4) Rebar from M2 used in Retika's tests [24].
5) Second batch of M2 rebar and was not used in bond tests.
6) Nominal area reported only.

Table 2.7 Pilot Test Average Concrete Strength Results

Pilot Test	mid test	end
Days	77	94
Compressive Strength (psi)	7750	7410
Split Tensile Strength (psi)	no test	605

Table 2.8 Primary Test 1 Average Concrete Strength Results

Primary Test 1	28-day	start	1/3 pt	2/3 pt	end
Days	28	39	87	119	132
Compressive Strength (psi)	6060	6320	6510	6690	6290
Modulus of Elasticity (ksi)	4350	4350	5300	4150	4250
Split Tensile Strength (psi)	520	590	525	530	450
Modulus of Rupture (psi)	430	no test	no test	no test	765

Table 2.9 Primary Test 2 Average Concrete Strength Results

Primary Test 2	28-day	start	1/3 pt	2/3 pt	end
Days	28	37	61	100	115
Compressive Strength (psi)	6180	6150	6550	6360	6300
Modulus of Elasticity (ksi)	4550	4400	4600	4200	4350
Split Tensile Strength (psi)	550	540	515	555	510
Modulus of Rupture (psi)	600	no test	no test	no test	935

Table 2.10 AE Wave Velocities

Test	Material	AE Wave Velocities (in./second)
Pilot Test	M1 GFRP rebar	170,000
	M3 GFRP rebar	175,000
	concrete	88,000
Primary Test 1	M1 GFRP rebar	171,000
	concrete	81,000
Primary Test 2	M1 GFRP rebar	169,000
	M2 GFRP rebar	146,000
	concrete	79,000

Table 3.1 Results 1M1-5-3-15.0
Prim. Test 1, Manf. 1, No. 5 GFRP, $3d_b$ (1.88 in.) cover, 15.0 in. emb., f'_c 6450 psi

Data	Units	Test Number						Average		
		1	2	3	4	5	6	All	Conc	Bar
1. Sequence Number	#	1	2	3	19	20	21			
2. Age of Specimen	days	39	46	49	108	110	112			
3. Def. Pre-Test/Avail.	#/#	2/80	13/80	4/80	3/80	2/80	0/80	4/80		4/80
4. Measured Cover	in.	1.88	1.88	1.88	1.81	1.81	1.88	1.86		1.86
5. LVDT Attachment	code	N	N	N	D	RA	RA			
6. LES Transition Load	kips	X	7.4	7.4	7.2	8.3	7.6	7.6		7.6
7. LES Transition Slip	in.	X	0.009	0.010	0.009	0.010	0.009	0.009		0.009
8. First Crack Load	kips	10.0	9.0	11.0	11.6	9.7	10.0	10.2		10.2
9. Perp. Crack Load	kips	10.5	11.8	12.3	11.8	10	12.1	11.4		11.4
10. Loc. Perp. Crack	in.	2.0	1.0	1.0	1.0	1.0	2.0	1.3		1.3
11. LES Diverging Load	kips	X	13.2	11.8	13.2	11.5	14.0	12.7		12.7
12. LES Diverging Slip	in.	X	0.030	0.024	0.030	0.020	0.028	0.026		0.026
13. Conc AE Peak, Load	kips	11	14	11	13	X	11	12		12
14. FES Transition Load	kips	18.3	15	16.6	18.2	17.2	18.7	17.3		17.3
15. FES Transition Slip	in.	0.0007	0.0005	0.0004	0.0003	0.0004	0.0006	0.0005		0.0005
16. Associated LES Slip	in.	0.097	0.045	0.063	0.057	0.051	0.087	0.067		0.067
17. Bar AE Peak, Load	kips	18	18	18	13	17	19	17		17
18. Ultimate Load	kips	18.3	18.9	18.8	18.2	19.7	20.1	19.0		19.0
19. Failure Type	code	IB	IB	IB	IB	IB	IB			
20. AE C2 Pattern	code	UD	UD	UD	D	X	UD			
21. AE C3 Peak	code	M	M	M	M	X	M			
22. AE B2 Pattern	code	UD	U	D	UD	UD	UD			
23. AE B3 Peak	code	U	U	U	M	U	U			
24. f_b / ω_{ult}	n.a.	X	0.11	0.08	0.07	0.07	0.12	0.09		0.09
25. Bar MOE	ksi	5980	5550	6000	6110	6000	6080	5950		5950
26. Mean Bond Stress	psi	621	642	638	618	669	682	645		645
27. Def Damaged/Avail.	#/#	10/78	12/67	14/76	44/77	26/78	36/80	24/76		24/76

Notes:
1) "X" indicates equipment malfunction or insufficient data for analysis.
2) Row 5: N (no protection), M (masking tape), D (duct tape), RA (rubber aluminum).
3) Row 19: C (concrete splitting), IA (spaghetti bar failure in embedment), IB (spaghetti failure out), IC (spaghetti bar failure both in and out), IIA (bar fracture in embedment), IIB (bar fracture out).
4) Rows 20 and 22: I (increasing), D (decreasing), UD (uniform/decreasing), ID (increasing/decreasing), U (uniform), X (insufficient data).
5) Rows 21 and 23: M (mid-load peak), U (ultimate load peak), X (insufficient data).

Table 3.2 Results 1M1-5-3-12.5
Prim. Test 1, Manf. 1, No. 5 GFRP, $3d_b$ (1.88 in.) cover, 12.5 in. emb., f'_c 6450 psi

Data	Units	Test Number						Average		
		1	2	3	4	5	6	All	Conc	Bar
1. Sequence Number	#	4	5	6	22	23	24			
2. Age of Specimen	days	55	56	59	115	117	119			
3. Def. Pre-Test/Avail.	#/#	0/68	1/68	2/68	0/68	0/68	1/68	1/68	1/68	0/68
4. Measured Cover	in.	1.88	1.88	1.81	1.88	1.88	1.88	1.87	1.87	1.88
5. LVDT Attachment	code	D	N	N	RA	RA	RA			
6. LES Transition Load	kips	6.2	7.2	8.6	7.8	7.0	7.2	7.3	7.2	7.8
7. LES Transition Slip	in.	0.008	0.008	0.011	0.009	0.006	0.007	0.008	0.008	0.009
8. First Crack Load	kips	10.0	10.2	11.0	10.0	11.6	9.5	10.4	10.5	10.0
9. Perp. Crack Load	kips	12.4	11.3	12.3	11.3	13.7	11.2	12.0	12.2	11.3
10. Loc. Perp. Crack	in.	2.0	2.0	2.0	1.0	2.0	1.0	1.7	1.8	1.0
11. LES Diverging Load	kips	13.7	13.6	13.1	12.1	12.0	X	12.9	13.1	12.1
12. LES Diverging Slip	in.	0.032	0.025	0.026	0.020	0.020	X	0.025	0.026	0.020
13. Conc AE Peak, Load	kips	12	17	12	13	13	X	13	14	13
14. FES Transition Load	kips	14.4	14.0	16.0	16.0	15.0	17.4	15.5	15.4	16.0
15. FES Transition Slip	in.	0.0006	0.0004	0.0006	0.0007	0.0006	0.0006	0.0006	0.0006	0.0007
16. Associated LES Slip	in.	0.045	0.040	0.078	0.050	0.044	0.041	0.050	0.050	0.050
17. Bar AE Peak, Load	kips	19	17	17	X	16	15	17	17	X
18. Ultimate Load	kips	19.8	17.6	18.2	17.7	19.7	20.7	19.0	19.2	17.7
19. Failure Type	code	C	C	C	IIA	C	C			
20. AE C2 Pattern	code	UD	UD	UD	D	UD	X			
21. AE C3 Peak	code	M	U	M	M	M	X			
22. AE B2 Pattern	code	ID	D	U	X	X	ID			
23. AE B3 Peak	code	U	U	U	X	X	M			
24. f_b / ω_{dlt}	n.a.	0.16	0.16	0.14	0.08	0.11	0.06	0.12	0.13	0.08
25. Bar MOE	ksi	6110	5710	6200	6000	6090	6000	6020	6020	6000
26. Mean Bond Stress	psi	807	717	742	721	803	843	772	782	721
27. Def Damaged/Avail.	#/#	33/68	22/67	21/66	13/68	36/68	21/67	24/67	27/67	13/68

Notes:
1) "X" indicates equipment malfunction or insufficient data for analysis.
2) Row 5: N (no protection), M (masking tape), D (duct tape), RA (rubber aluminum).
3) Row 19: C (concrete splitting), IA (spaghetti bar failure in embedment), IB (spaghetti failure out), IC (spaghetti bar failure both in and out), IIA (bar fracture in embedment), IIB (bar fracture out).
4) Rows 20 and 22: I (increasing), D (decreasing), UD (uniform/decreasing), ID (increasing/decreasing), U (uniform), X (insufficient data).
5) Rows 21 and 23: M (mid-load peak), U (ultimate load peak), X (insufficient data).

Table 3.3 Results 1M1-5-3-10.0
Prim. Test 1, Manf. 1, No. 5 GFRP, $3d_b$ (1.88 in.) cover, 10.0 in. emb., f'_c 6450 psi

Data	Units	Test Number						Average		
		1	2	3	4	5	6	All	Conc	Bar
1. Sequence Number	#	7	8	9	25	26	27			
2. Age of Specimen	days	61	62	62	122	124	126			
3. Def. Pre-Test/Avail.	#/#	2/54	1/54	0/54	1/54	6/54	4/54	2/54	3/54	23/54
4. Measured Cover	in.	1.88	1.94	1.88	1.88	1.81	1.88	1.88	1.88	1.88
5. LVDT Attachment	code	N	M	M	RA	RA	RA			
6. LES Transition Load	kips	7.0	9.0	6.4	6.0	9.2	6.8	7.4	6.9	7.7
7. LES Transition Slip	in.	0.009	0.012	0.008	0.005	0.010	0.008	0.009	0.009	0.009
8. First Crack Load	kips	9.0	8.7	10.4	9.5	10.2	10.1	9.7	9.6	9.7
9. Perp. Crack Load	kips	10.5	10.0	13.3	10.0	11.0	10.1	10.8	10.3	11.1
10. Loc. Perp. Crack	in.	1.0	1.0	1.0	1.0	1.0	1.0	1.0	1.0	1.0
11. LES Diverging Load	kips	13	13.2	13.8	13	12.0	13.5	13.1	13.3	13.0
12. LES Diverging Slip	in.	0.025	0.031	0.028	0.021	0.019	0.028	0.025	0.027	0.025
13. Conc AE Peak, Load	kips	11	X	13	11	11	16	12	14	12
14. FES Transition Load	kips	11.6	12	13.2	11.8	11.8	11.8	12.0	11.7	12.2
15. FES Transition Slip	in.	0.0003	0.0007	0.0002	0.0005	0.0005	0.0005	0.0004	0.0004	0.0005
16. Associated LES Slip	in.	0.020	0.021	0.027	0.018	0.020	0.020	0.021	0.020	0.022
17. Bar AE Peak, Load	kips	15	16	14	16	20	16	16	16	17
18. Ultimate Load	kips	16.0	16.9	17.4	16.8	20.8	17.3	17.5	16.7	18.0
19. Failure Type	code	C	IC	IC	IB	IC	C			
20. AE C2 Pattern	code	D	X	UD	UD	UD	UD			
21. AE C3 Peak	code	M	X	M	M	M	U			
22. AE B2 Pattern	code	UD	ID	D	X	UD	I			
23. AE B3 Peak	code	U	U	M	X	U	U			
24. f_b / ω_{dlt}	n.a.	0.09	0.13	0.07	0.10	0.09	0.20	0.11	0.15	0.10
25. Bar MOE	ksi	6110	6130	5660	6140	6040	6060	6020	6090	5990
26. Mean Bond Stress	psi	815	861	886	856	1060	881	893	848	916
27. Def Damaged/Avail.	#/#	16/52	16/53	18/54	10/53	47/48	21/50	21/52	19/51	23/53

Notes:
1) "X" indicates equipment malfunction or insufficient data for analysis.
2) Row 5: N (no protection), M (masking tape), D (duct tape), RA (rubber aluminum).
3) Row 19: C (concrete splitting), IA (spaghetti bar failure in embedment), IB (spaghetti failure out), IC (spaghetti bar failure both in and out), IIA (bar fracture in embedment), IIB (bar fracture out).
4) Rows 20 and 22: I (increasing), D (decreasing), UD (uniform/decreasing), ID (increasing/decreasing), U (uniform), X (insufficient data).
5) Rows 21 and 23: M (mid-load peak), U (ultimate load peak), X (insufficient data).

Table 3.4 Results 1M1-5-2-47.0
Prim. Test 1, Manf. 1, No. 5 GFRP, $2d_b$ (1.25 in.) cover, 47.0 in. emb., f'_c 6450 psi

Data	Units	Test Number						Average		
		1	2	3	4	5	6	All	Conc	Bar
1. Sequence Number	#	10	11	12	28	29	30			
2. Age of Specimen	days	80	82	84	136	138	140			
3. Def. Pre-Test/Avail.	#/#	21/252	15/252	8/252	8/252	5/252	2/252	10/252		10/252
4. Measured Cover	in.	1.31	1.31	1.31	1.31	1.25	1.38	1.31		1.31
5. LVDT Attachment	code	D	M	D	RA	RA	RA			
6. LES Transition Load	kips	8.5	6.0	7.0	8.0	8.0	6.4	7.3		7.3
7. LES Transition Slip	in.	0.015	0.007	0.010	0.010	0.010	0.006	0.010		0.010
8. First Crack Load	kips	9.0	12.7	8.3	8.0	10.8	9.8	9.8		9.8
9. Perp. Crack Load	kips	13.5	15.0	10.8	10.0	10.8	11.0	11.9		11.9
10. Loc. Perp. Crack	in.	1.0	5.0	1.0	1.0	1.0	1.0	1.7		1.7
11. LES Diverging Load	kips	X	16.0	13.0	11.0	11.1	11.1	12.4		12.4
12. LES Diverging Slip	in.	X	0.047	0.028	0.019	0.020	0.022	0.027		0.027
13. Conc AE Peak, Load	kips	15	16	X	11	13	22	15		15
14. FES Transition Load	kips	16.0	21.7	12.9	18.7	14.3	22.6	17.7		17.7
15. FES Transition Slip	in.	0.0001	0.0001	0.0001	0.0000	0.0000	0.0000	0.0000		0.0000
16. Associated LES Slip	in.	0.052	0.156	0.028	X	0.039	X	0.069		0.069
17. Bar AE Peak, Load	kips	X	X	X	16	14	22	17		17
18. Ultimate Load	kips	16.2	21.9	12.9	18.7	14.3	22.6	17.8		17.8
19. Failure Type	code	IB	IC	IB	IB	IC	IC			
20. AE C2 Pattern	code	UD	U	X	UD	UD	UD			
21. AE C3 Peak	code	U	M	X	M	U	U			
22. AE B2 Pattern	code	X	X	X	D	U	UD			
23. AE B3 Peak	code	X	X	X	U	U	U			
24. f_b / ω_{dlt}	n.a.	0.06	0.09	0.12	0.08	0.14	0.08	0.10		0.10
25. Bar MOE	ksi	6330	5730	6150	5990	6040	5990	6040		6040
26. Mean Bond Stress	psi	177	240	141	205	157	248	195		195
27. Def Damaged/Avail.	#/#	48/231	36/237	0/244	13/244	35/247	93/250	38/242		38/242

Notes:
1) "X" indicates equipment malfunction or insufficient data for analysis.
2) Row 5: N (no protection), M (masking tape), D (duct tape), RA (rubber aluminum).
3) Row 19: C (concrete splitting), IA (spaghetti bar failure in embedment), IB (spaghetti failure out), IC (spaghetti bar failure both in and out), IIA (bar fracture in embedment), IIB (bar fracture out).
4) Rows 20 and 22: I (increasing), D (decreasing), UD (uniform/decreasing), ID (increasing/decreasing), U (uniform), X (insufficient data).
5) Rows 21 and 23: M (mid-load peak), U (ultimate load peak), X (insufficient data).

Table 3.5 Results 1M1-5-2-15.0
Prim. Test 1, Manf. 1, No. 5 GFRP, $2d_b$ (1.25 in.) cover, 15.0 in. emb., f'_c 6450 psi

Data	Units	Test Number						Average		
		1	2	3	4	5	6	All	Conc	Bar
1. Sequence Number	#	13	14	15	31	32	33			
2. Age of Specimen	days	87	96	98	143	145	147			
3. Def. Pre-Test/Avail.	#/#	1/80	1/80	5/80	2/80	2/80	3/80	2/80	5/80	2/80
4. Measured Cover	in.	1.25	1.31	1.31	1.31	1.38	1.38	1.32	1.31	1.33
5. LVDT Attachment	code	D	D	D	RA	RA	RA			
6. LES Transition Load	kips	8.0	8.0	9.0	8.2	8.0	8.0	8.2	9.0	8.0
7. LES Transition Slip	in.	0.010	0.011	0.013	0.011	0.010	0.010	0.011	0.013	0.010
8. First Crack Load	kips	9.0	9.1	9.2	9.2	10.8	8.8	9.4	9.2	9.4
9. Perp. Crack Load	kips	10.1	10.0	10.0	10.0	12.2	8.8	10.2	10.0	10.2
10. Loc. Perp. Crack	in.	2.0	1.0	1.0	2.0	2.0	1.0	1.5	1.0	1.6
11. LES Diverging Load	kips	11.5	11.8	11.6	12.2	13.1	11.1	11.9	11.6	11.9
12. LES Diverging Slip	in.	0.02	0.02	0.021	0.023	0.028	0.018	0.022	0.021	0.022
13. Conc AE Peak, Load	kips	15	13	22	15	X	11	15	22	14
14. FES Transition Load	kips	18.4	13.7	19.6	15.9	17.4	17.8	17.1	19.6	16.6
15. FES Transition Slip	in.	0.0007	0.0003	0.0006	0.0005	0.0005	0.0006	0.0005	0.0006	0.0005
16. Associated LES Slip	in.	X	0.031	0.060	0.033	0.069	0.033	0.045	0.060	0.042
17. Bar AE Peak, Load	kips	19	X	22	15	17	X	18	22	17
18. Ultimate Load	kips	20.0	13.7	22.5	15.9	17.4	18.1	17.9	22.5	17.0
19. Failure Type	code	IB	IB	C	IB	IA	IA			
20. AE C2 Pattern	code	UD	UD	U	D	X	UD			
21. AE C3 Peak	code	M	U	U	U	X	M			
22. AE B2 Pattern	code	D	X	ID	UD	D	X			
23. AE B3 Peak	code	U	X	U	U	U	X			
24. f_b / ω_{4lt}	n.a.	0.11	0.06	0.07	0.17	0.08	0.20	0.11	0.07	0.12
25. Bar MOE	ksi	5980	6330	6180	6340	6370	6220	6240	6180	6250
26. Mean Bond Stress	psi	679	465	764	540	591	615	609	764	578
27. Def Damaged/Avail.	#/#	23/79	0/79	35/75	11/78	32/78	43/77	24/78	35/75	22/78

Notes:
1) "X" indicates equipment malfunction or insufficient data for analysis.
2) Row 5: N (no protection), M (masking tape), D (duct tape), RA (rubber aluminum).
3) Row 19: C (concrete splitting), IA (spaghetti bar failure in embedment), IB (spaghetti failure out), IC (spaghetti bar failure both in and out), IIA (bar fracture in embedment), IIB (bar fracture out).
4) Rows 20 and 22: I (increasing), D (decreasing), UD (uniform/decreasing), ID (increasing/decreasing), U (uniform), X (insufficient data).
5) Rows 21 and 23: M (mid-load peak), U (ultimate load peak), X (insufficient data).

Table 3.6 Results 1M1-5-2-12.5
Prim. Test 1, Manf. 1, No. 5 GFRP, $2d_b$ (1.25 in.) cover, 12.5 in. emb., f'_c 6450 psi

Data	Units	Primary Test 1 Test Number						Primary Test 1 Average		
		1-1	1-2	1-3	1-4	1-5	1-6	All	Conc	Bar
1. Sequence Number	#	16	17	18	34	35	36			
2. Age of Specimen	days	101	103	105	147	147	148			
3. Def. Pre-Test/Avail.	#/#	0/68	1/68	1/68	1/68	0/68	1/68	1/68	1/68	1/68
4. Measured Cover	in.	1.31	1.25	1.31	1.31	1.31	1.31	1.30	1.29	1.31
5. LVDT Attachment	code	D	D	D	RA	RA	RA			
6. LES Transition Load	kips	4.4	9.4	7.6	8.4	7.6	8.6	7.7	8.5	6.8
7. LES Transition Slip	in.	0.006	0.022	0.009	0.010	0.006	0.010	0.011	0.013	0.008
8. First Crack Load	kips	X	10.6	11.5	9.0	10.3	10.5	10.4	10.5	10.3
9. Perp. Crack Load	kips	X	13.0	16.0	9.0	10.3	11.2	11.9	11.5	12.5
10. Loc. Perp. Crack	in.	X	2.0	3.0	1.0	2.0	2.0	2.0	2.0	2.0
11. LES Diverging Load	kips	7.0	X	13.6	11.1	15.0	12.1	11.8	13.6	10.6
12. LES Diverging Slip	in.	0.008	X	0.022	0.018	0.030	0.021	0.020	0.026	0.016
13. Conc AE Peak, Load	kips	X	13	13	14	10	15	13	13	14
14. FES Transition Load	kips	9.1	13.8	X	14.8	15.3	15.4	13.6	14.8	12.0
15. FES Transition Slip	in.	0.0003	0.0005	X	0.0006	0.0006	0.0006	0.0006	0.0006	0.0005
16. Associated LES Slip	in.	0.030	0.040	X	0.052	0.060	0.045	0.045	0.048	0.041
17. Bar AE Peak, Load	kips	X	X	17	14	15	16	16	16	16
18. Ultimate Load	kips	9.1	18.5	17.9	16.1	16.7	17.1	15.9	17.4	14.4
19. Failure Type	code	IIB	C	IC	IB	C	C			
20. AE C2 Pattern	code	D	UD	UD	U	UD	UD			
21. AE C3 Peak	code	M	M	M	M	M	M			
22. AE B2 Pattern	code	X	X	U	ID	D	UD			
23. AE B3 Peak	code	X	X	U	U	U	U			
24. f_b / ω_{ult}	n.a.	0.18	0.11	0.08	0.10	0.15	0.15	0.13	0.14	0.12
25. Bar MOE	ksi	6390	5480	6060	5800	5990	5950	5950	5810	6080
26. Mean Bond Stress	psi	371	754	729	656	680	697	648	710	585
27. Def Damaged/Avail.	#/#	6/68	59/67	3/67	14/67	47/68	53/67	30/68	53/67	8/67

Notes:
1) "X" indicates equipment malfunction or insufficient data for analysis.
2) Row 5: N (no protection), M (masking tape), D (duct tape), RA (rubber aluminum).
3) Row 19: C (concrete splitting), IA (spaghetti bar failure in embedment), IB (spaghetti failure out), IC (spaghetti bar failure both in and out), IIA (bar fracture in embedment), IIB (bar fracture out).
4) Rows 20 and 22: I (increasing), D (decreasing), UD (uniform/decreasing), ID (increasing/decreasing), U (uniform), X (insufficient data).
5) Rows 21 and 23: M (mid-load peak), U (ultimate load peak), X (insufficient data).

Table 3.6 Results 2M1-5-2-12.5 continued
Prim. Test 2, Manf. 1, No. 5 GFRP, $2d_b$ (1.25 in.) cover, 12.5 in. emb., f'_c 6450 psi

Data	Units	Primary Test 2 Test Number				Primary Test 2 Average				Primary Test 1 & 2 Average
		2-1	2-2	2-3	All	Conc	Bar	All	Conc	Bar
1. Sequence Number	#	7	8	9						
2. Age of Specimen	days	51	53	55						
3. Def. Pre-Test/Avail.	#/#	6/68	2/68	1/68	3/68	3/68		1/68	2/68	1/68
4. Measured Cover	in.	1.25	1.25	1.25	1.25	1.25		1.28	1.28	1.31
5. LVDT Attachment	code	RA	RA	RA						
6. LES Transition Load	kips	X	7.2	7.6	7.4	7.4		7.6	8.1	6.8
7. LES Transition Slip	in.	X	0.008	0.008	0.01	0.01		0.010	0.011	0.008
8. First Crack Load	kips	9.0	10.7	9.0	9.6	9.6		10.1	10.0	10.3
9. Perp. Crack Load	kips	11.0	11.8	10.2	11.0	11.0		11.6	11.3	12.5
10. Loc. Perp. Crack	in.	2.0	3.0	1.0	2.0	2.0		2.0	2.0	2.0
11. LES Diverging Load	kips	X	15.1	12.9	14.0	14.0		12.4	13.8	10.6
12. LES Diverging Slip	in.	X	0.032	0.023	0.028	0.028		0.022	0.027	0.016
13. Conc AE Peak, Load	kips	11	X	16	14	14		13	13	14
14. FES Transition Load	kips	X	13.0	13.0	13.0	13.0		13.5	14.1	12.0
15. FES Transition Slip	in.	X	0.0005	0.0005	0.0005	0.0005		0.0005	0.0005	0.0005
16. Associated LES Slip	in.	X	0.034	0.030	0.032	0.032		0.042	0.042	0.041
17. Bar AE Peak, Load	kips	18	X	X	18	18		16	17	16
18. Ultimate Load	kips	18.7	16.5	17.1	17.4	17.4		16.4	17.4	14.4
19. Failure Type	code	C	C	C						
20. AE C2 Pattern	code	UD	X	UD						
21. AE C3 Peak	code	M	X	U						
22. AE B2 Pattern	code	U	X	X						
23. AE B3 Peak	code	U	X	X						
24. f_b / ω_{ult}	n.a.	X	0.12	0.16	0.14	0.14		0.13	0.13	0.12
25. Bar MOE	ksi	X	5580	5790	5690	5690		5880	5760	6080
26. Mean Bond Stress	psi	762	672	697	710	710		669	710	585
27. Def Damaged/Avail.	#/#	36/62	30/66	18/67	28/65	28/65		30/67	45/66	8/67

Notes:
1) "X" indicates equipment malfunction or insufficient data for analysis.
2) Row 5: N (no protection), M (masking tape), D (duct tape), RA (rubber aluminum).
3) Row 19: C (concrete splitting), IA (spaghetti bar failure in embedment), IB (spaghetti failure out), IC (spaghetti bar failure both in and out), IIA (bar fracture in embedment), IIB (bar fracture out).
4) Rows 20 and 22: I (increasing), D (decreasing), UD (uniform/decreasing), ID (increasing/decreasing), U (uniform), X (insufficient data).
5) Rows 21 and 23: M (mid-load peak), U (ultimate load peak), X (insufficient data).

Table 3.7 Results 2M2-6-3-20.0
Prim. Test 2, Manf. 2, No. 6 GFRP, $3d_b$ (2.25 in.) cover, 20.0 in. emb., f'_c 6340 psi

Data	Units	Test Number						Average		
		1	2	3	4	5	6	All	Conc	Bar
1. Sequence Number	#	1	2	3	22	23	24			
2. Age of Specimen	days	38	39	40	98	99	100			
3. Def. Pre-Test/Avail.	#/#	0/21	0/20	0/25	0/24	0/25	1/20	0/23	0/23	1/23
4. Measured Cover	in.	2.25	2.25	2.25	2.25	2.25	2.25	2.25	2.25	2.25
5. LVDT Attachment	code	RA	RA	RA	RA	RA	RA			
6. LES Transition Load	kips	10.0	7.5	7.7	10.0	10.1	8.5	9.0	8.8	9.3
7. LES Transition Slip	in.	0.012	0.009	0.010	0.012	0.010	0.011	0.011	0.011	0.011
8. First Crack Load	kips	9.0	13.8	9.2	23.0	31.5	24.2	18.5	13.8	27.9
9. FES Transition Load	kips	25.0	24.0	23.5	25.5	31.5	26	25.9	24.5	28.8
10. FES Transition Slip	in.	0.0005	0.0004	0.0003	0.0004	0.0004	0.0005	0.0004	0.0004	0.0005
11. Associated LES Slip	in.	0.045	0.061	0.058	0.060	0.085	0.068	0.063	0.056	0.077
12. Conc AE Peak, Load	kips	32	34	35	33	X	X	35	35	X
13. Bar AE Peak, Load	kips	X	34	35	X	41	X	37	35	41
14. Ultimate Load	kips	32.8	34.8	35.3	33.6	42.5	36.5	35.9	34.1	39.5
15. Failure Type	code	C	C	C	C	III	III			
16. AE C2 Pattern	code	U	UD	UD	U	X	X			
17. AE C3 Peak	code	U	U	U	U	X	X			
18. AE B2 Pattern	code	X	D	UD	X	U	X			
19. AE B3 Peak	code	X	U	U	X	U	X			
20. f_b / ω_{ult}	n.a.	0.10	0.10	0.06	0.08	0.07	0.04	0.07	0.09	0.06
21. Bar MOE	ksi	6190	6290	6070	6190	6260	6130	6190	6190	6200
22. Mean Bond Stress	psi	696	738	749	713	902	775	762	724	838
23. Def. Damaged/Avail.	#/#	5/21	20/20	6/25	24/24	11/25	10/19	13/23	14/23	11/22

Notes:
1) "X" indicates equipment malfunction or insufficient data for analysis.
2) Row 5: N (no protection), M (masking tape), D (duct tape), RA (rubber aluminum).
3) Row 15: C (concrete splitting), IA (spaghetti bar failure in embedment), IB (spaghetti failure out), IC (spaghetti bar failure both in and out), IIA (bar fracture in embedment), IIB (bar fracture out).
4) Rows 16 and 18: I (increasing), D (decreasing), UD (uniform/decreasing), ID (increasing/decreasing), U (uniform), X (insufficient data).
5) Rows 17 and 19: M (mid-load peak), U (ultimate load peak), X (insufficient data).

Table 3.8 Results 2M2-6-3-15.0
Prim. Test 2, Manf. 2, No. 6 GFRP, $3d_b$ (2.25 in.) cover, 15.0 in. emb., f'_c 6340 psi

Data	Units	Test Number						Average		
		1	2	3	4	5	6	All	Conc	Bar
1. Sequence Number	#	4	5	6	25	26	27			
2. Age of Specimen	days	46	47	48	100	110	117			
3. Def. Pre-Test/Avail.	#/#	0/15	0/16	0/18	0/14	0/16	0/15	0/16	0/16	
4. Measured Cover	in.	2.25	2.25	2.25	2.25	2.25	2.25	2.25	2.25	
5. LVDT Attachment	code	RA	RA	RA	RA	RA	RA			
6. LES Transition Load	kips	X	5.2	X	6.7	6.0	6.9	6.2	6.2	
7. LES Transition Slip	in.	X	0.004	X	0.004	0.006	0.006	0.005	0.005	
8. First Crack Load	kips	11.0	16.0	22.0	19.8	23.4	19.6	18.6	18.6	
9. FES Transition Load	kips	16.0	19.0	X	26.5	25.2	20.5	21.4	21.4	
10. FES Transition Slip	in.	0.0004	0.0004	X	0.0007	0.0007	0.0004	0.0005	0.0005	
11. Associated LES Slip	in.	X	0.035	X	0.066	0.062	0.032	0.049	0.049	
12. Conc AE Peak, Load	kips	27	X	24	X	31	20	26	26	
13. Bar AE Peak, Load	kips	25	X	25	X	X	30	27	27	
14. Ultimate Load	kips	27.5	26.3	25.5	33.4	31.9	30.7	29.2	29.2	
15. Failure Type	code	C	C	C	C	C	C			
16. AE C2 Pattern	code	UD	X	UD	X	U	U			
17. AE C3 Peak	code	U	X	U	X	U	U			
18. AE B2 Pattern	code	U	X	I	X	X	U			
19. AE B3 Peak	code	M	X	U	X	X	U			
20. f_b / ω_{ult}	n.a.	X	0.18	X	0.11	0.09	0.04	0.11	0.11	
21. Bar MOE	ksi	6290	6330	X	6200	6420	6250	6300	6300	
22. Mean Bond Stress	psi	778	744	722	945	903	869	827	827	
23. Def. Damaged/Avail.	#/#	11/15	3/16	18/18	14/14	13/16	15/15	12/16	12/16	

Notes:
1) "X" indicates equipment malfunction or insufficient data for analysis.
2) Row 5: N (no protection), M (masking tape), D (duct tape), RA (rubber aluminum).
3) Row 15: C (concrete splitting), IA (spaghetti bar failure in embedment), IB (spaghetti failure out), IC (spaghetti bar failure both in and out), IIA (bar fracture in embedment), IIB (bar fracture out).
4) Rows 16 and 18: I (increasing), D (decreasing), UD (uniform/decreasing), ID (increasing/decreasing), U (uniform), X (insufficient data).
5) Rows 17 and 19: M (mid-load peak), U (ultimate load peak), X (insufficient data).

Table 3.9 Results 2M2-6-2-47.0
Prim. Test 2, Manf. 2, No. 6 GFRP, $2d_b$ (1.50 in.) cover, 47.0 in. emb., f'_c 6340 psi

Data	Units	Test Number				Average	
		1	2	3	All	Conc	Bar
1. Sequence Number	#	10	11	12			
2. Age of Specimen	days	55	61	84			
3. Def. Pre-Test/Avail.	#/#	0/50	0/50	0/50	0/50		0/50
4. Measured Cover	in.	1.50	1.50	1.50	1.50		1.50
5. LVDT Attachment	code	RA	RA	RA			
6. LES Transition Load	kips	12.5	12.7	X	12.6		12.6
7. LES Transition Slip	in.	0.013	0.008	X	0.011		0.011
8. First Crack Load	kips	15.4	16.0	19.0	16.8		16.8
9. FES Transition Load	kips	34.1	45.7	X	39.9		39.9
10. FES Transition Slip	in.	0.0000	0.0000	X	0.0000		0.0000
11. Associated LES Slip	in.	0.240	0.190	X	0.215		0.215
12. Conc AE Peak, Load	kips	33	44	X	39		39
13. Bar AE Peak, Load	kips	32	44	32	36		36
14. Ultimate Load	kips	34.1	45.7	35.5	38.4		38.4
15. Failure Type	code	III	III	IA			
16. AE C2 Pattern	code	UD	D	X			
17. AE C3 Peak	code	U	U	X			
18. AE B2 Pattern	code	U	U	U			
19. AE B3 Peak	code	U	U	U			
20. f_b / ω_{ult}	n.a.	0.10	0.12	X	0.11		0.11
21. Bar MOE	ksi	6130	6240	X	6190		6190
22. Mean Bond Stress	psi	308	413	321	360		360
23. Def. Damaged/Avail.	#/#	9/50	17/50	16/50	14/50		14/50

Notes:
1) "X" indicates equipment malfunction or insufficient data for analysis.
2) Row 5: N (no protection), M (masking tape), D (duct tape), RA (rubber aluminum).
3) Row 15: C (concrete splitting), IA (spaghetti bar failure in embedment), IB (spaghetti failure out), IC (spaghetti bar failure both in and out), IIA (bar fracture in embedment), IIB (bar fracture out).
4) Rows 16 and 18: I (increasing), D (decreasing), UD (uniform/decreasing), ID (increasing/decreasing), U (uniform), X (insufficient data).
5) Rows 17 and 19: M (mid-load peak), U (ultimate load peak), X (insufficient data).

Table 3.10 Results 2M2-6-2-25.0
Prim. Test 2, Manf. 2, No. 6 GFRP, $2d_b$ (1.50 in.) cover, 25.0 in. emb., f'_c 6340 psi

Data	Units	Test Number						Average		
		1	2	3	4	5	6	All	Conc	Bar
1. Sequence Number	#	13	14	15	34	35	36			
2. Age of Specimen	days	90	91	92	119	120	120			
3. Def. Pre-Test/Avail.	#/#	0/27	0/25	0/25	0/26	0/25	0/29	0/26	0/27	0/26
4. Measured Cover	in.	1.50	1.50	1.50	1.50	1.50	1.50	1.50	1.50	1.50
5. LVDT Attachment	code	RA	RA	RA	RA	RA	RA			
6. LES Transition Load	kips	8.0	8.0	8.0	8.5	8.0	8.0	8.1	8.0	8.3
7. LES Transition Slip	in.	0.007	0.007	0.008	0.007	0.007	0.007	0.007	0.007	0.007
8. First Crack Load	kips	16.8	15.0	14.3	18.5	15.2	19.0	16.5	16.3	16.8
9. FES Transition Load	kips	35.5	38.5	29.0	39.1	33.5	30.5	34.4	32.1	38.8
10. FES Transition Slip	in.	0.0003	0.0004	0.0004	0.0004	0.0004	0.0004	0.0004	0.0004	0.0004
11. Associated LES Slip	in.	0.153	0.179	0.102	0.168	0.143	0.126	0.145	0.131	0.174
12. Conc AE Peak, Load	kips	36	X	29	38	41	X	36	35	38
13. Bar AE Peak, Load	kips	36	41	27	28	41	36	35	35	35
14. Ultimate Load	kips	36.2	41.9	30.1	39.1	41.5	36.3	37.5	36.0	40.5
15. Failure Type	code	C	III	C	III	C	C			
16. AE C2 Pattern	code	UD	X	UD	UD	U	X			
17. AE C3 Peak	code	U	X	U	U	U	X			
18. AE B2 Pattern	code	U	U	ID	D	ID	ID			
19. AE B3 Peak	code	U	U	M	M	U	U			
20. f_b / ω_{ult}	n.a.	0.11	0.09	0.05	0.07	0.10	0.11	0.09	0.10	0.08
21. Bar MOE	ksi	6410	6550	6290	6320	6250	6160	6330	6280	6440
22. Mean Bond Stress	psi	615	711	511	664	705	616	637	612	688
23. Def. Damaged/Avail.	#/#	11/27	15/25	4/25	0/26	25/25	28/29	14/26	17/27	8/26

Notes:
1) "X" indicates equipment malfunction or insufficient data for analysis.
2) Row 5: N (no protection), M (masking tape), D (duct tape), RA (rubber aluminum).
3) Row 15: C (concrete splitting), IA (spaghetti bar failure in embedment), IB (spaghetti failure out), IC (spaghetti bar failure both in and out), IIA (bar fracture in embedment), IIB (bar fracture out).
4) Rows 16 and 18: I (increasing), D (decreasing), UD (uniform/decreasing), ID (increasing/decreasing), U (uniform), X (insufficient data).
5) Rows 17 and 19: M (mid-load peak), U (ultimate load peak), X (insufficient data).

Table 3.11 Results 2M2-6-2-20.0
Prim. Test 2, Manf. 2, No. 6 GFRP, $2d_b$ (1.50 in.) cover, 20.0 in. emb., f'_c 6340 psi

Data	Units	Test Number						Average		
		1	2	3	4	5	6	All	Conc	Bar
1. Sequence Number	#	16	17	18	31	32	33			
2. Age of Specimen	days	93	93	93	118	119	119			
3. Def. Pre-Test/Avail.	#/#	0/23	0/23	0/22	1/21	0/21	0/22	0/22	0/22	0/21
4. Measured Cover	in.	1.50	1.50	1.63	1.44	1.50	1.50	1.51	1.51	1.50
5. LVDT Attachment	code	RA	RA	RA	RA	RA	RA			
6. LES Transition Load	kips	X	9.5	8.5	7.0	9.5	9.5	8.8	6.9	9.5
7. LES Transition Slip	in.	X	0.008	0.005	0.008	0.007	0.008	0.007	0.006	0.007
8. First Crack Load	kips	13.6	15.2	12.0	19.3	18.5	16.0	15.8	15.2	18.5
9. FES Transition Load	kips	X	29.0	33.9	29.8	35.5	31.0	31.8	24.7	35.5
10. FES Transition Slip	in.	X	0.0005	0.0006	0.0006	0.0007	0.0006	0.0006	0.0005	0.0007
11. Associated LES Slip	in.	X	0.086	0.126	0.094	0.117	0.107	0.106	0.083	0.117
12. Conc AE Peak, Load	kips	28	X	26	34	29	38	32	32	29
13. Bar AE Peak, Load	kips	29	32	27	34	40	38	33	32	40
14. Ultimate Load	kips	32.0	32.6	37.7	34.6	40.8	38.0	36.0	35.0	40.8
15. Failure Type	code	C	C	C	C	III	C			
16. AE C2 Pattern	code	ID	X	U	U	UD	UD			
17. AE C3 Peak	code	U	X	U	U	U	U			
18. AE B2 Pattern	code	ID	UD	ID	UD	D	UD			
19. AE B3 Peak	code	U	U	U	U	M	U			
20. f_b / ω_{ult}	n.a.	X	0.13	0.07	0.09	0.09	0.05	0.08	0.08	0.09
21. Bar MOE	ksi	6070	6210	5920	6300	6180	6320	6170	6160	6180
22. Mean Bond Stress	psi	683	692	800	734	866	806	743	743	866
23. Def. Damaged/Avail.	#/#	10/23	23/23	22/22	20/19	16/21	22/22	19/22	19/22	16/21

Notes:
1) "X" indicates equipment malfunction or insufficient data for analysis.
2) Row 5: N (no protection), M (masking tape), D (duct tape), RA (rubber aluminum).
3) Row 15: C (concrete splitting), IA (spaghetti bar failure in embedment), IB (spaghetti failure out), IC (spaghetti bar failure both in and out), IIA (bar fracture in embedment), IIB (bar fracture out).
4) Rows 16 and 18: I (increasing), D (decreasing), UD (uniform/decreasing), ID (increasing/decreasing), U (uniform), X (insufficient data).
5) Rows 17 and 19: M (mid-load peak), U (ultimate load peak), X (insufficient data).

Table 3.12 Results 2M2-6-2-15.0
Prim. Test 2, Manf. 2, No. 6 GFRP, $2d_b$ (1.50 in.) cover, 15.0 in. emb., f'_c 6340 psi

Data	Units	Test Number						Average		
		1	2	3	4	5	6	All	Conc	Bar
1. Sequence Number	#	19	20	21	28	29	30			
2. Age of Specimen	days	96	96	97	117	117	118			
3. Def. Pre-Test/Avail.	#/#	0/14	0/14	1/14	0/17	0/14	0/17	0/15	0/15	
4. Measured Cover	in.	1.50	1.44	1.50	1.50	1.50	1.75	1.53	1.53	
5. LVDT Attachment	code	RA	RA	RA	RA	RA	RA			
6. LES Transition Load	kips	9.0	9.2	9.2	9.9	9.0	10.0	9.4	9.4	
7. LES Transition Slip	in.	0.007	0.010	0.010	0.011	0.011	0.011	0.010	0.010	
8. First Crack Load	kips	12.5	14.3	16.5	20.6	28.0	19.0	18.5	18.5	
9. FES Transition Load	kips	14.7	20.0	19.5	21.1	20.0	19.5	19.1	19.1	
10. FES Transition Slip	in.	0.0004	0.0005	0.0005	0.0007	0.0005	0.0005	0.0005	0.0005	
11. Associated LES Slip	in.	0.017	0.043	0.038	0.038	0.032	0.038	0.034	0.034	
12. Conc AE Peak, Load	kips	25	25	X	24	28	27	26	26	
13. Bar AE Peak, Load	kips	25	26	X	X	28	X	26	26	
14. Ultimate Load	kips	25.8	26.6	29.2	24.8	28.1	28.5	27.2	27.2	
15. Failure Type	code	C	C	C	C	C	C			
16. AE C2 Pattern	code	U	UD	X	UD	ID	UD			
17. AE C3 Peak	code	U	U	X	U	U	U			
18. AE B2 Pattern	code	U	ID	X	X	I	X			
19. AE B3 Peak	code	U	U	X	X	U	X			
20. f_b / ω_{ult}	n.a.	0.10	0.16	0.13	0.09	0.16	0.08	0.12	0.12	
21. Bar MOE	ksi	6160	6390	6250	6380	6310	6410	6320	6320	
22. Mean Bond Stress	psi	730	753	826	702	795	806	769	769	
23. Def. Damaged/Avail.	#/#	11/14	1/14	13/13	0/17	14/14	17/17	10/15	10/15	

Notes:

1) "X" indicates equipment malfunction or insufficient data for analysis.
2) Row 5: N (no protection), M (masking tape), D (duct tape), RA (rubber aluminum).
3) Row 15: C (concrete splitting), IA (spaghetti bar failure in embedment), IB (spaghetti failure out), IC (spaghetti bar failure both in and out), IIA (bar fracture in embedment), IIB (bar fracture out).
4) Rows 16 and 18: I (increasing), D (decreasing), UD (uniform/decreasing), ID (increasing/decreasing), U (uniform), X (insufficient data).
5) Rows 17 and 19: M (mid-load peak), U (ultimate load peak), X (insufficient data).

Table 3.13 M1, GFRP Rebar Ultimate Loads

Cover (in.)	Embedment (in.)	Target $\%f_u$[1]	Concrete Splitting Failures Avg. Ult. Load (kips) (# tests)	Actual $\%f_u$[2]	Bar Failures Avg. Ult. Load (kips) (# tests)
3	15.0	85[3]	none	100[4]	19.0 (6)
3	12.5	70[3]	19.2 (5)	100	17.7 (1)
3	10.0	55[3]	16.7 (2)	87	18.0 (4)
2	47.0	100	none	100[4]	17.8 (6)
2	15.0	85	22.5 (1)	100[5]	17.0 (5)
2	12.5	70	17.4 (6)	91	14.4 (3)

Notes:

1) Target $\%f_u$ was based on the Pilot Test results with concrete splitting failures.
2) Actual $\%f_u$ was based on tensile test average failure load of 19.2 kips for M1 rebar (Table 2.6) and the average concrete splitting failure load.
3) The target $\%f_u$ for $3d_b$ cover was expected to be low because the design was with Pilot Test and $2d_b$ cover.
4) 100% f_u was achieved because all the tests exhibited bar failures.
5) Actual ultimate load exceeded the tensile test average load of 19.2 kips.

Table 3.14 M1, Bar Failures

Test Identification	LVDT Attach.	Failure Type	f_b / ω_{ult}	Ult Load (kips)
1M1-5-3-15.0-1	N	IB	X	18.3
1M1-5-3-15.0-2	N	IB	0.11	18.9
1M1-5-3-15.0-3	N	IB	0.08	18.8
1M1-5-3-15.0-4	D	IB	0.07	18.2
1M1-5-3-15.0-5*	RA	IB	0.07	19.7
1M1-5-3-15.0-6*	RA	IB	0.12	20.1
1M1-5-3-12.5-4	RA	IIA	0.08	17.7
1M1-5-3-10.0-2	M	IC	0.13	16.9
1M1-5-3-10.0-3	M	IC	0.07	17.4
1M1-5-3-10.0-4*	RA	IB	0.10	16.8
1M1-5-3-10.0-5*	RA	IC	0.09	20.8
1M1-5-2-46.5-1	D	IB	0.06	16.2
1M1-5-2-46.5-2	M	IC	0.09	21.9
1M1-5-2-46.5-3	D	IB	0.12	12.9
1M1-5-2-46.5-4*	RA	IB	0.08	18.7
1M1-5-2-46.5-5*	RA	IC	0.14	14.3
1M1-5-2-46.5-6*	RA	IC	0.09	22.6
1M1-5-2-15.0-1	D	IB	0.10	20.0
1M1-5-2-15.0-2	D	IB	0.06	13.7
1M1-5-2-15.0-4*	RA	IB	0.17	15.9
1M1-5-2-15.0-5*	RA	IA	0.08	17.4
1M1-5-2-15.0-6	RA	IA	0.21	18.1
1M1-5-2-12.5-1	D	IIB	0.18	9.1
1M1-5-2-12.5-3	D	IC	0.08	17.9
1M1-5-2-12.5-4*	RA	IB	0.10	16.1
average of all bar failures (25 bars) standard deviation				17.5 2.9
average of selected tests* (10 bars) standard deviation				18.2 2.6
average of tensile test (10 bars) standard deviation				19.2 1.7
manufacturer reported tensile strength standard deviation				29.4 0.5

Table 3.15 M1, Concrete Splitting Failures

Test Identification	Ult Load (kips)	Avg / SD (kips)	COV (%)
1M1-5-3-12.5-1	19.8	18.8 / 1.1	5.9%
1M1-5-3-12.5-2	17.6		
1M1-5-3-12.5-3	18.2		
1M1-5-3-12.5-5	19.7		
1M1-5-3-12.5-6	20.7		
1M1-5-3-10.0-1	16.0	16.7 / 0.9	5.4%
1M1-5-3-10.0-6	17.3		
1M1-5-2-15.0-3	22.5	22.5 / n.a.	n.a.
1M1-5-2-12.5-2	18.5	17.4 / 0.9	5.2%
1M1-5-2-12.5-5	16.7		
1M1-5-2-12.5-6	17.1		
2M1-5-2-12.5-1	18.7		
2M1-5-2-12.5-2	16.5		
2M1-5-2-12.5-3	17.1		

Table 3.16 M1, GFRP Bond Behavior Selected Results

			M1 GFRP Rebar (cover-embedment length) (total tests/concrete splitting failures/bar failures)							
			3-15.0 6/0/6	3-12.5 6/5/1	3-10.0 6/2/4	2-15.0 6/1/5	2-12.5 9/6/3	Avg	SD	2-47.0 6/0/6
LES	Load	kips	7.6	7.3	7.4	8.2	7.6	7.6	0.3	7.3
Trans. Pt.	LES	in.	0.009	0.008	0.009	0.011	0.010	0.009	0.001	0.010
First Crack	Load	kips	10.2	10.4	9.7	9.4	10.1	10.0	0.4	9.8
Perp. Crack	Load	kips	11.4	12.0	10.8	10.2	11.6	11.2	0.7	11.9
	Loc	in.	1.3	1.7	1.0	1.5	2.0	1.5	0.4	1.7
Conc AE Pk	Load	kips	12	13	12	15	13	13	1	15
LES	LES	in.	12.7	12.9	13.1	11.9	12.4	12.6	0.5	12.4
Diverge	Load	kips	0.026	0.025	0.025	0.022	0.022	0.024	0.002	0.027
FES	Load	kips	17.3	15.5	12.0	17.1	13.5	15.1	2.3	17.7
Trans. Pt.	FES	in.	0.0005	0.0006	0.0004	0.0005	0.0005	0.0005	0.0001	0.0001
Bar AE Pk	FES	kips	18	17	16	18	16	17	1	17
Ultimate	Load	kips	19.0	19.0	17.5	17.9	16.4	18.0	1.1	17.8

Table 3.17 M1, GFRP Rebar FES Transition Loads

Cover ($\#d_b$)	Embedment (in.)	Transition Load (kips)
3	15.0	17.3
3	12.5	15.5
3	10.0	12.0
2	15.0	17.1
2	12.5	13.5

Table 3.18 M2, GFRP Rebar Ultimate Loads

Cover (in.)	Embedment (in.)	Target $\%f_u$[1]	Concrete Splitting Failures Avg. Ult. Load (kips) (# tests)	Actual $\%f_u$[2]	Bar Failures Avg. Ult. Load (kips) (# tests)
3	20.0	80[3]	34.1 (4)	78	39.5 (2)
3	15.0	60[3]	29.2 (6)	67	none
2	47.0	100	none	100[4]	38.4 (3)
2	25.0	100	36.0 (4)	83	40.5 (2)
2	20.0	80	35.0 (5)	80	40.8 (1)
2	15.0	60	27.2 (6)	63	none

Notes:

1) Target $\%f_u$ was based on the Pilot Test results with concrete splitting failures.
2) Actual $\%f_u$ was based on tensile test average failure load of 43.5 kips for M2 rebar (Table 2.6) and the average concrete splitting failure load.
3) The target $\%f_u$ for $3d_b$ cover was expected to be low because the design was with Pilot Test and $2d_b$ cover.
4) 100% f_u was achieved because all the tests exhibited bar failures.

Table 3.19 M2, Bar Failures

Test Identification	Failure Type	f_b / ω_{ult}	Ultimate Load (kips)
2M2-6-2-20.0-5	III	0.09	40.8
2M2-6-2-25.0-2	III	0.09	41.9
2M2-6-2-25.0-4	III	0.08	39.1
2M2-6-2-47.0-1	III	0.10	34.1
2M2-6-2-47.0-2	III	0.12	45.7
2M2-6-3-20.0-5	III	0.07	42.5
2M2-6-3-20.0-6	III	0.04	36.5
2M2-6-2-47.0-3	IA	X	35.5
ultimate bar failure load (only one test exhibited a non-Type III failure)			35.5
average tensile test (3 bars) standard deviation			43.5 1.3
manufacturer reported average tensile strength			43.5

Table 3.20 M2, Concrete Splitting Failures

Test Identification	Ult Load (kips)	Avg / SD (kips)	COV (%)
2M2-6-3-20.0-1	32.8	34.1 / 1.1	3.2%
2M2-6-3-20.0-2	34.8		
2M2-6-3-20.0-3	35.3		
2M2-6-3-20.0-4	33.6		
2M2-6-3-15.0-1	27.5	29.2 / 3.2	10.9%
2M2-6-3-15.0-2	26.3		
2M2-6-3-15.0-3	25.5		
2M2-6-3-15.0-4	33.4		
2M2-6-3-15.0-5	31.9		
2M2-6-3-15.0-6	30.7		

Test Identification	Ult Load (kips)	Avg / SD (kips)	COV (%)
2M2-6-2-25.0-1	36.2	36.0 / 4.7	13.1%
2M2-6-2-25.0-3	30.1		
2M2-6-2-25.0-5	41.5		
2M2-6-2-25.0-6	36.3		
2M2-6-2-20.0-1	32.2	35.0 / 2.7	7.7%
2M2-6-2-20.0-2	32.6		
2M2-6-2-20.0-3	37.7		
2M2-6-2-20.0-4	34.6		
2M2-6-2-20.0-6	38.0		
2M2-6-2-15.0-1	25.8	27.2 / 1.7	6.3%
2M2-6-2-15.0-2	26.6		
2M2-6-2-15.0-3	29.2		
2M2-6-2-15.0-4	24.8		
2M2-6-2-15.0-5	28.1		
2M2-6-2-15.0-6	28.5		

Table 3.21 M2, GFRP Bond Behavior Selected Results

			M2 GFRP Rebar (cover-embedment length) (total tests/concrete splitting failures/bar failures)							
			3-20.0 6/4/2	3-15.0 6/6/0	2-25.0 6/4/2	2-20.0 6/5/1	2-15.0 6/6/0	Avg	SD	2-47.0 3/0/3
LES	Load	kips	9.0	6.2	8.1	8.8	9.4	8.3	1.3	12.6
Trans. Pt.	LES	in.	0.011	0.005	0.007	0.007	0.010	0.008	0.002	0.011
First Crack	Load	kips	18.5	18.6	16.5	15.8	18.5	17.6	1.3	16.8
FES	Load	kips	25.9	21.4	34.4	31.8	19.1	26.5	6.6	39.9
Trans. Pt.	FES	in.	0.0004	0.0005	0.0004	0.0006	0.0005	0.0005	0.0001	0.0000
Conc AE Pk	Load	kips	34	26	36	33	26	31	5	39
Bar AE Pk	Load	kips	37[1]	27	37	32	26	32	5	36
Ultimate	Load	kips	35.9	29.2	37.5	36.0	27.2	33.2	4.6	38.4

Notes:

1) The "Bar AE Pk" average was based on only three tests with sufficient AE data for analysis and those tests presented some of the largest ultimate loads. However, the "Ultimate" load was based on all six tests.

Table 3.22 M2, GFRP Rebar FES Transition Loads

Cover ($\#d_b$)	Embedment (in.)	Transition Load (kips)
3	20.0	25.9
3	15.0	21.4
2	25.0	34.4
2	20.0	31.8
2	15.0	19.1

Table 3.23 Comparison of Patterns in the AE C2 Graphs

Type of Distribution Pattern	M1 GFRP Rebar	M2 GFRP Rebar
Decreasing	8%	0%
Uniform/Decreasing	92%	53%
Increasing/Decreasing	0%	11%
Uniform	0%	42%

Table 3.24 Comparison of Bar Failures

Test	M1 GFRP Rebar	M2 GFRP Rebar
Bond Test Bar Failures COV % (# tests)	14.3% (10)	n.a.
Tensile Tests COV % (# tests)	8.9% (10)	2.9% (3)

Table 3.25 Comparison of Concrete Spitting Failures

M1 GFRP Rebar			M2 GFRP Rebar		
Series	COV (%)	Conc. Split. Failures/Total	Series	COV (%)	Conc. Split. Failures/Total
M1-5-3-15.0	n.a.	0 / 6	M2-6-3-20.0	3.2%	4 / 6
M1-5-3-12.5	5.9%	5 / 6	M2-6-3-15.0	10.9%	6 / 6
M1-5-3-10.0	5.4%	2 / 6	M2-6-2-47.0	n.a.	0 / 0
M1-5-2-47.0	n.a.	0 / 6	M2-6-2-25.0	13.1%	4 / 6
M1-5-2-15.0	n.a.	1 / 6	M2-6-2-20.0	7.7%	5 / 6
M1-5-2-12.5	5.2%	6 / 9	M2-6-2-15.0	6.3%	6 / 6

FIGURES

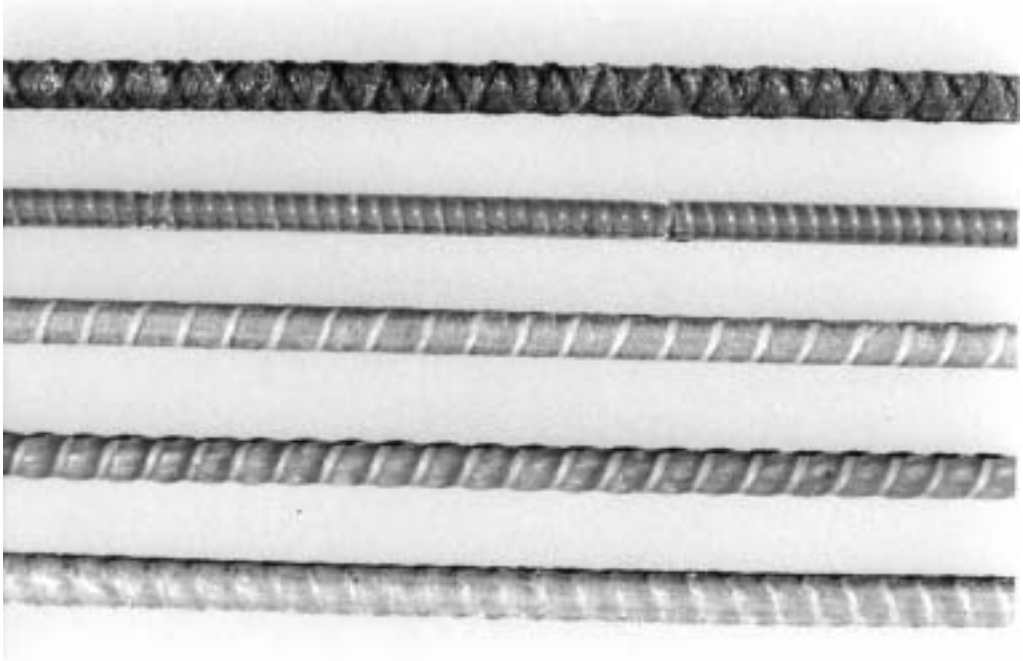

Figure 1.1 GFRP Rebar

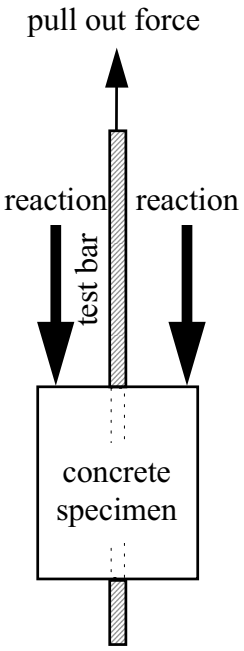

Figure 1.2 Pullout Bond Test

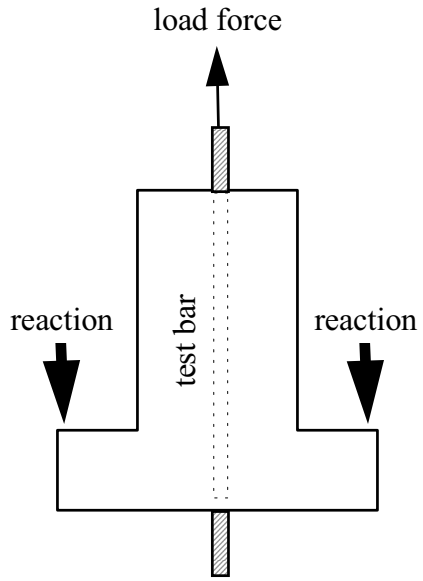

Figure 1.3 Tee Beam Bond Test

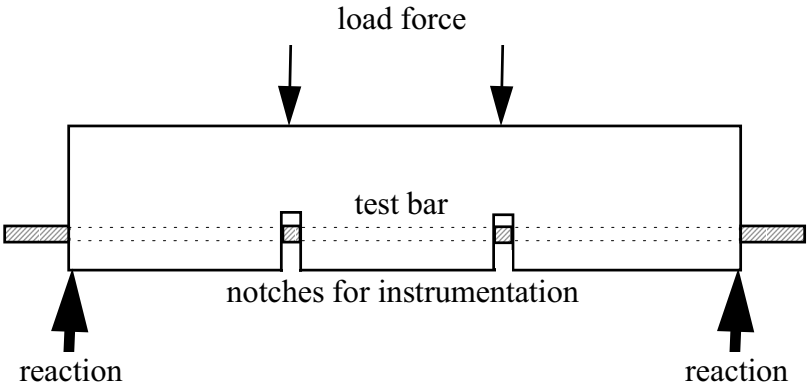

Figure 1.4 Notch Beam Bond Test

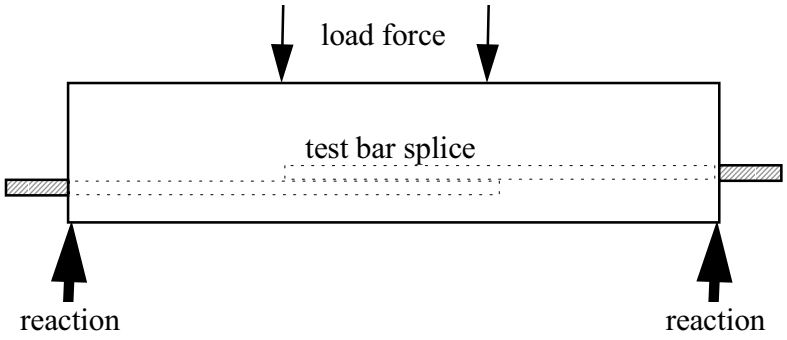

Figure 1.5 Splice Beam Bond Test

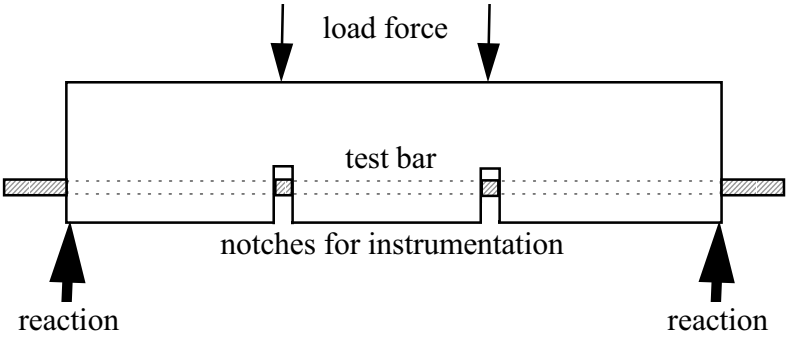

Figure 1.6 Hinge Beam Bond Test

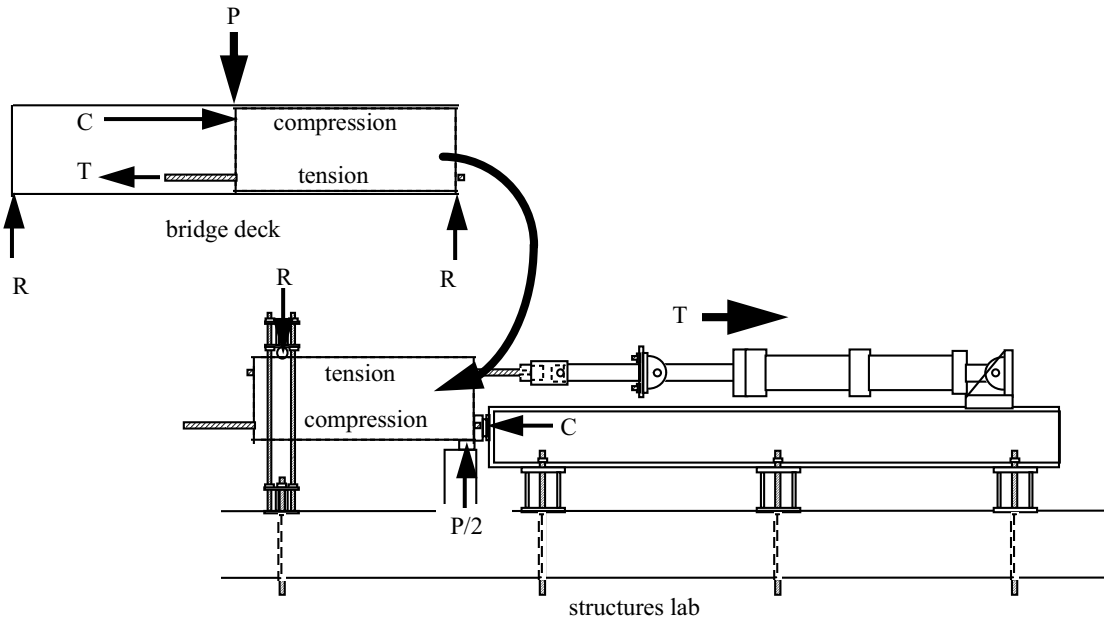

Figure 1.7 Inverted Half-Beam Bond Test

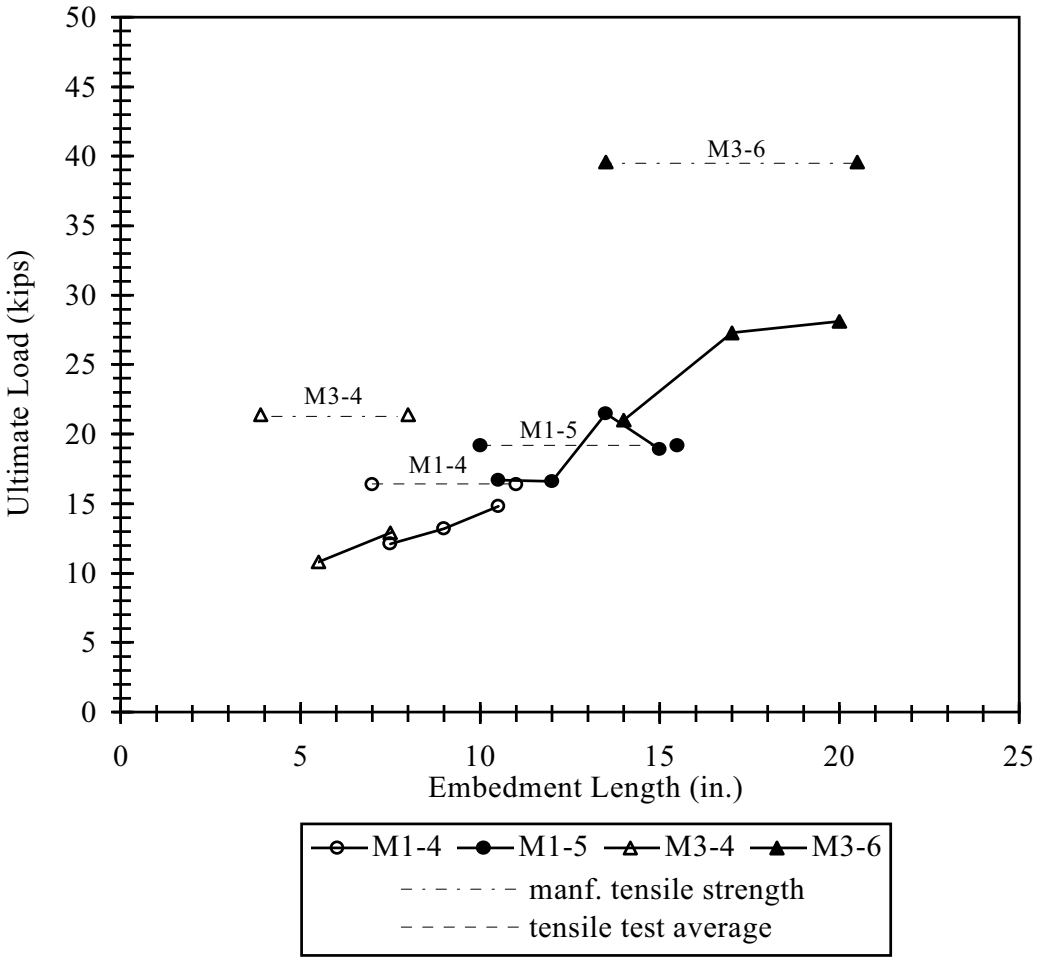

Figure 2.1 Pilot Test Results

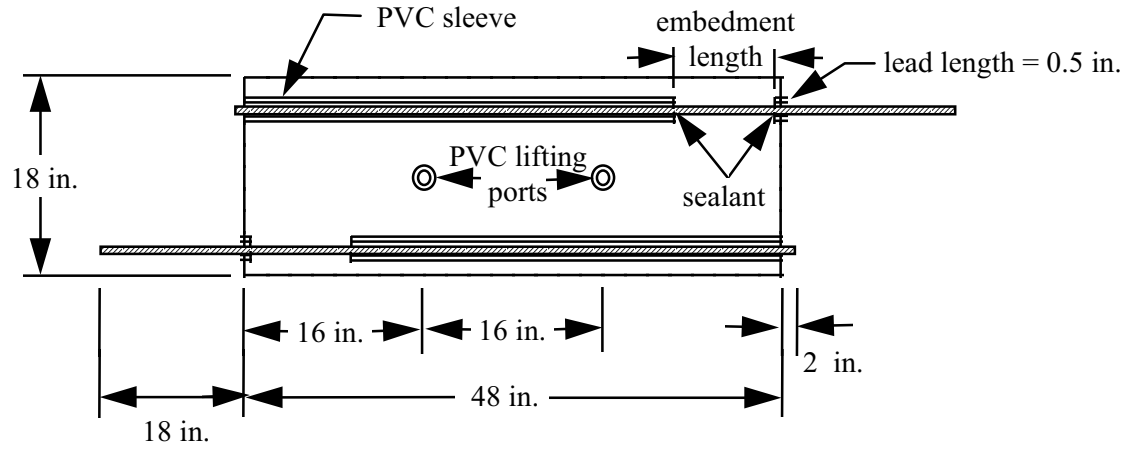

Figure 2.2 Typical Half Beam Dimensions

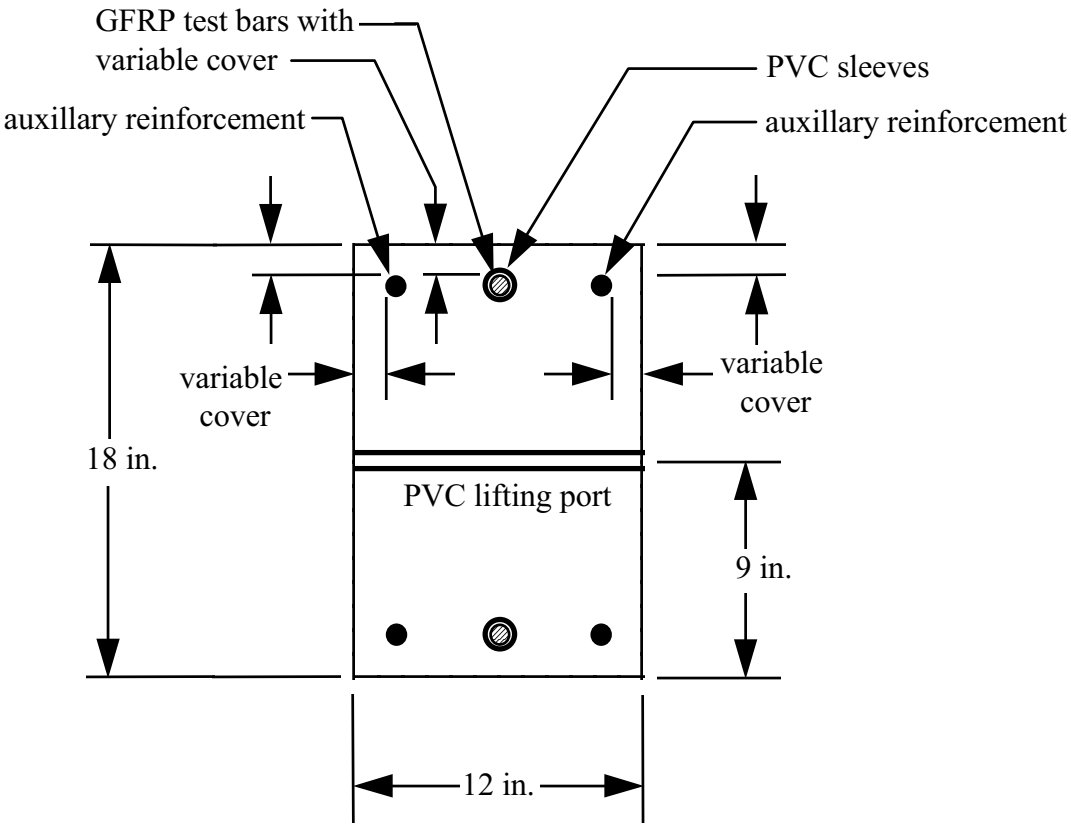

Figure 2.3 Typical Cross Section Dimensions

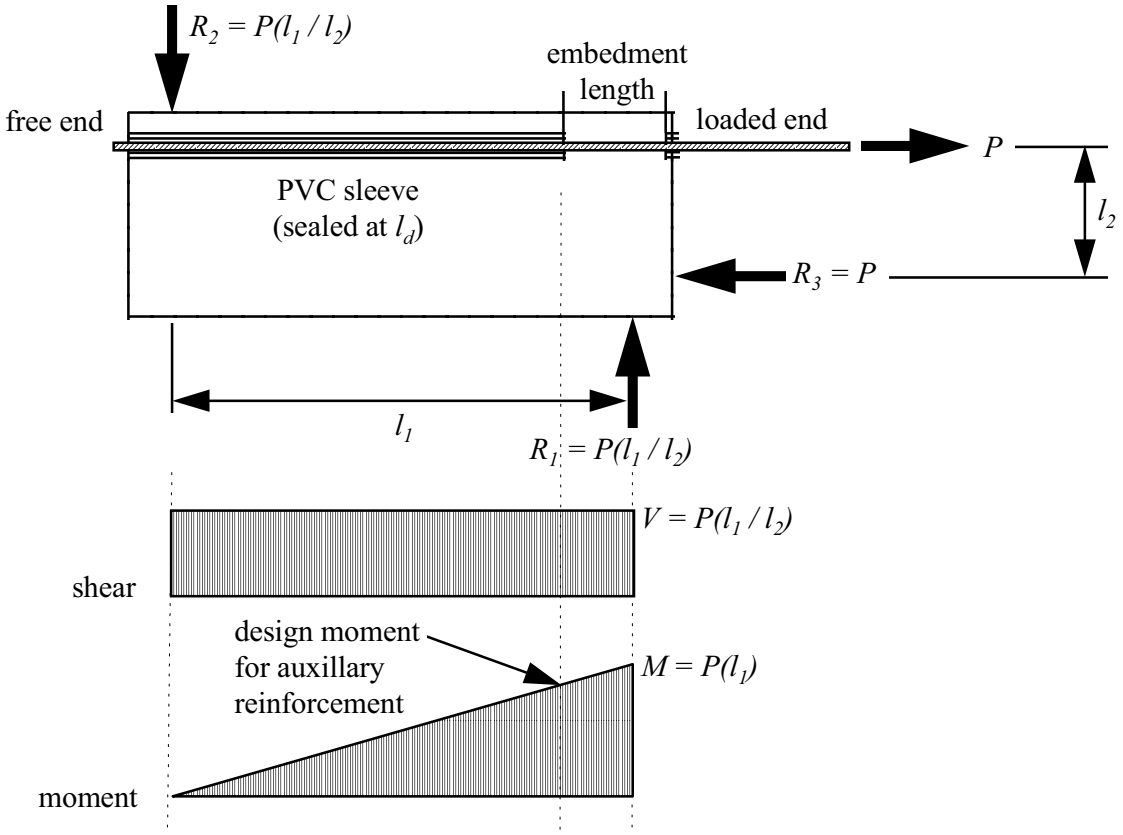

Figure 2.4 Shear and Moment Diagrams

Figure 2.5 M1 GFRP Rebar

Figure 2.6 M2 GFRP Rebar

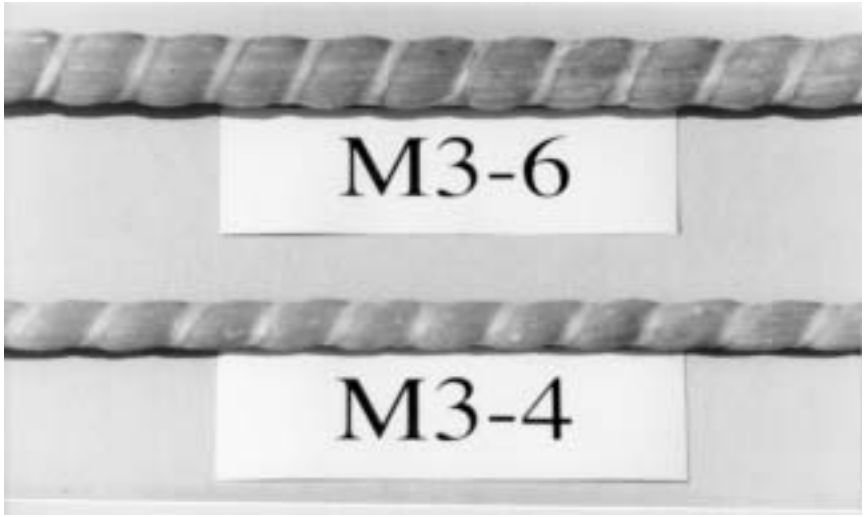

Figure 2.7 M3 GFRP Rebar

Figure 2.8 Concrete Specimen Forms

Figure 2.9 Concrete Specimen Forms with Burlap

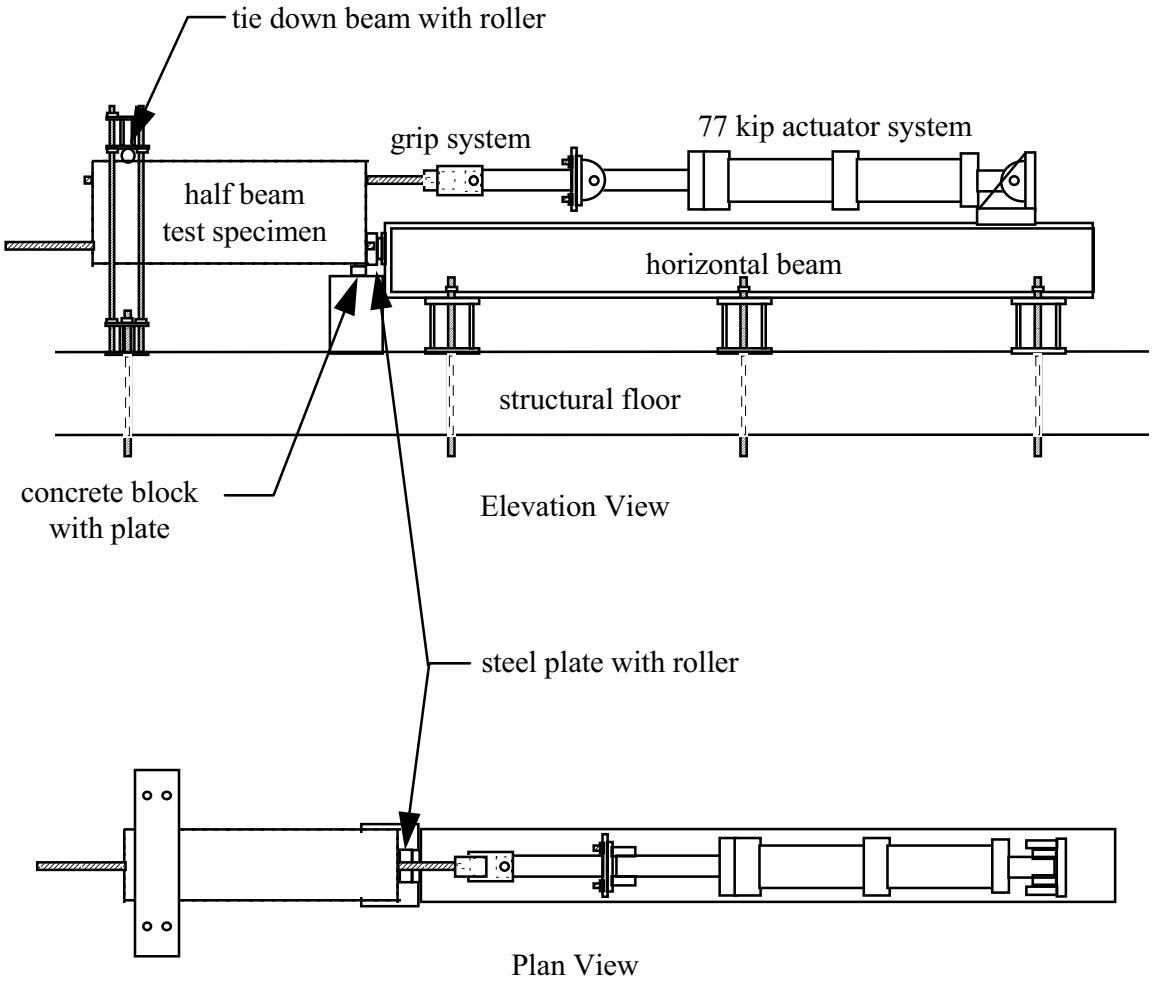

Figure 2.10 Test Frame Setup

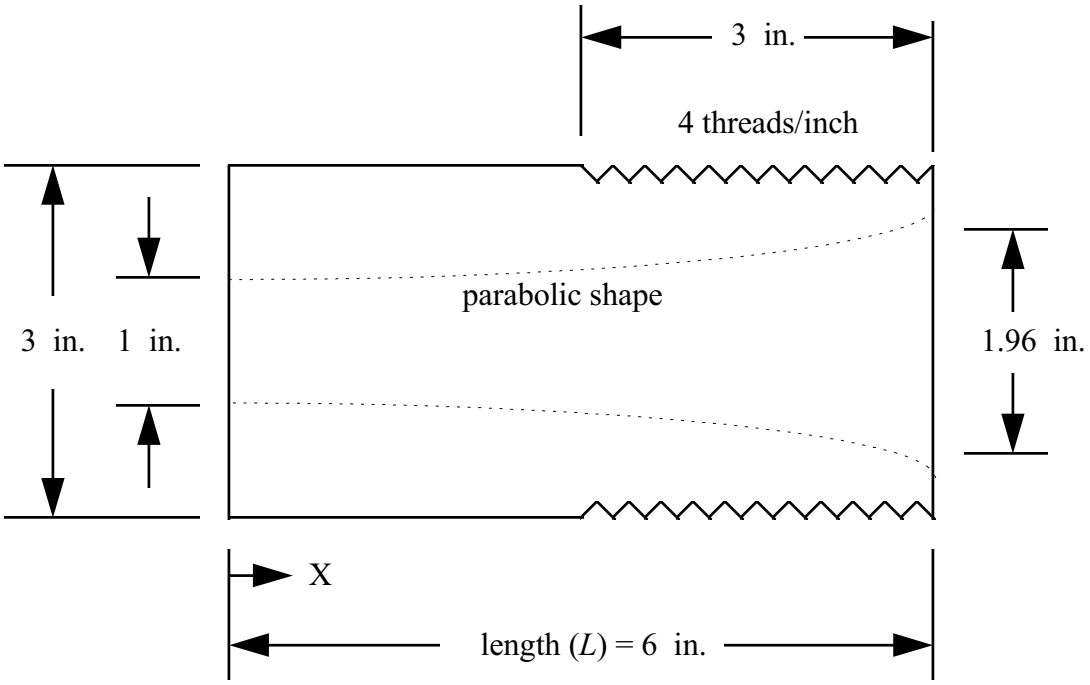

Figure 2.11 Aluminum Parabolic Grip for No.5 and No.6 GFRP Rebar

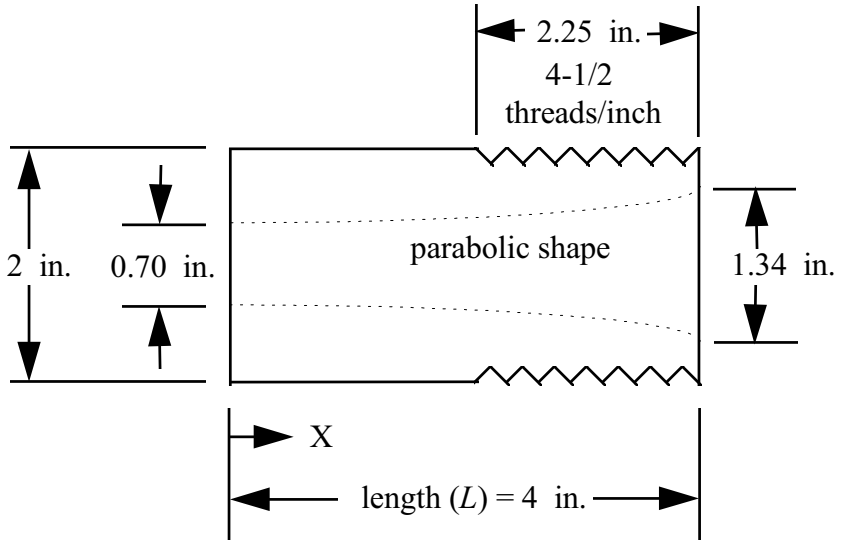

Figure 2.12 Aluminum Parabolic Grip for No.4 GFRP Rebar

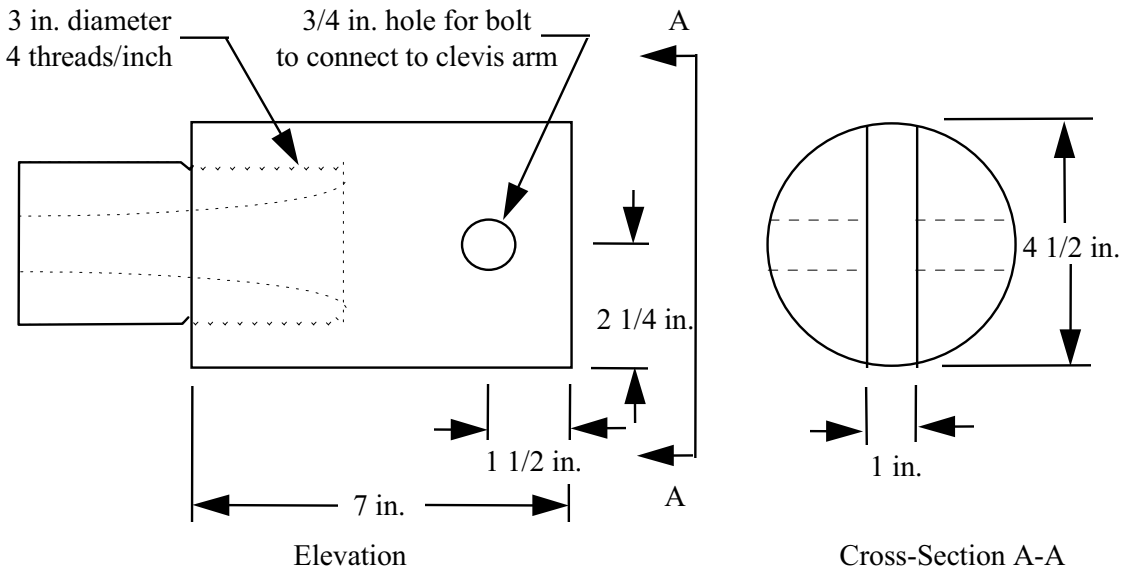

Figure 2.13 Steel Connector for No.5 and 6 GFRP Rebar Aluminum Parabolic Grip

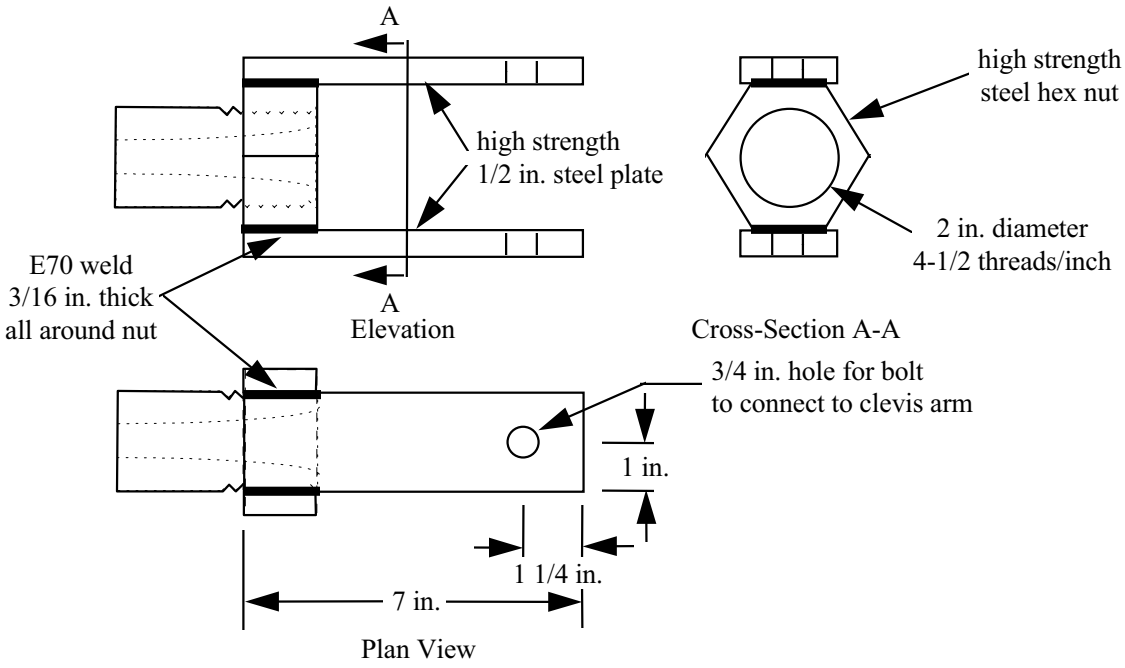

Figure 2.14 Steel Connector for No.4 GFRP Rebar Aluminum Parabolic Grip

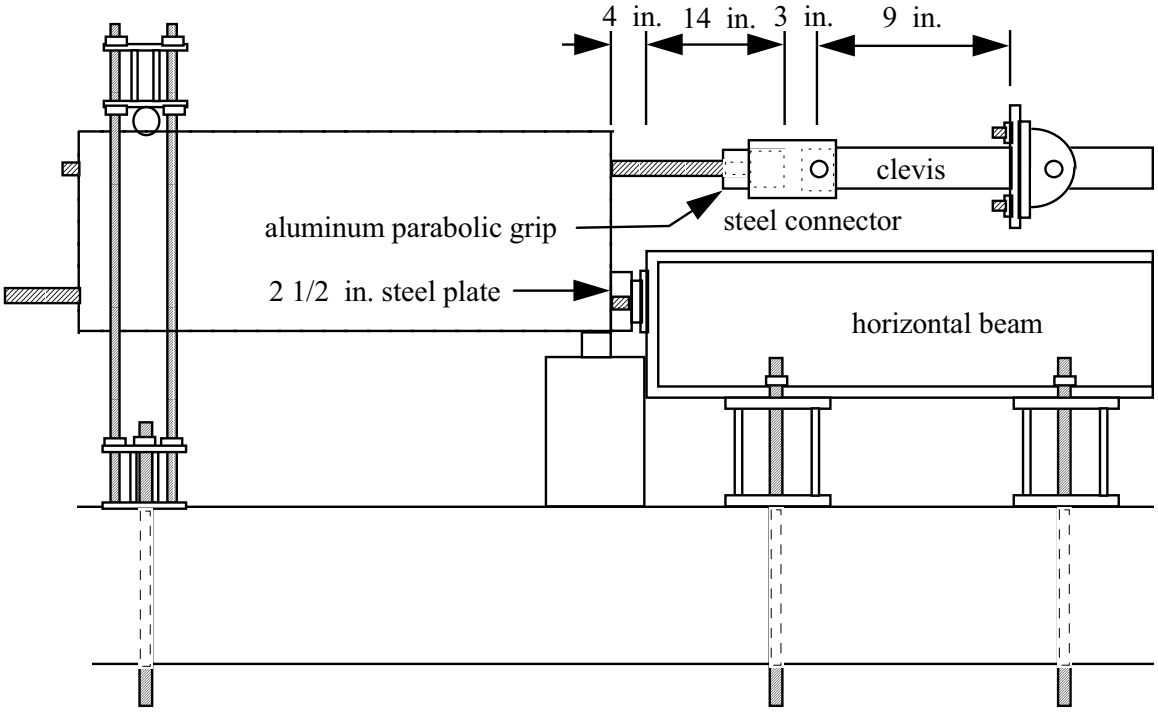

Figure 2.15 Aluminum Parabolic Grip Overall Setup

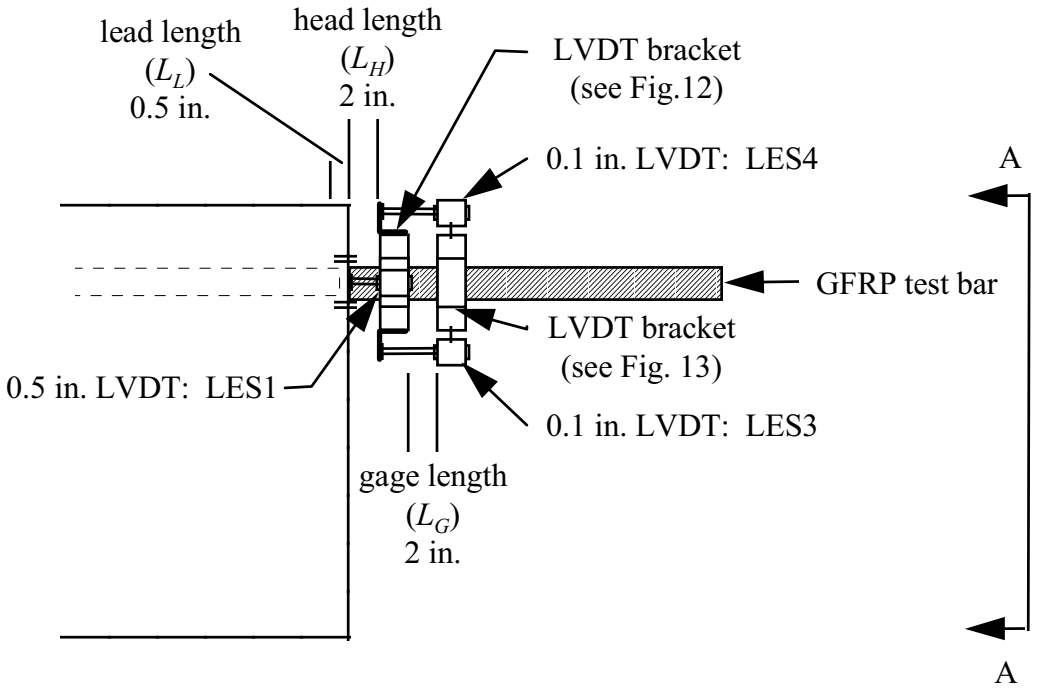

Elevation

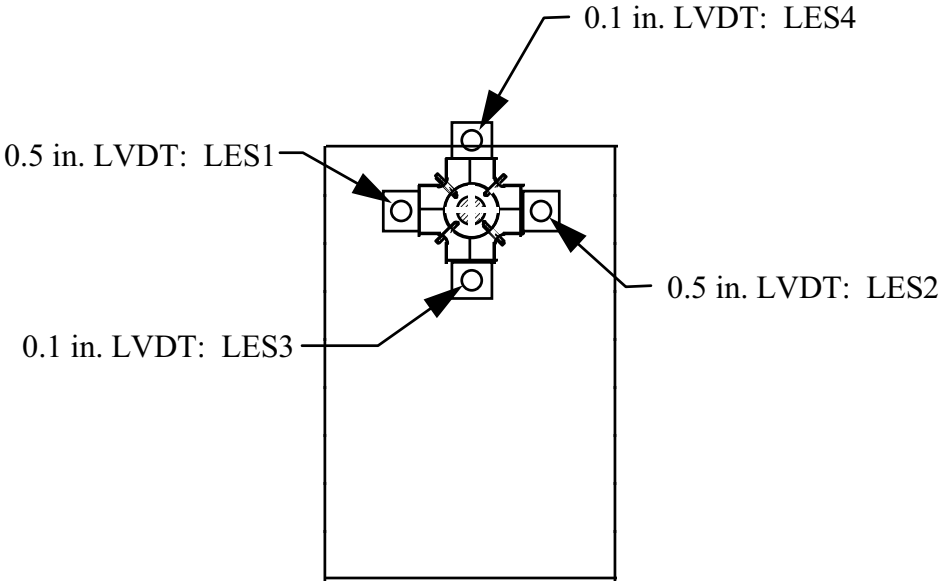

Cross-Section A-A

Figure 2.16 Loaded-End Slip Instrumentation

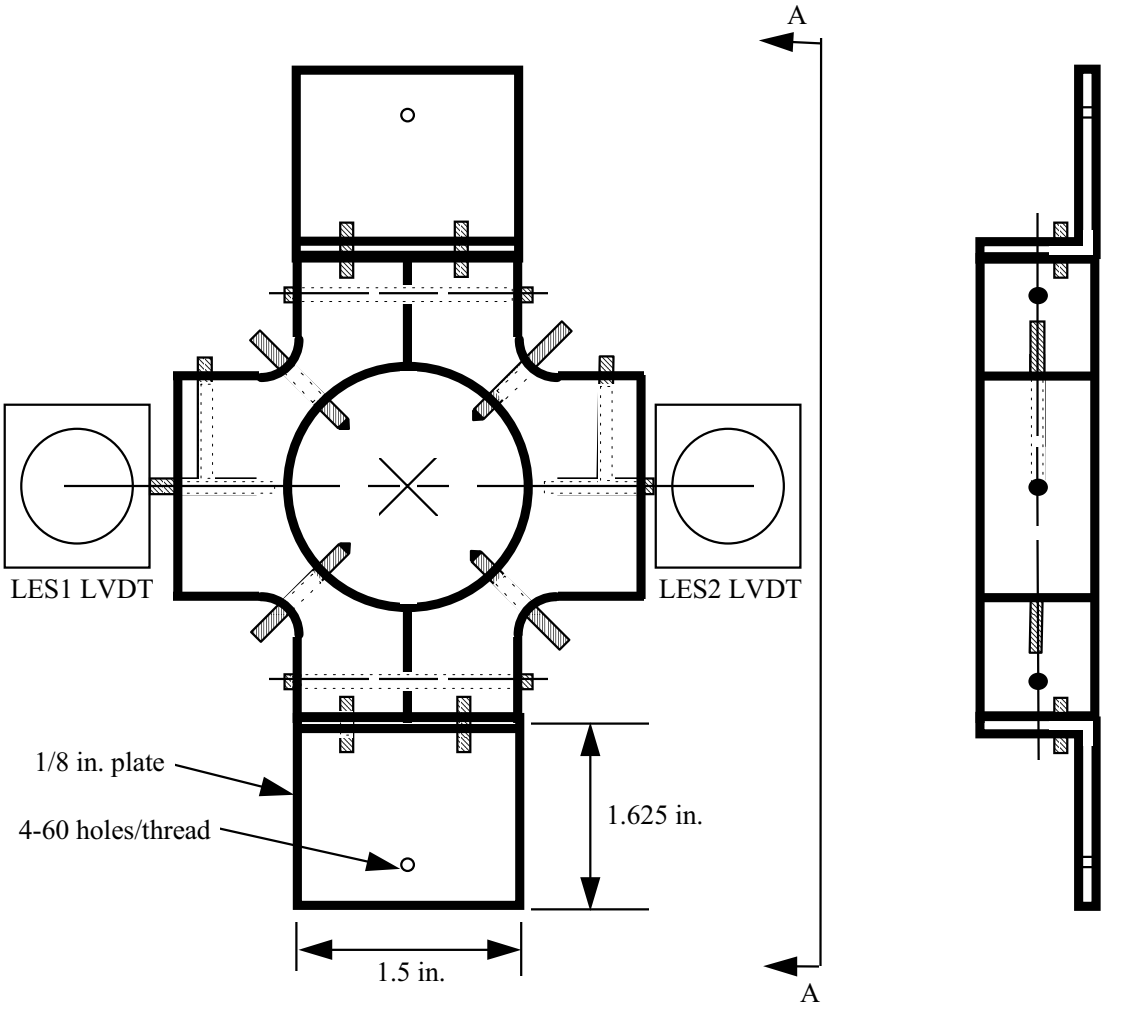

Notes:
1) All bracket parts made from aluminum.
2) All screws are steel.
3) Holes for steel screws are threaded for the screws.

Figure 2.17 LVDT Bracket With Plate

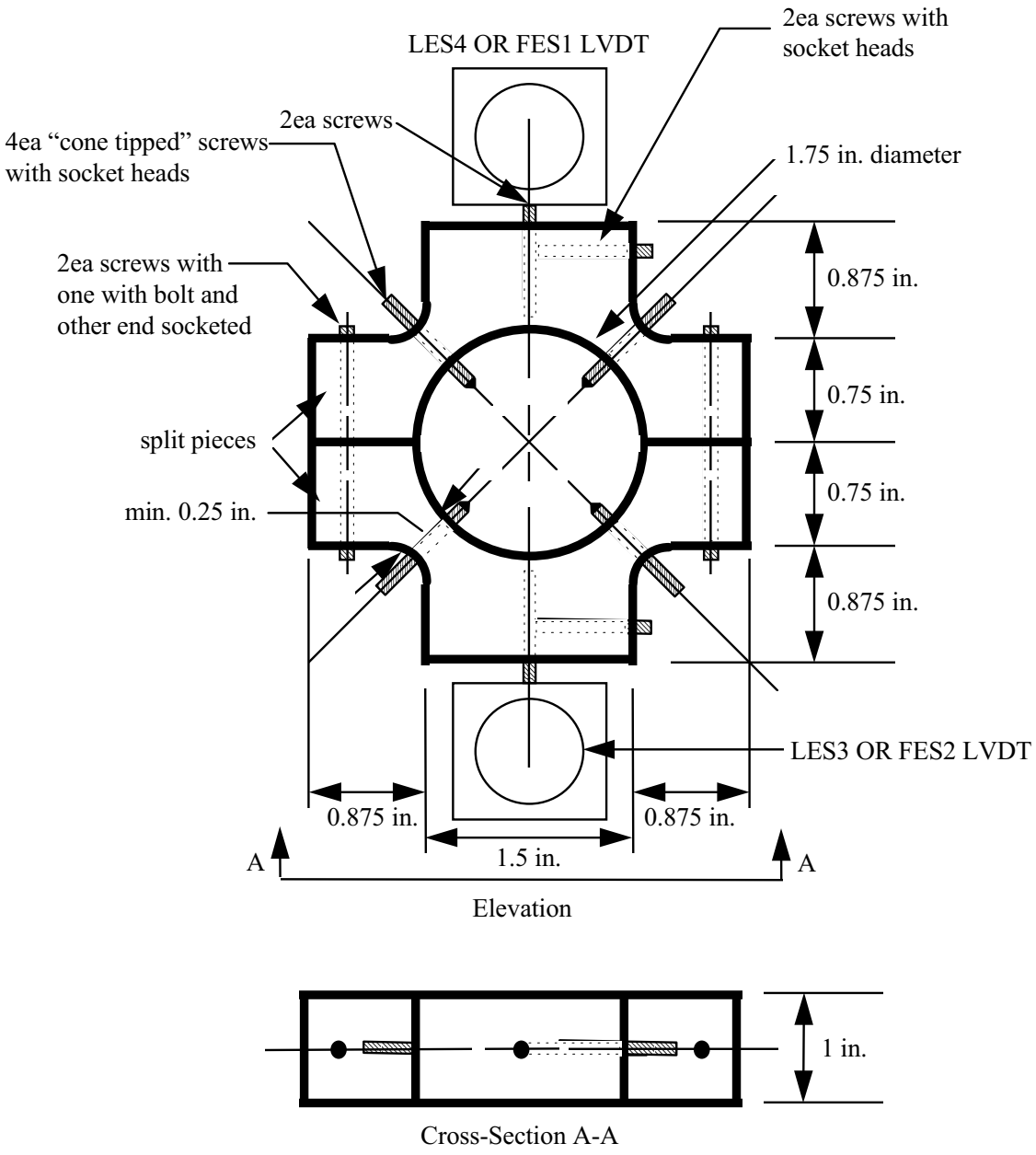

Figure 2.18 LVDT Bracket

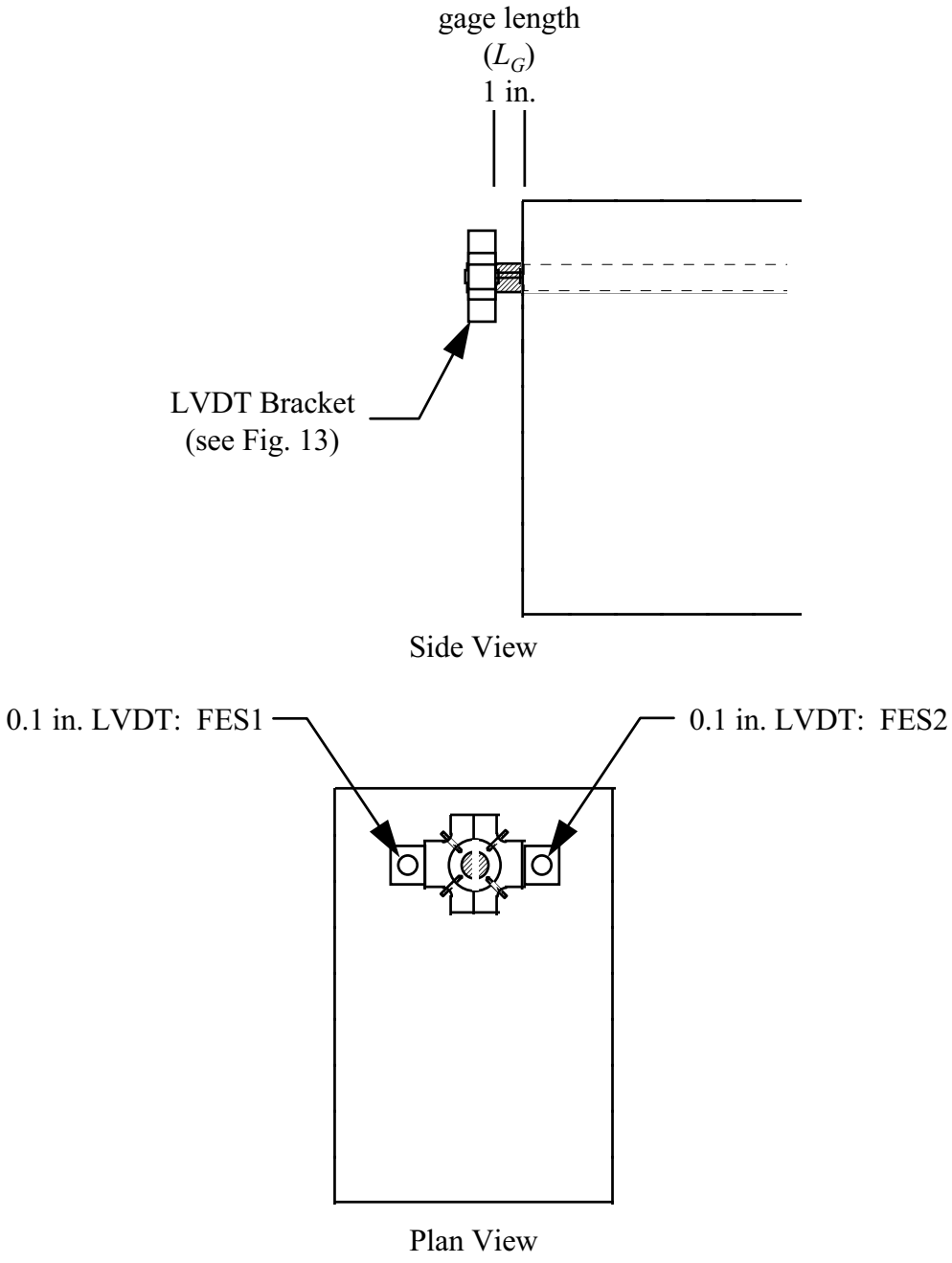

Figure 2.19 Free-End Slip Instrumentation

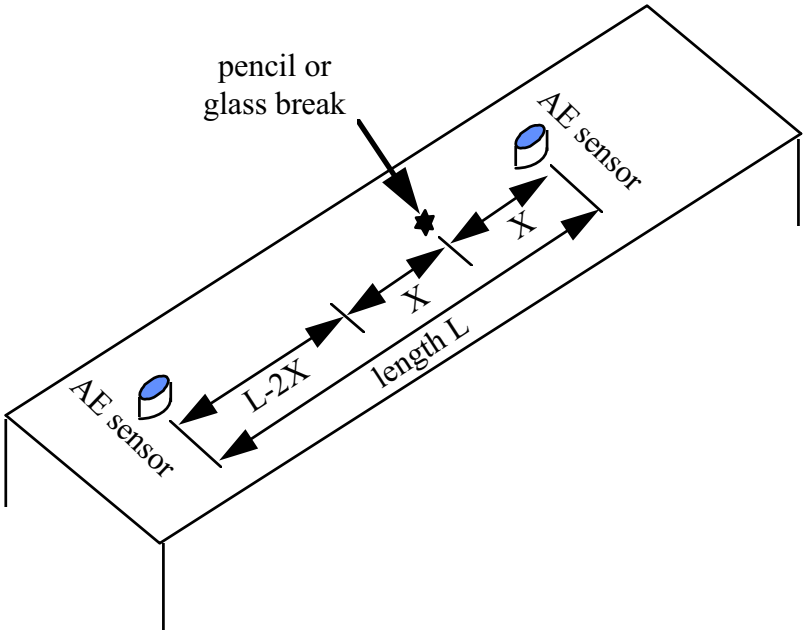

Figure 2.20 Stress Wave Calculation

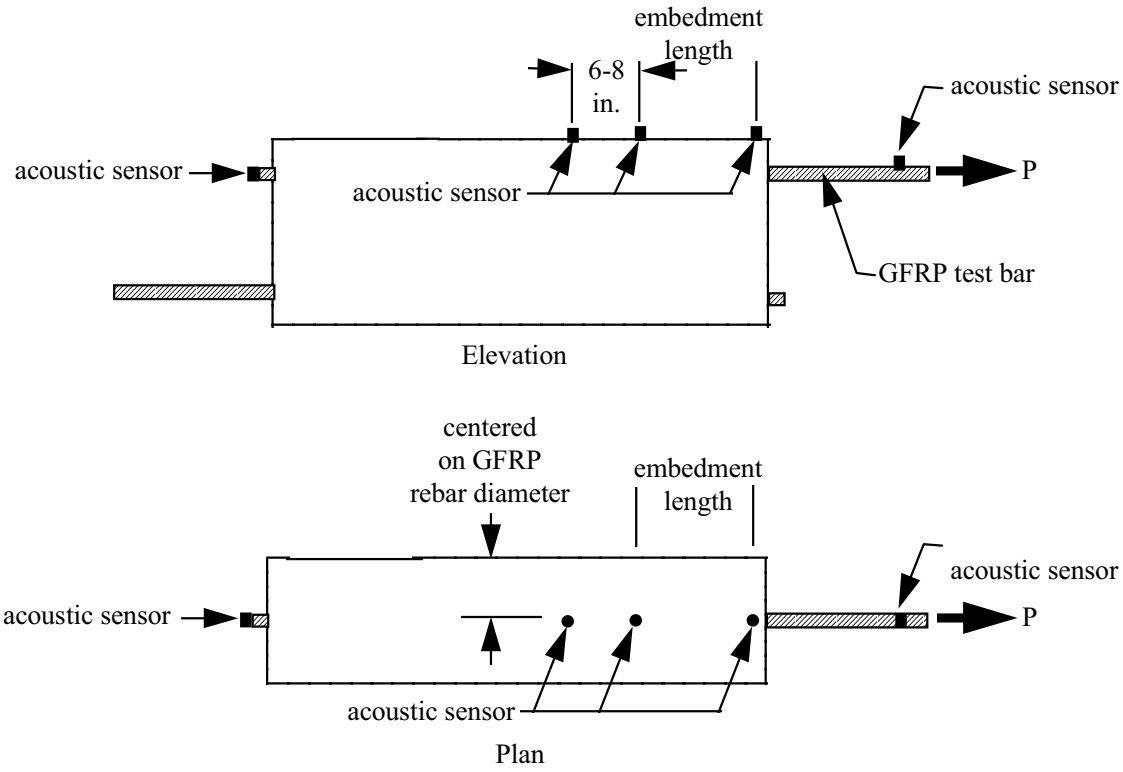

Figure 2.21 Acoustic Sensor Layout

Figure 3.3 FES vs. Load, M1-5-3-12.5
Figure 3.4 LES vs. Load, M1-5-3-12.5

Figure 3.5 FES vs. Load, M1-5-3-10.0
Figure 3.6 LES vs. Load, M1-5-3-10.0

Figure 3.9 FES vs. Load, M1-5-2-15.0
Figure 3.10 LES vs. Load, M1-5-2-15.0

Figure 3.13 FES vs. Load, M2-6-3-20.0
Figure 3.14 LES vs. Load, M2-6-3-20.0

Figure 3.23 FES vs. Load, M2-6-2-15.0
Figure 3.24 LES vs. Load, M2-6-2-15.0

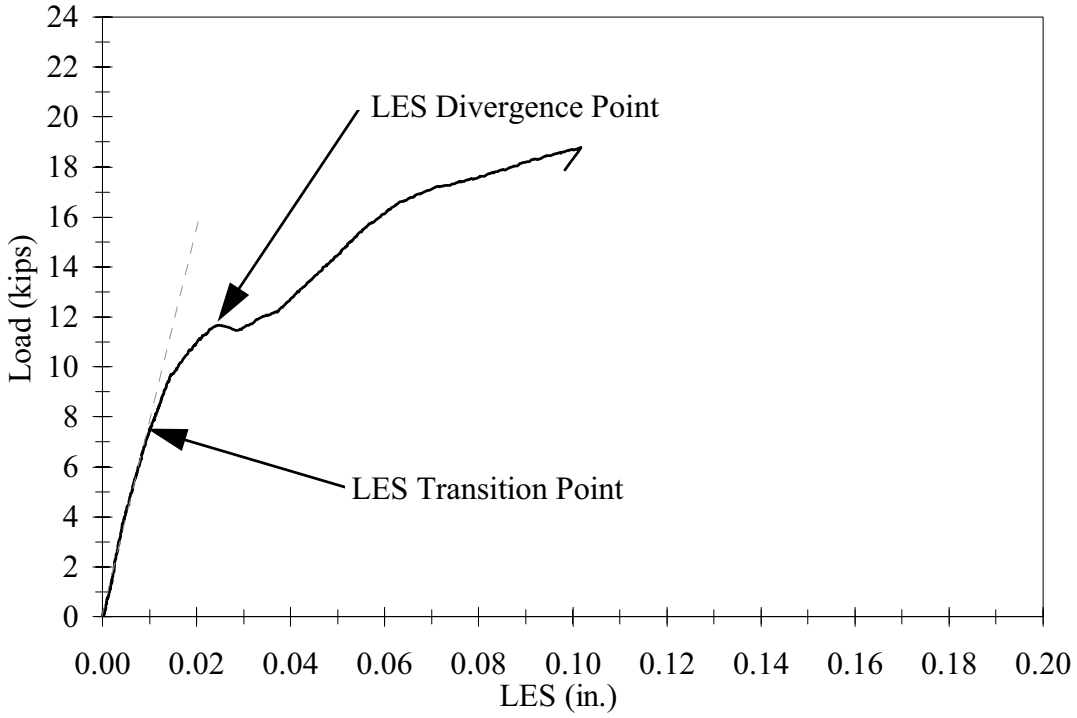

Figure 3.25 M1, Sample LES Graph

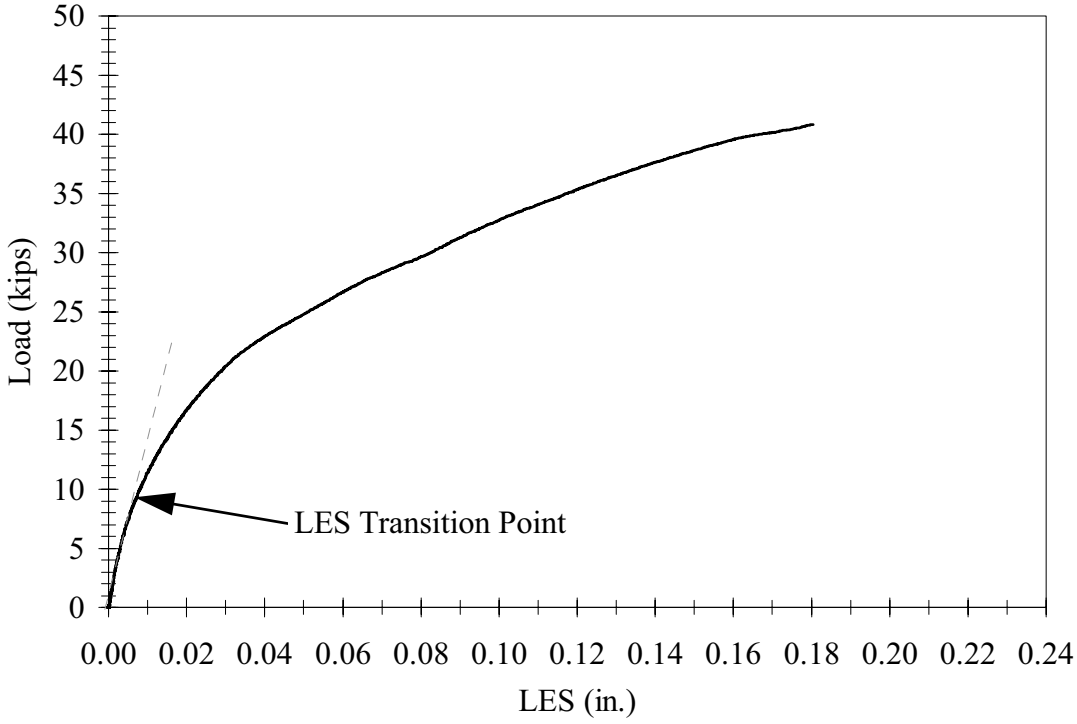

Figure 3.26 M2, Sample LES Graph

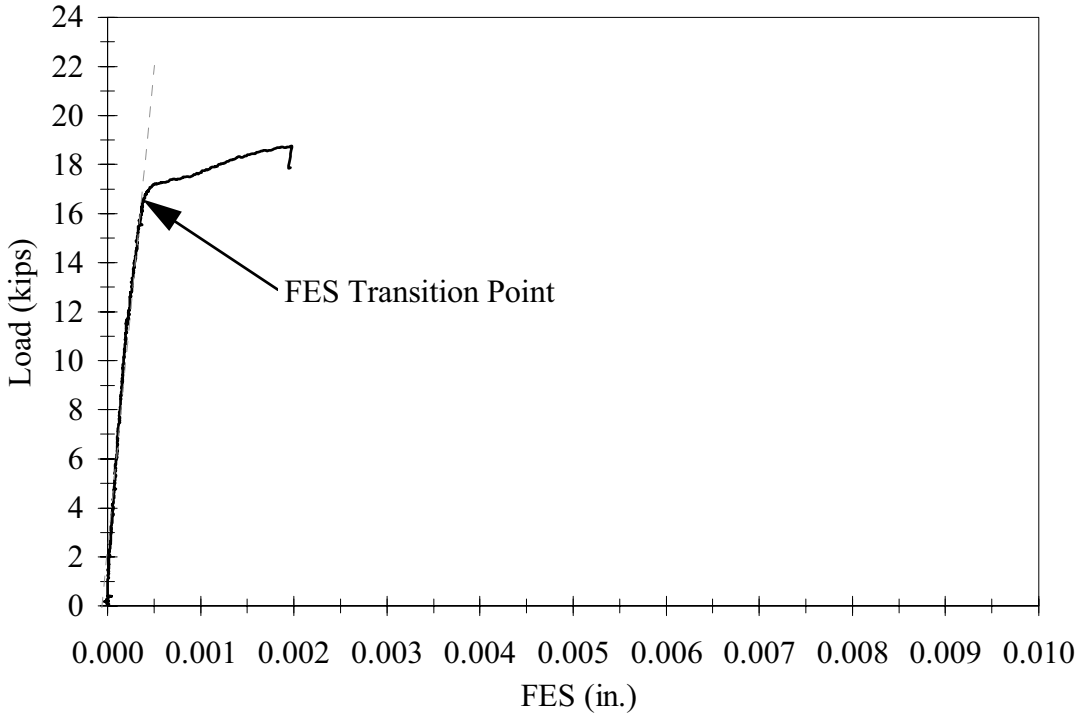

Figure 3.27 M1, Sample FES Graph

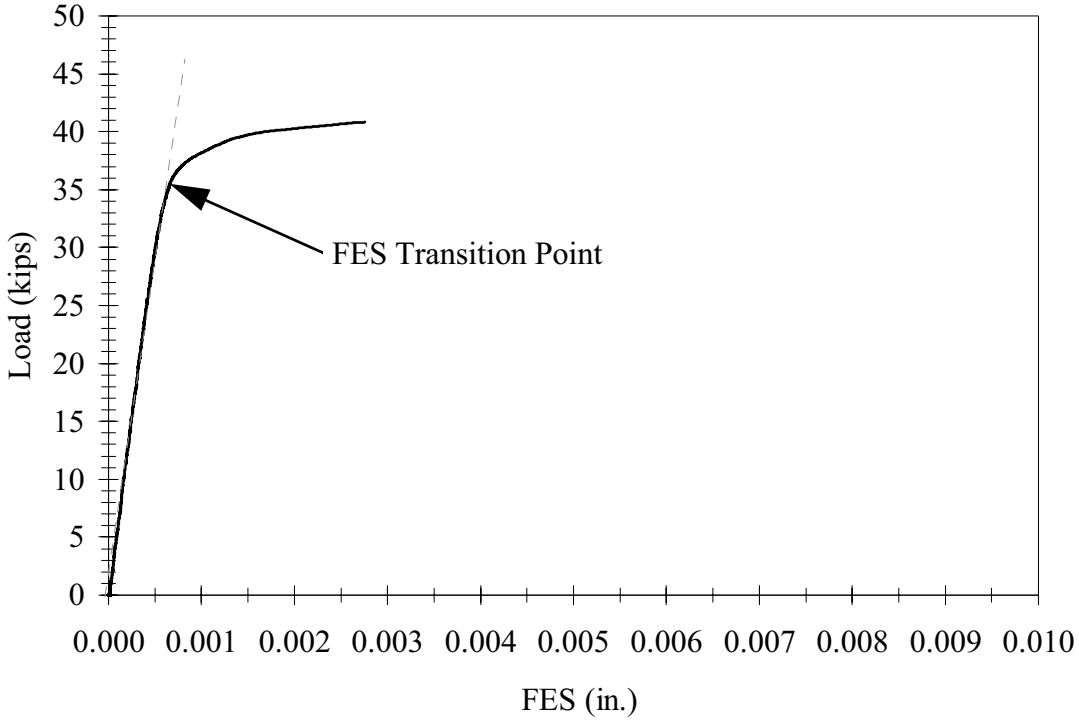

Figure 3.28 M2, Sample FES Graph

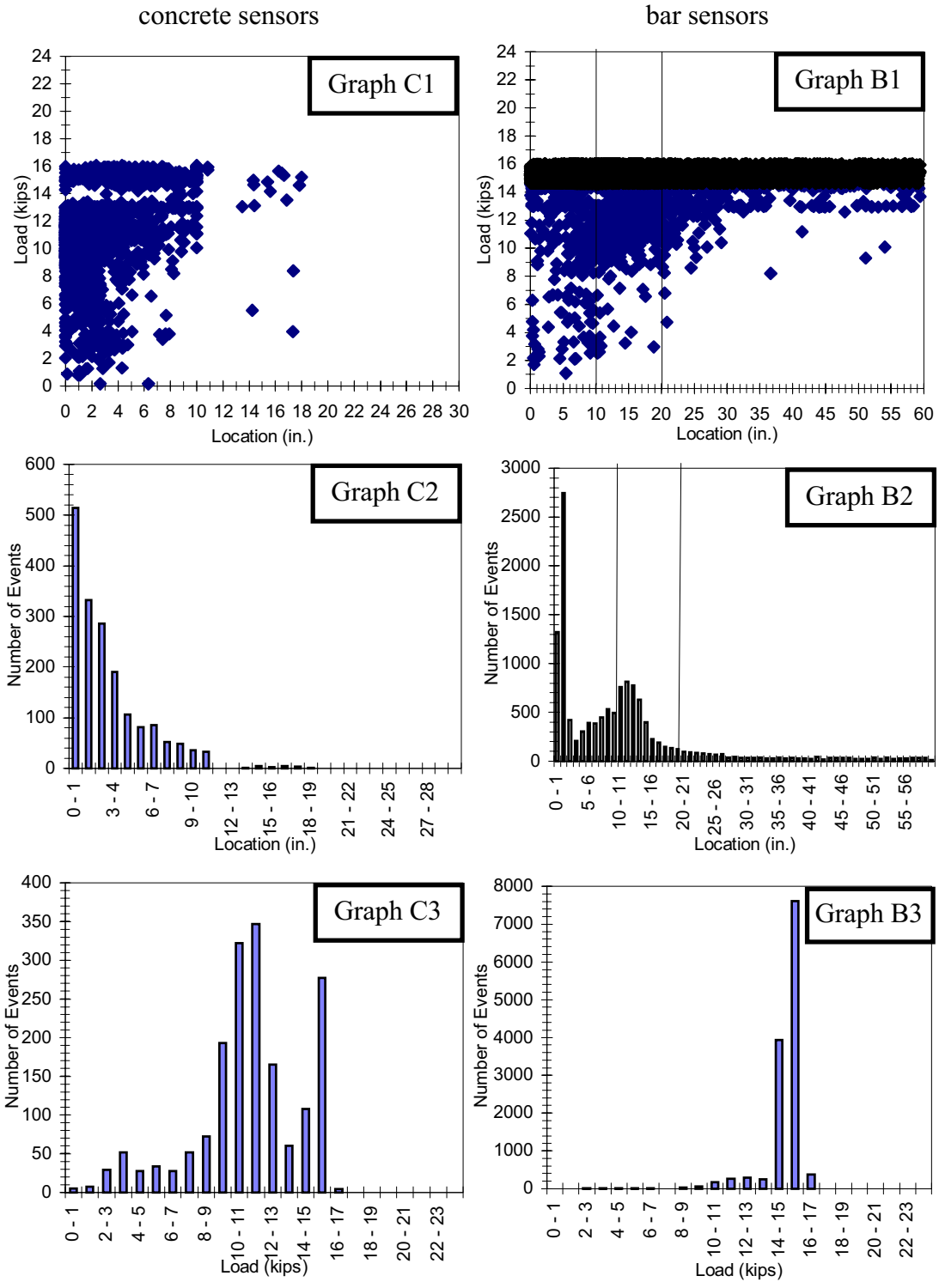

Figure 3.29 M1, Sample AE Graphs

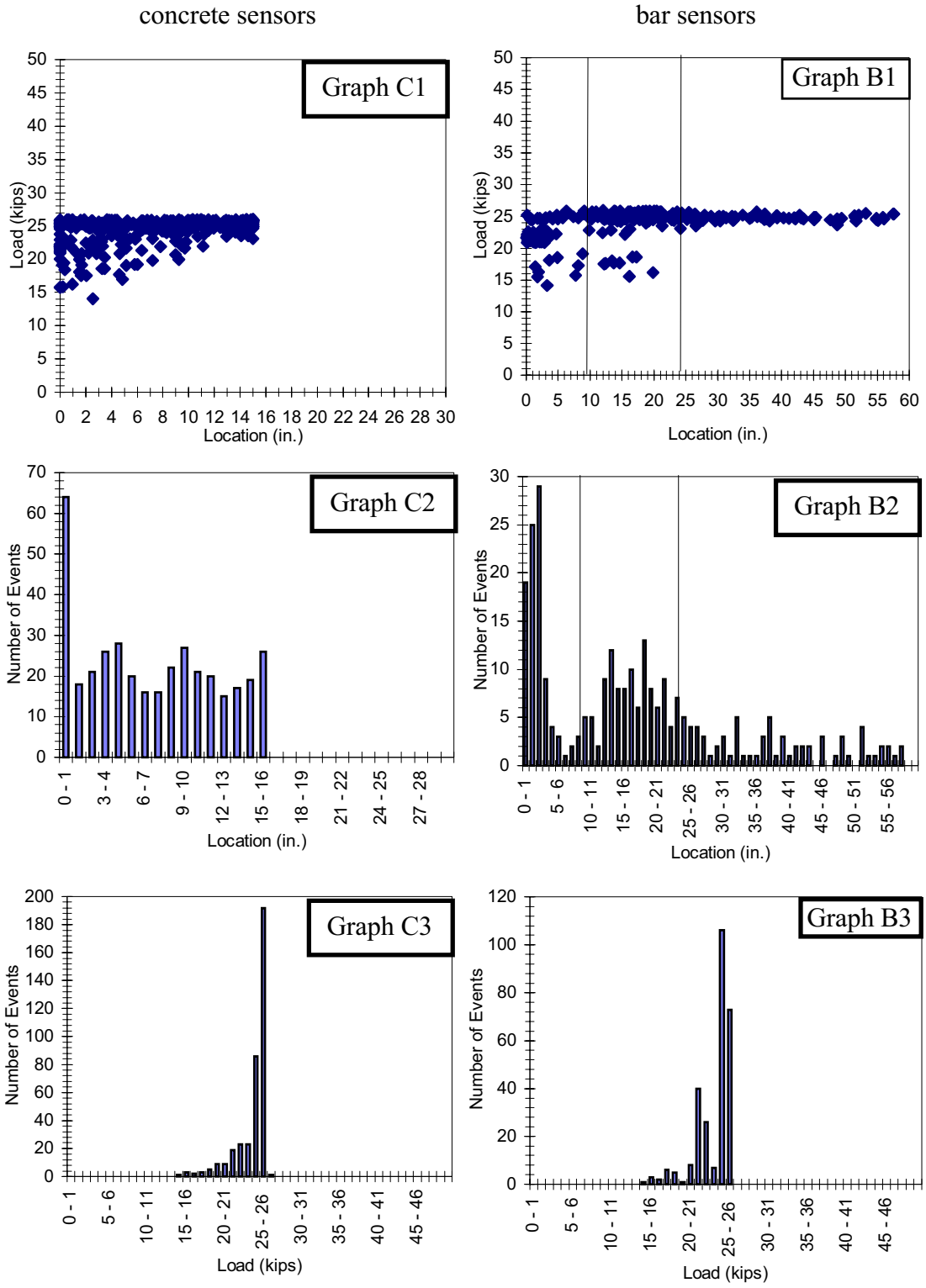

Figure 3.30 M2, Sample AE Graphs

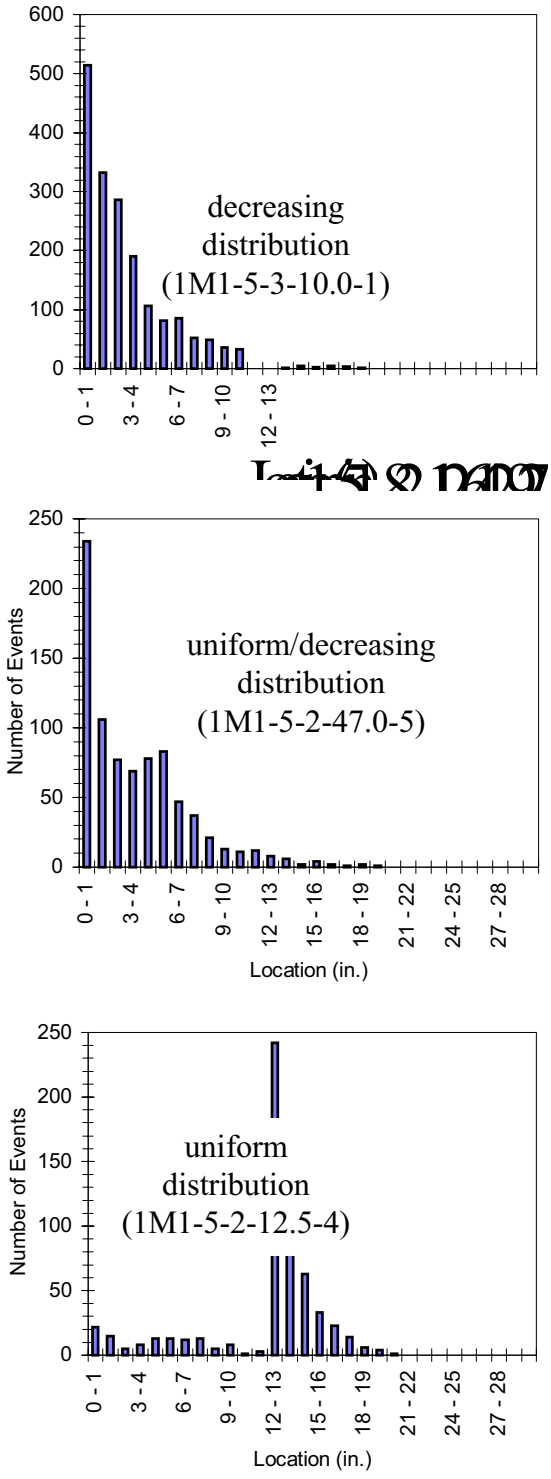

Figure 3.31 M1, C2 (concrete sensors) Distribution Patterns

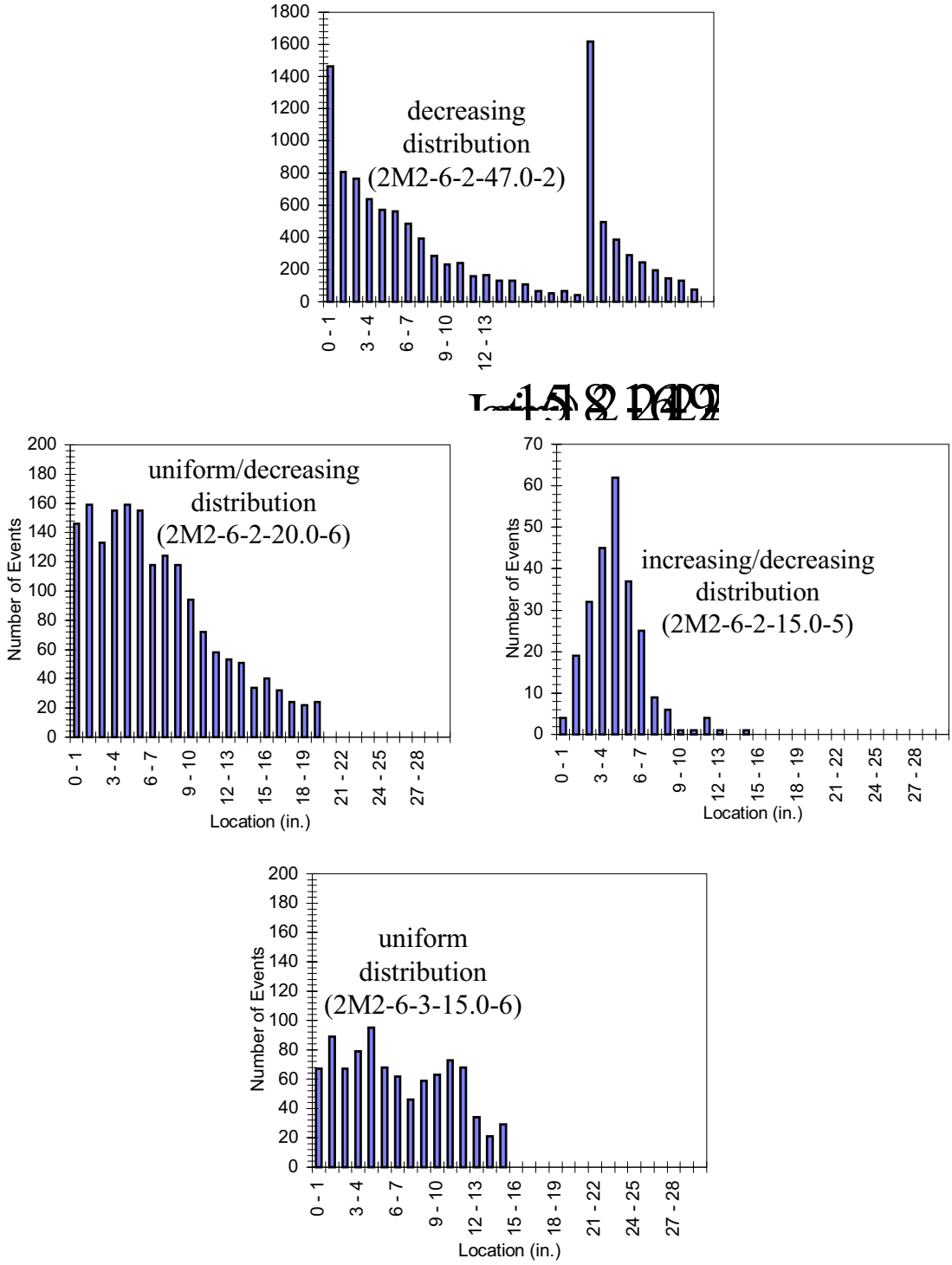

Figure 3.32 M2, C2 (concrete sensors) Distribution Patterns

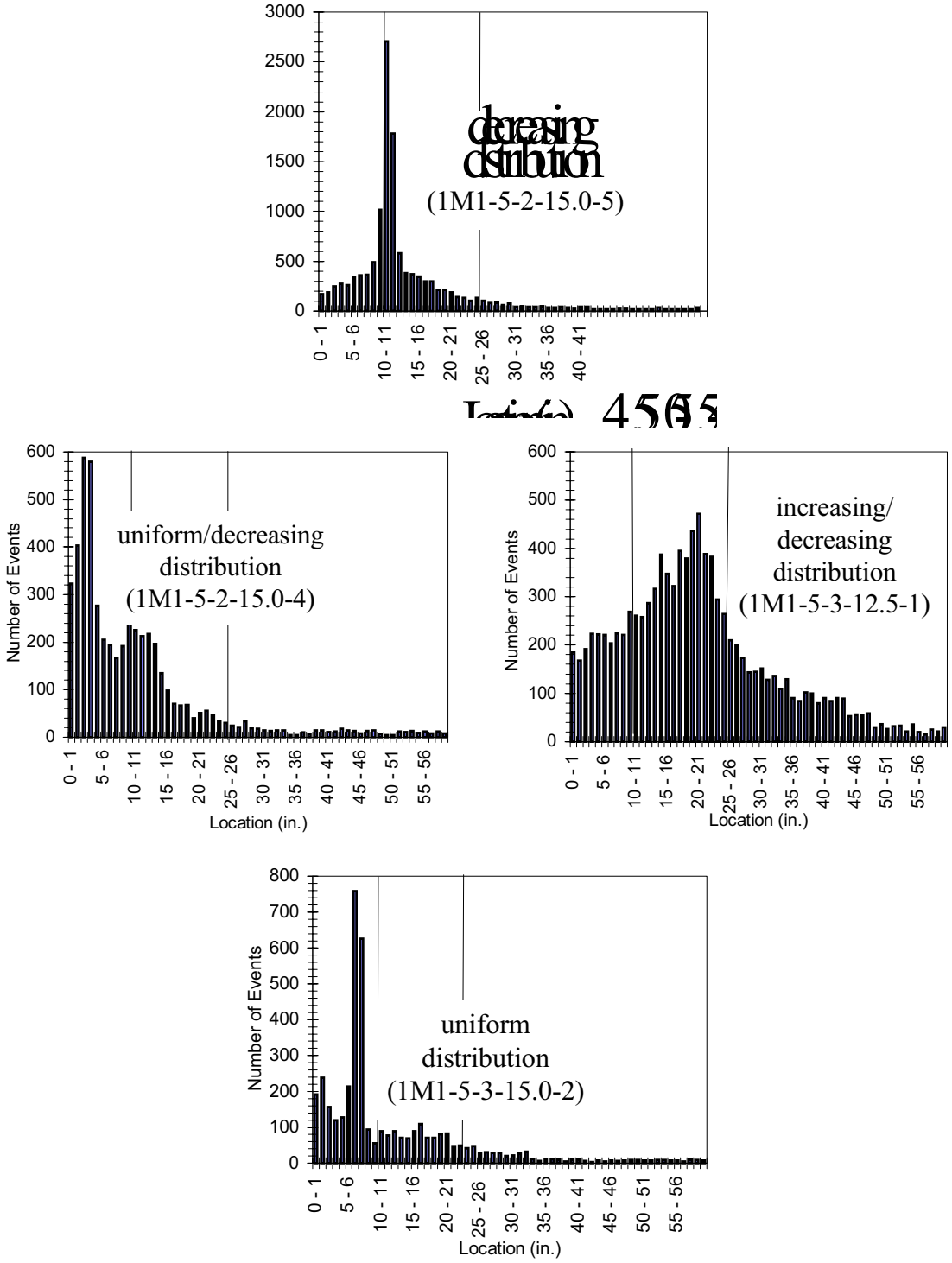

Figure 3.33 M1, B2 (bar sensors) Distribution Patterns

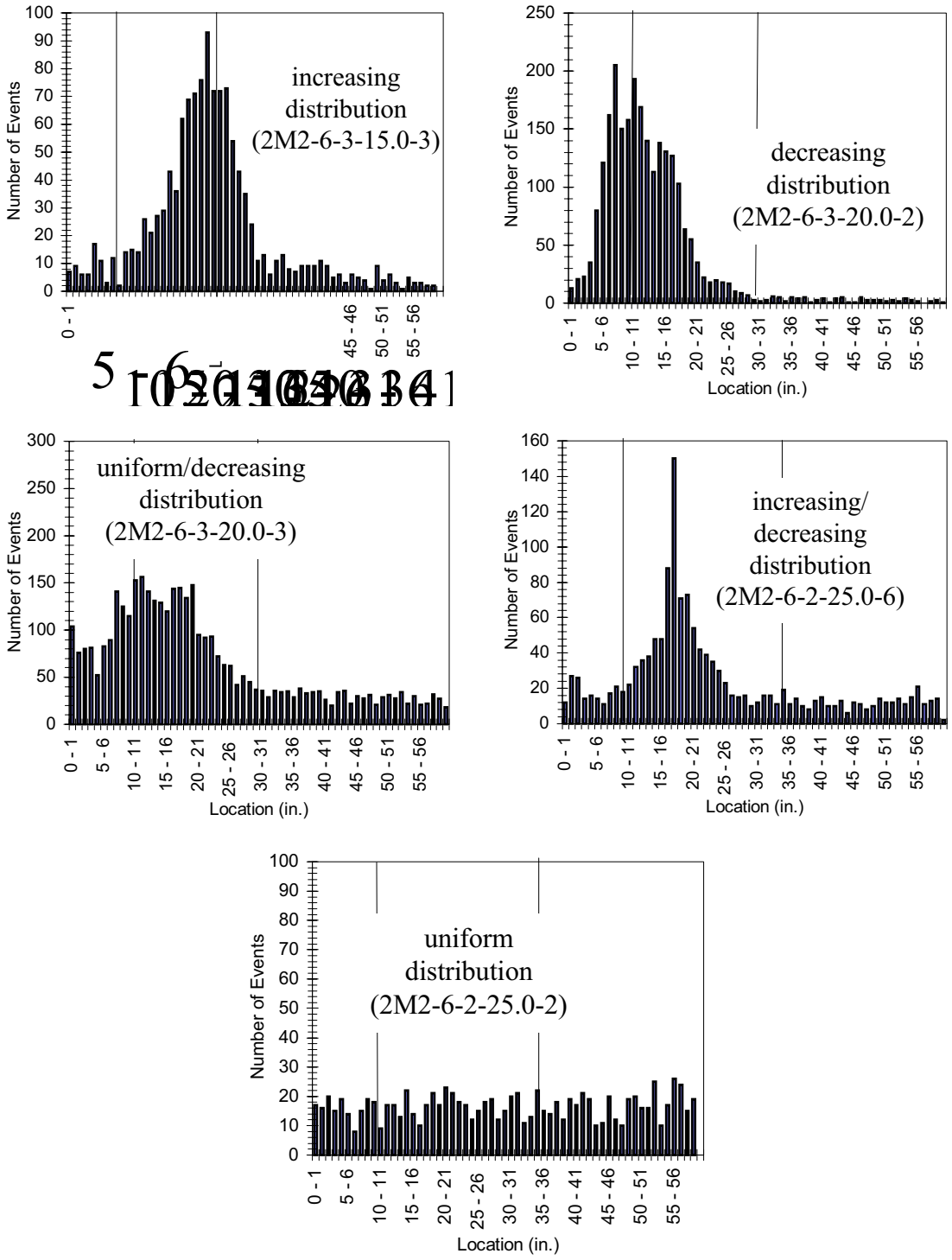

Figure 3.34 M2, B2 (bar sensors) Distribution Patterns

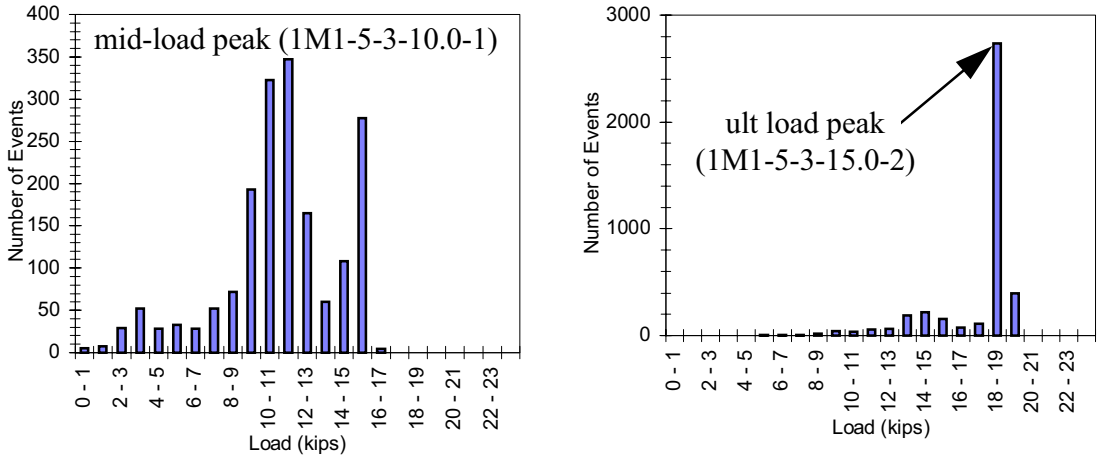

Figure 3.35 M1, C3 (concrete sensors) AE Peaks

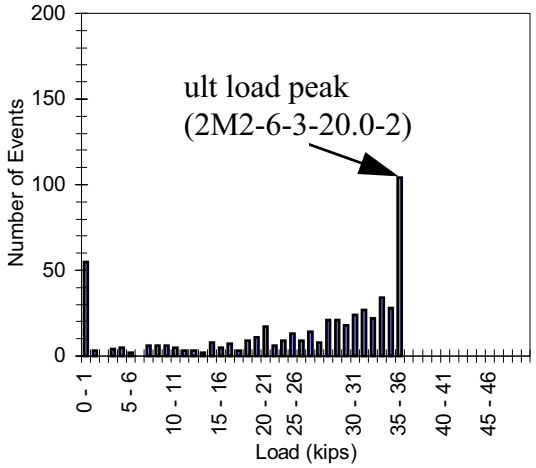

Figure 3.36 M2, C3 (concrete sensors) AE Peaks

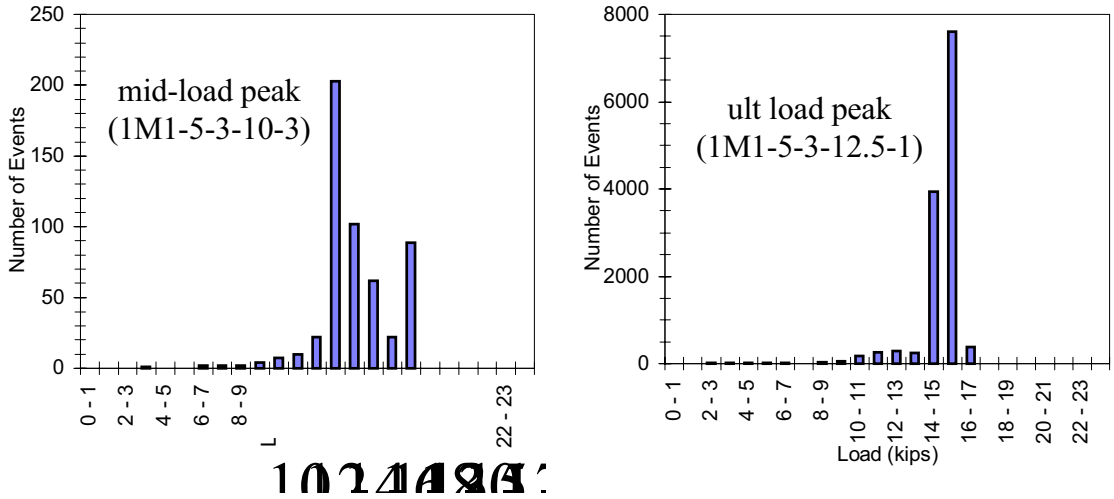

Figure 3.37 M1, B3 (bar sensors) AE Peaks

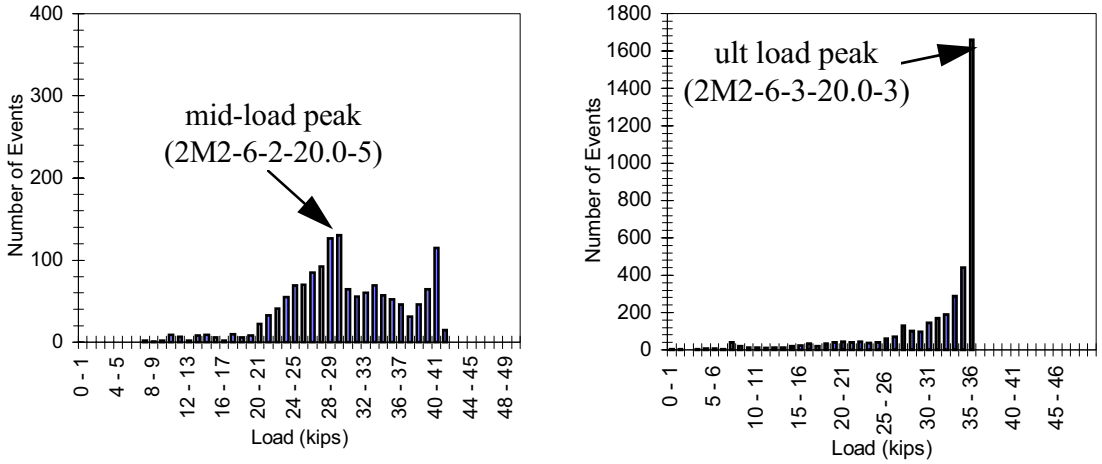

Figure 3.38 M2, B3 (bar sensors) AE Peaks

Figure 3.39 M1, Sample Crack Pattern

Figure 3.40 M2, Sample Crack Pattern

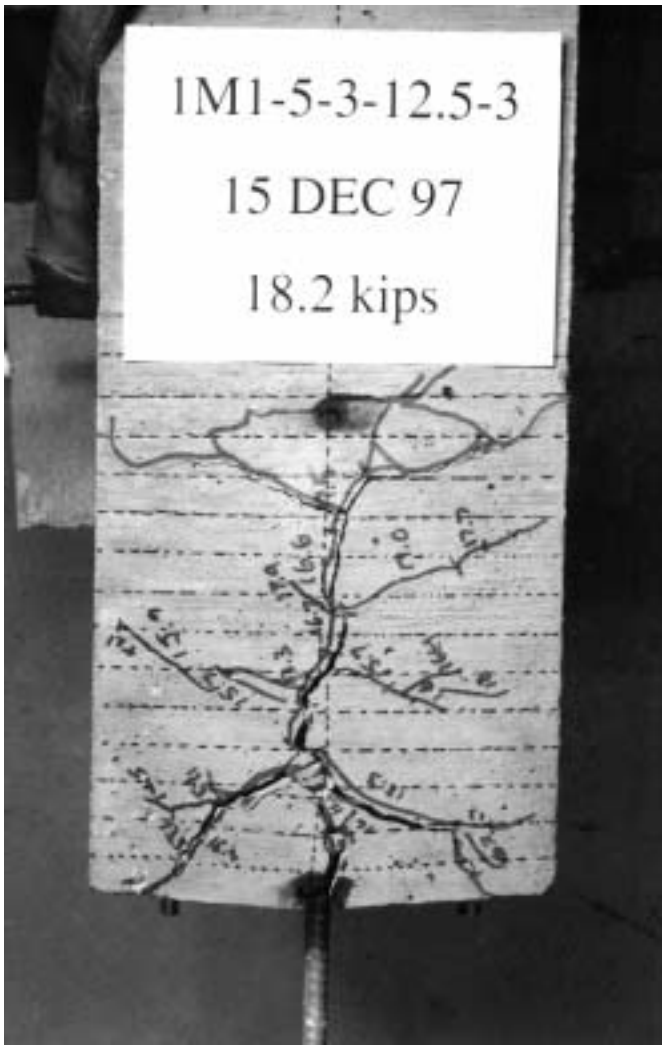

Figure 3.41 Type C Failure

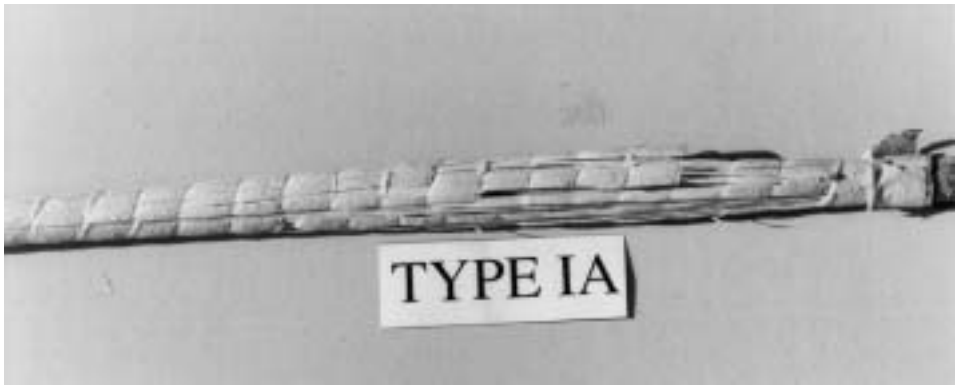

Figure 3.42 Type IA Failure

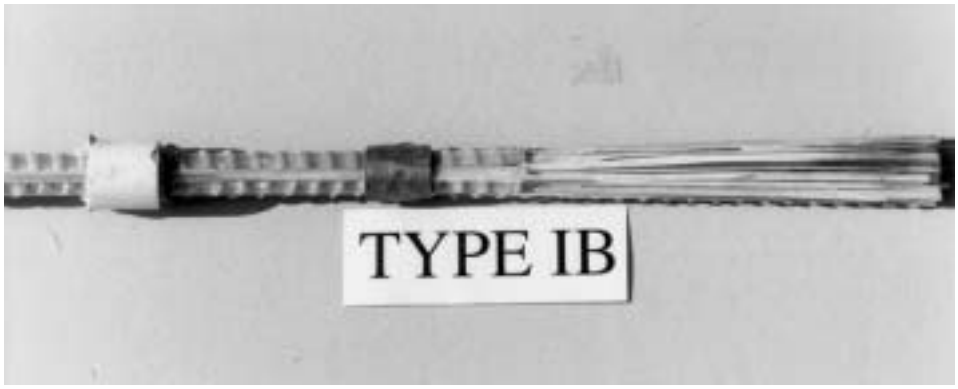

Figure 3.43 Type IB Failure

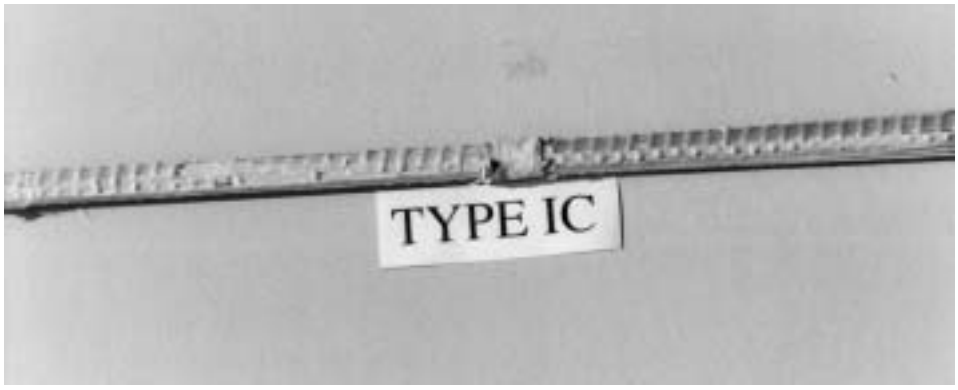

Figure 3.44 Type IC Failure

Figure 3.45 Type IIA Failure

Figure 3.46 Type IIB Failure


Figure 3.47 Type III Failure

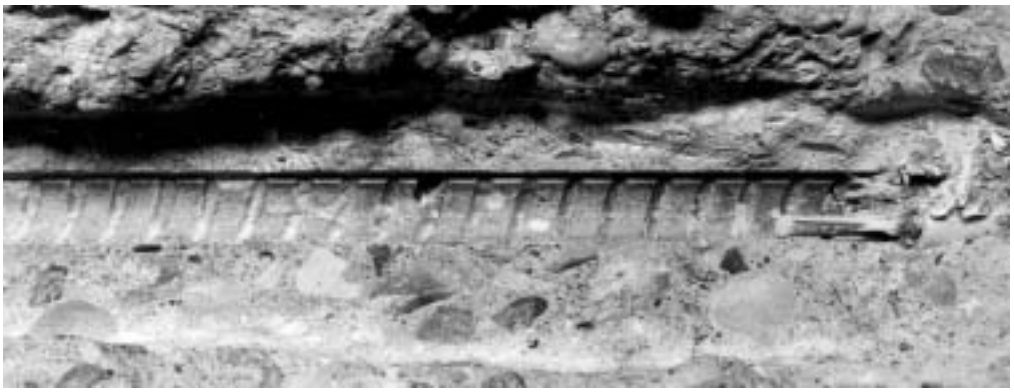

Figure 3.48 M1, Bar Impressions in Concrete

Figure 3.49 M2, Bar Impressions in Concrete

Figure 3.50 2M2-6-3-15.0-3 Side Photograph

Figure 3.51 2M2-6-3-15.0-3 Crack Pattern

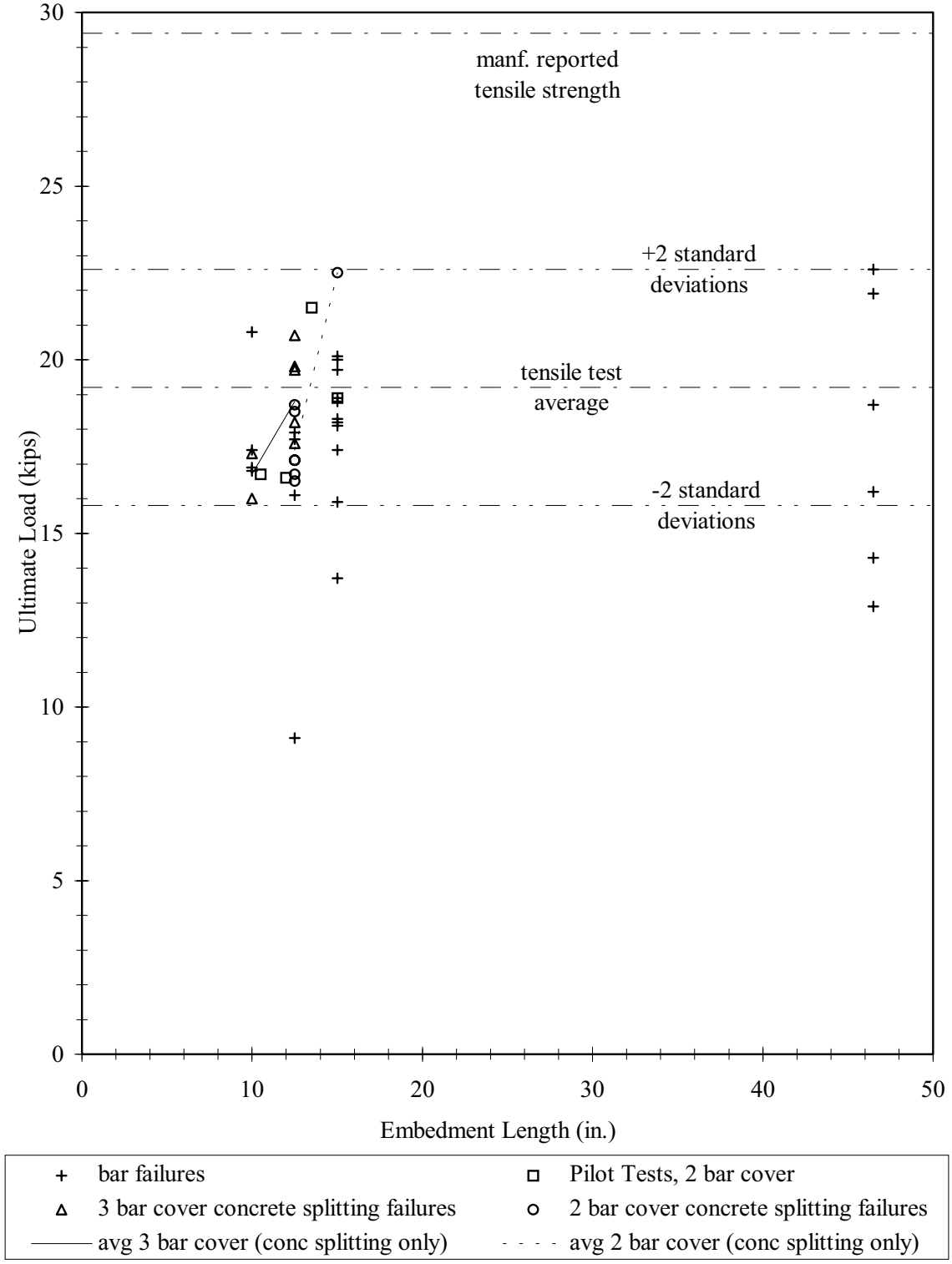

Figure 3.52 M1, Embedment Length versus Ultimate Load

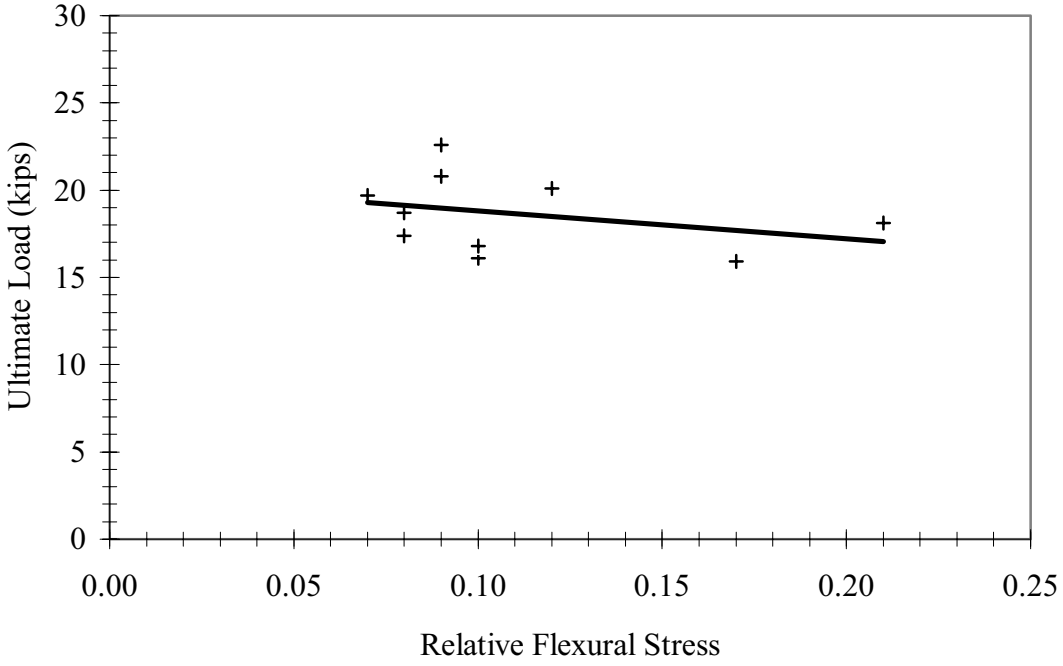

Figure 3.53 M1, Bond Test Relative Induced Flexural Stress

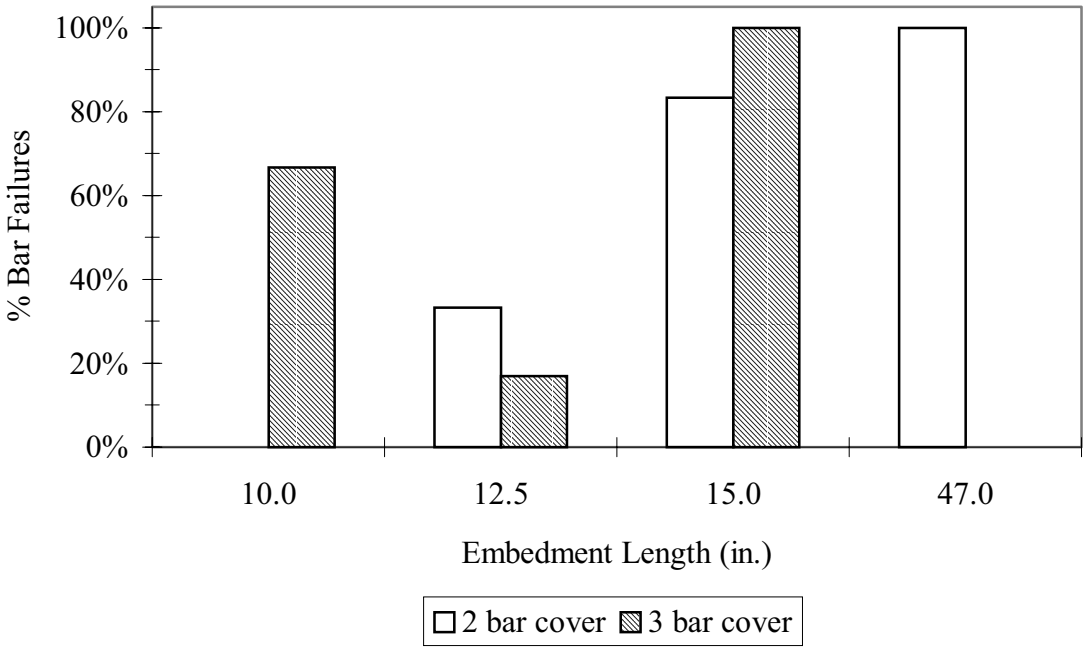

Figure 3.54 M1, Failure Rates

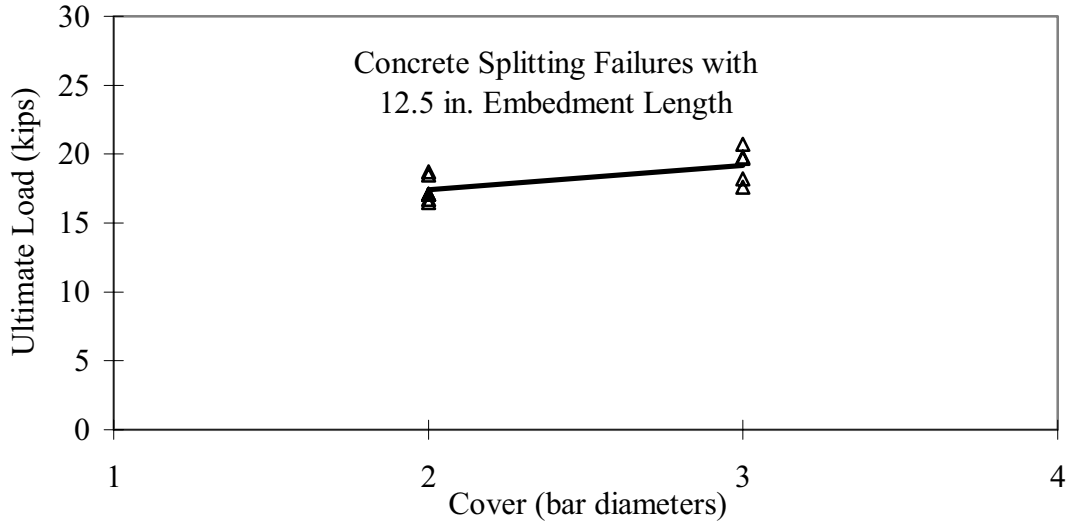

Figure 3.55 M1, Cover versus Ultimate Load

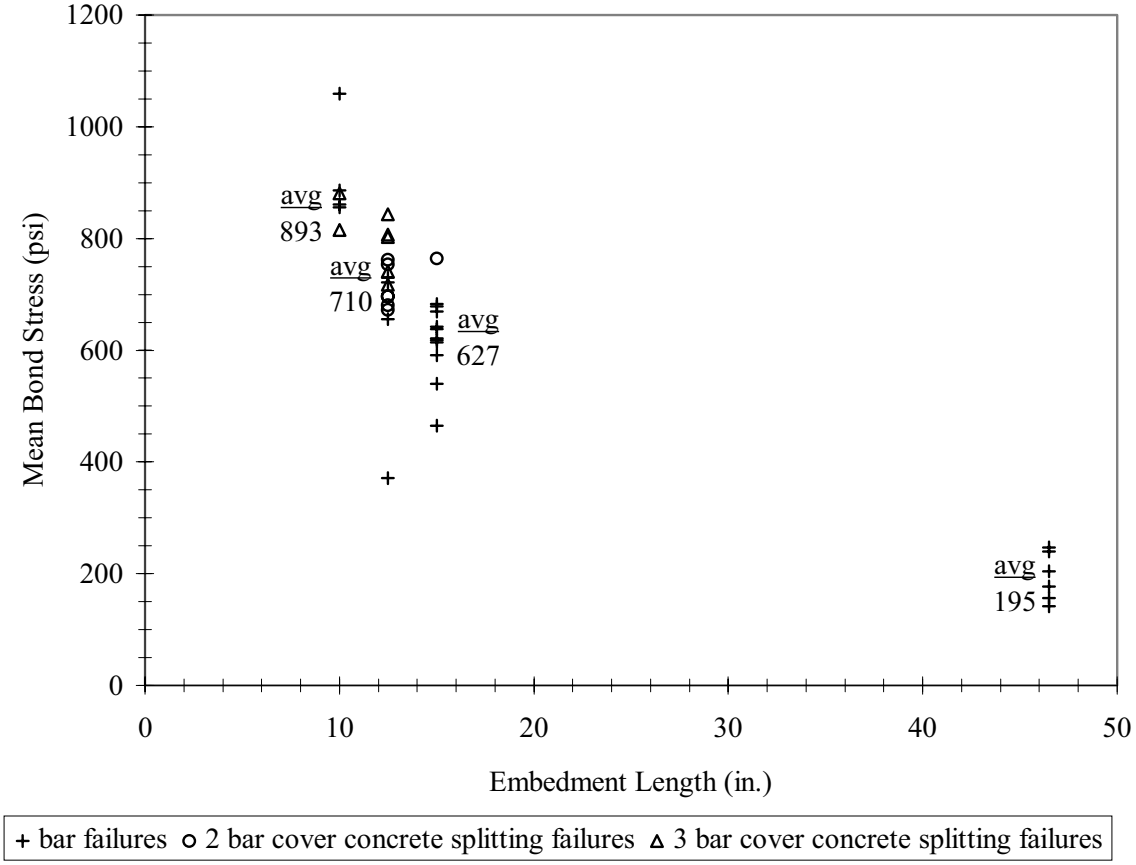

Figure 3.56 M1, Mean Bond Stress

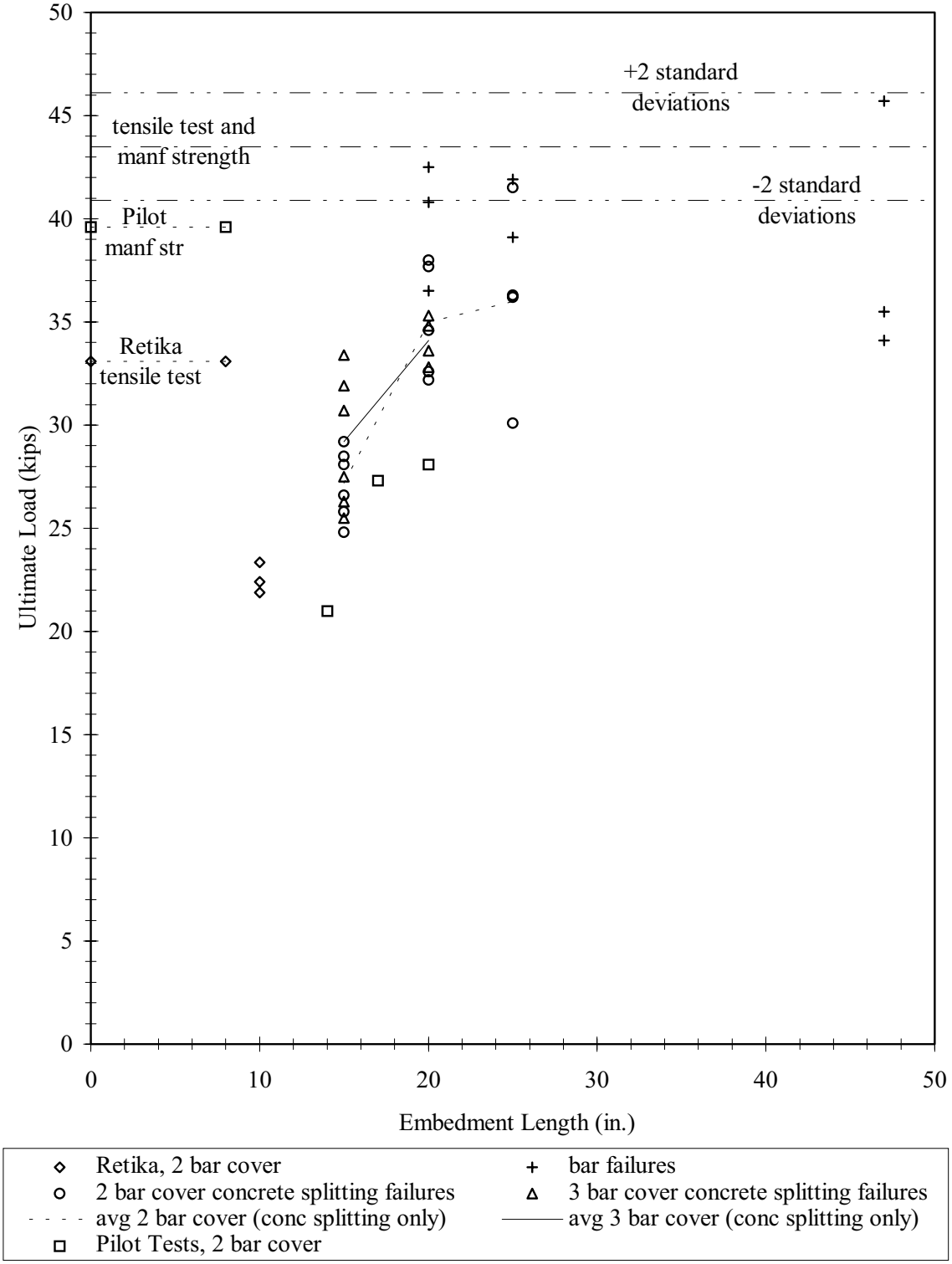

Figure 3.57 M2, Embedment Length versus Ultimate Load

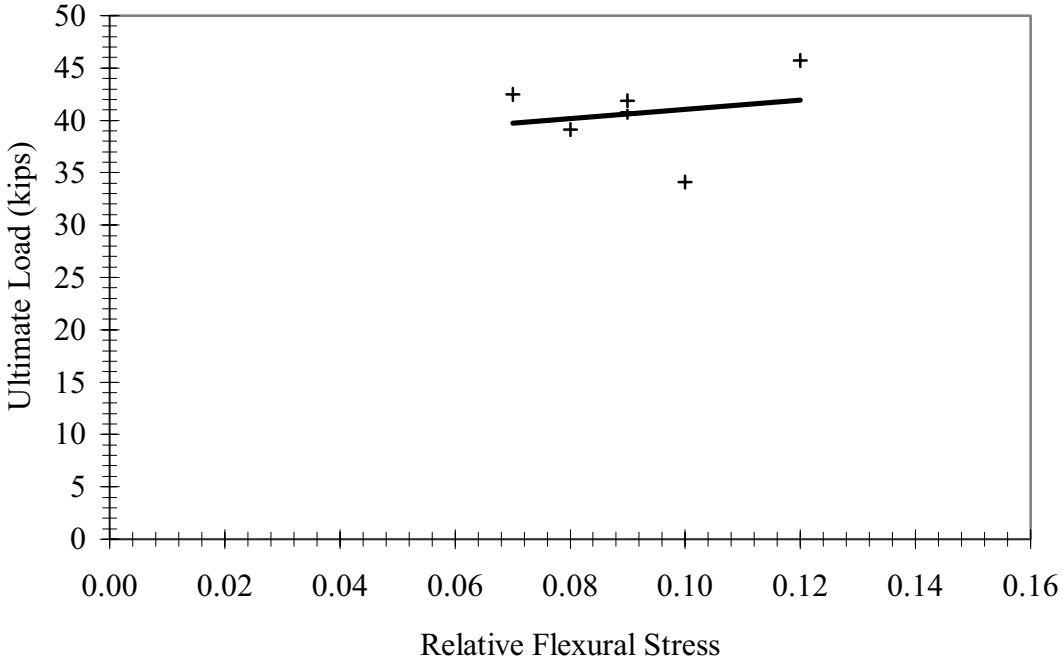

Figure 3.58 M2, Bond Test Relative Induced Flexural Stress

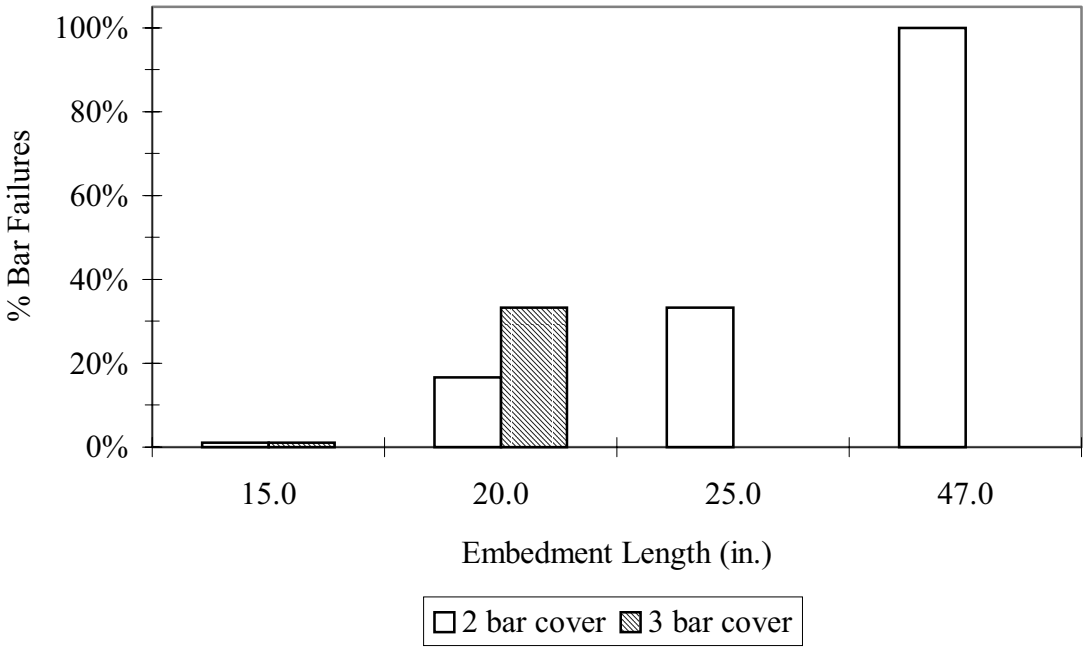

Figure 3.59 M2, Failure Rate

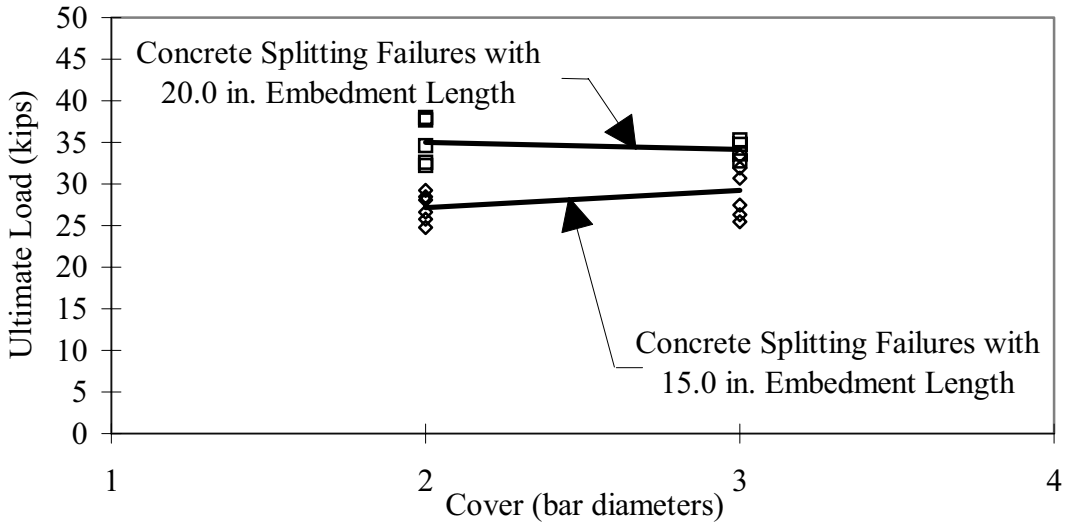

Figure 3.60 M2, Cover versus Ultimate Load

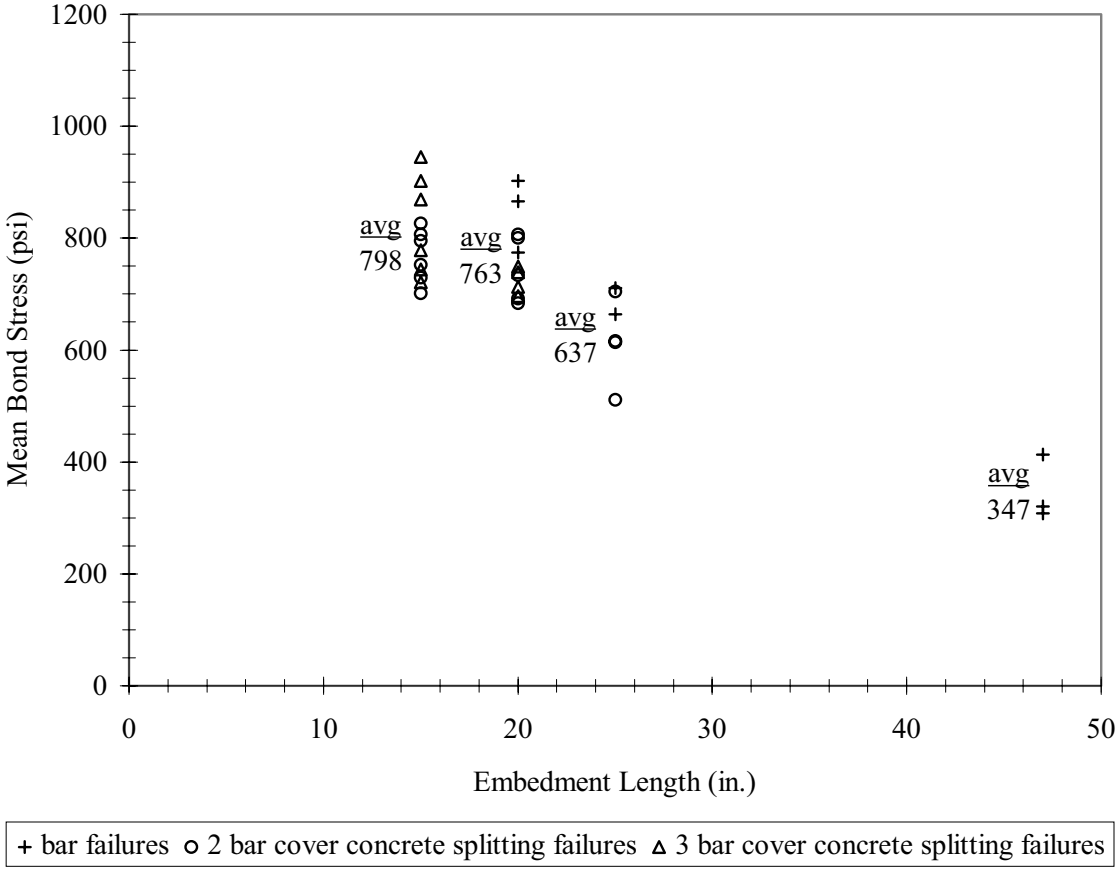

Figure 3.61 M2, Mean Bond Stress

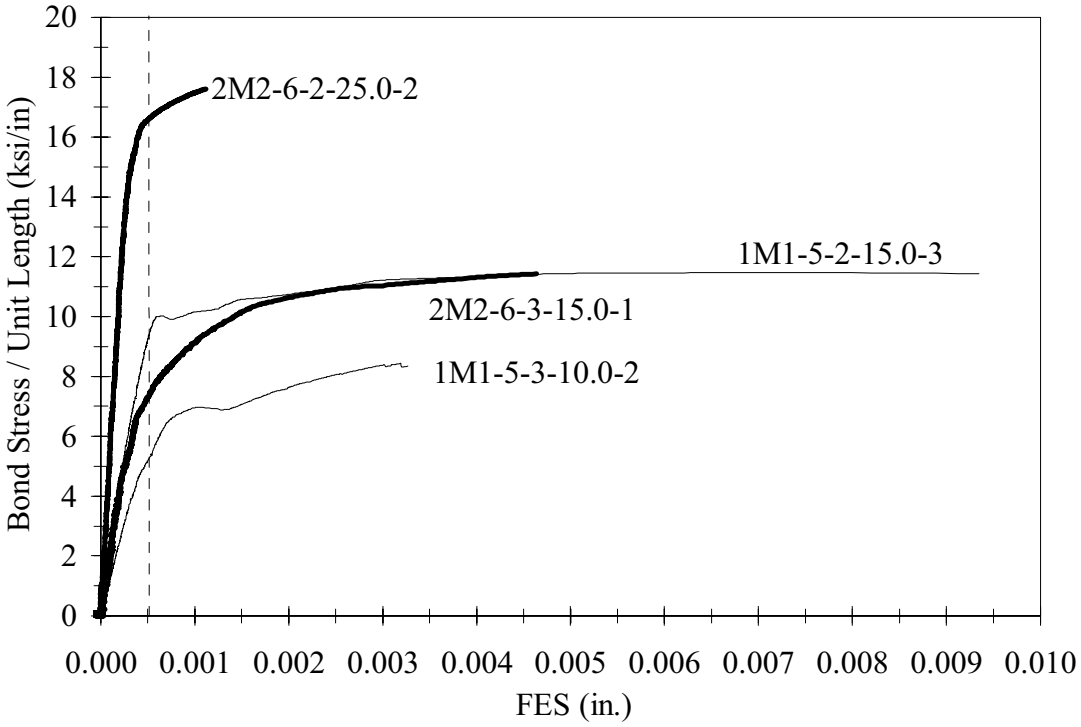

Figure 3.62 FES Comparison

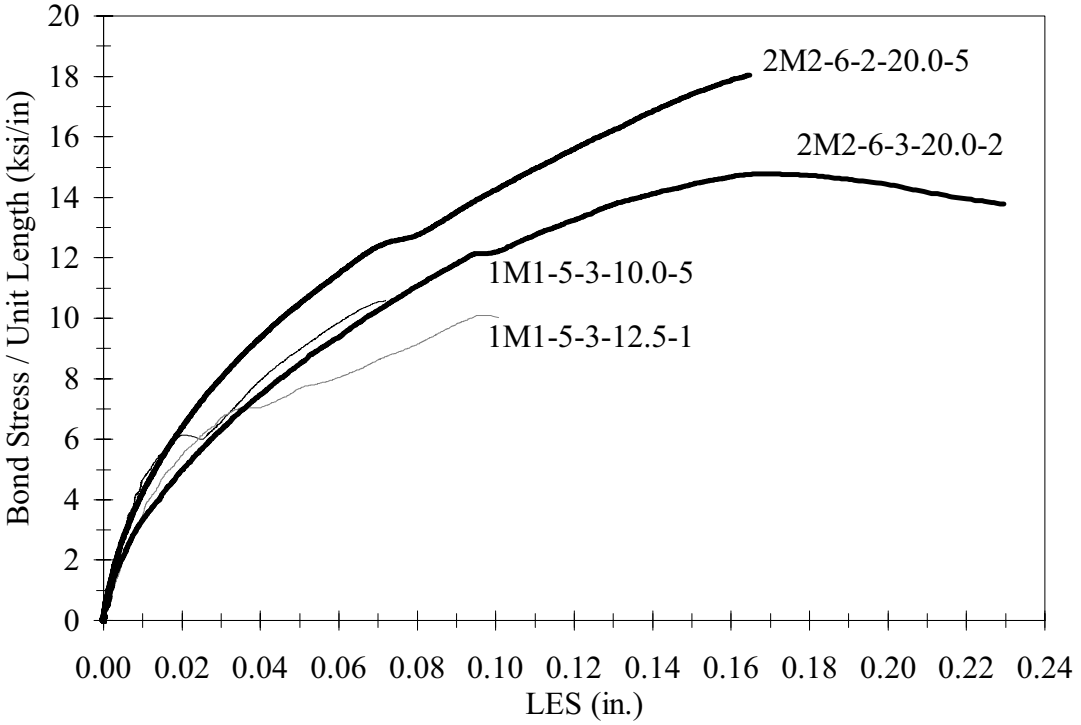

Figure 3.63 LES Comparison

Appendix A: Tensile Tests

Tensile strength and modulus of elasticity (MOE) tests were conducted on the GFRP rebar in accordance with ASTM D3916-94, "Tensile Properties of Pultruded Glass-Fiber-Reinforced-Plastic Rod." The bars tested were No. 4 and 5 from the M1 manufacturer and No. 6 from the M2 manufacturer. The M1 bars were all the same batch received from the manufacturer. However, three separate batches of M2 bars were tested. One batch of bars was received from the M2 manufacturer for the bond tests and these bars were also tested for tensile capacity. A second batch of bars was also received from the M2 manufacturer and these bars were tested for comparison. Finally, the rebar tested by Retika [25] was available and tensile tests were conducted to establish initial variables for the bond tests and comparison. All of the tensile tests were conducted using a 600 kip MTS load frame with an OPTIM data acquisition system. A 2 in. extensometer and four 0.1 in. LVDTs were used to measure axial strain.

Two grip systems were used. The first system consisted of aluminum parabolic grips filled with resin as described in Section 2.10.2. The second system consisted of two 20.0 in. long pipes with a 2.25 in. outside diameter filled with Bristar Demolition Cement. This system was only used for the second batch of M2 bars.

The specimen were loaded three times to approximately 50% of the manufacturer average tensile strength. An average modulus of elasticity (MOE) was calculated from these load sequences. Following these iterations the instrumentation was removed and the specimen were loaded to failure. The average ultimate loads were calculated for failures that occurred outside of the grips. All bar failures that occurred inside the grips were excluded from the average values. The average results for all the tests and only those which failed outside the grips are shown in Table A.1. The results for the individual tests are shown in Tables A.2 through A.6. The tests are listed with their associated bar code (refer to Section 2.2), MOE, failure load, nominal area, ultimate stress based on nominal area, relative induced flexural stress (f_b / ω_{ult}) and the failure location. The ultimate loads for the tensile test were all within +/- two standard deviations of the average. The f_b was calculated according to Appendix D and analyzed. Only a limited number of M1 bars were instrumented with LVDTs and an accurate assessment of f_b could not be done. The M2 bar tensile tests exhibited an average relative induced flexural stress value of 0.02 with a standard deviation of 0.01., which was not considered excessive. Additionally, the tensile test average failure loads were compared relative to the location of the bar failure. The average ultimate tensile strength did not increase for tests that exhibited bar

failures outside the grips, except for the batch B M2 bars. This was not the expected trend. This indicates that although several tests failed within the grips, their failure loads were close to the actual tensile strength.

Table A.1 M1-4 Tensile Test Results

Manf.	Size	Notes	All Failures		Failures Outside of Grips Only	
			Avg (kips) (# tests)	Std Dev (kips)	Avg (kips) (# tests)	Std Dev (kips)
M1	No. 4	Used in Pilot Test	16.5 (4)	0.8	16.4 (2)	1.3
M1	No. 5	Used in Primary Tests	19.2 (10)	1.7	19.2 (10)	1.7
M2	No. 6	Used in Primary Tests	43.8 (5)	1.2	43.5 (3)	1.6
M2	No. 6	Retika's Bars [25] Not Used in Primary Tests	33.0 (3)	5.5	33.1 (1)	n.a.
M2	No. 6	Batch B Bars Not Used in Primary Tests	45.8 (11)	2.1	46.5 (7)	2.1

Table A.2 M1-4 Tensile Test Results

Date/Test	Bar Code	MOE (ksi)	$P_{Ult.}$ (kips)	Area (in^2)	Ult. Stress (ksi)	f_b / ω_{ult}	Failure Location
6 Aug 97 - 3	M1-4-1	5589	17.0	0.18	94.2	X	grip
19 Aug 97 - 2	M1-4-2	6140	15.5	0.18	86.0	X	outside grips
19 Aug 97 - 5	M1-4-3	5716	17.3	0.18	95.8	X	outside grips
19 Aug 97 - 4	M1-4-4	5924	16.3	0.18	90.6	X	grip

Note: "X" = LVDT malfunction or not used in the test

Table A.3 M1-5 Tensile Test Results

Date/Test	Bar Code	MOE (ksi)	$P_{Ult.}$ (kips)	Area (in^2)	Ult. Stress (ksi)	f_b / ω_{ult}	Failure Location
30 Jul 97 - 1	M1-5-1	6060	19.1	0.27	70.6	X	outside grips
30 Jul 97 - 6	M1-5-2	5669	19.7	0.27	73.1	X	outside grips
18 Mar 98 - 1	M1-5-3	5650	17.6	0.27	65.2	X	outside grips
18 Mar 98 - 2	M1-5-4	5448	18.7	0.27	69.3	X	outside grips
18 Mar 98 - 3	M1-5-5	5570	17.8	0.27	65.9	X	outside grips
20 Mar 98 - 1	M1-5-6	6286	20.5	0.27	75.9	0.05	outside grips
20 Mar 98 - 2	M1-5-7	5967	15.8	0.27	58.5	X	outside grips
23 Mar 98 - 1	M1-5-8	6405	21.1	0.27	78.1	0.08	outside grips
23 Mar 98 - 2	M1-5-9	6520	20.9	0.27	77.4	X	outside grips
26 Mar 98 - 3	M1-5-10	6289	20.8	0.27	77.0	0.09	outside grips

Note: "X" = LVDT malfunction or not used in the test

Table A.4 M2-6 (Primary Test Bars) Tensile Test Results

Date/Test	Bar Code	MOE (ksi)	$P_{ult.}$ (kips)	Area (in^2)	Ult. Stress (ksi)	f_b / ω_{ult}	Failure Location
27 Mar 98 -1	M2-6-4	6600	41.9	0.44	95.2	0.02	outside grips
27 Mar 98 - 2	M2-6-5	6559	43.7	0.44	99.3	0.03	outside grips
31 Mar 98 - 1	M2-6-6	6486	45.0	0.44	102.3	0.02	outside grips
31 Mar 98 - 2	M2-6-7	6711	43.7	0.44	99.3	0.01	grip
31 Mar 98 - 3	M2-6-8	6540	44.6	0.44	101.4	0.02	grip

Table A.5 M2-6 (Retika's Bars) Tensile Test Results

Date/Test	Bar Code	MOE (ksi)	$P_{Ult.}$ (kips)	Area (in^2)	Ult. Stress (ksi)	f_b / ω_{ult}	Failure Location
20 Feb 97 - 1	M2-6-1	5113	33.1	0.44	75.2	X	outside grips
20 Feb 97 - 2	M2-6-2	5881	38.4	0.44	87.3	X	grip
20 Feb 97 - 3	M2-6-3	5443	27.4	0.44	62.3	X	grip

Note: "X" = LVDT malfunction or not used in the test

Table A.6 M2-6 (Batch B Bars) Tensile Test Results

Date/Test	Bar Code	MOE (ksi)	$P_{Ult.}$ (kips)	Area (in^2)	Ult. Stress (ksi)	f_b / ω_{ult}	Failure Location
24 Mar 98 - 1	M2B-6-1	6417	43.2	0.44	98.2	0.04	grip
25 Mar 98 - 1	M2B-6-2	6430	43.3	0.44	98.4	0.02	outside grips
25 Mar 98 - 2	M2B-6-3	6421	44.3	0.44	100.7	0.01	grip
26 Mar 98 - 1	M2B-6-4	6434	43.4	0.44	98.6	0.03	grip
27 Mar 98 - 3	M2B-6-5	6632	44.3	0.44	100.7	0.02	grip
26 Mar 98 -2	M2B-6-1B	6265	44.9	0.44	102.0	0.01	outside grips
28 Mar 98 - 1	M2B-6-2B	6352	50.1	0.44	113.9	0.01	outside grips
28 Mar 98 - 2	M2B-6-3B	6585	46.2	0.44	105.0	0.01	outside grips
28 Mar 98 - 3	M2B-6-4B	6520	46.9	0.44	106.6	0.01	outside grips
29 Mar 98 - 1	M2B-6-5B	6711	46.9	0.44	106.6	0.02	outside grips
29 Mar 98 - 2	M2B-6-6B	6572	47.3	0.44	107.5	0.03	outside grips

Appendix B

Cross-Sectional Area: Volume Displacement Method

The cross-sectional area of the GFRP rebar was checked with a volume displacement method. Seven samples were cut and measured for each bar type. The test samples were then submerged in water in a graduated beaker and the amount of water displaced by the samples was recorded. The cross-sectional area was then calculated by dividing the volume displaced by the sample length as shown below. The individual results are shown in Table B.1 and the average values are listed in Table 2.6.

$$A \mid \frac{V}{L} \tag{B-1}$$

where A is the cross-sectional area of rebar, V is the volume of water displaced, and L is the length of rebar submerged.

Table B.1 Volume Displacement Test Results

Manufacturer-Bar Size and Sample #	Length	Volume of Water Displaced		Cross-Sectional Area
	in.	ml	$in.^3$	$in.^2$
M1-5-1	5.721	29.3	1.79	0.31
M1-5-2	5.619	23.3	1.42	0.25
M1-5-3	5.499	27.3	1.67	0.30
M1-5-4	5.320	27.2	1.66	0.31
M1-5-5	5.433	27.8	1.70	0.31
M1-5-6	4.256	21.5	1.31	0.31
M1-5-7	3.576	18.6	1.14	0.32
M2-6-1	5.295	40.1	2.45	0.46
M2-6-2	5.134	39.0	2.38	0.46
M2-6-3	5.497	41.4	2.53	0.46
M2-6-4	4.638	34.9	2.13	0.46
M2-6-5	5.349	40.1	2.45	0.46
M2-6-6	4.495	34.2	2.09	0.46
M2-6-7	4.415	38.5	2.35	0.53

Appendix C

Concrete Testing

The concrete tests were performed in accordance with the ASTM specifications listed in Table C.1. Air content and slump tests were done at the beginning, middle and end of each specimen casting and the results are shown in Table C.2 with the associated construction date information. Compressive and split tensile strength tests were conducted at the beginning and end of the Pilot Test. In addition to the compressive and split tensile strength tests, modulus of rupture and modulus of elasticity tests were conducted for the Primary Tests. The tests for the primary investigation were conducted at 28 days, at the beginning of the testing, 1/3 of the way through testing, 2/3 of the way through testing and at the end of the tests. The individual test results are shown in Tables C.3 - C.6 for the modulus of elasticity, compressive strength, modulus of rupture, split tensile strength tests, respectively. The average values for concrete strength tests are shown in Tables 2.7 - 2.9 for the Pilot Test, Primary Test 1 and Primary Test 2, respectively.

The concrete compressive strengths, split tensile strengths and modulus of elasticity did not significantly change over all three testing periods (Pilot Test, Primary Test 1 and Primary Test 2); however, the modulus of rupture did increase over the course of the Primary Tests. Because all the test cylinders and beams were constructed and cured similarly, the modulus of ruptures results should be considered anomalies. Based on this and considering the other three tests it is reasonable to assume that the concrete strength did not significantly change over the course of the testing periods.

Table C.1 ASTM Used in Concrete Testing

C31	Making and Curing Concrete Test Specimen in the Field
C231	Air Content of Freshly Mixed Concrete by Pressure Method
C143	Slump of Hydraulic Cement Concrete
C78	Flexural Strength of Concrete (Third-Point Loading)
C496	Splitting Tensile Strength of Cylindrical Concrete Specimen
C39	Compressive Strength of Cylindrical Concrete Specimen
C469	Static Modulus of Elasticity and Poisson's Ratio of Concrete in Compression

Table C.2 Specimen Construction Date Information

Test	Date of Construction	Start/Finish (hours)	Air Content (%)	Slump (inches)
Pilot Test	15 May 97	1106/1148	3.5/3.0	2.00/1.25
Primary Test 1	17 Oct 97	1430/1605	4.3/3.5/3.5	3.00/3.00/2.25
Primary Test 2	27 Feb 98	1200/1315	5.0/3.9/4.9	2.50/2.25/2.00

Table C.3 Modulus of Elasticity Results

Primary Test 1			Primary Test 2		
date / test	results (ksi)	average (ksi)	date / test	results (ksi)	average (ksi)
111497	4250		032798	4600	
28-day	4400	4350	28-day	4500	4550
112597	4350		040698	4300	
start	4350	4350	start	4450	4400
011298	5100		043098	4450	
1/3	5450	5300	1/3	4700	4600
021398	4200		060898	4300	
2/3	4100	4150	2/3	4050	4200
032098	4200		062398	4450	
end	4300	4250	end	4250	4350

Table C.4 Compressive Strength Results

Pilot Test			Primary Test 1			Primary Test 2		
date / test	results (psi)	average (psi)	date / test	results (psi)	average (psi)	date / test	results (psi)	average (psi)
080197	7280		111497	3590[1]		032798	6090	
	8420		28-day	5770		28-day	6390	
	7560	7750		6010[2]			5790	
081897	7370			6420			6590[2]	
	7700			5910			6060[2]	6180
	7160	7410		6180[2]	6060	040698	5800	
			112597	6190		start	6260	
			start	5860			5840	
				3760[1]			6330[2]	
				6470[2]			6510[2]	6150
				6740[2]	6320	043098	6780[2]	
			011298	6960[2]		1/3	5890	
			1/3	6520[2]			6790	
				6050	6510		6430	
			021398	7160			6850[2]	6550
			2/3	6950		060898	6090	
				6780[2]		2/3	2690[1]	
				5940[2]			6670	
				6640	6690		6730[2]	
			032098	6390			5940[2]	6360
			end	6680		062398	6740	
				5870		end	5630	
				5860[2]			6340	
				6640[2]	6290		6540[2]	
							6270[2]	6300

Notes:
1) Low test result not included in the average.
2) Specimen had been used in the Modulus of Elasticity Test.

Table C.5 Modulus of Rupture Results

Primary Test 1			Primary Test 2		
date / test	results (psi)	average (psi)	date / test	results (psi)	average (psi)
111497	420		032798	670	
28-day	360		28-day	555	
	510	430		565	600
032098	705		062398	915	
end	745		end	1020	
	850	765		870	935

Table C.6 Split Tensile Strength Results

Pilot Test			Primary Test 1			Primary Test 2		
date / test	results (psi)	average (psi)	date / test	results (psi)	average (psi)	date / test	results (psi)	average (psi)
011897	695		111497	550		032798	600	
	720		28-day	495		28-day	560	
	620			515	520		490	550
	545		112597	470		040698	555	
	440	605	start	590		start	555	
				710	590		510	540
			011298	505		043098	505	
			1/3	545		1/3	475	
				520	525		565	515
			021398	530		060898	575	
			2/3	470		2/3	565	
				580	530		525	555
			032098	445		062398	530	
			end	450		end	470	
				450	450		520	510

Appendix D

Flexural Stress Calculations

Flexural stress was imposed on the test bars from the inverted half-beam setup and from any misalignment in the tensile test grips. The magnitude of the flexural stress was calculated at the location of the LES LVDT bracket as shown in Fig. D.1. The strain recorded by each LVDT was calculated as follows:

$$\kappa_1 = \frac{LVDT_1}{L} \text{ and } \kappa_2 = \frac{LVDT_2}{L} \tag{D-1}$$

where κ is the strain for LVDT, $LVDT$ is the displacement measured by the Linear Variable Differential Transformers, and L is the span for LVDT, recorded for each test.

The strain distribution through the bar was equal to the average strain in the bar plus a linear variation of strain through the bar cross section as shown in Fig. D.2. The curvature was determined from the linear strain variation as shown in Fig. D.3:

$$\lambda = \frac{(\kappa_1 + \kappa_2)/2}{h/2} \tag{D-2}$$

where λ is the curvature, κ is the strains as calculated in Eqn. (D-1), and h is the distance between LVDTs, constant at 6.125 in.

Curvature was also expressed in terms moment and material properties:

$$\lambda = \frac{M}{EI} \tag{D-3}$$

where M is the moment at cross section of interest, E is the modulus of elasticity (M1: E = 6090 ksi and M2: E = 5800 ksi), and I is the moment of inertia for bar.

Equating Eqns. (D-2) and (D-3) yielded the term M/EI in terms of strains:

$$\frac{M}{EI} = \frac{\kappa_1 + \kappa_2}{h/2} \tag{D-4}$$

Each set of loaded-end slip LVDTs measured the curvature in the plane of instrumentation. The resultant curvature was determined from the two M/EI values:

$$\left(\frac{M}{EI}\right)_{resultant} = \sqrt{\left(\frac{M}{EI}\right)^2_{LES1\&2} + \left(\frac{M}{EI}\right)^2_{LES3\&4}} \tag{D-5}$$

where $\left(\frac{M}{EI}\right)_{resultant}$ is the combined curvature applied to bar, $\left(\frac{M}{EI}\right)_{LES1\&2}$ is the curvature applied in plane of loaded-end slip LVDTs 1 and 2, and $\left(\frac{M}{EI}\right)_{LES3\&4}$ is the curvature applied in plane of loaded-end slip LVDTs 3 and 4.

From the resultant curvature, a flexural stress was calculated for each test:

$$f_b = \left(\frac{d_b E}{2}\right)\left(\frac{M}{EI}\right)_{resultant} \tag{D-6}$$

where f_b is the largest flexural stress at extreme bar fiber, $\left(\frac{M}{EI}\right)_{resultant}$ is the total curvature applied to bar from Eqn. (D-5), d_b is the nominal bar diameter (M1: d_b = 0.625 in. and M2: d_b = 0.75 in.), and E is the modulus of elasticity (M1: E = 6090 ksi and M2: E = 5800 ksi). A f_b value was calculated for each test and is included in Data Tables 3.1 through 3.13 relative to each test's ultimate stress ($P_u/A_{nominal}$).

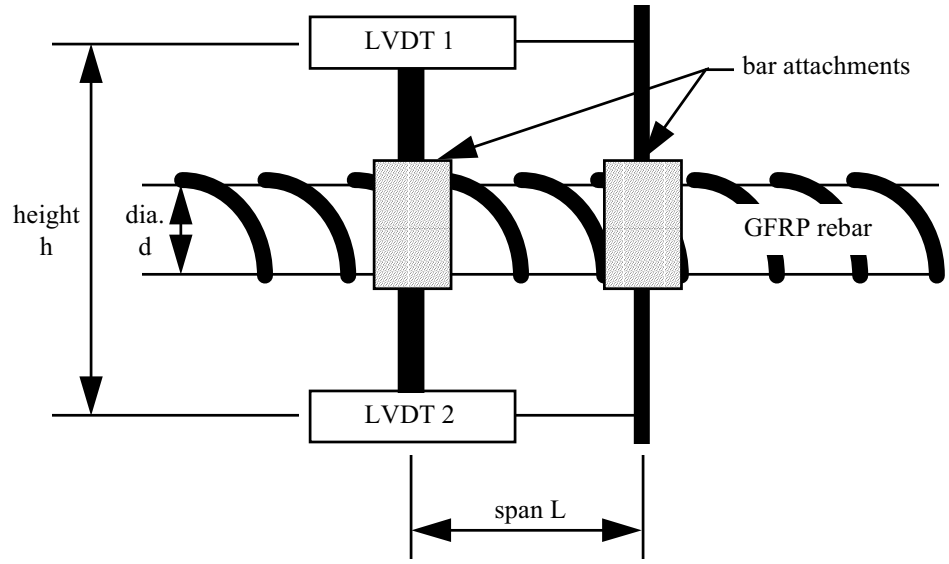

Figure D.1 LVDT Setup

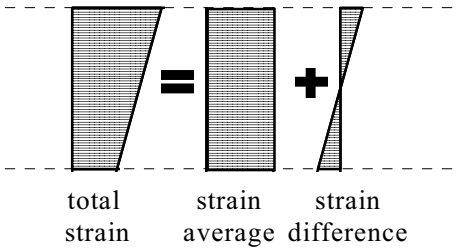

Figure D.2 Strain Distribution

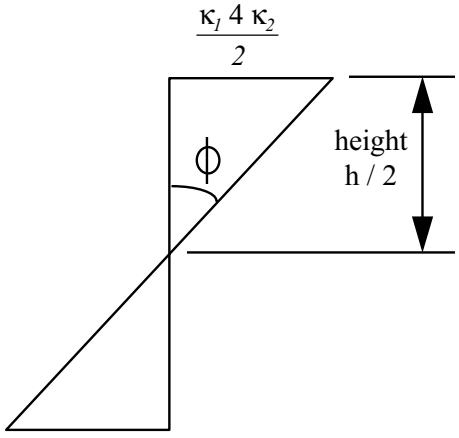

Figure D.3 Curvature Calculation

Appendix E

Crack Patterns

Appendix F

AE Figures

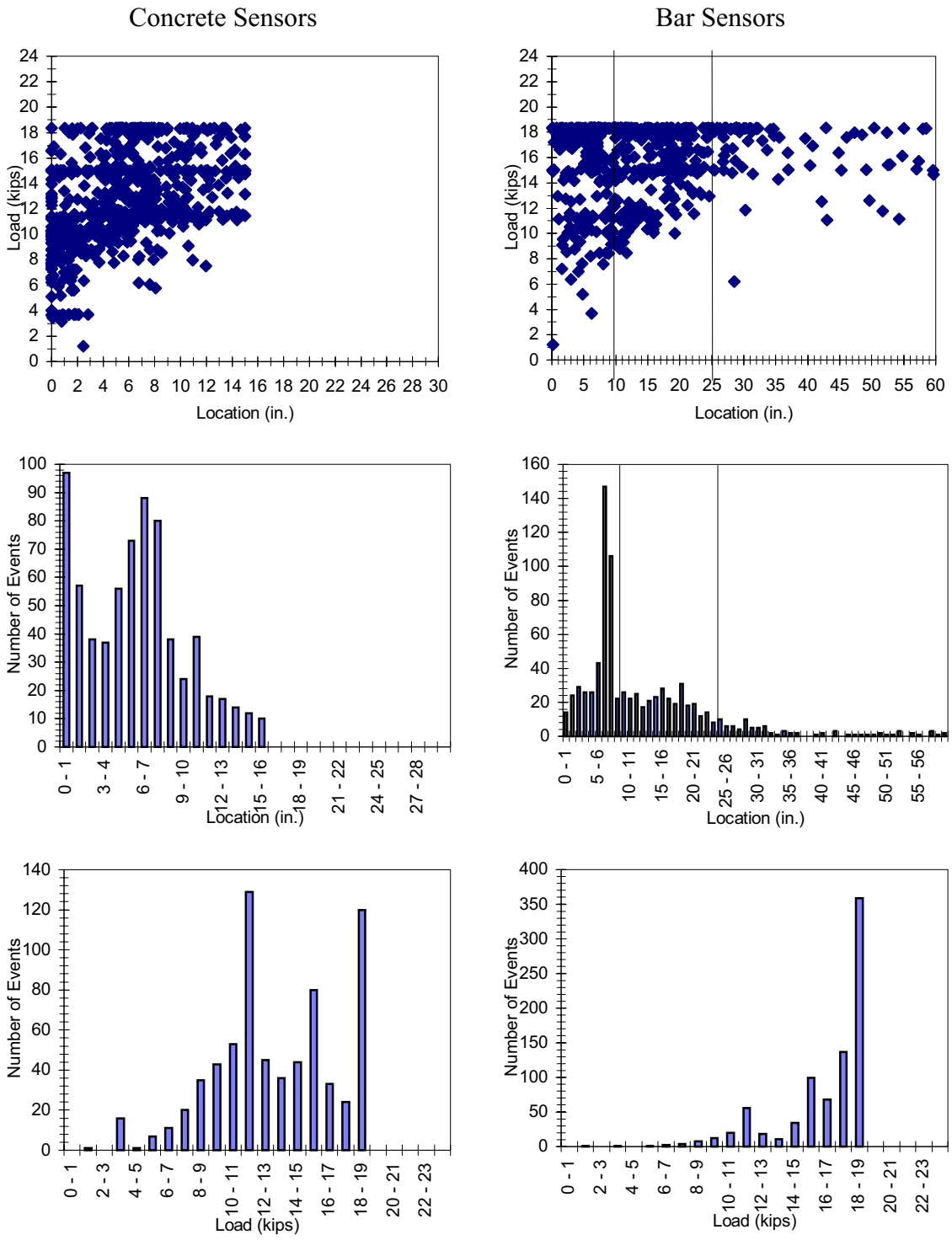

Figure F.1 1M1-5-3-15.0-1

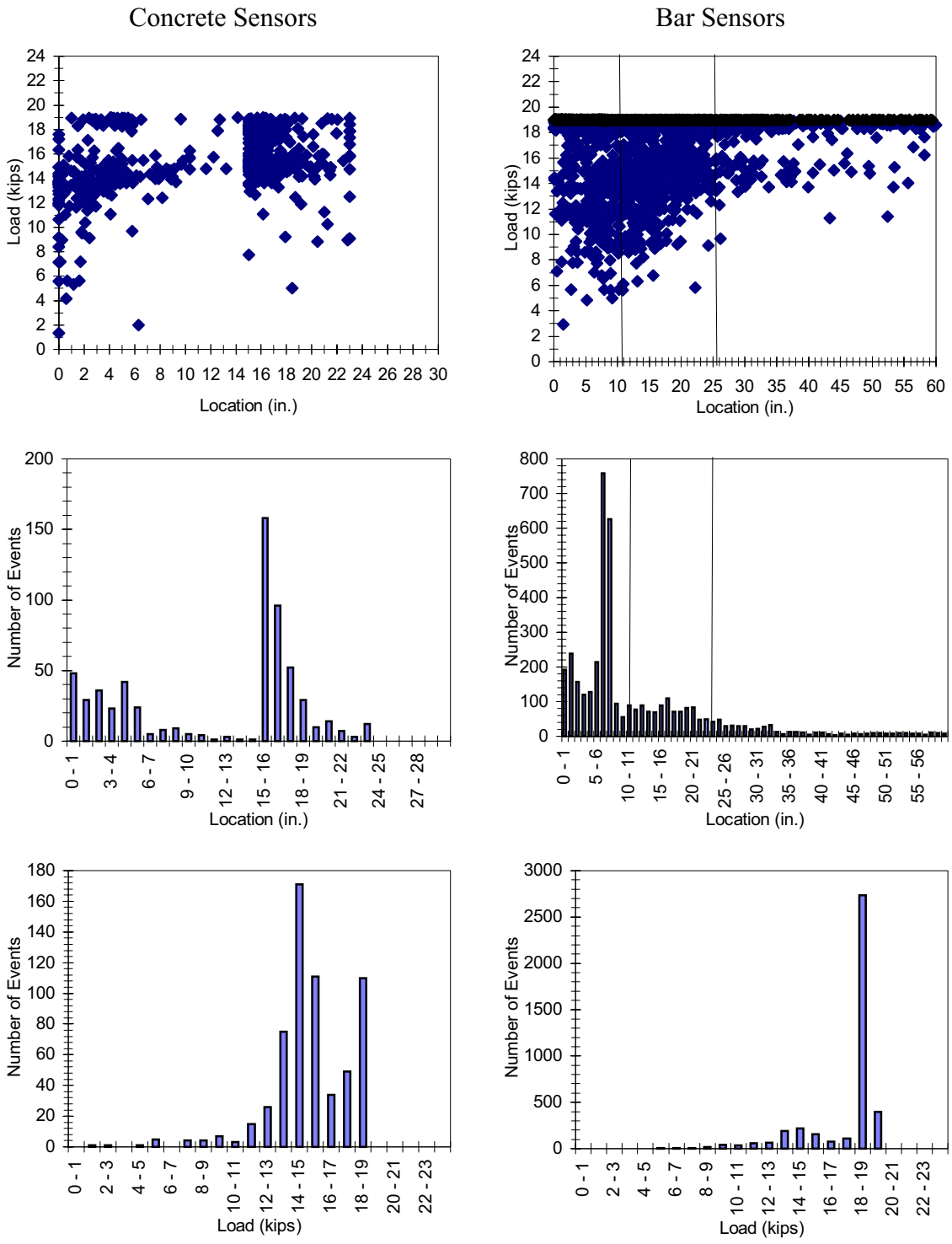

Figure F.2 1M1-5-3-15.0-2

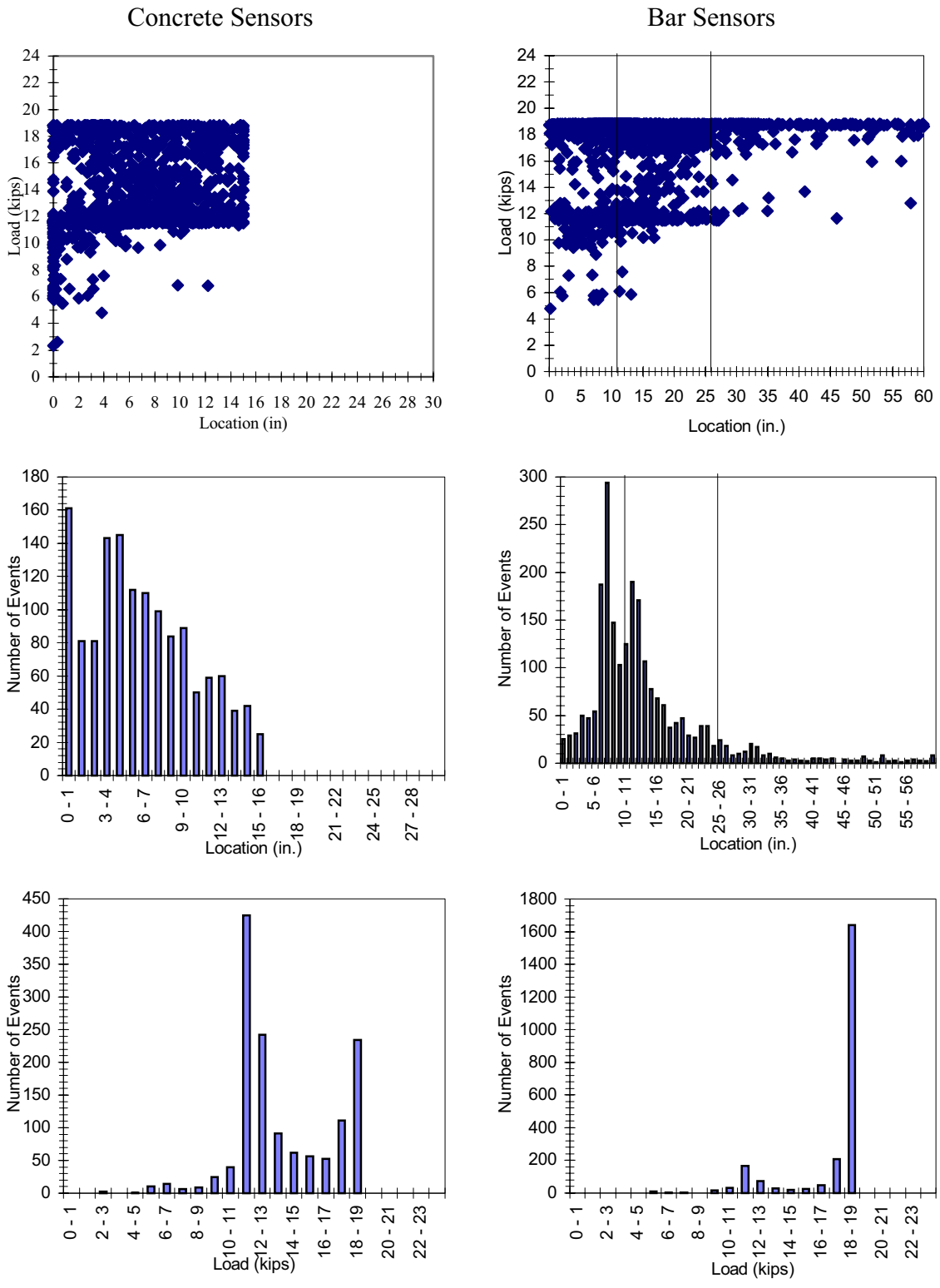

Figure F.3 1M1-5-3-15.0-3

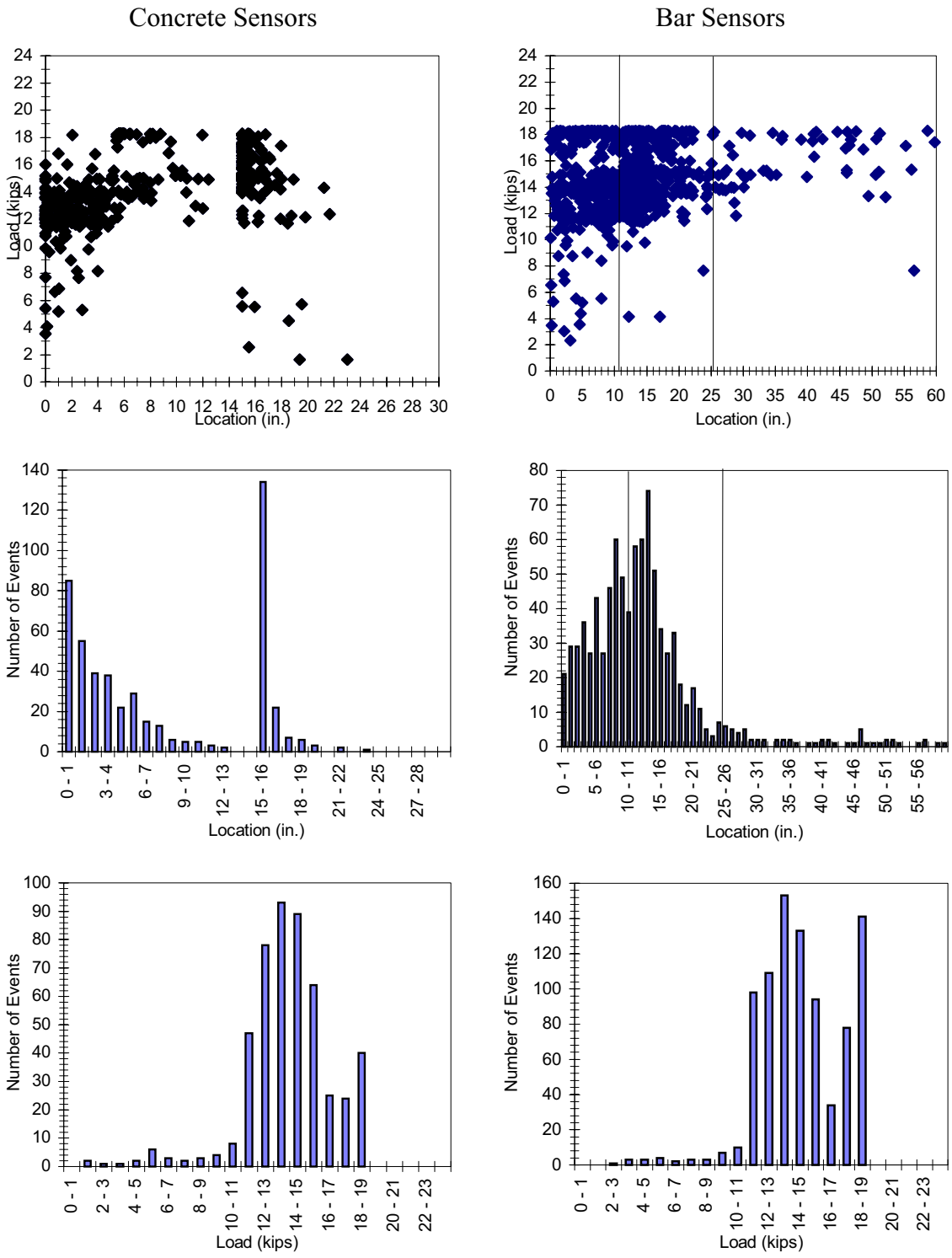

Figure F.4 1M1-5-3-15.0-4

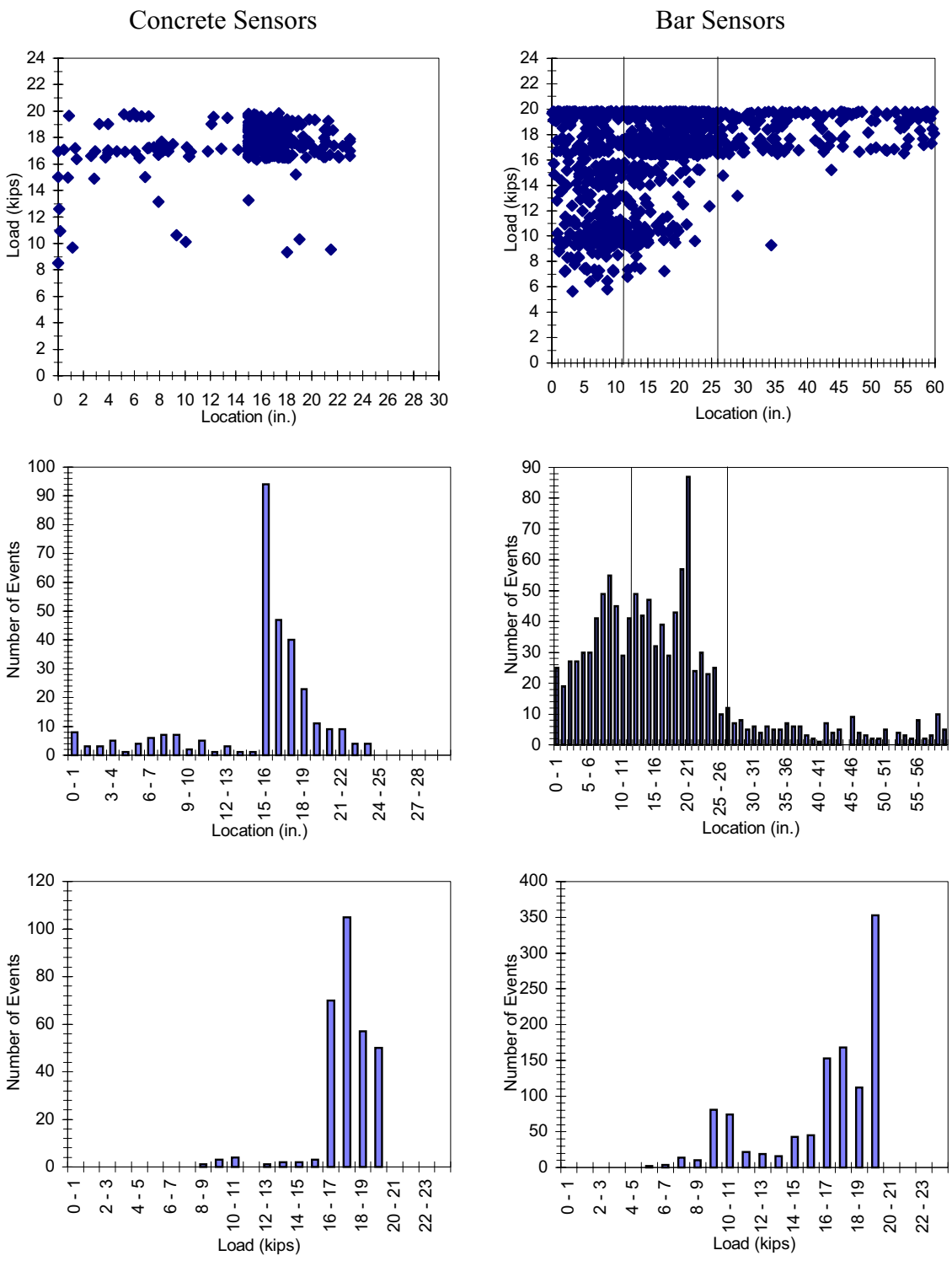

Figure F.5 1M1-5-3-15.0-5

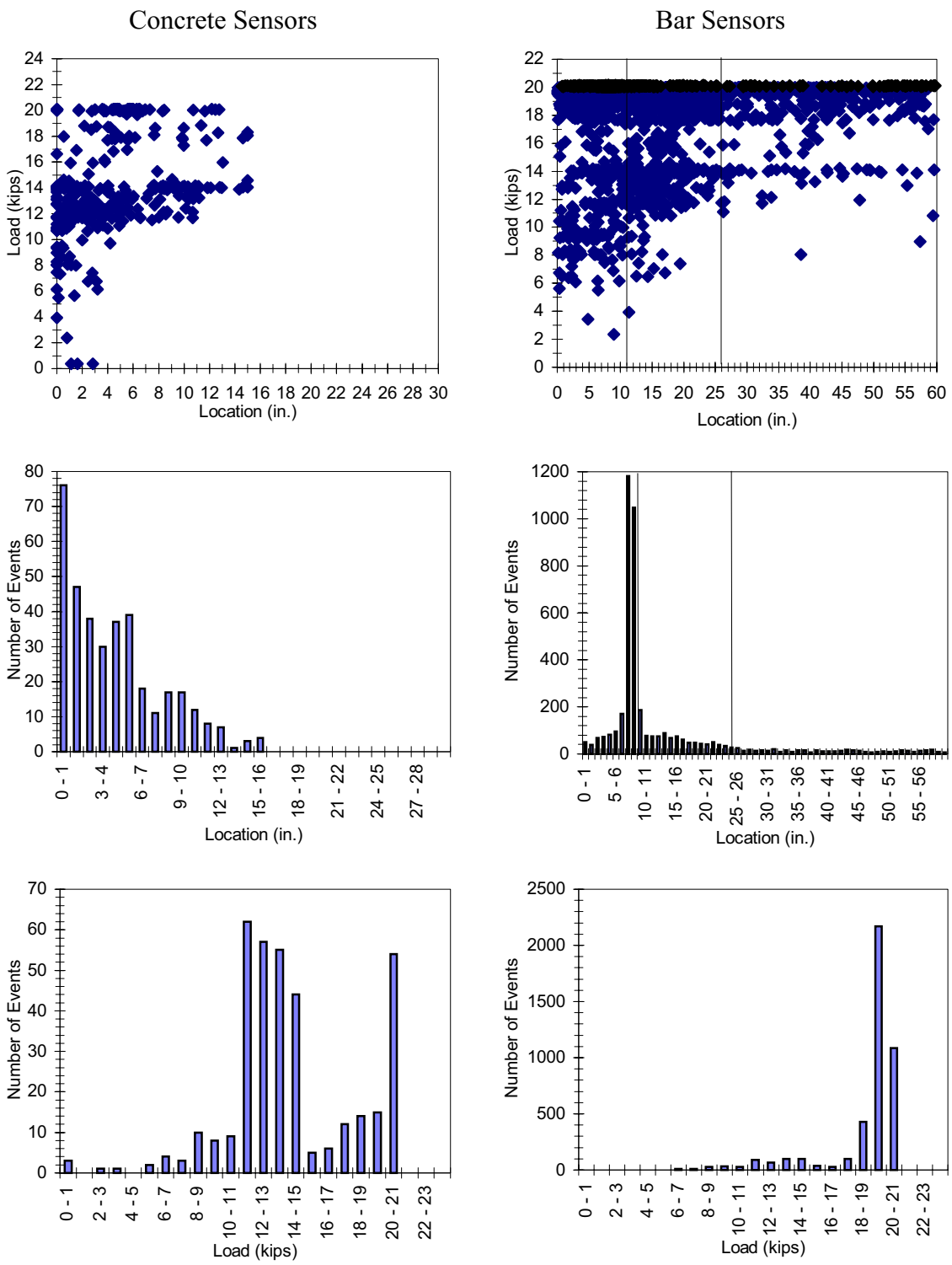

Figure F.6 1M1-5-3-15.0-6

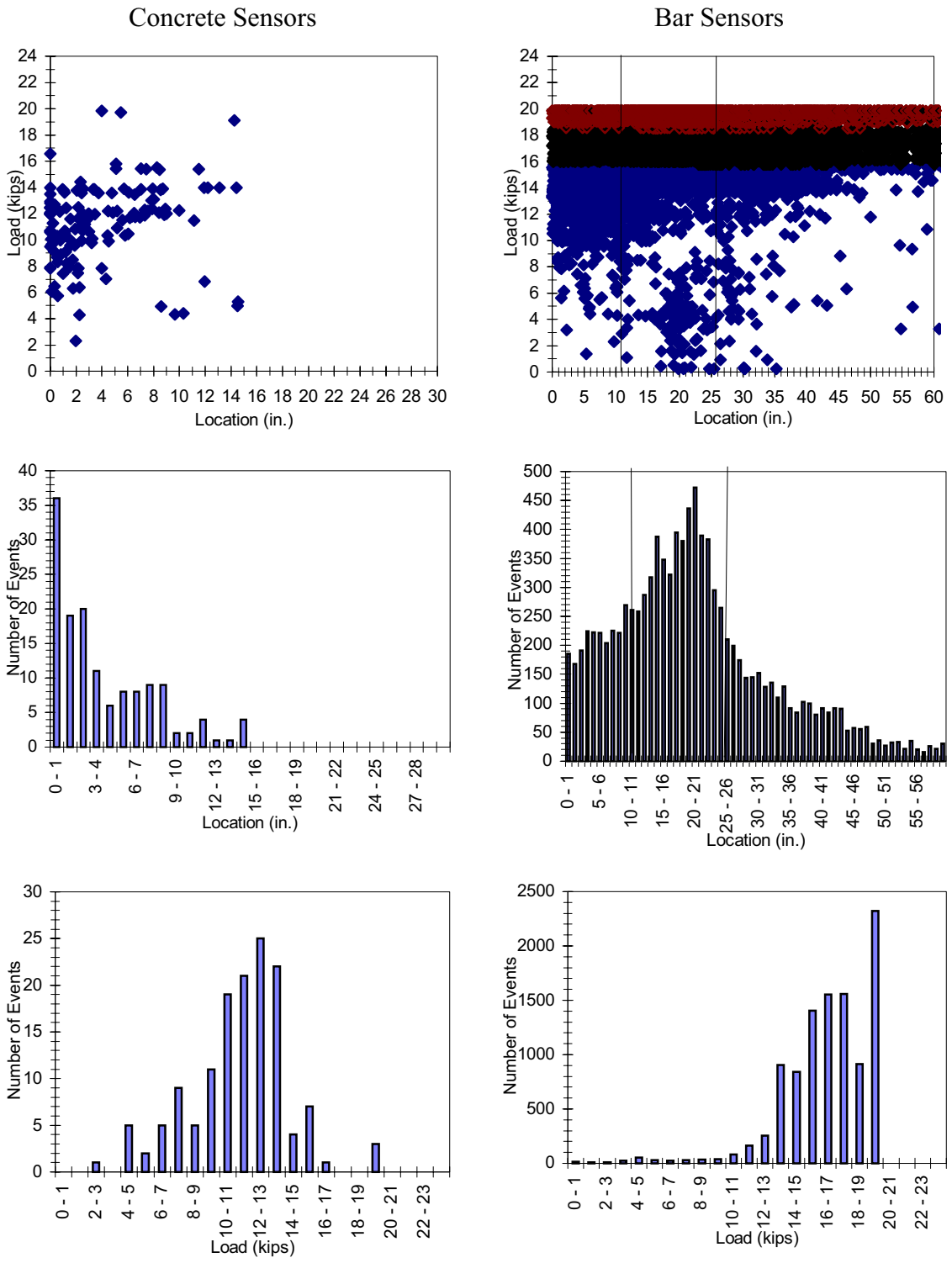

Figure F.7 1M1-5-3-12.5-1

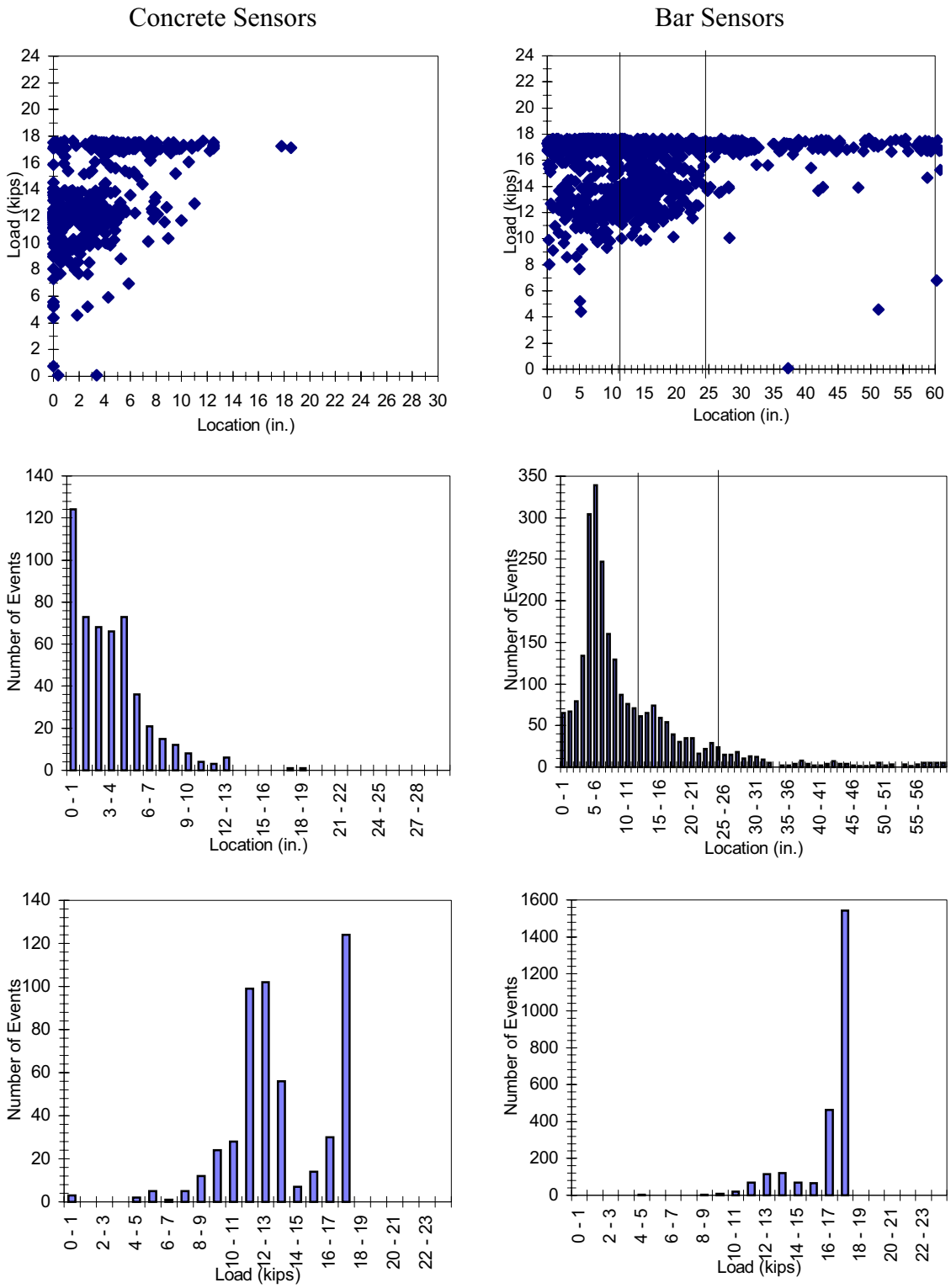

Figure F.8 1M1-5-3-12.5-2

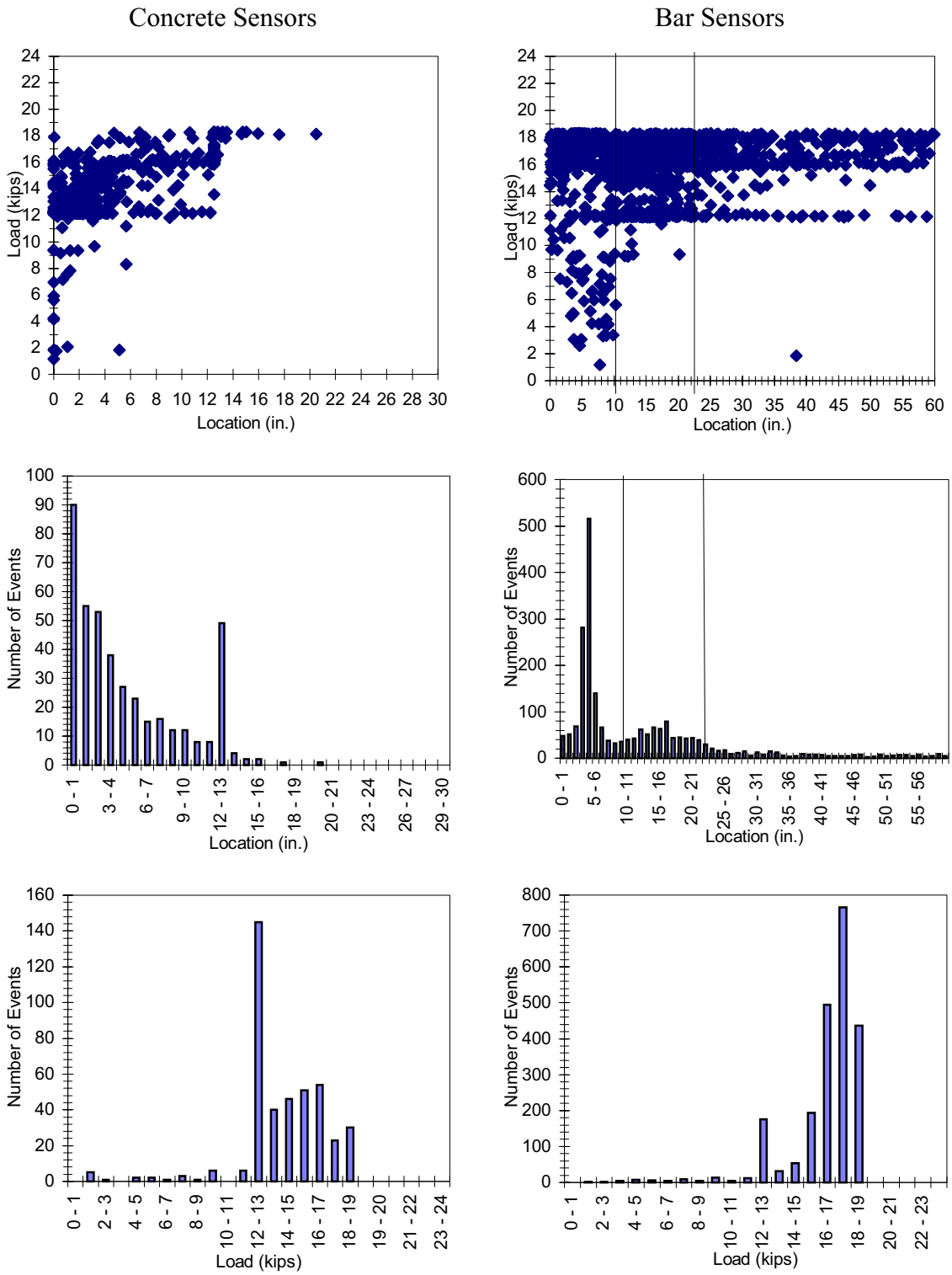

Figure F.9 1M1-5-3-12.5-3

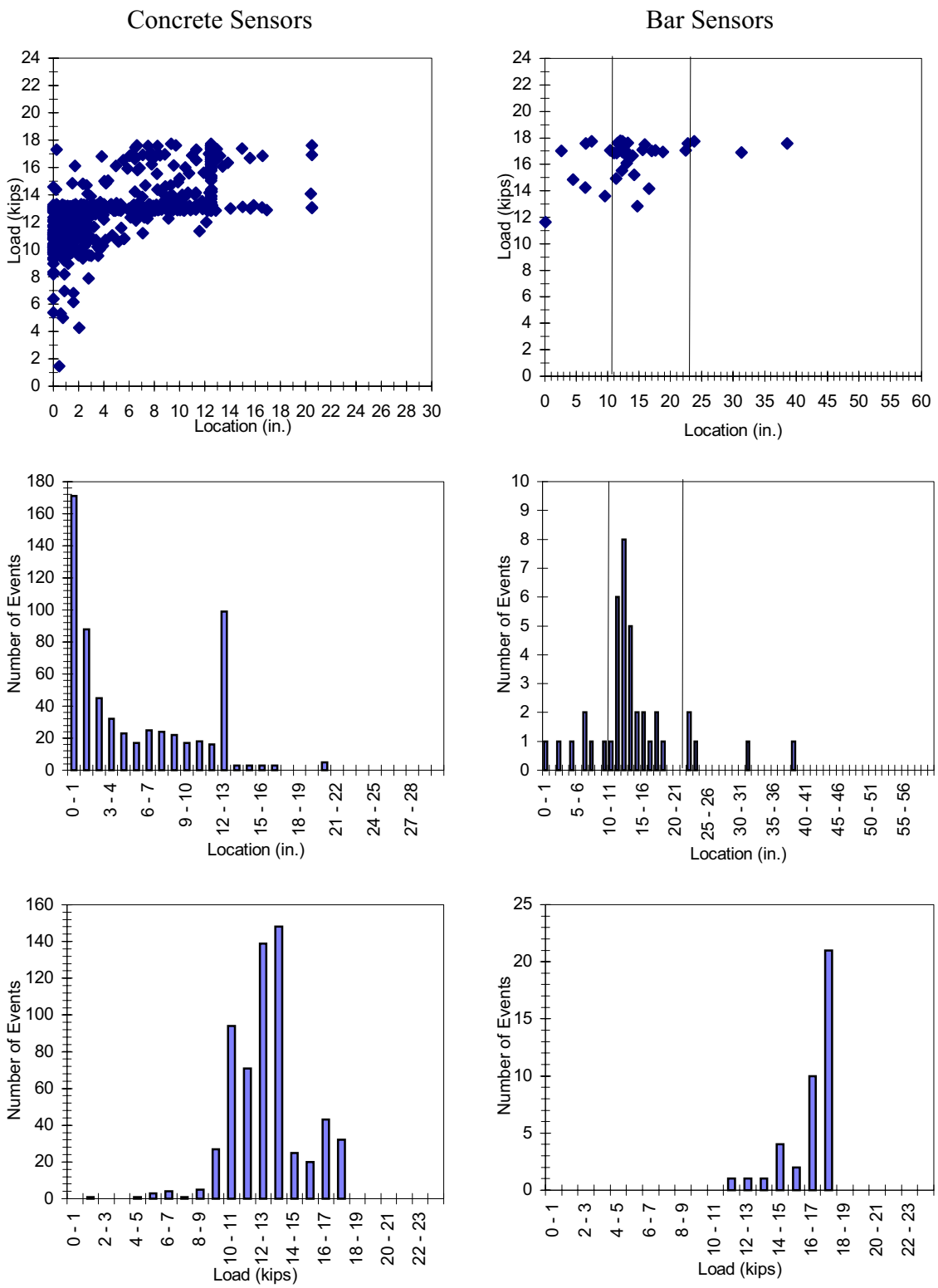

Figure F.10 1M1-5-3-12.5-4

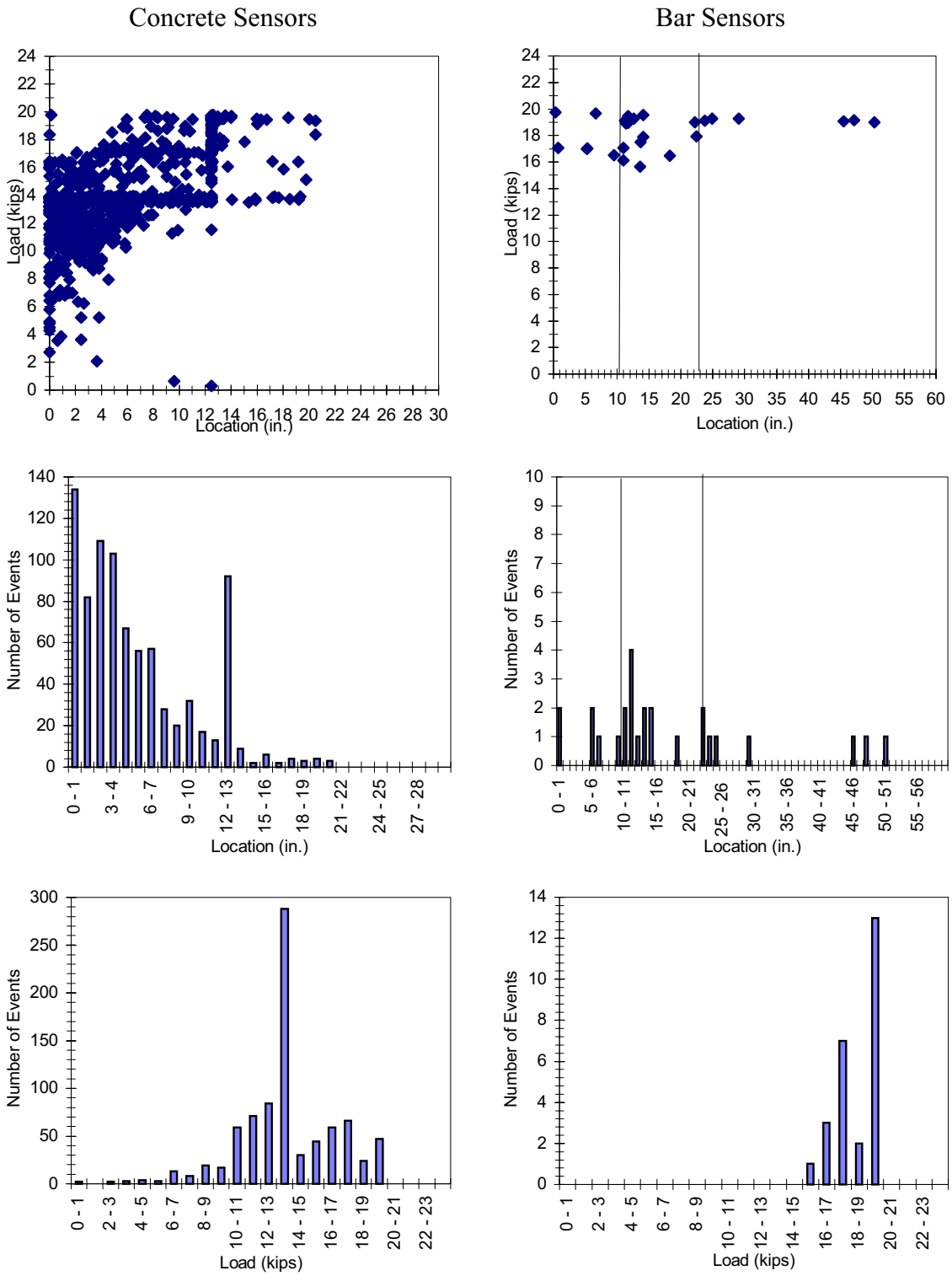

Figure F.11 1M1-5-3-12.5-5

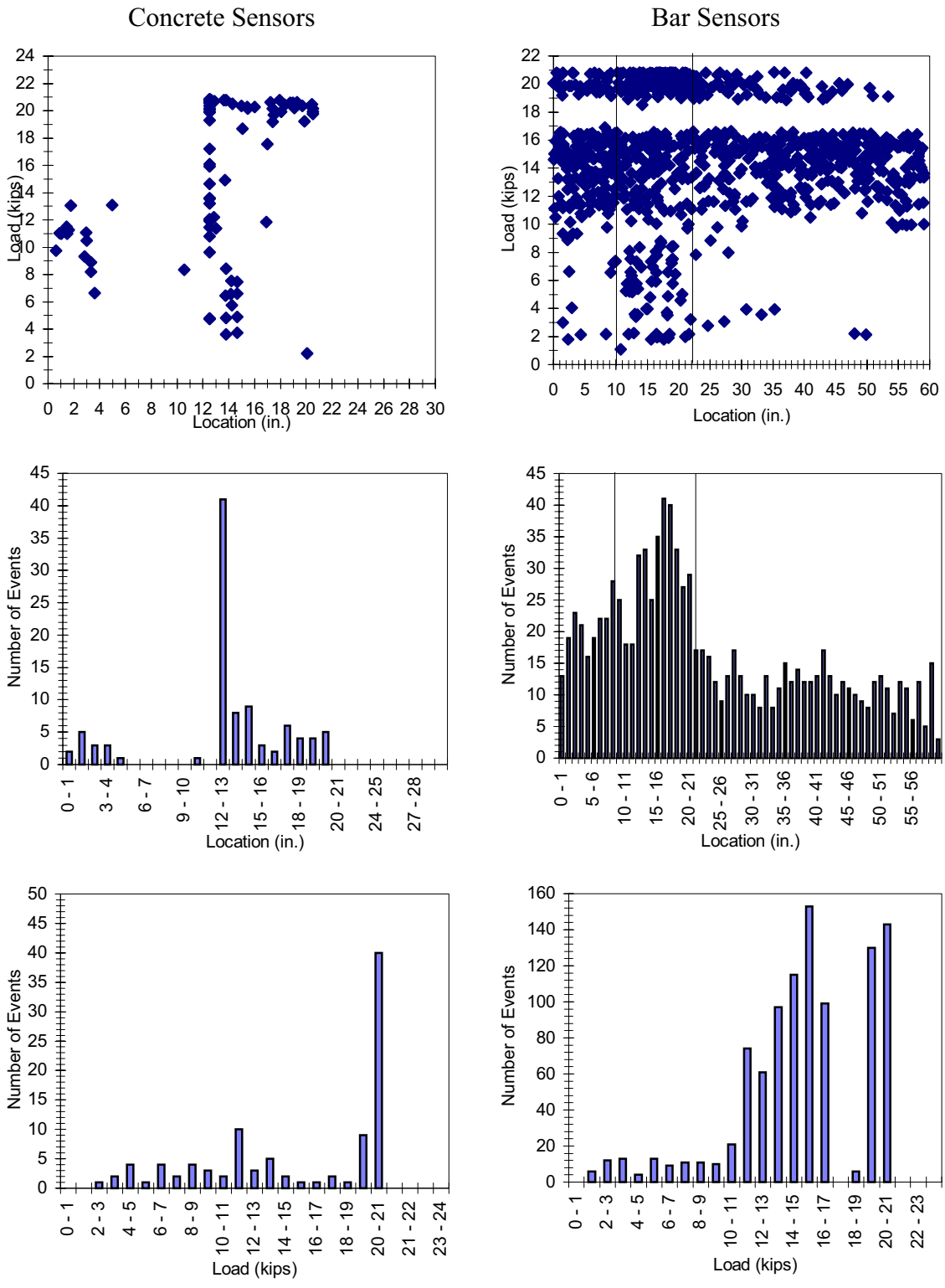

Figure F.12 1M1-5-3-12.5-6

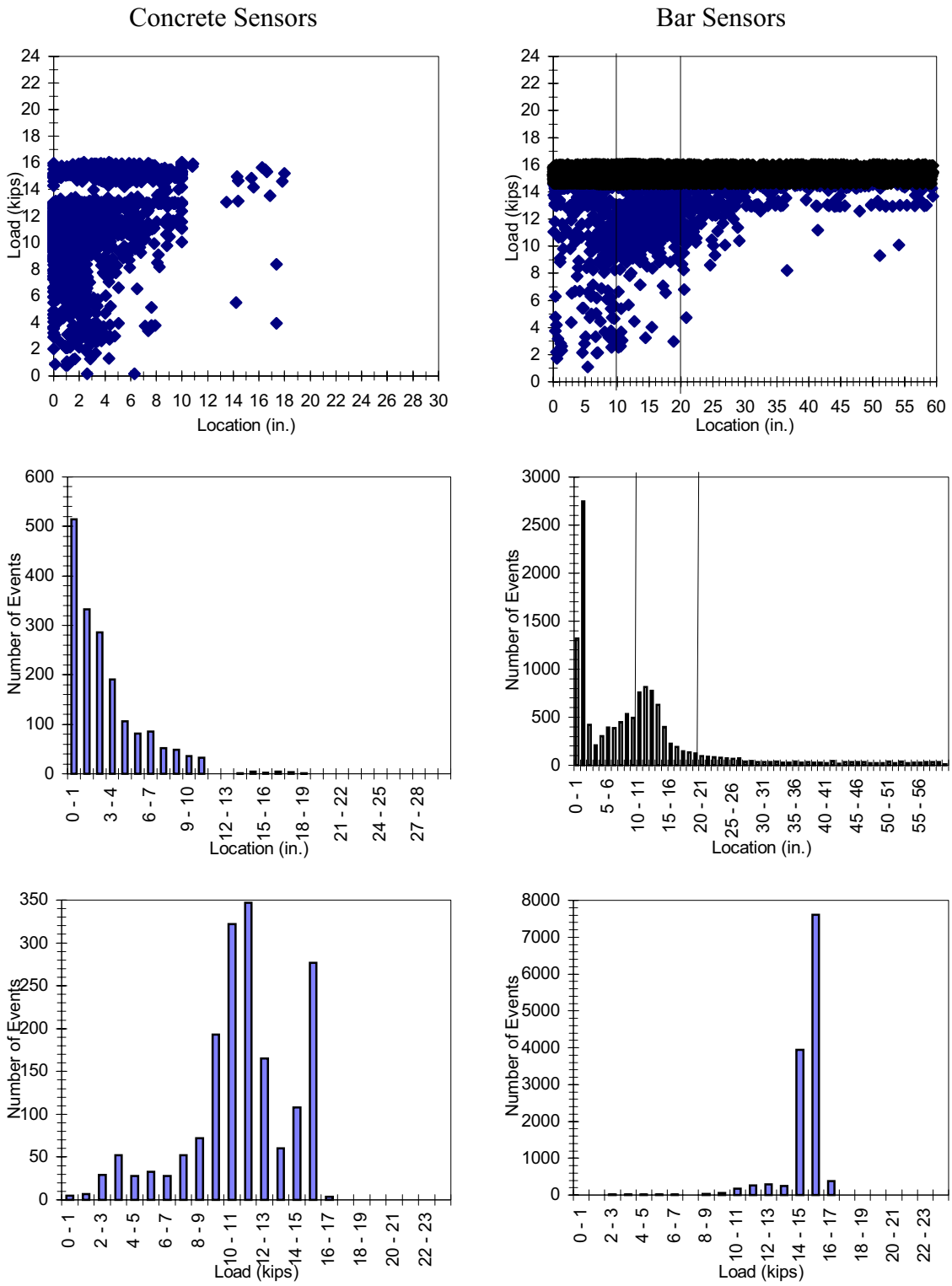

Figure F.13 1M1-5-3-10.0-1

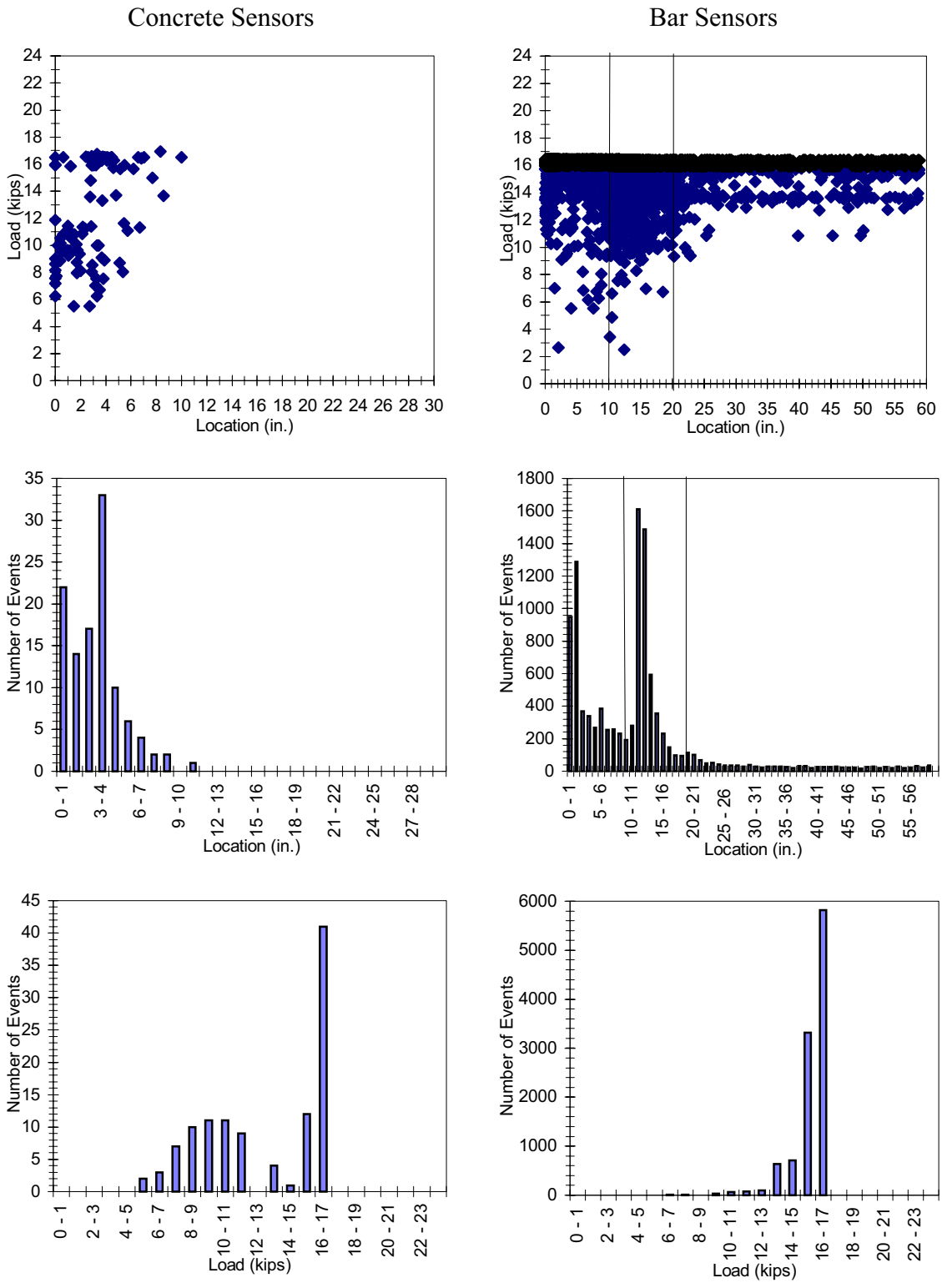

Figure F.14 1M1-5-3-10.0-2

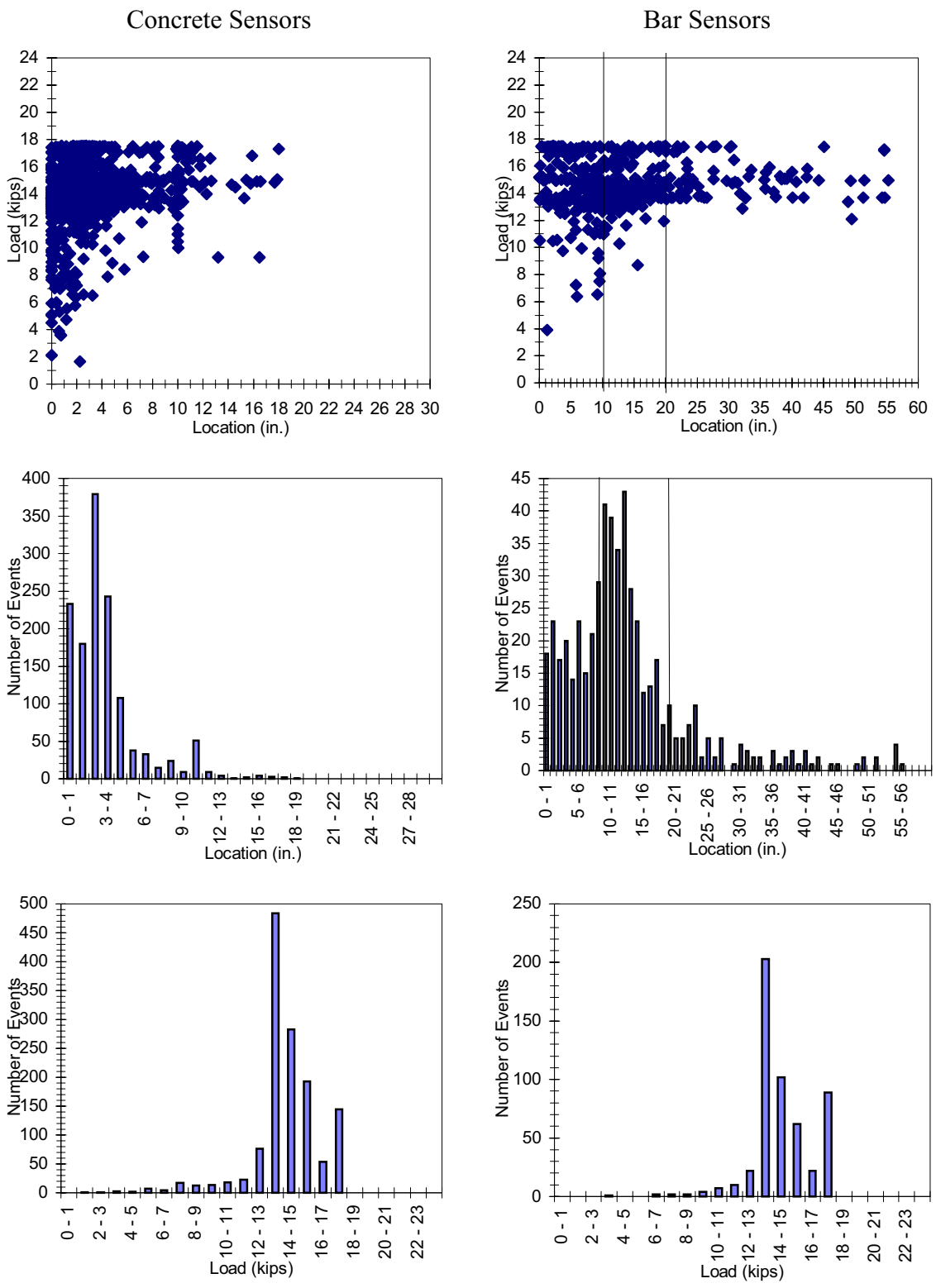

Figure F.15 1M1-5-3-10.0-3

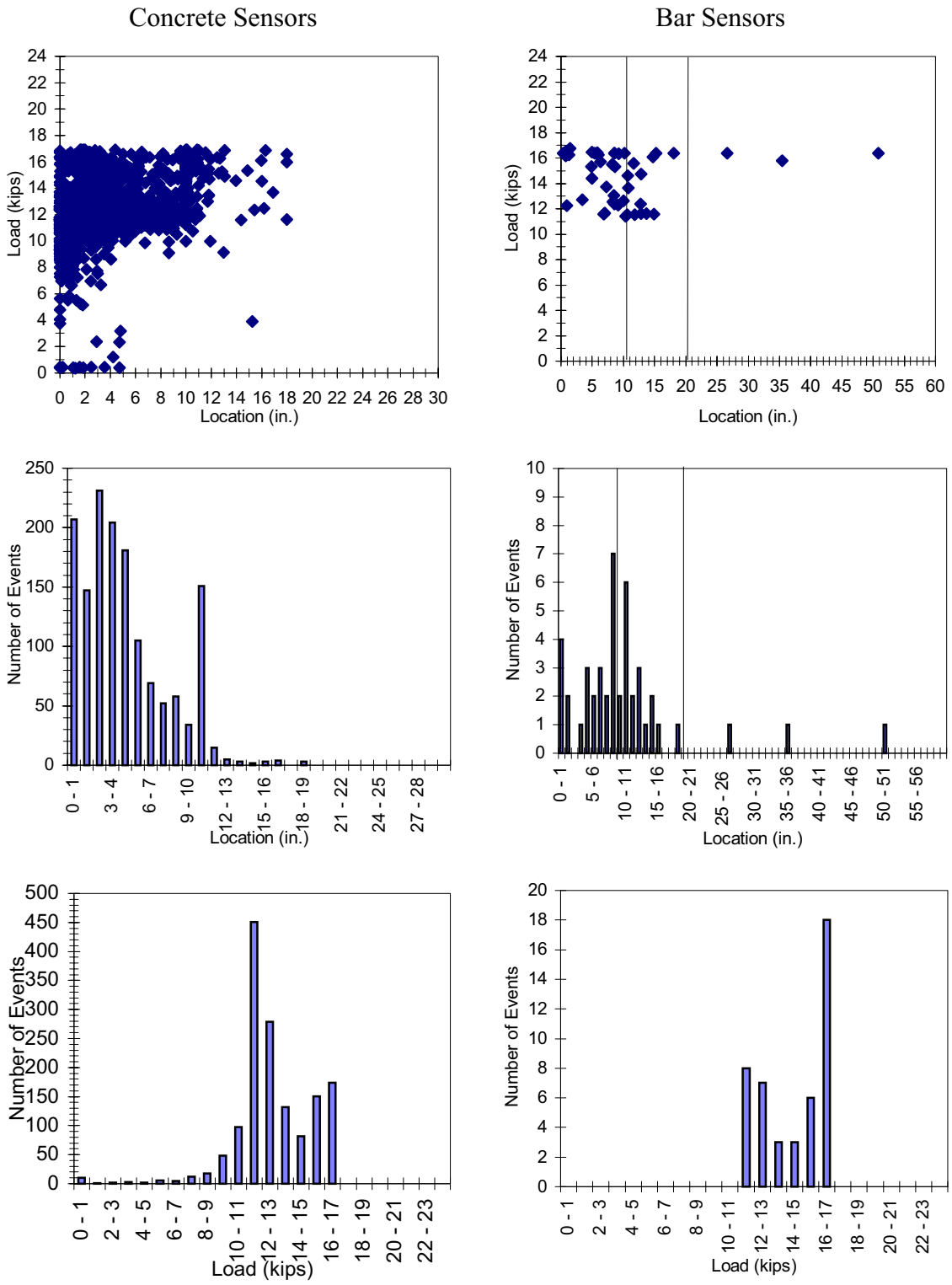

Figure F.16 1M1-5-3-10.0-4

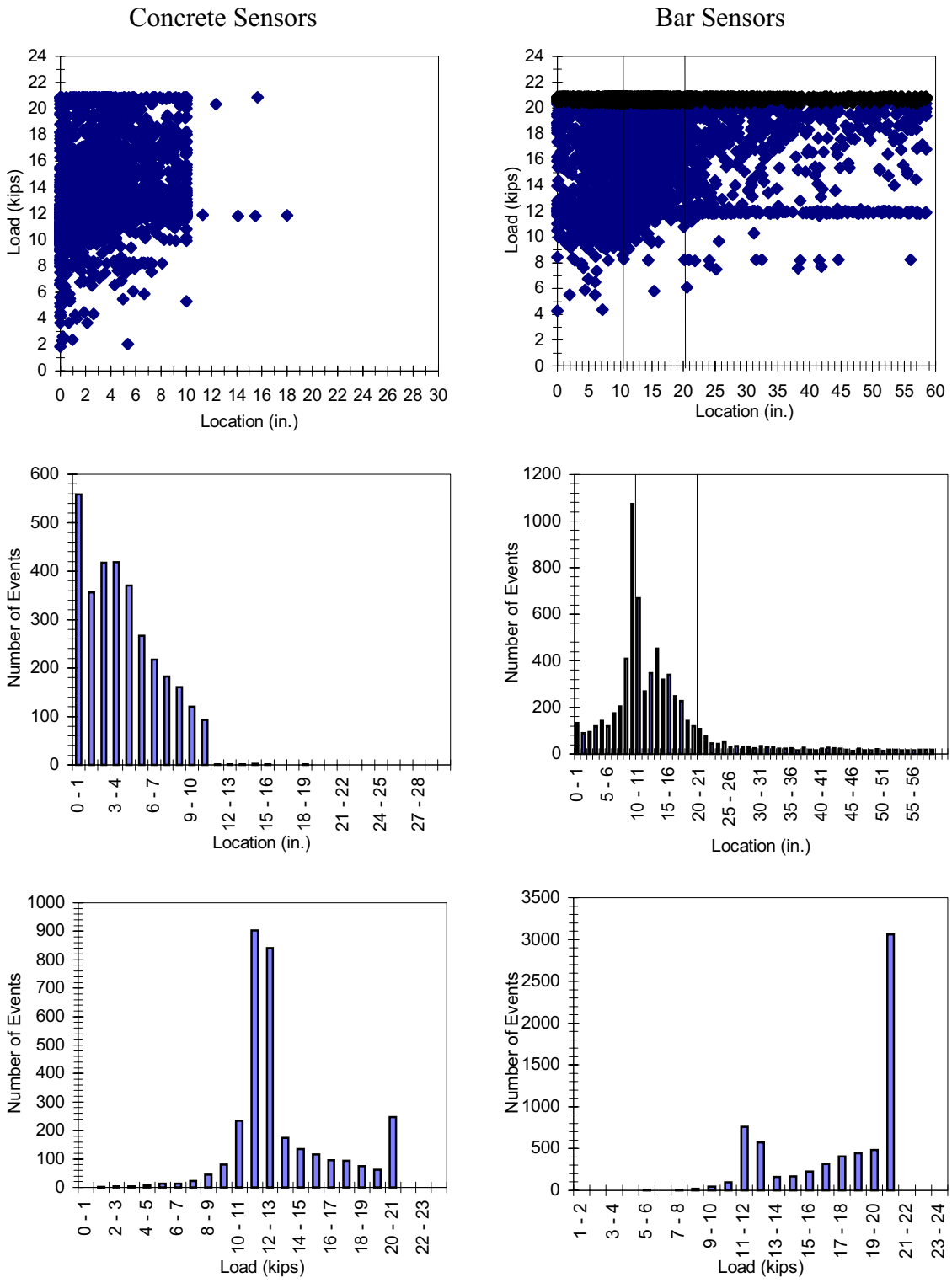

Figure F.17 1M1-5-3-10.0-5

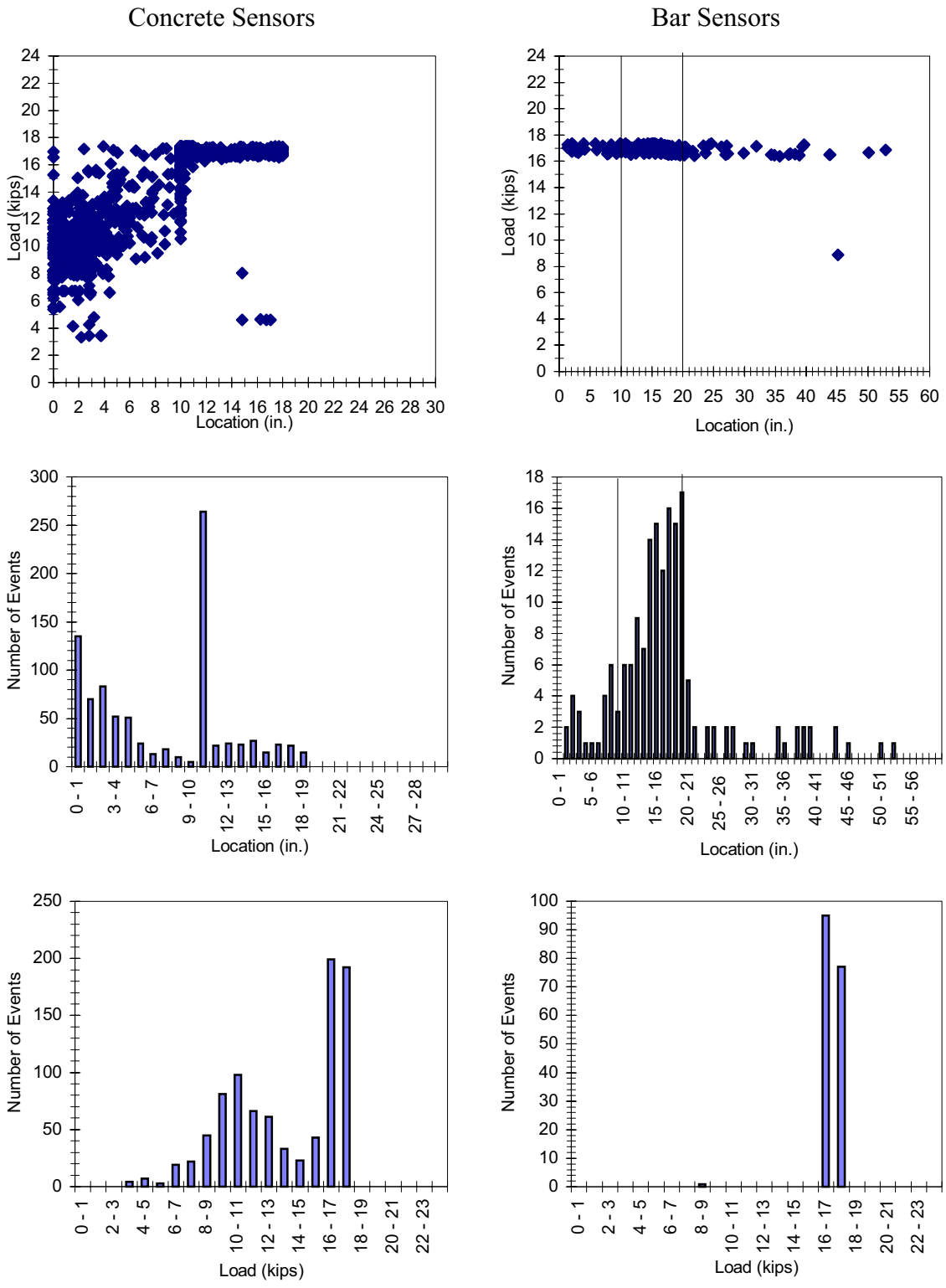

Figure F.18 1M1-5-3-10.0-6

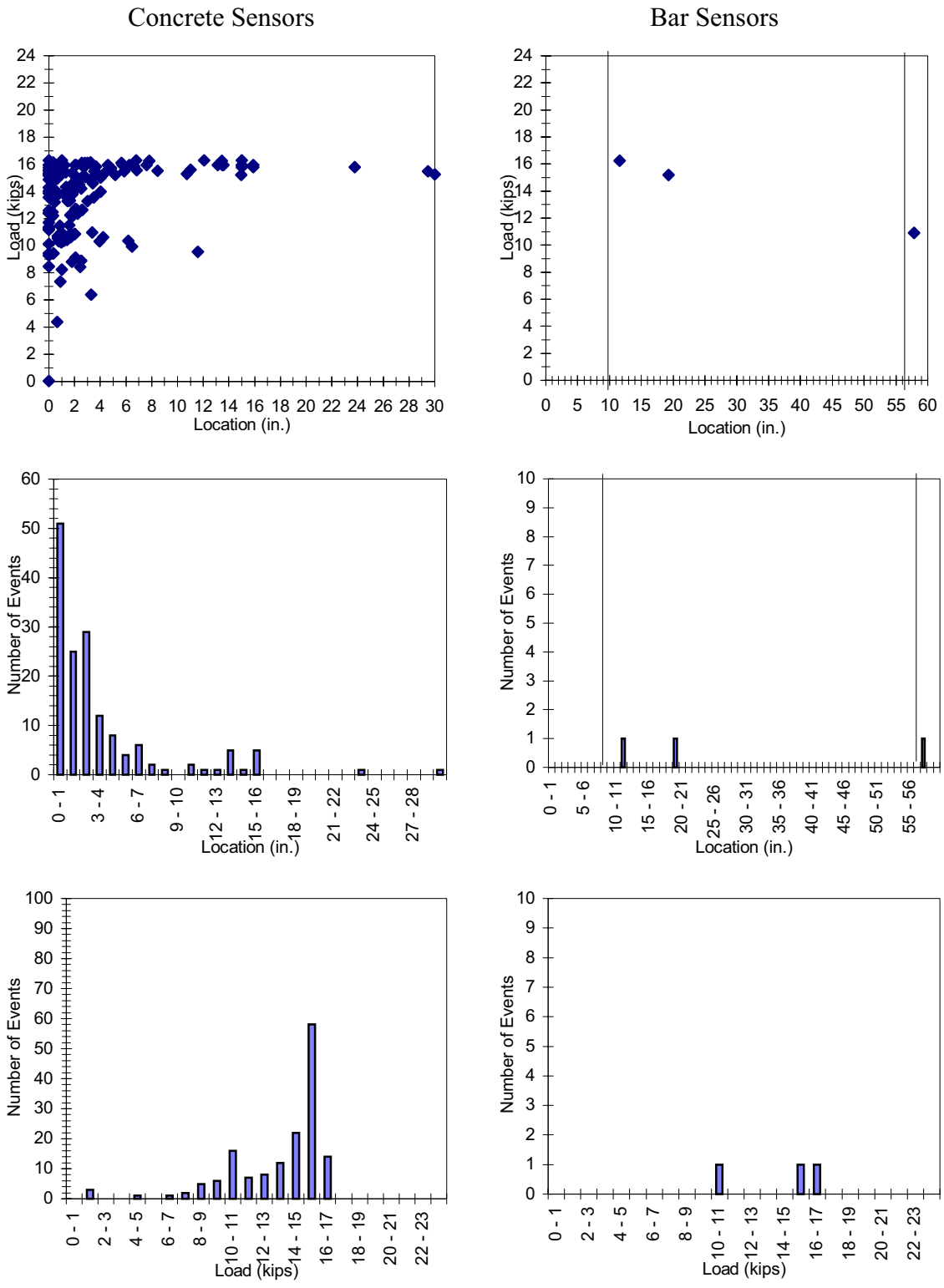

Figure F.19 1M1-5-2-47.0-1

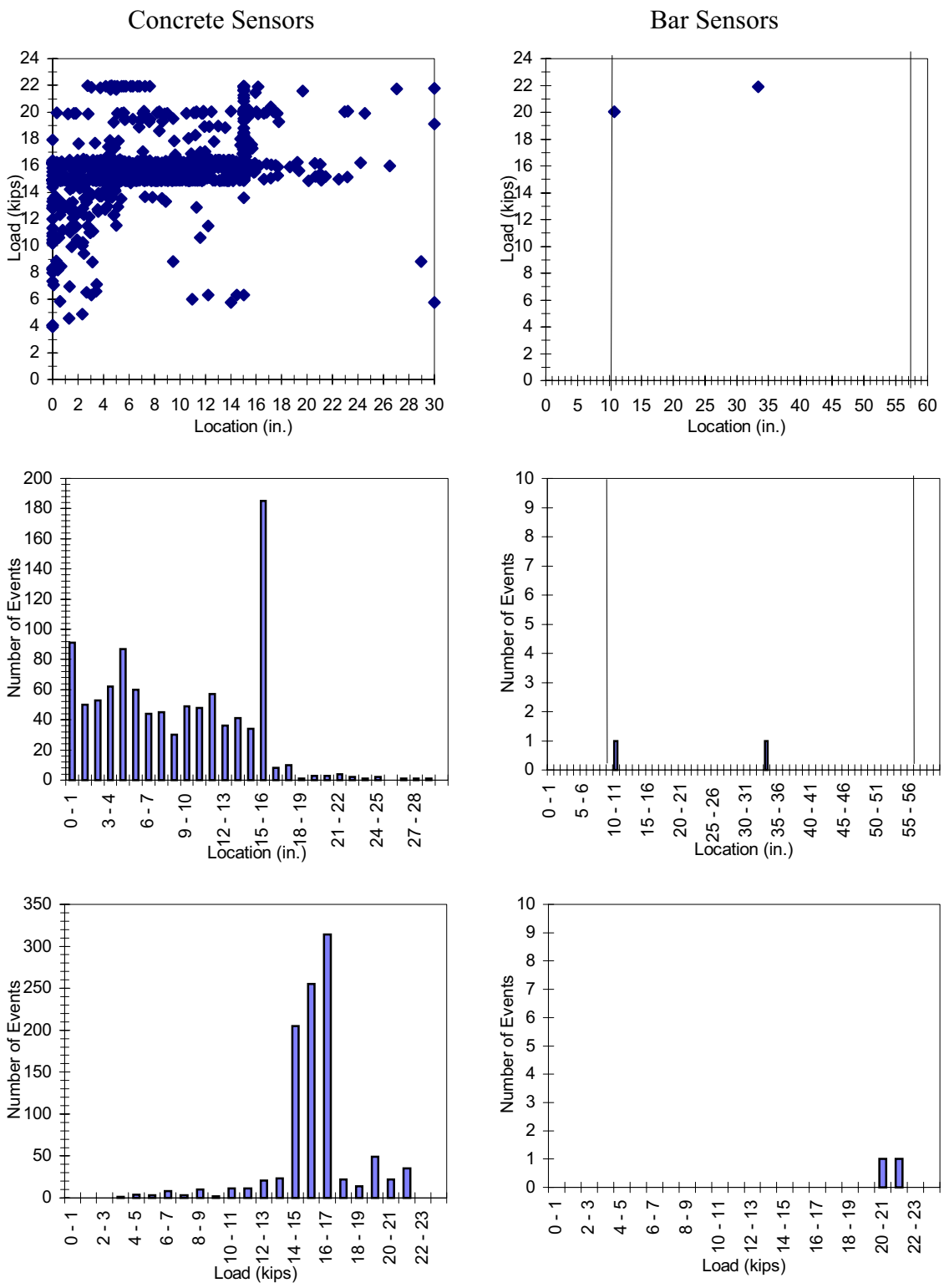

Figure F.201M1-5-2-47.0-2

no AE data recorded

Figure F.21 1M1-5-2-47.0-3

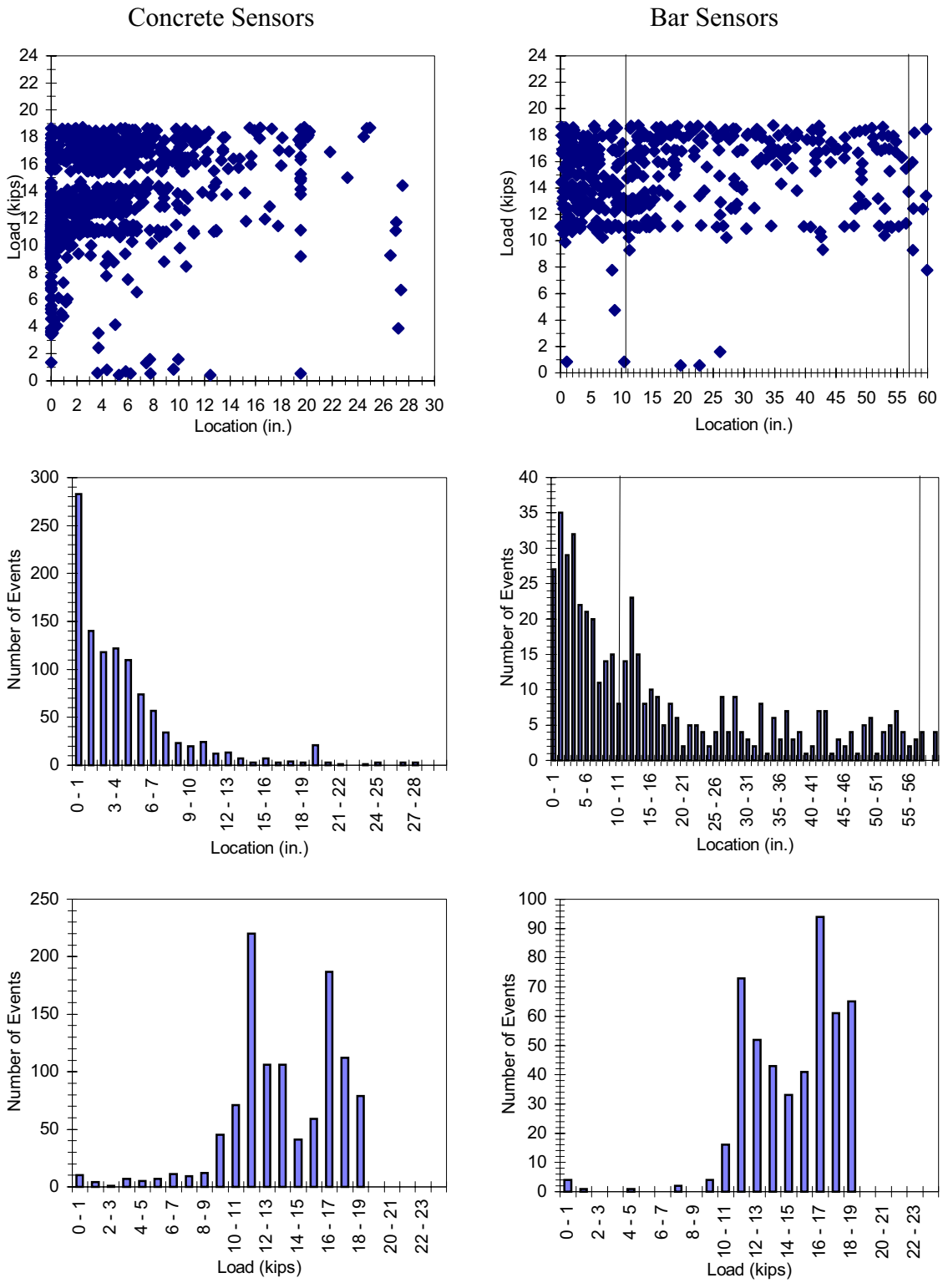

Figure F.22 1M1-5-2-47.0-4

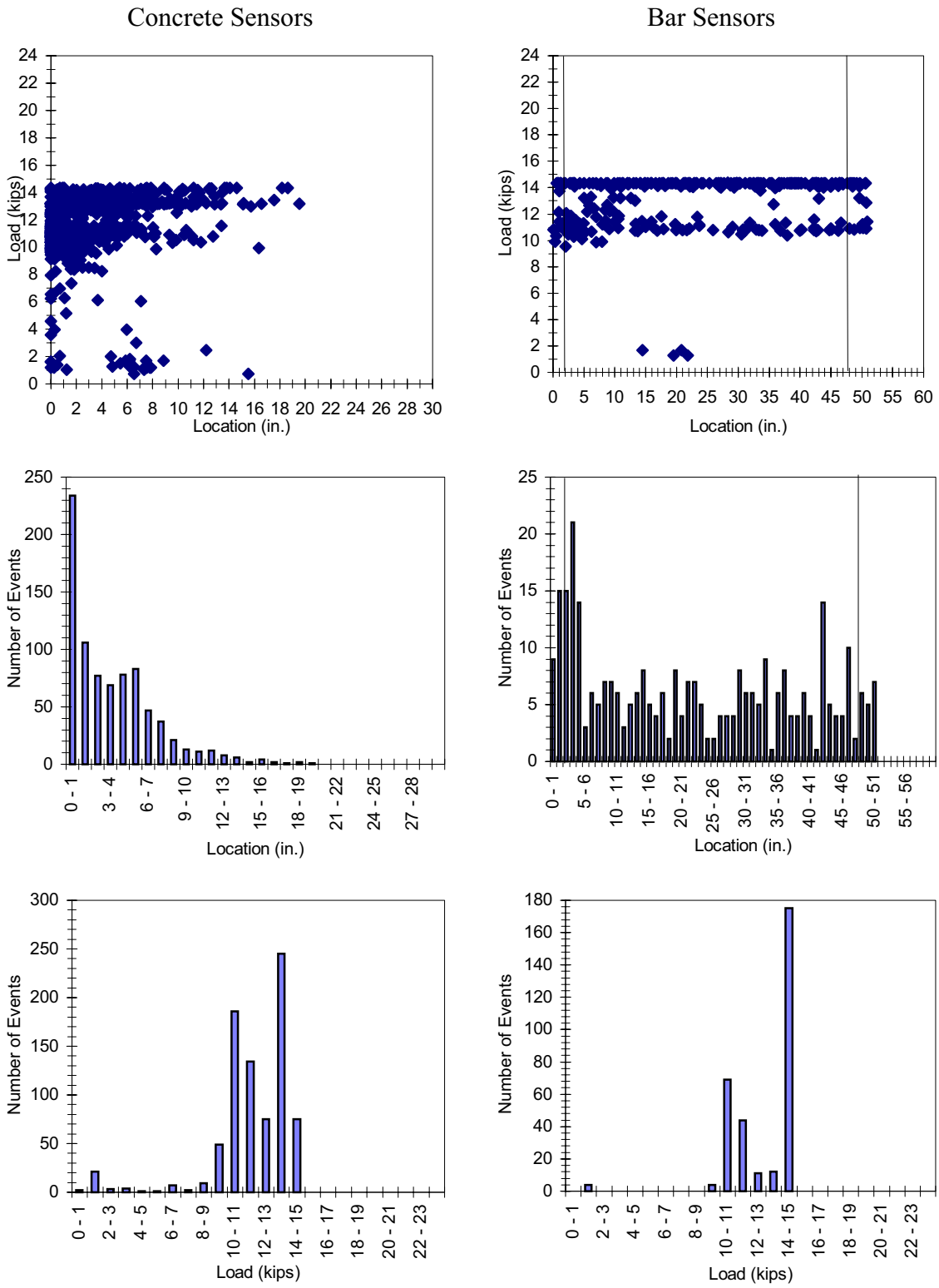

Figure F.23 1M1-5-2-47.0-5

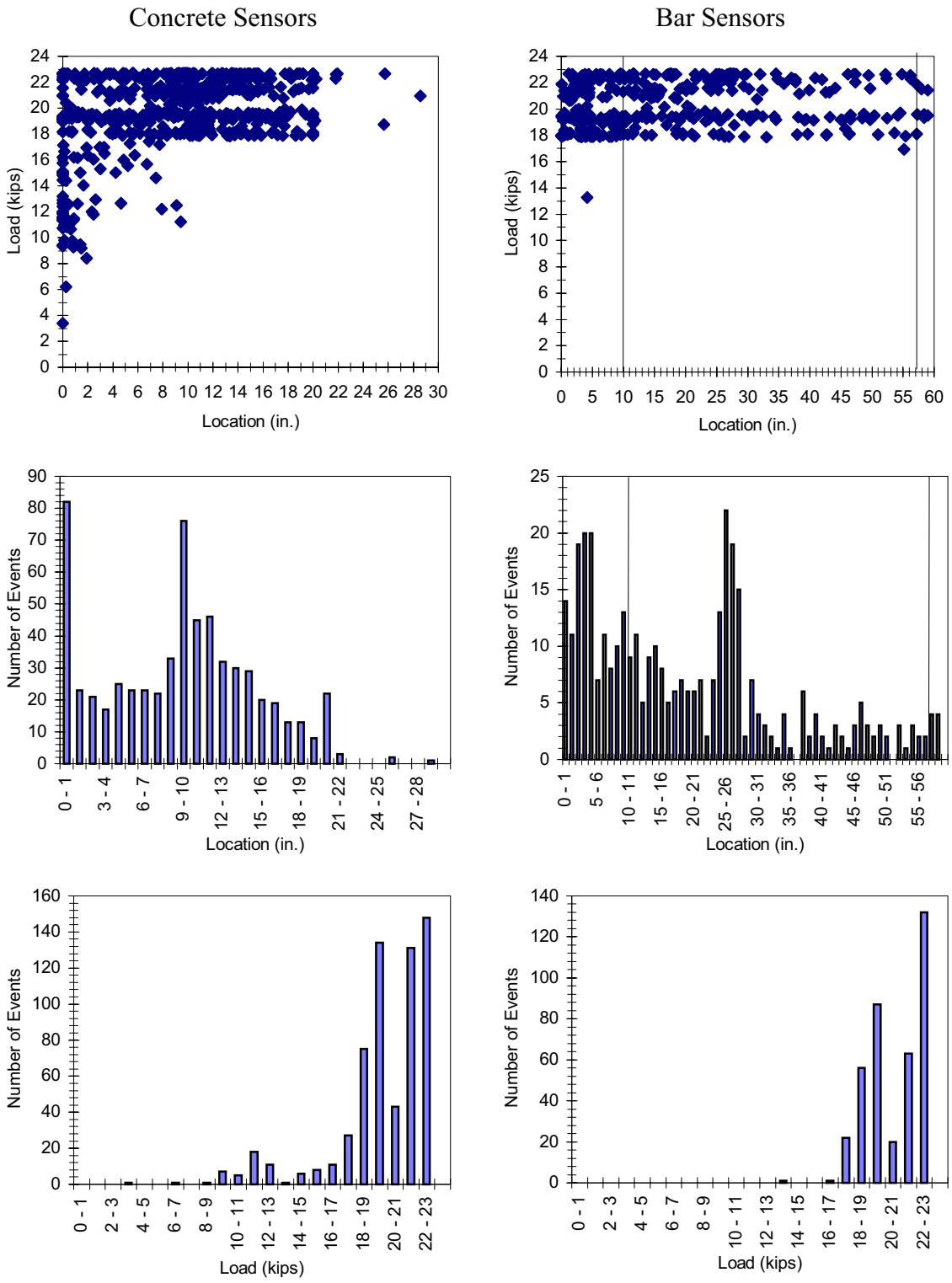

Figure F.24 1M1-5-2-47.0-6

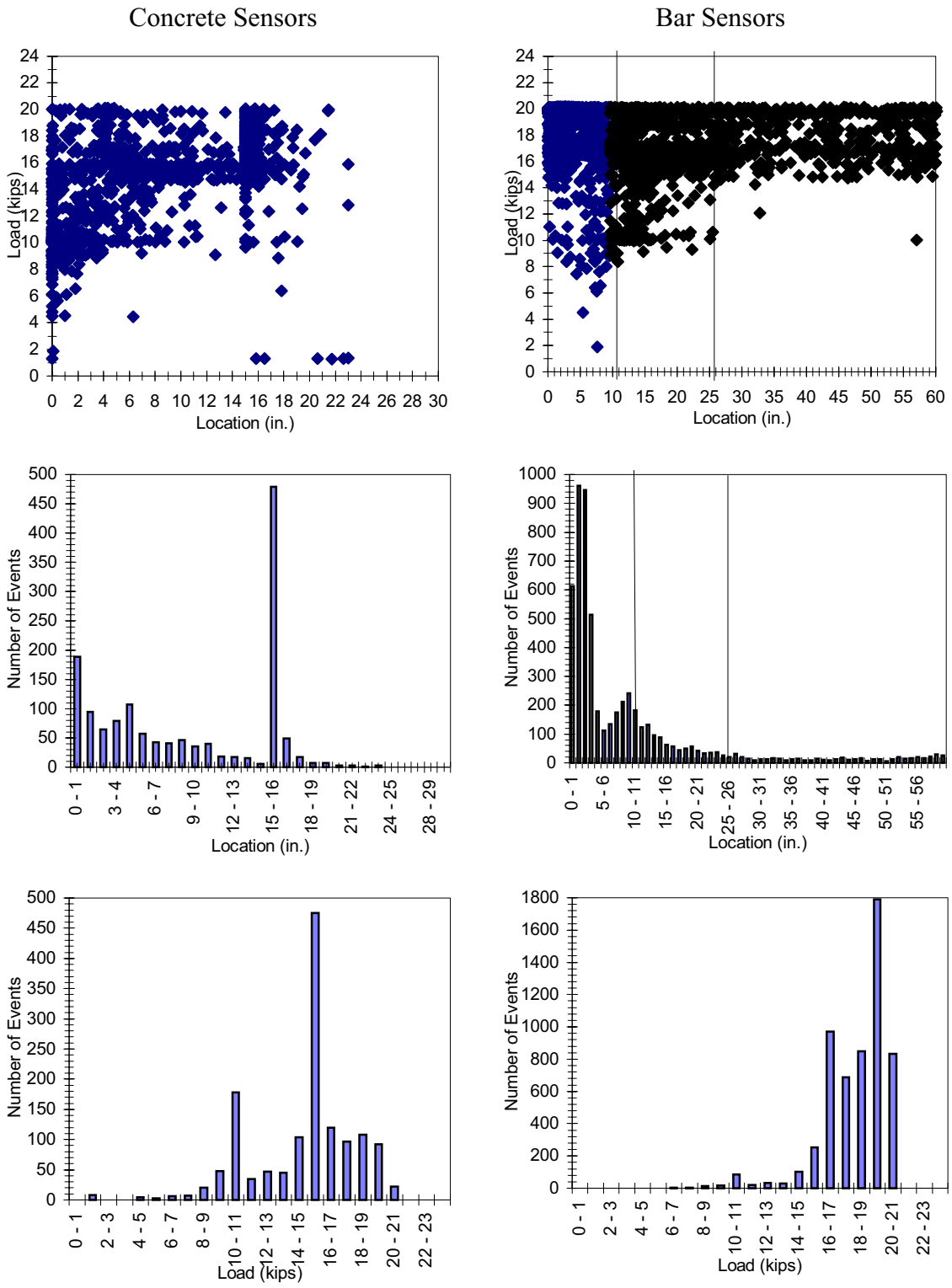

Figure F.25 1M1-5-2-15.0-1

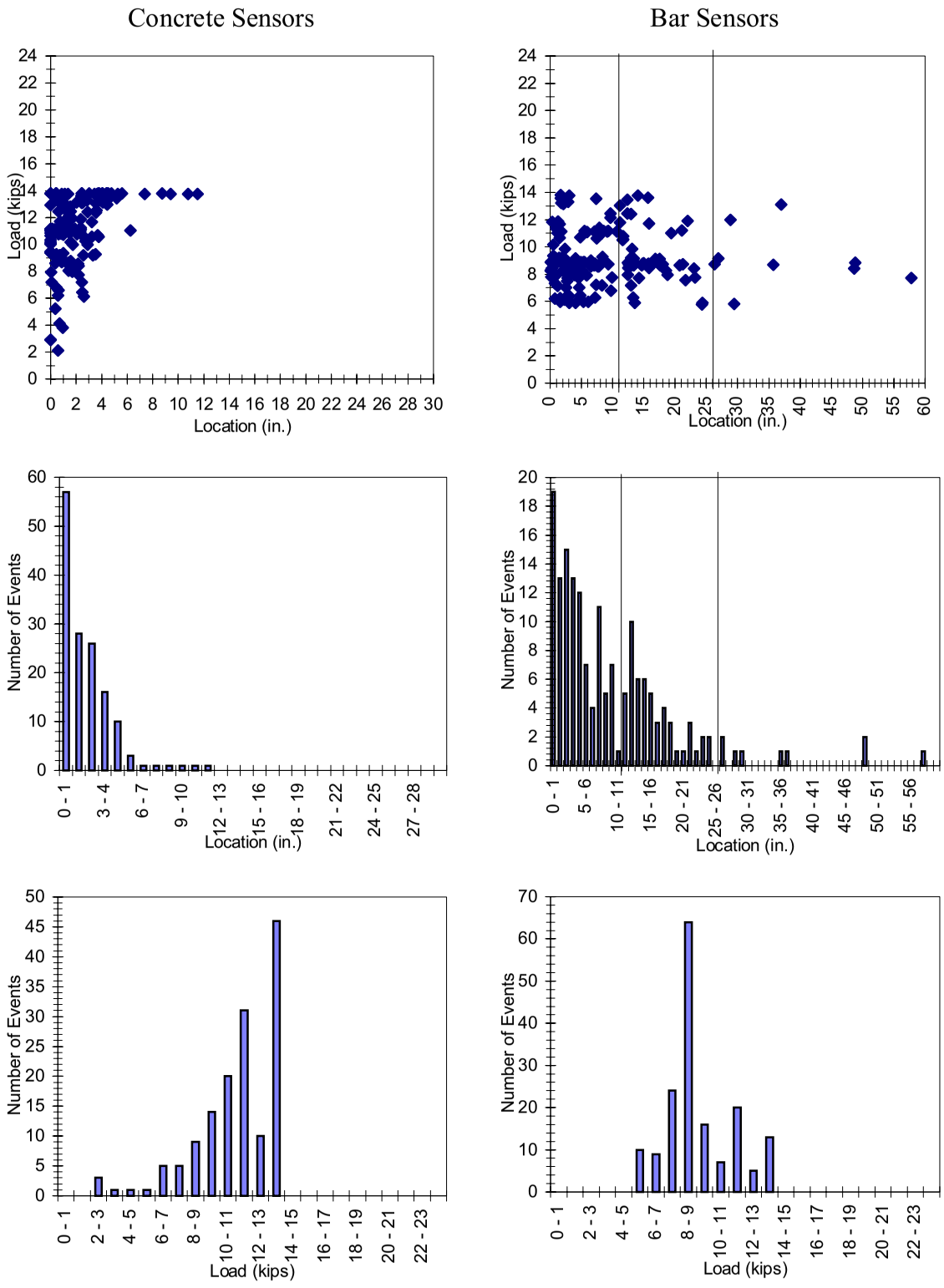

Figure F.26 1M1-5-2-15.0-2

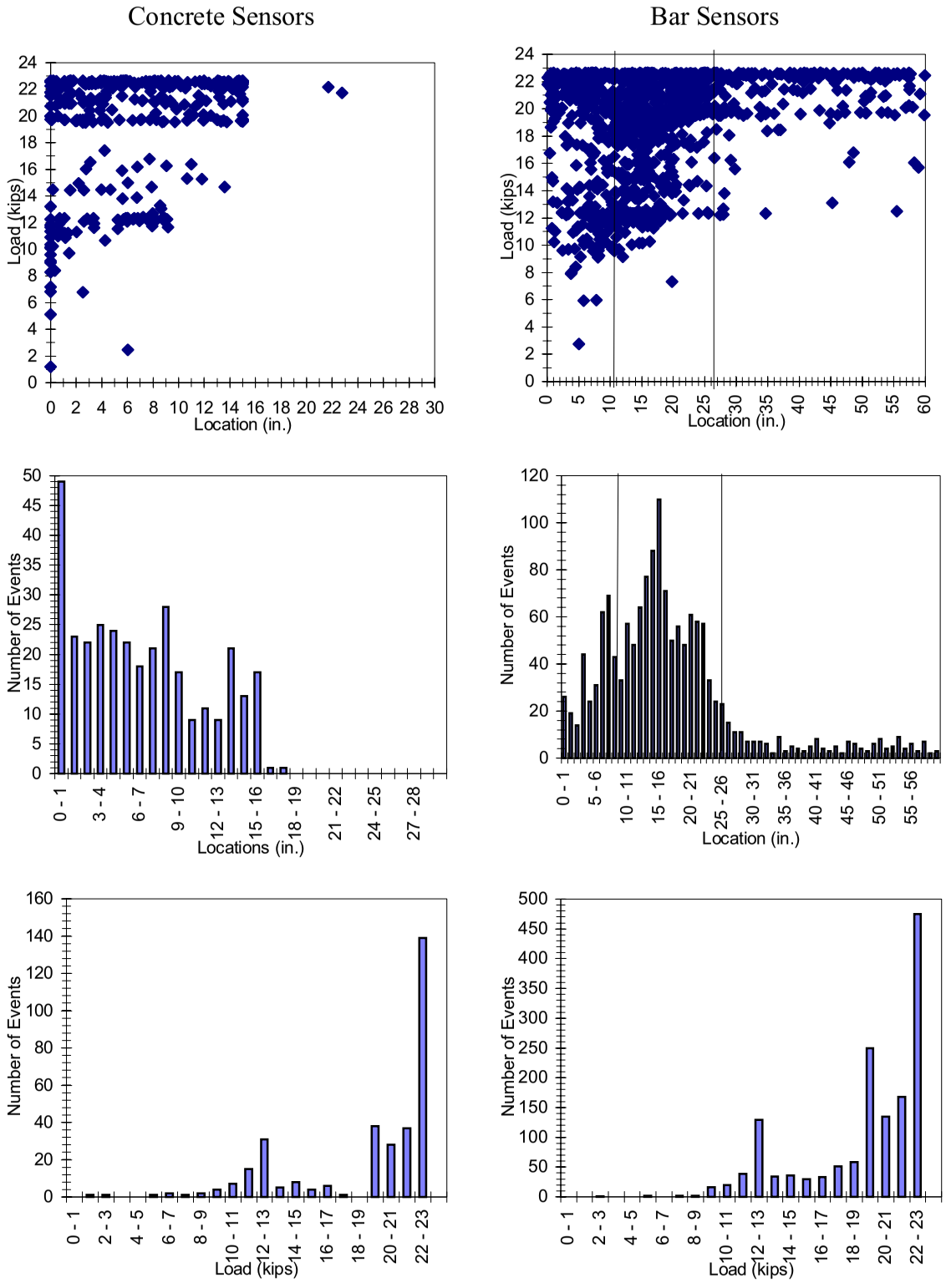

Figure F.27 1M1-5-2-15.0-3

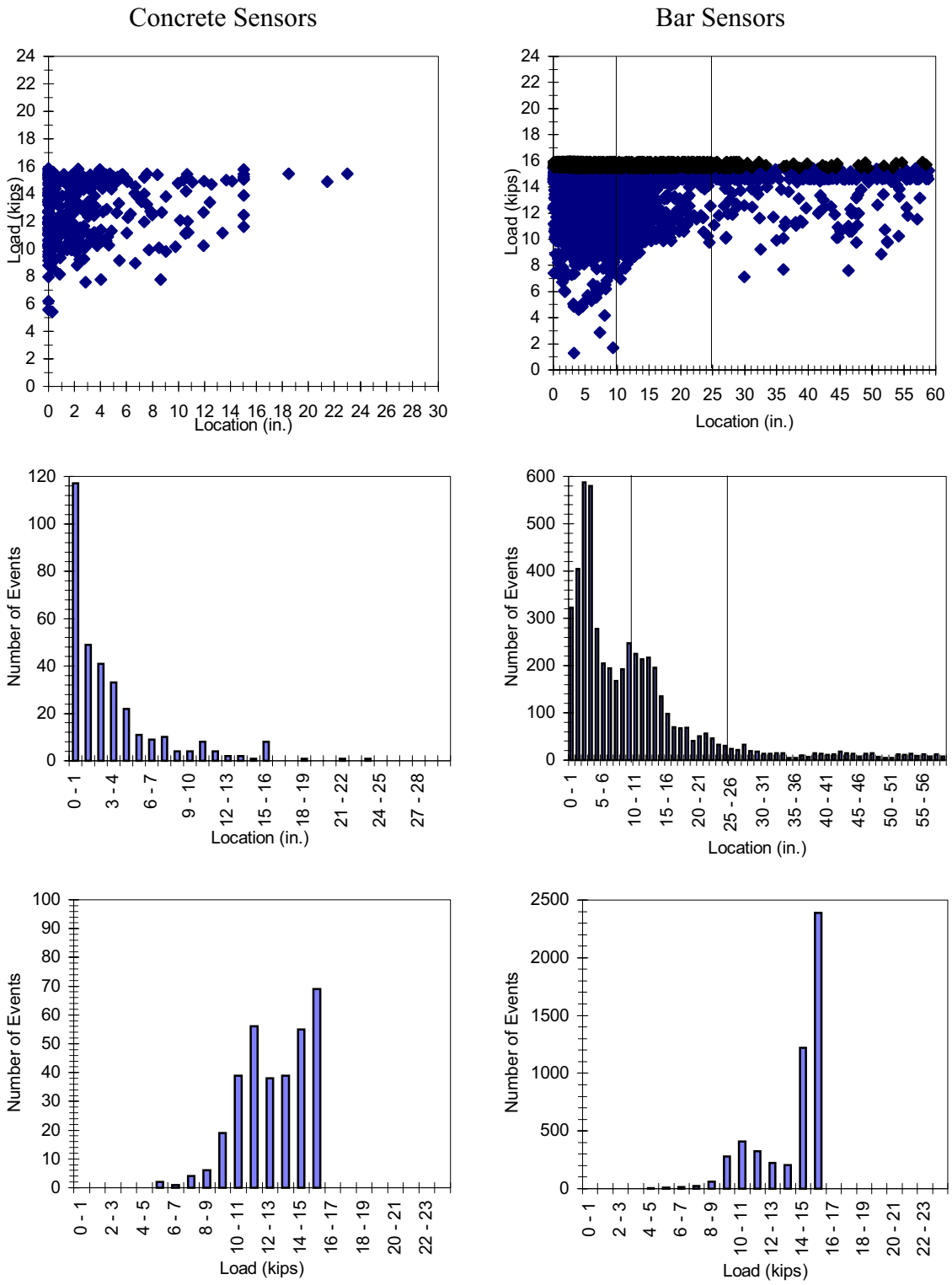

Figure F.28 1M1-5-2-15.0-4

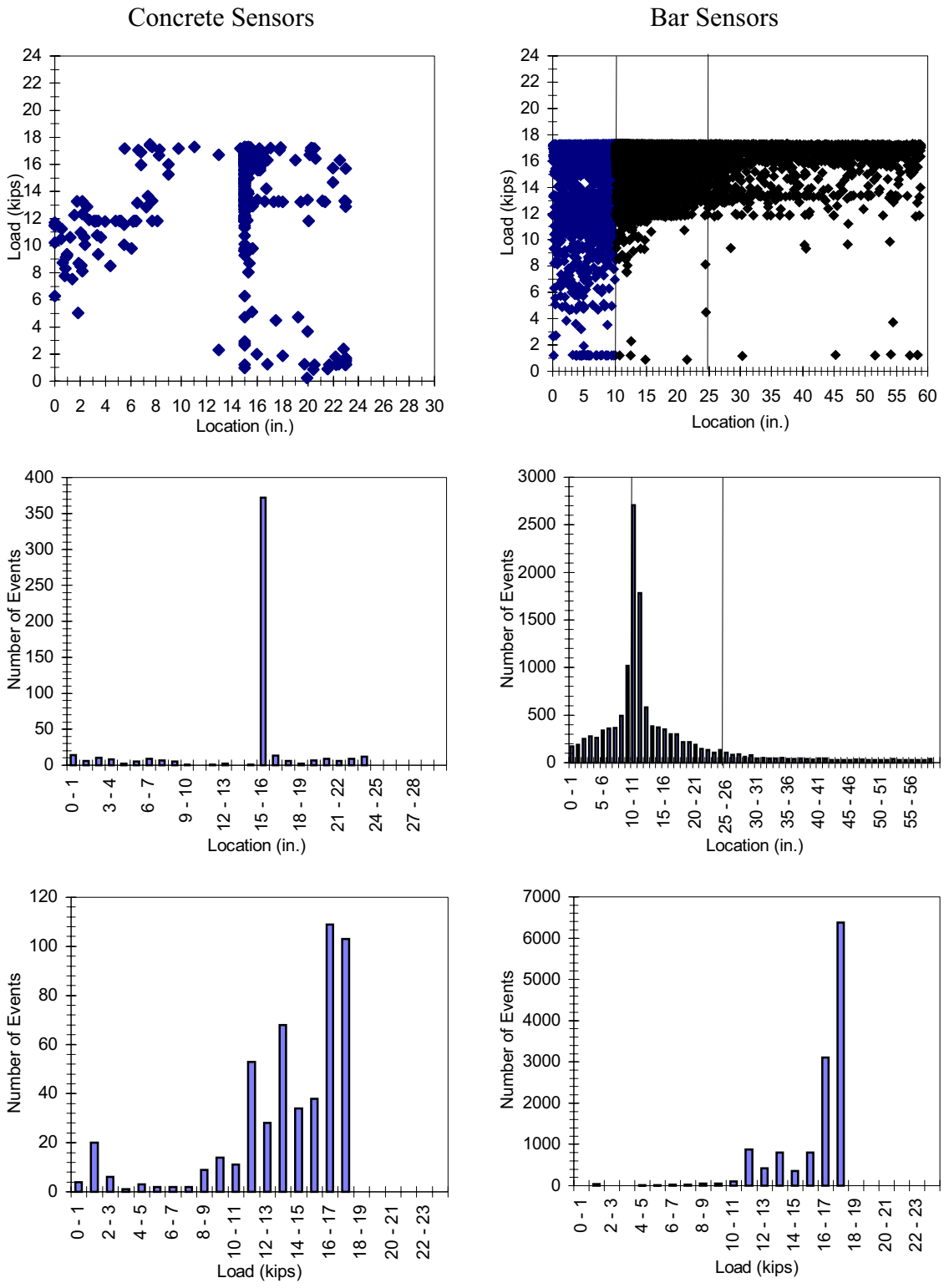

Figure F.29 1M1-5-2-15.0-5

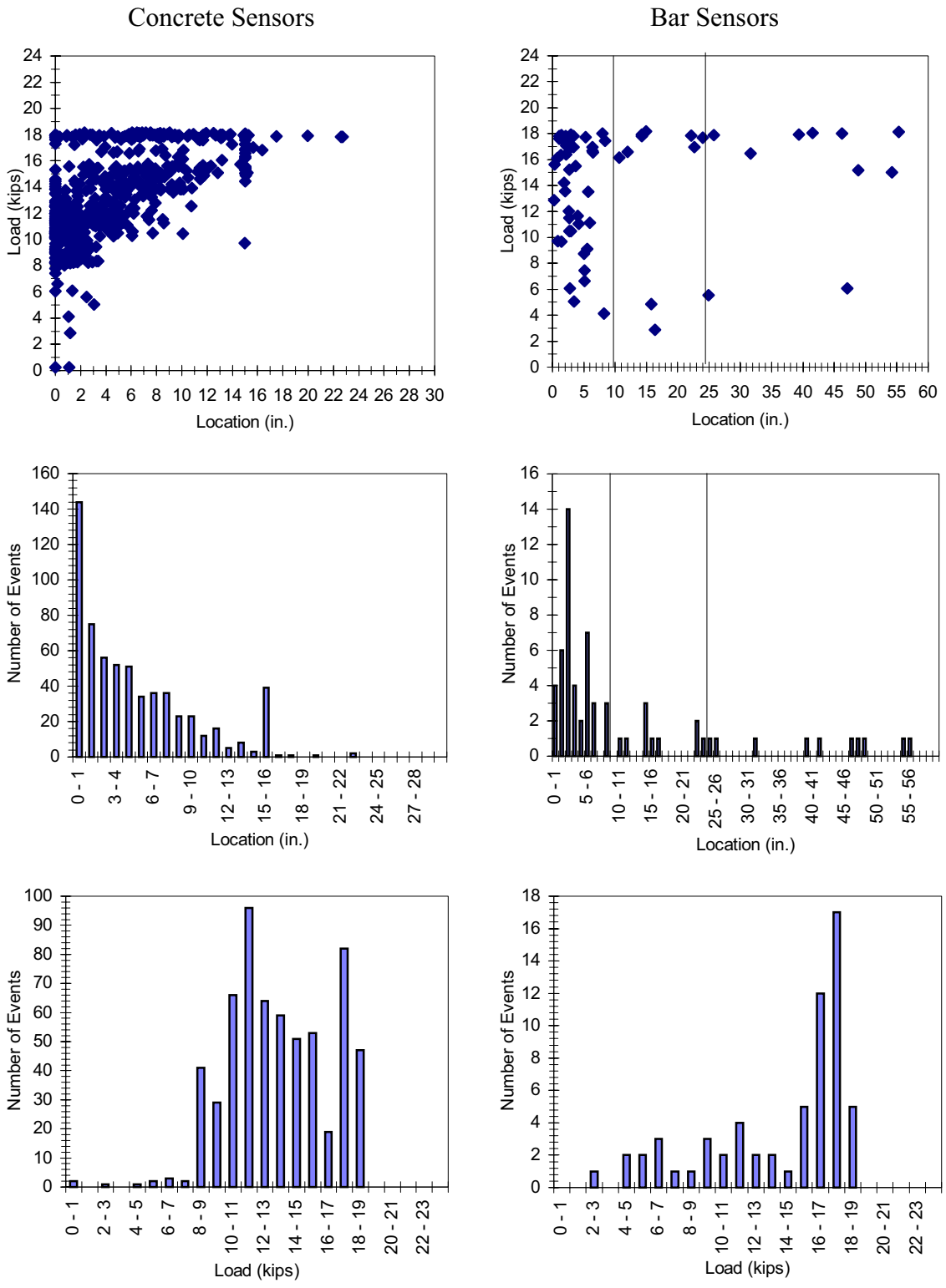

Figure F.30 1M1-5-2-15.0-6

Concrete Sensors

Bar Sensors

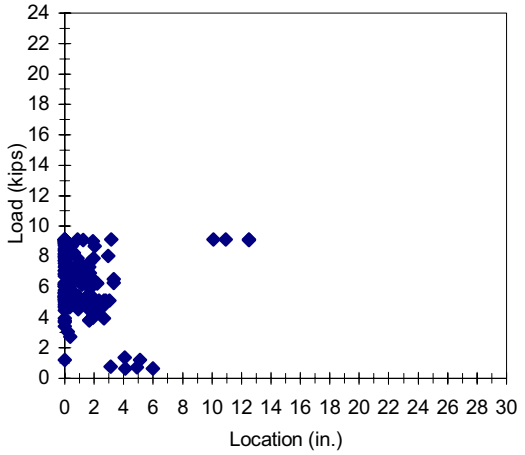

no bar AE data recorded

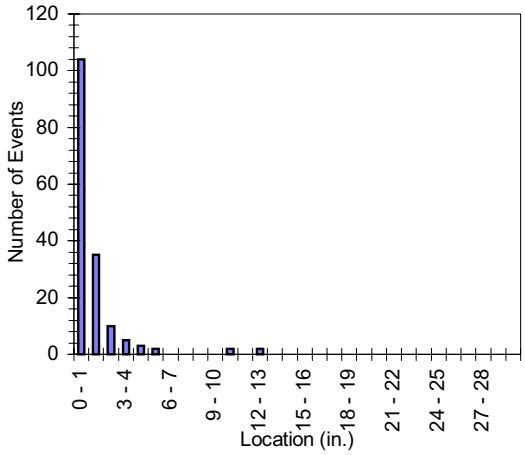

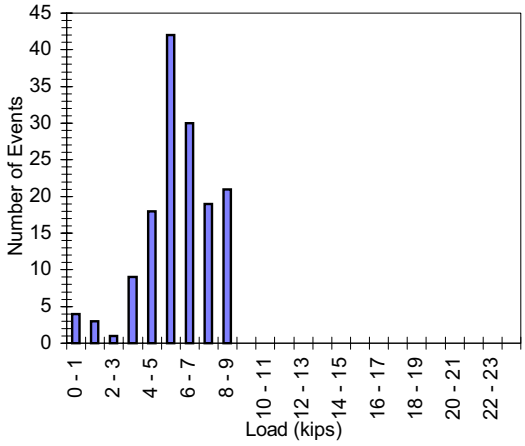

Figure F.31 1M1-5-2-12.5-1

Concrete Sensors

Bar Sensors

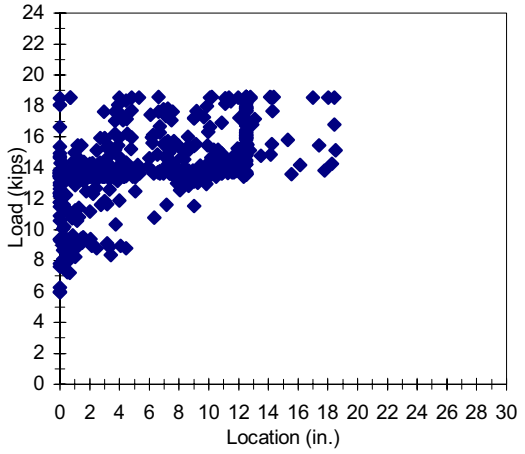

no bar AE data recorded

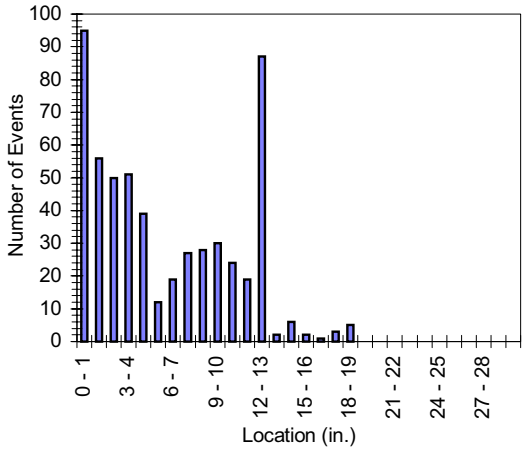

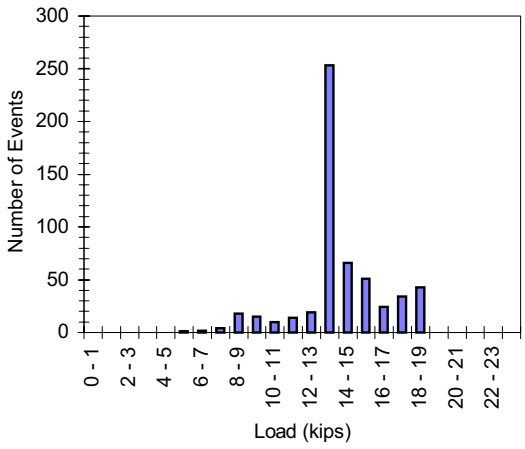

Figure F.32 1M1-5-2-12.5-2

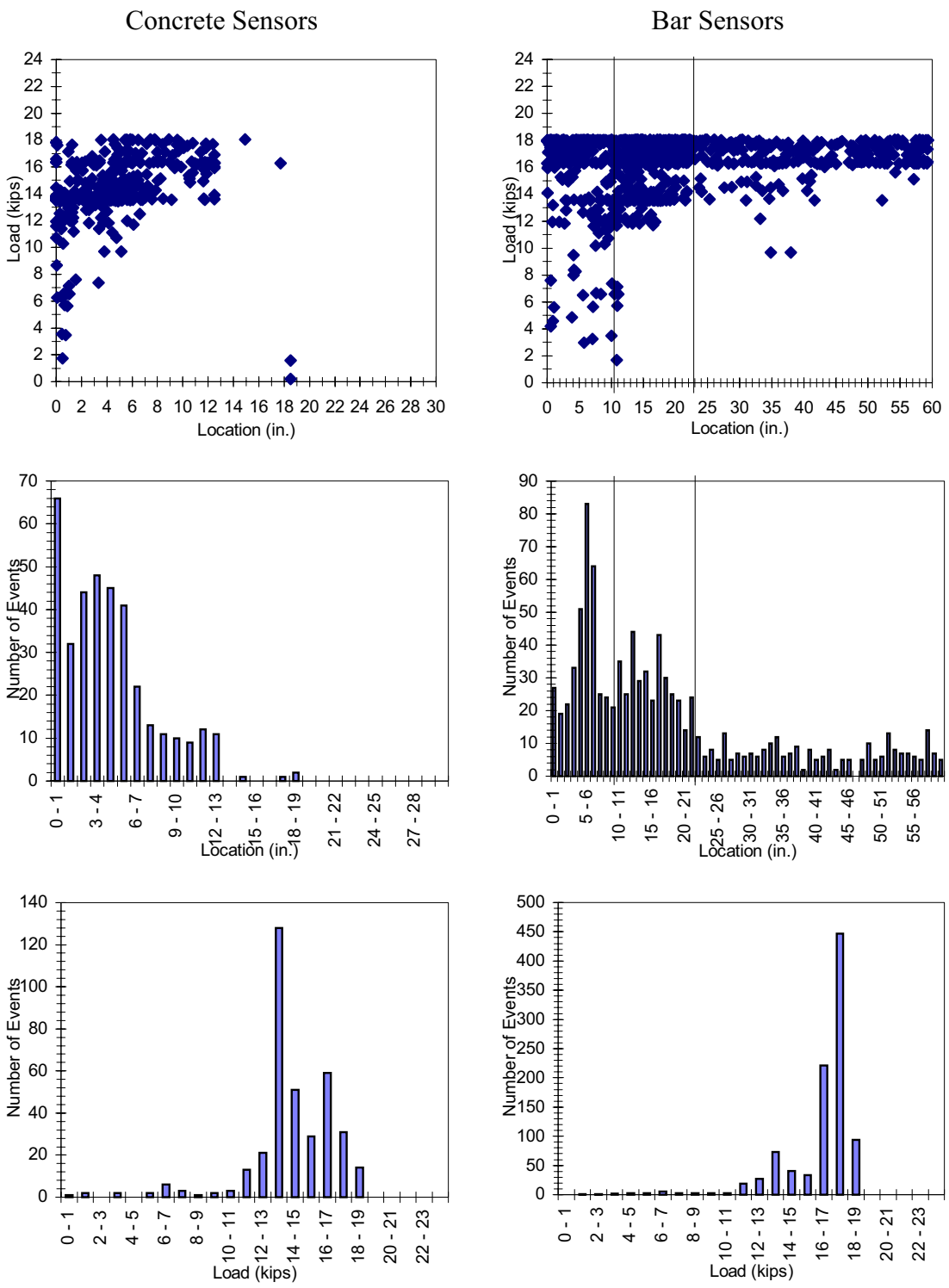

Figure F.33 1M1-5-2-12.5-3

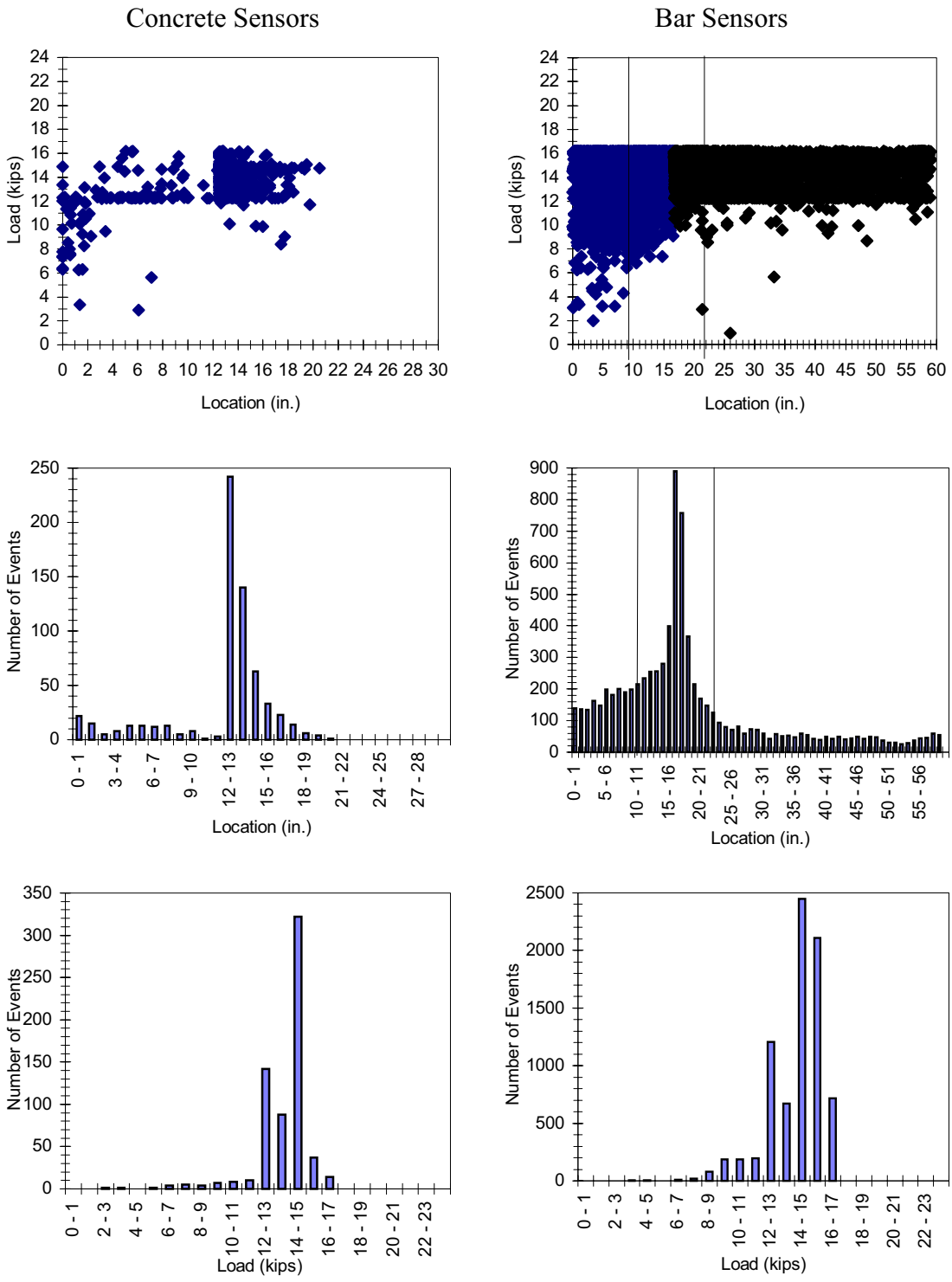

Figure F.34 1M1-5-2-12.5-4

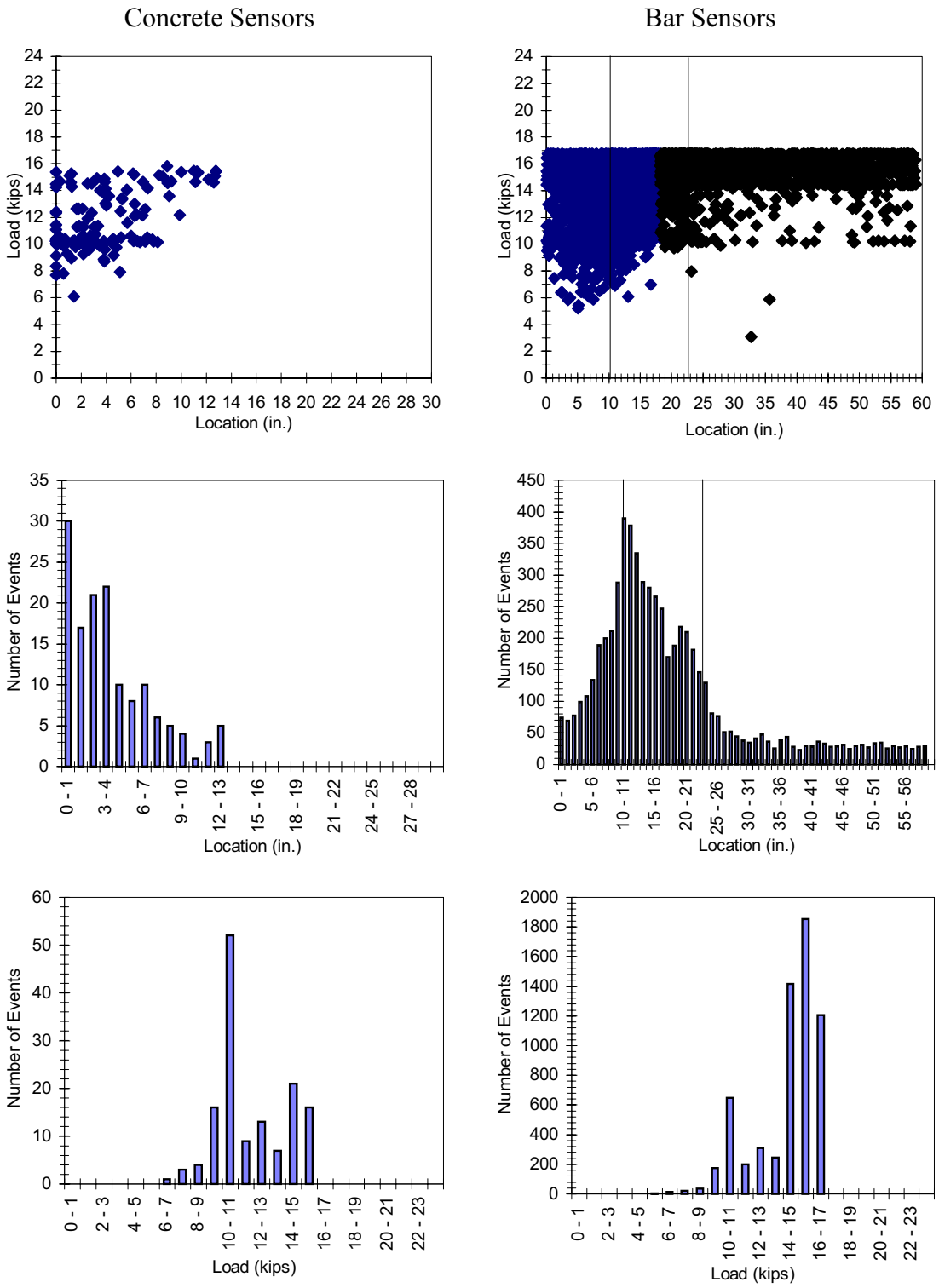

Figure F.35 1M1-5-2-12.5-5

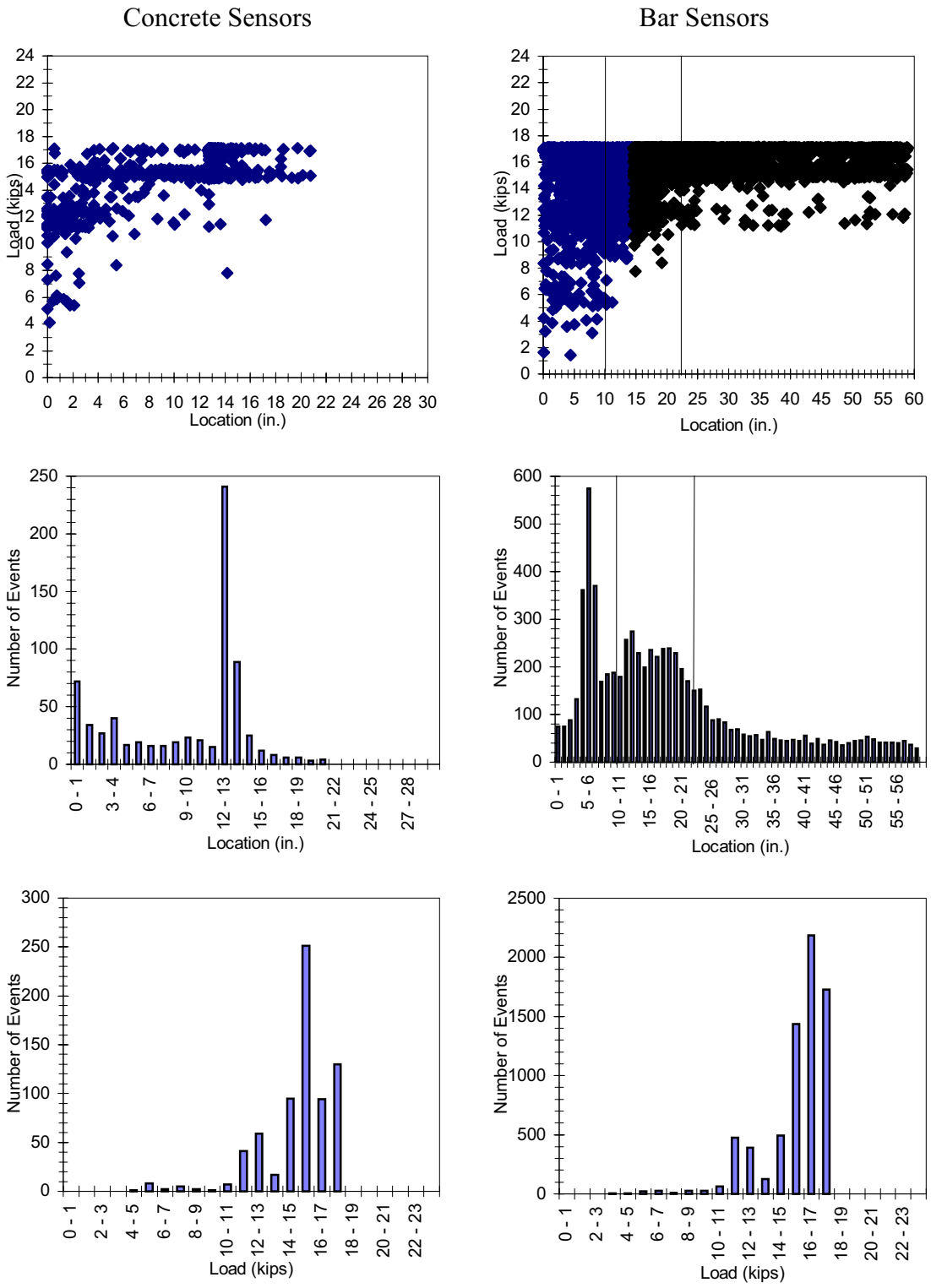

Figure F.36 1M1-5-2-12.5-6

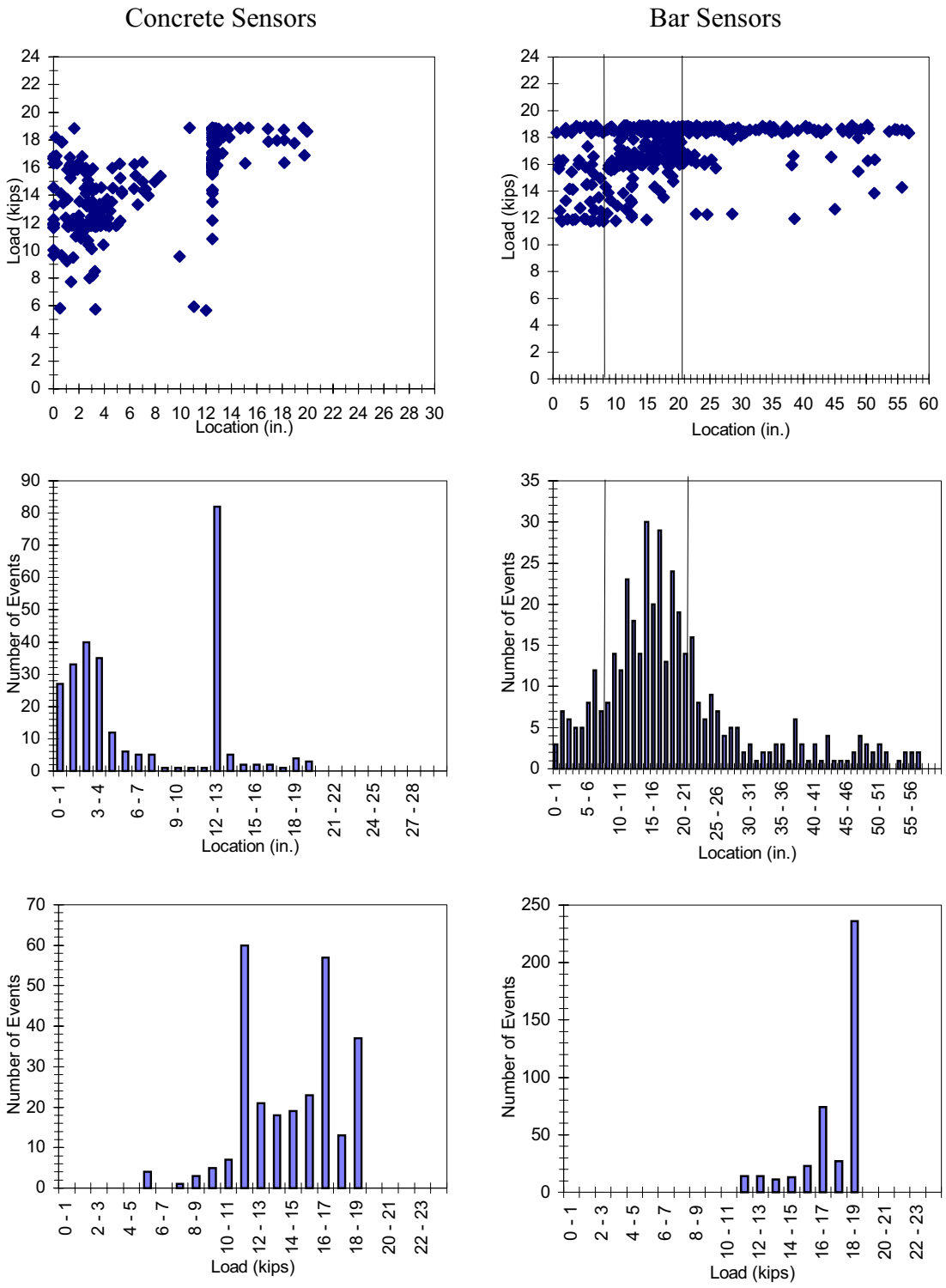

Figure F.37 2M1-5-2-12.5-1

Concrete Sensors

Bar Sensors

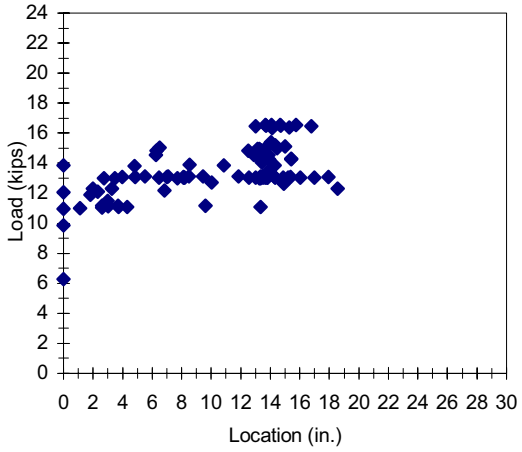

no bar AE data recorded

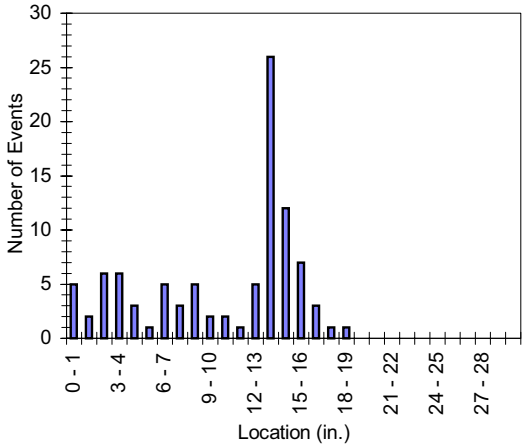

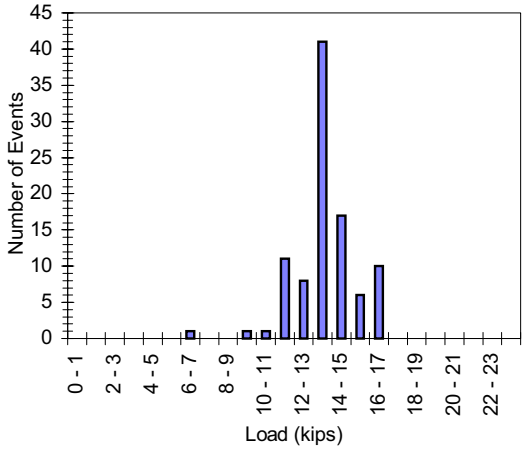

Figure F.38 2M1-5-2-12.5-2

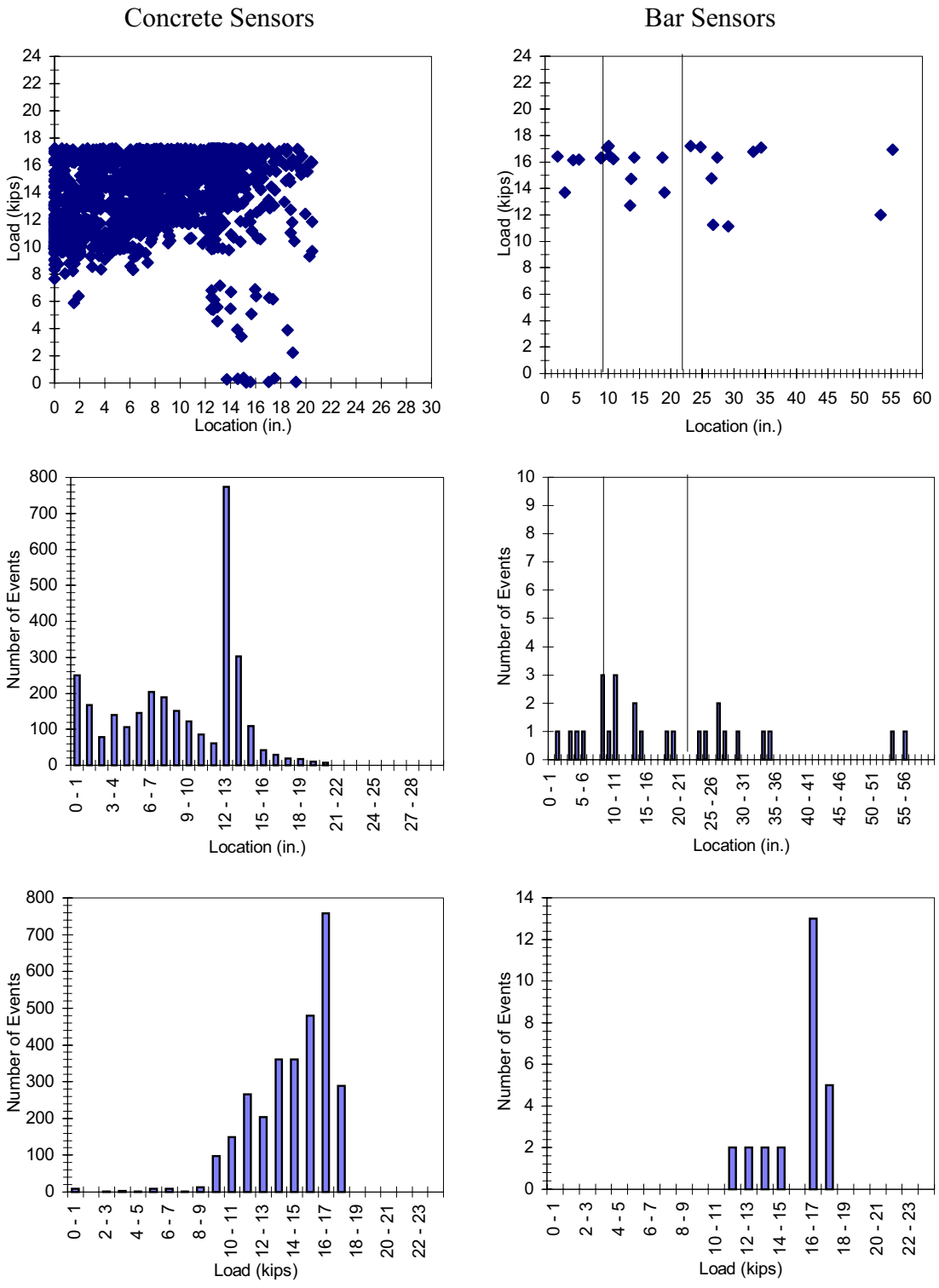

Figure F.39 2M1-5-2-12.5-3

Concrete Sensors

Bar Sensors

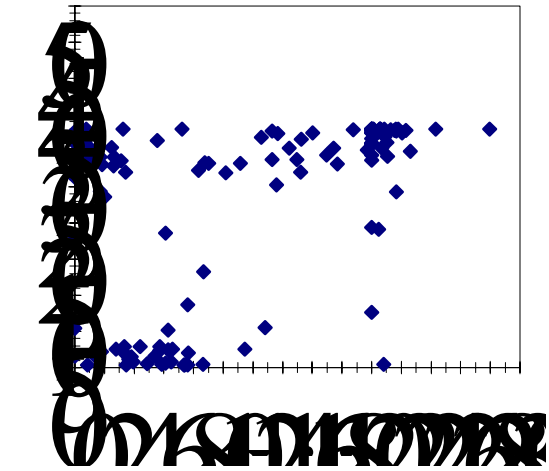

no bar AE data recorded

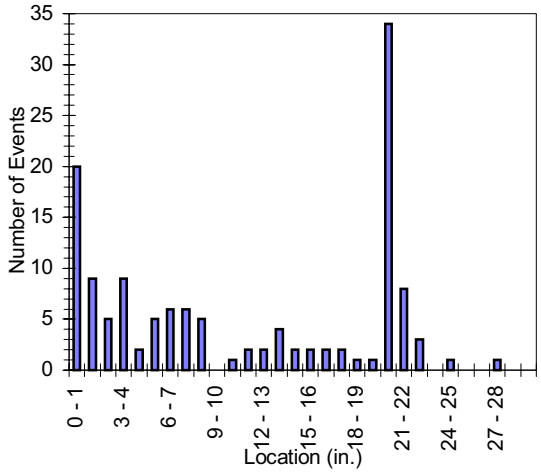

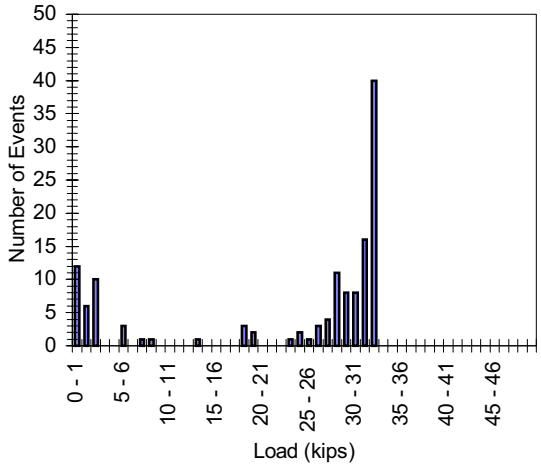

Figure F.40 2M2-6-3-20.0-1

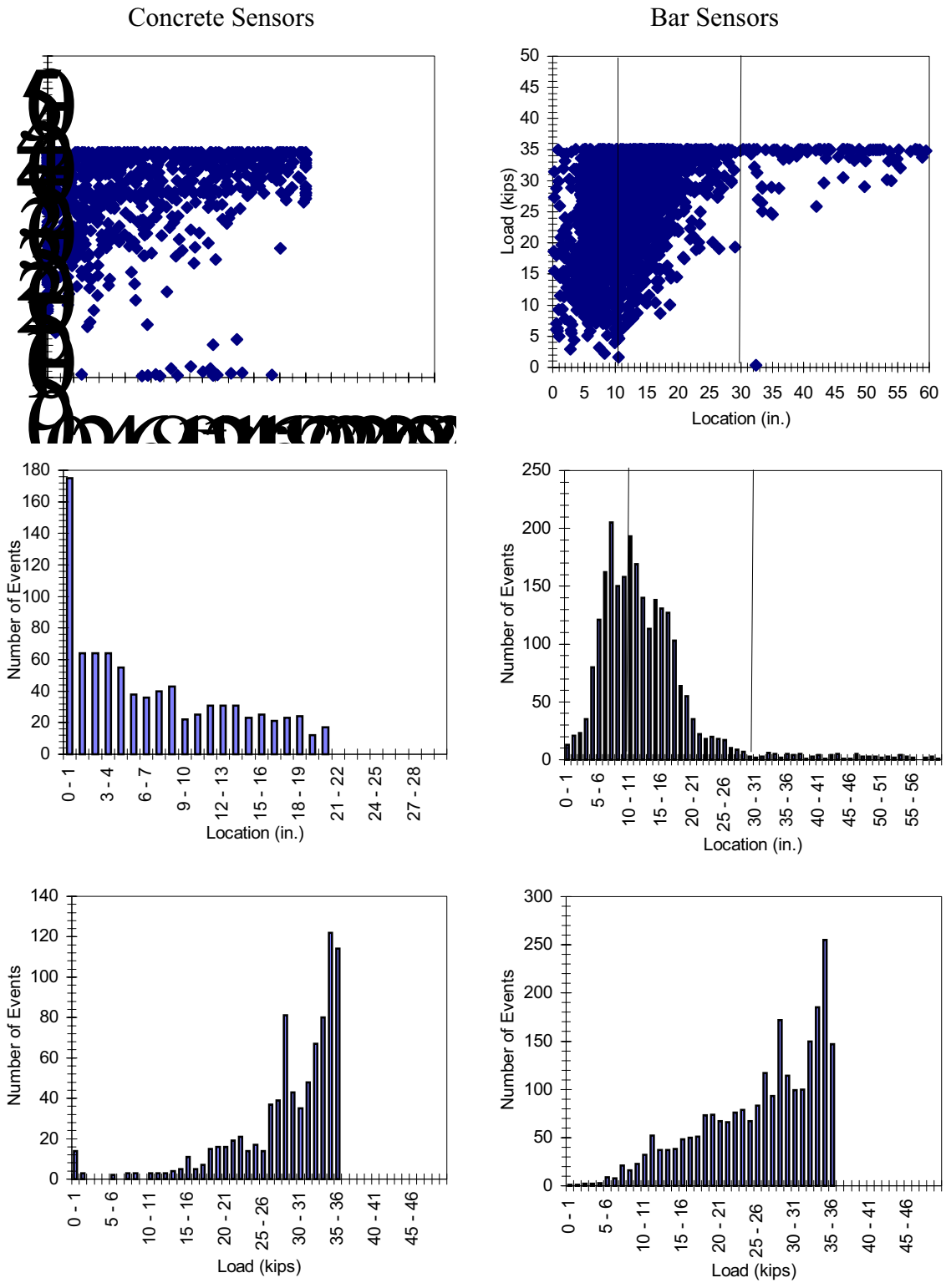

Figure F.41 2M2-6-3-20.0-2

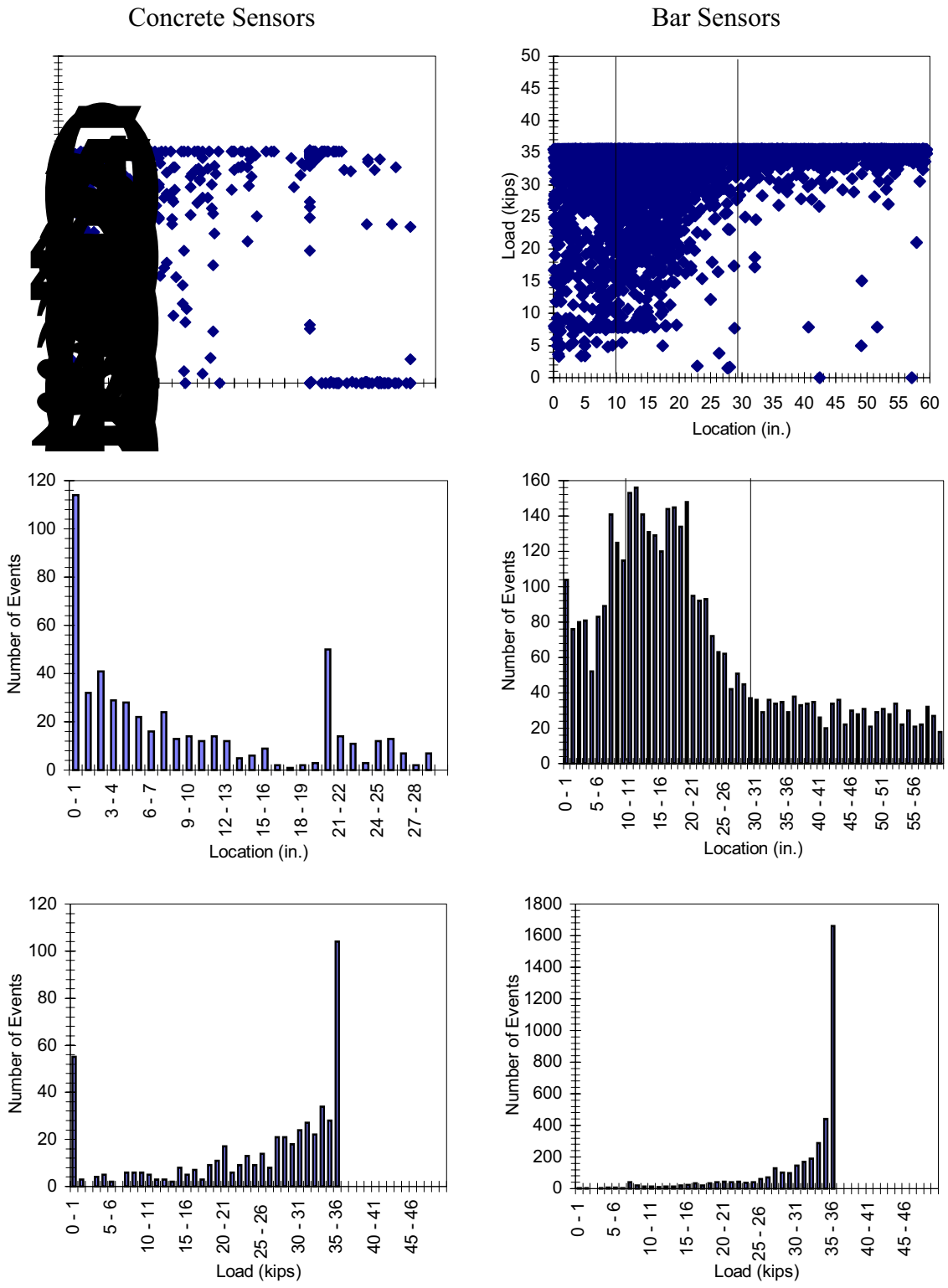

Figure F.42 2M2-6-3-20.0-3

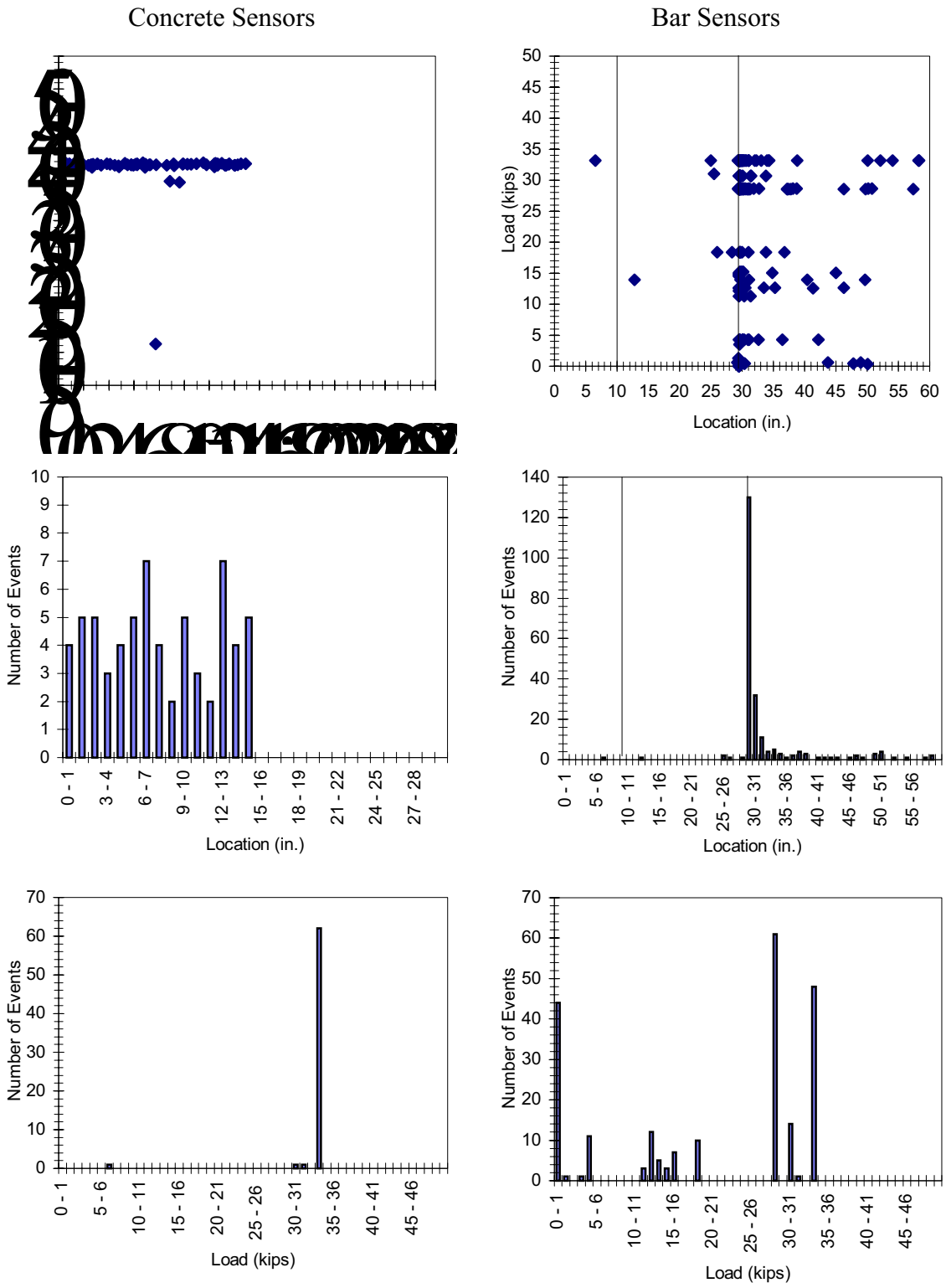

Figure F.43 2M2-6-3-20.0-4

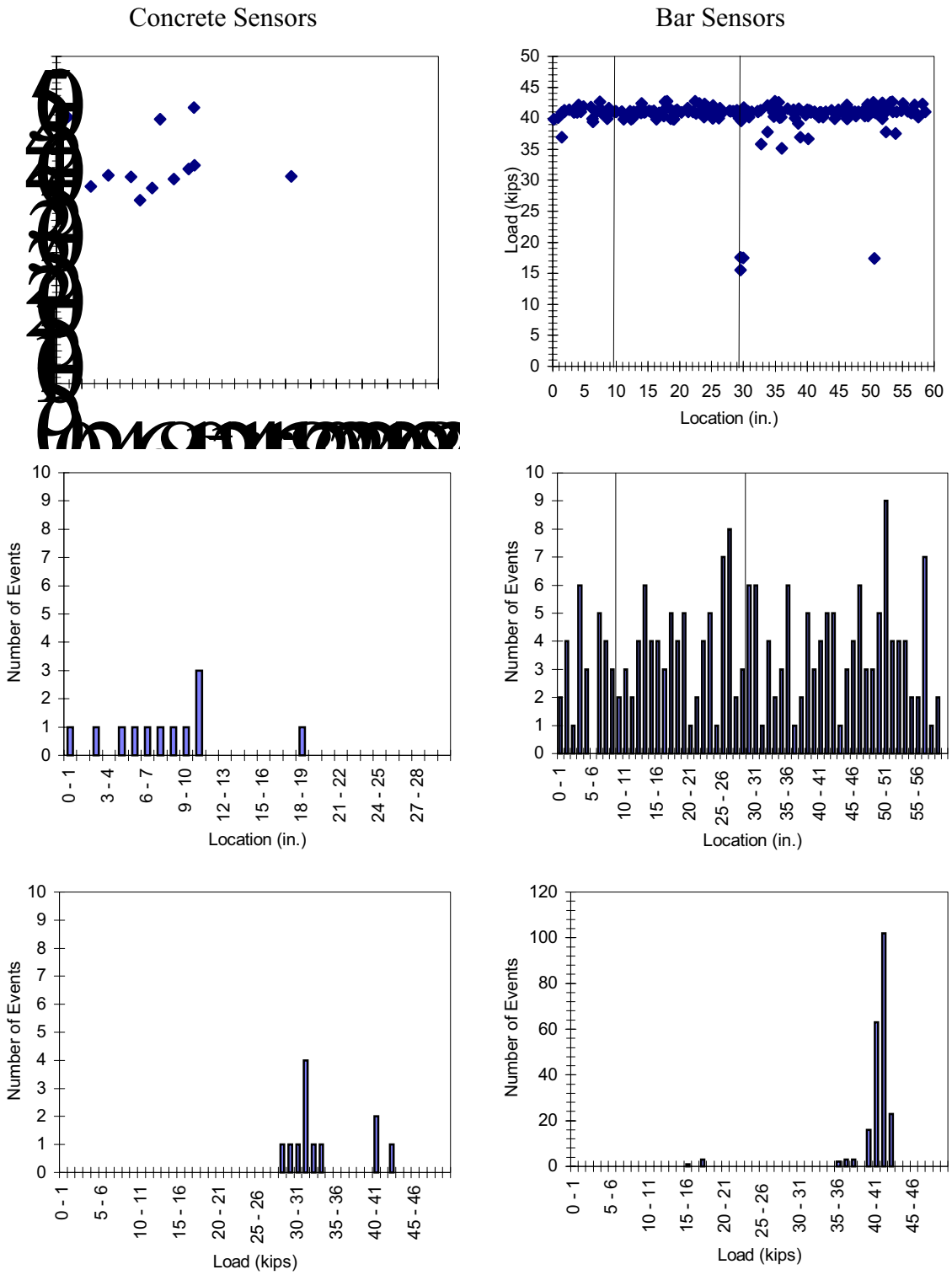

Figure F.44 2M2-6-3-20.0-5

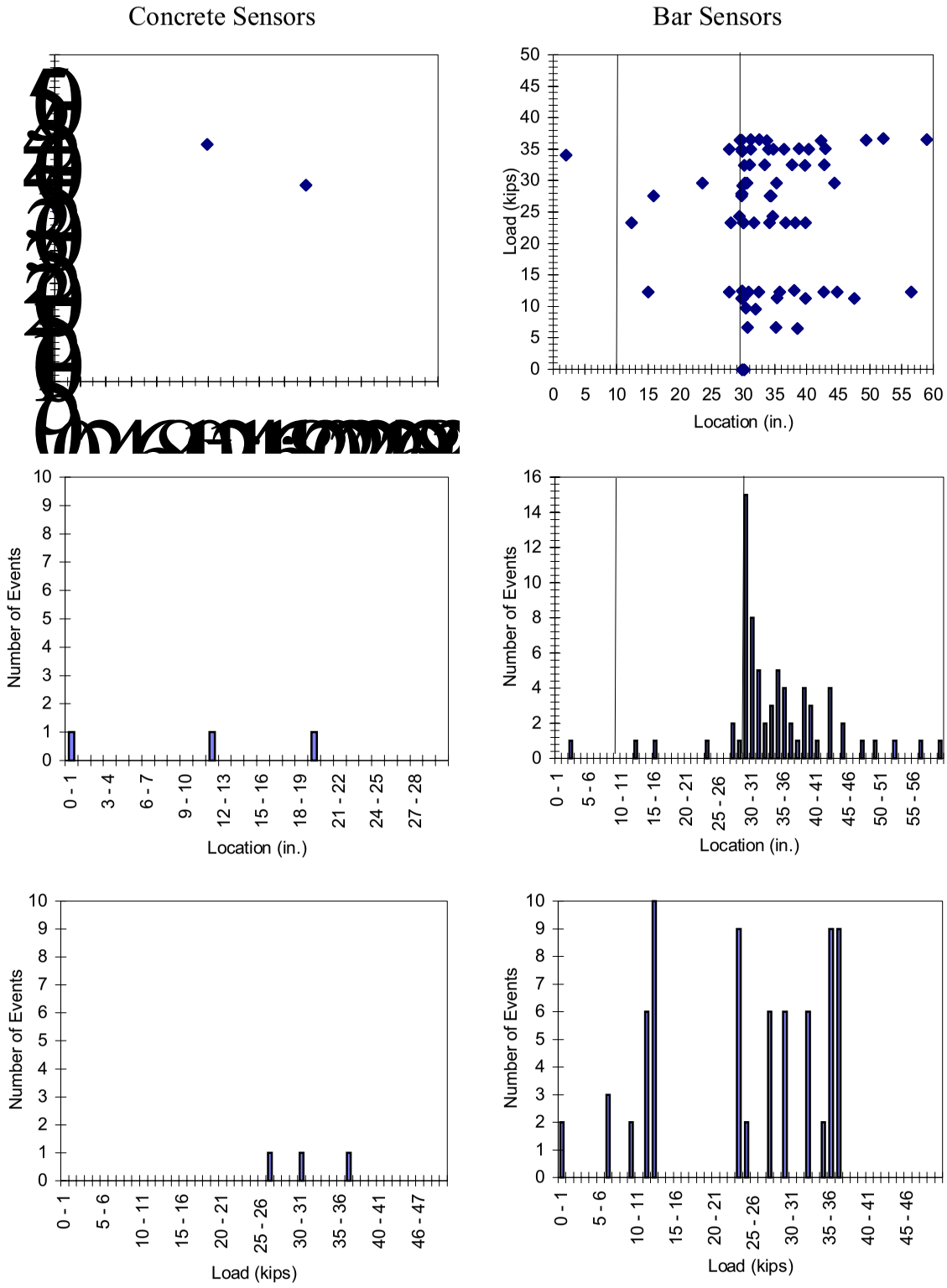

Figure F.45 2M2-6-3-20.0-6

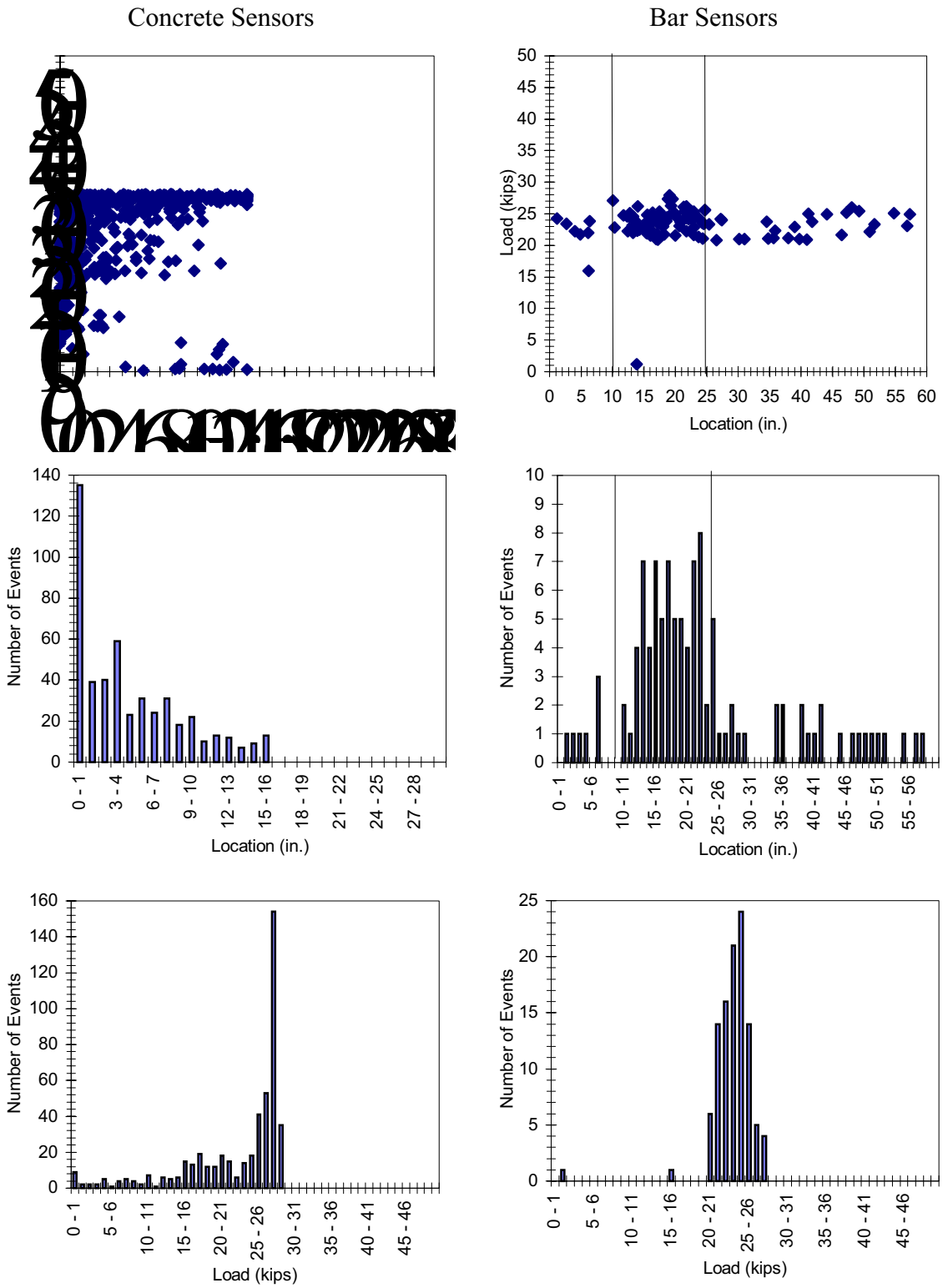

Figure F.46 2M2-6-3-15.0-1

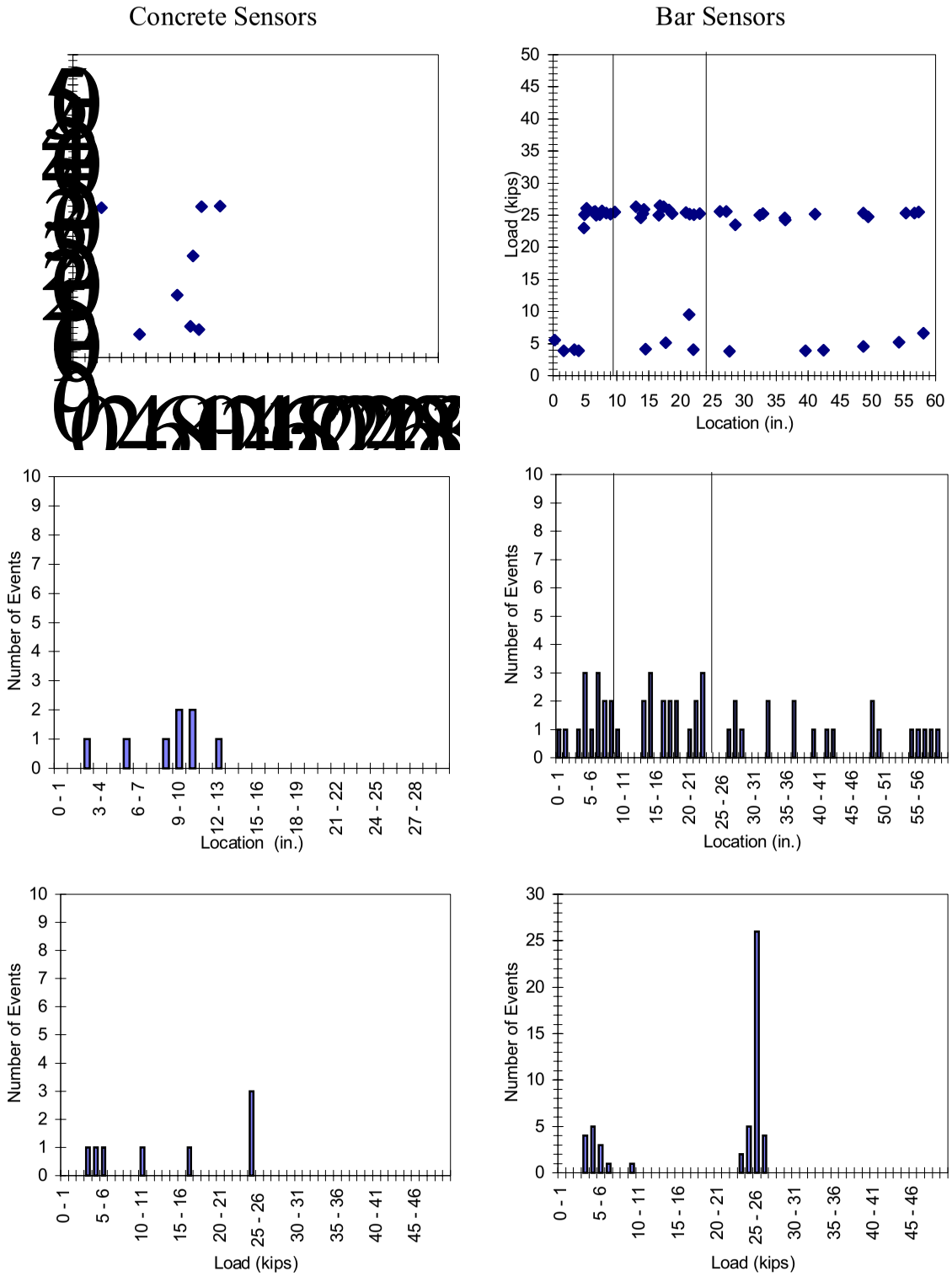

Figure F.47 2M2-6-3-15.0-2

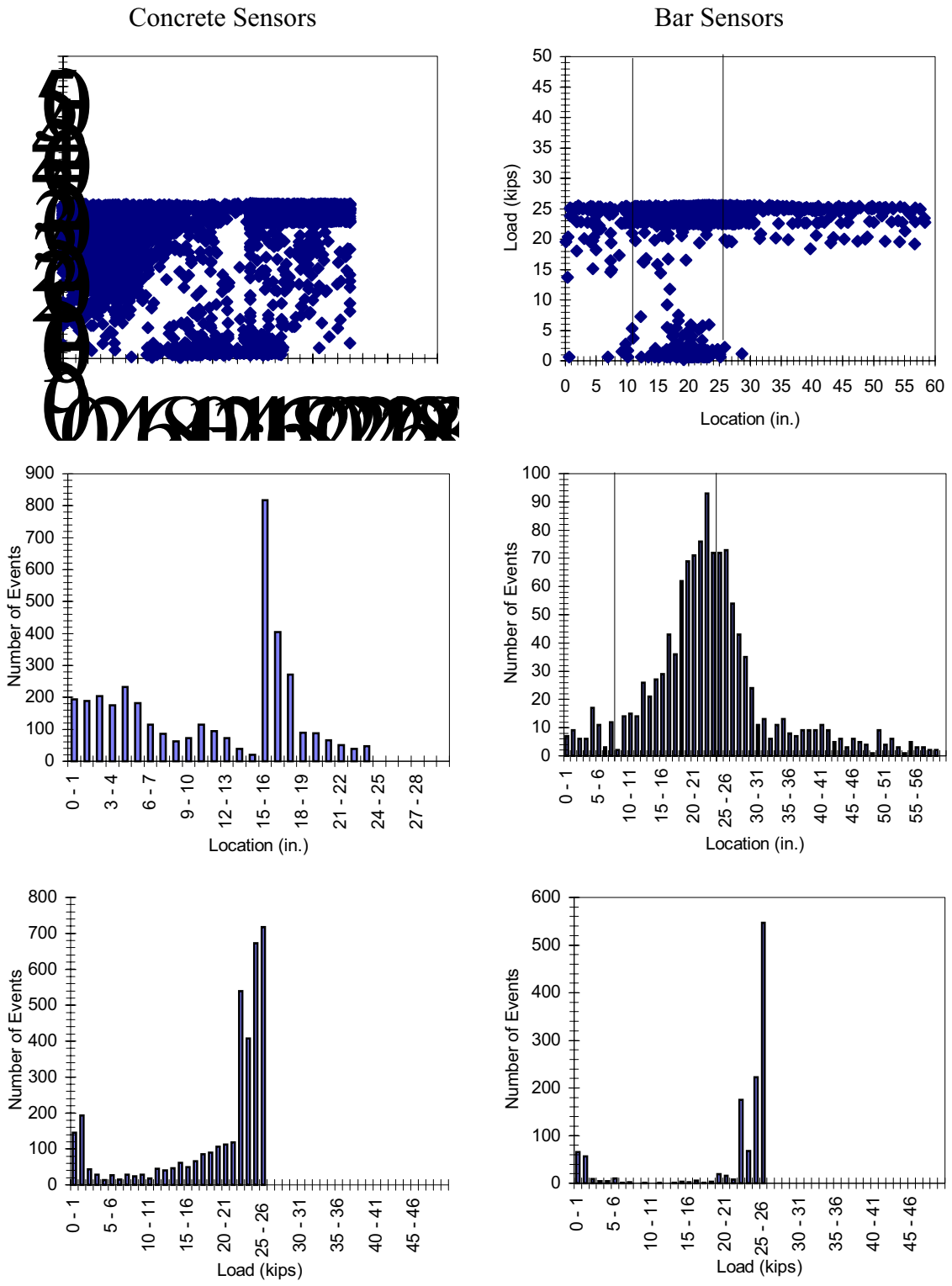

Figure F.48 2M2-6-3-15.0-3

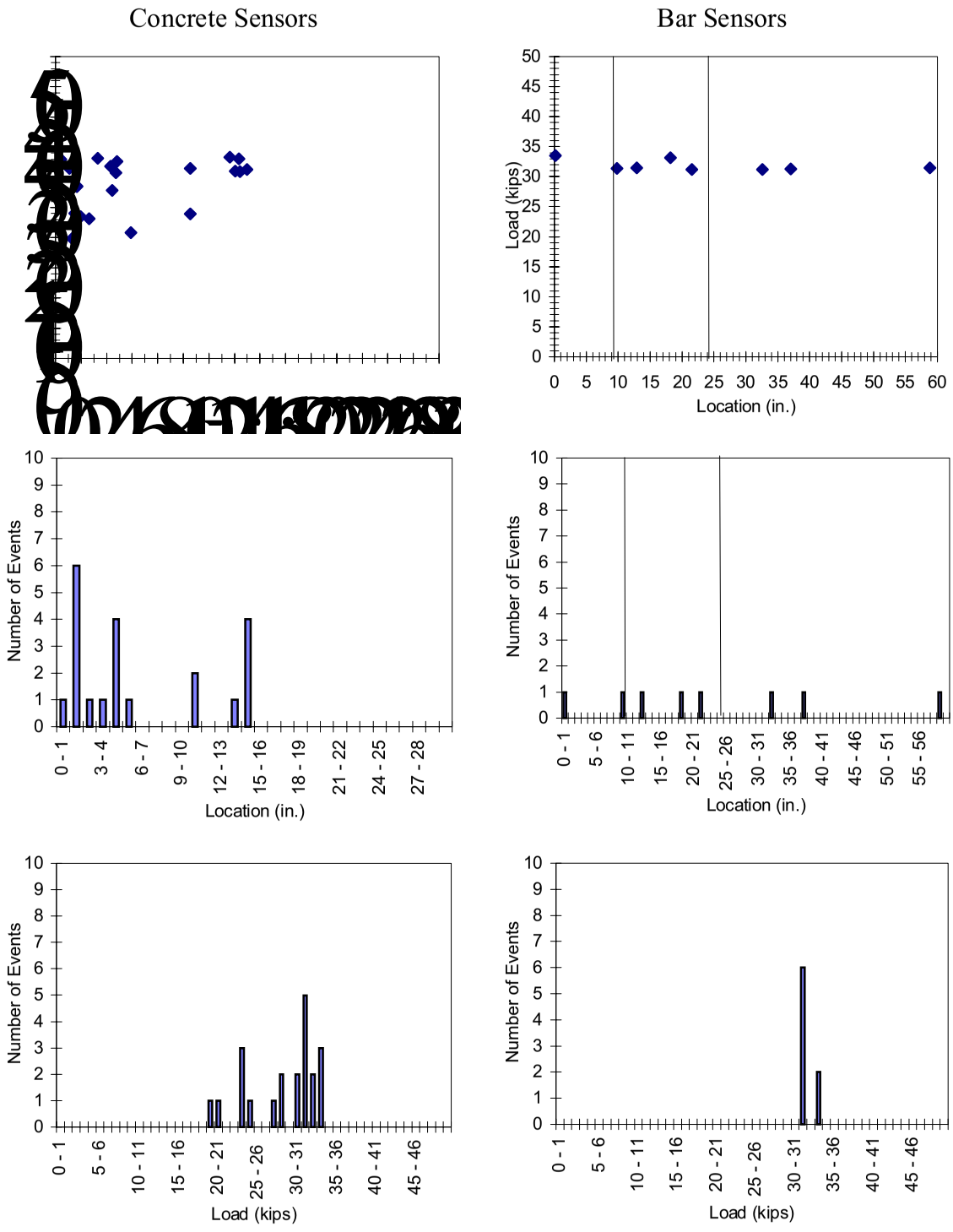

Figure F.49 2M2-6-3-15.0-4

Concrete Sensors

Bar Sensors

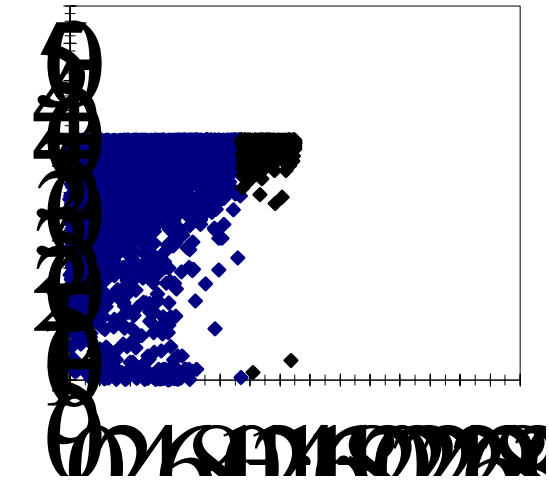

no bar AE data recorded

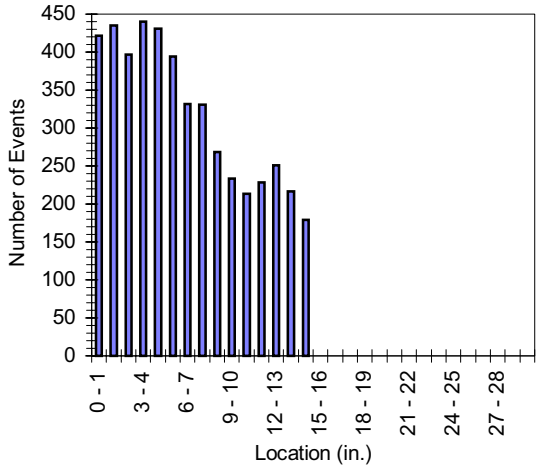

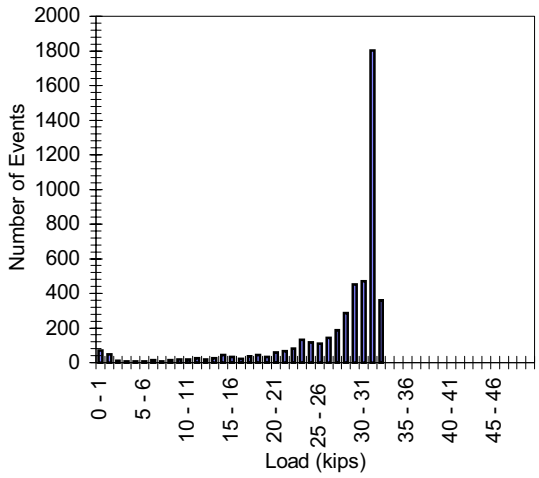

Figure F.50 2M2-6-3-15.0-5

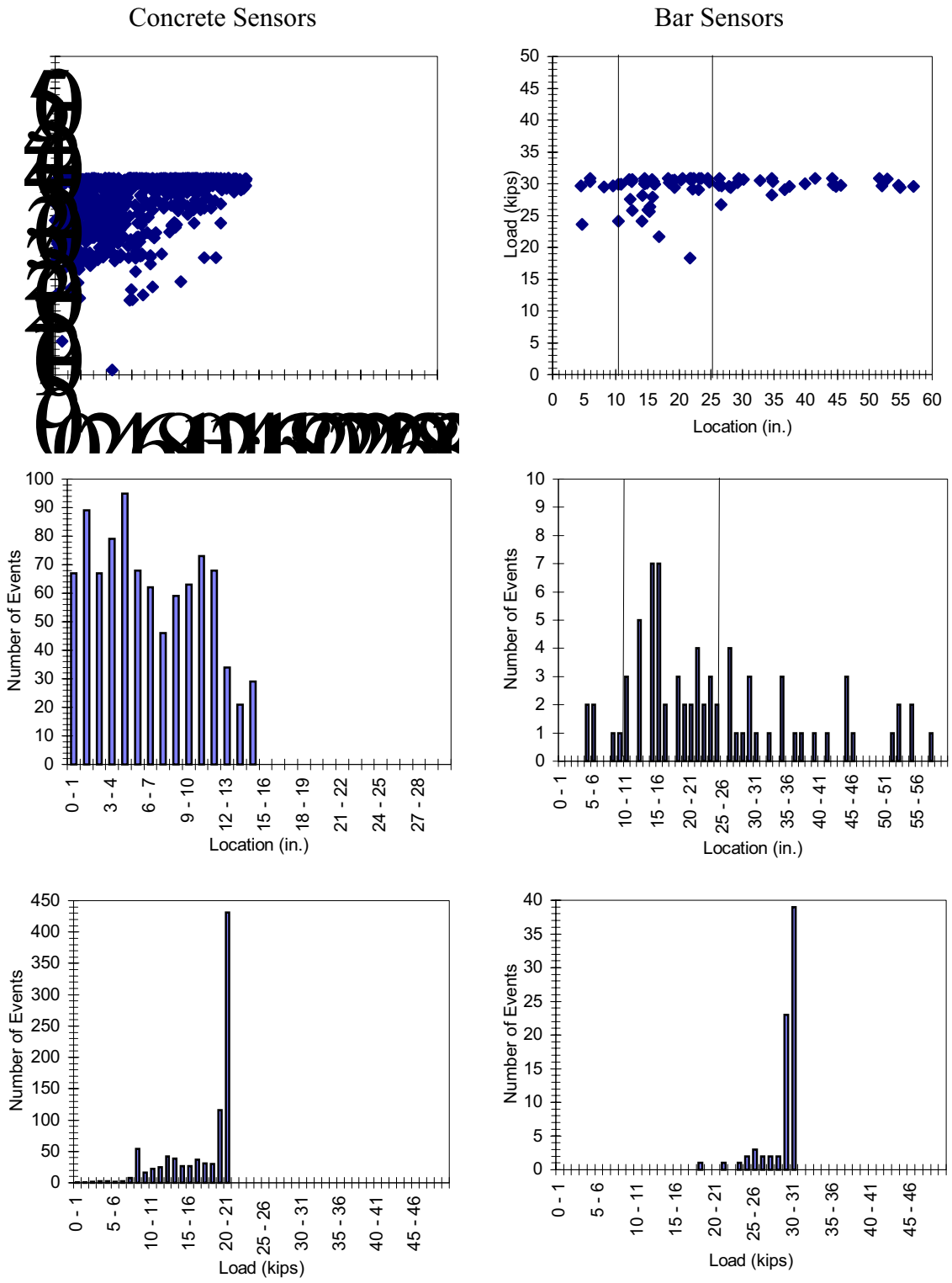

Figure F.51 2M2-6-3-15.0-6

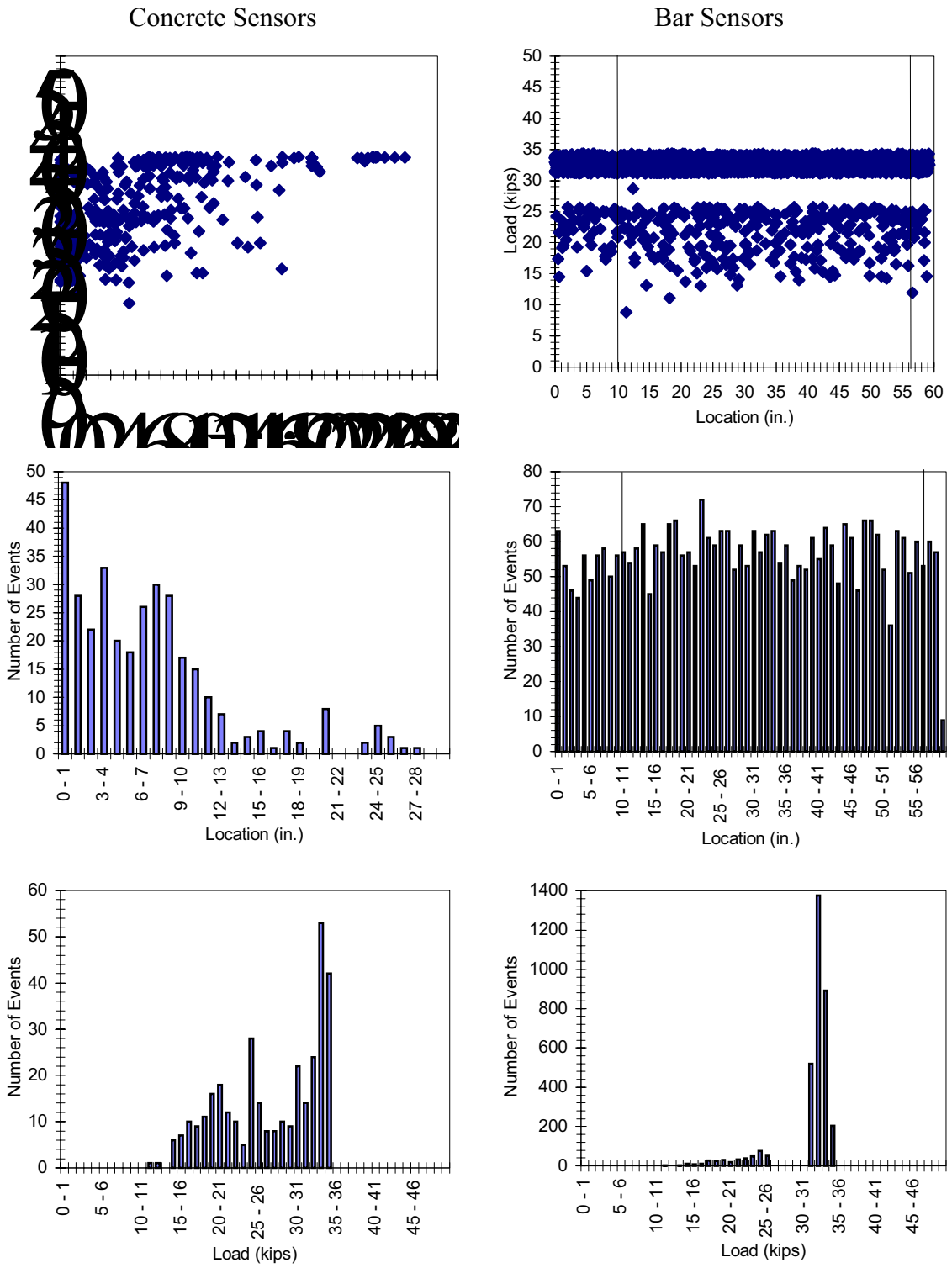

Figure F.52 2M2-6-2-47.0-1

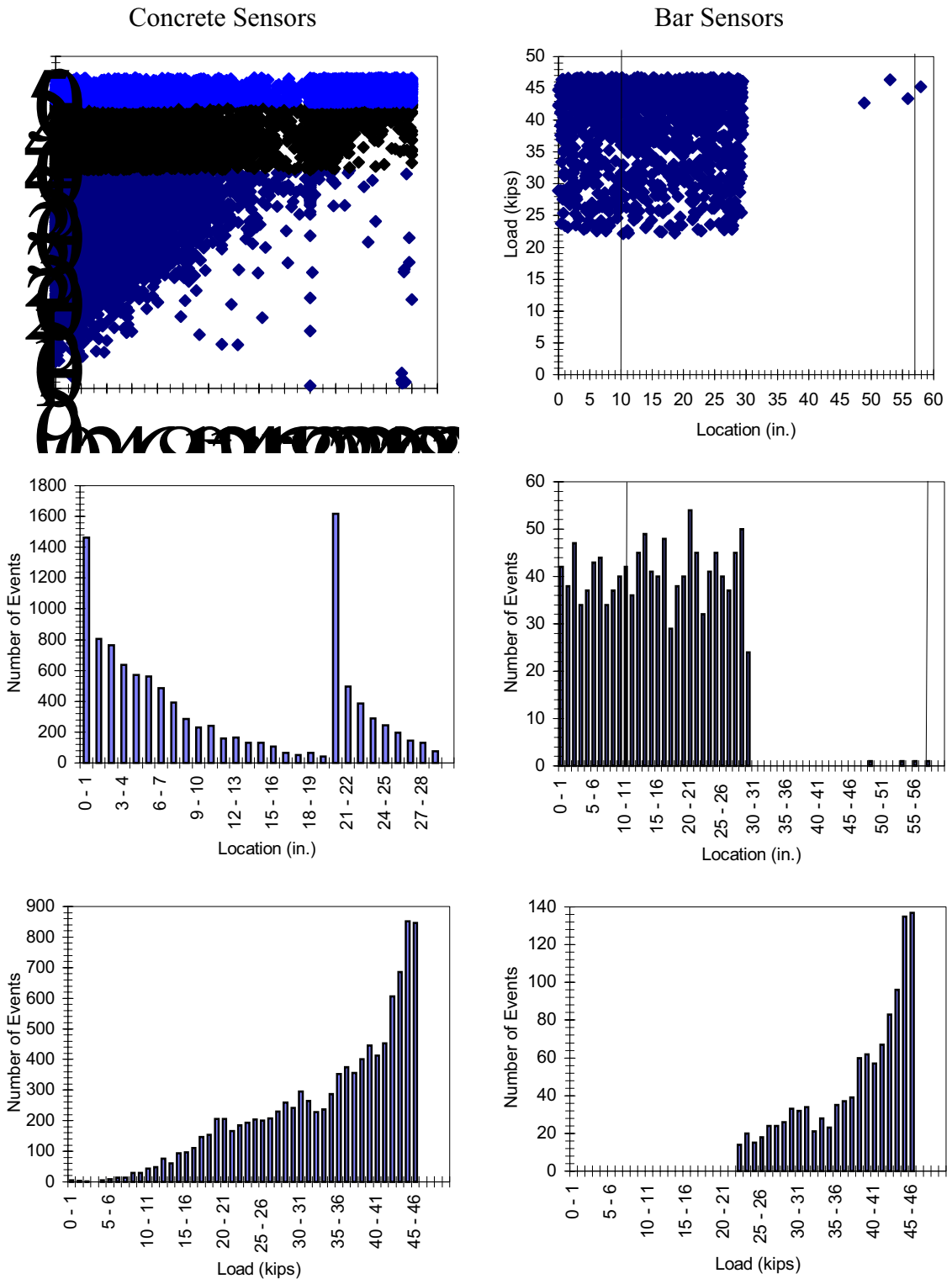

Figure F.53 2M2-6-2-47.0-2

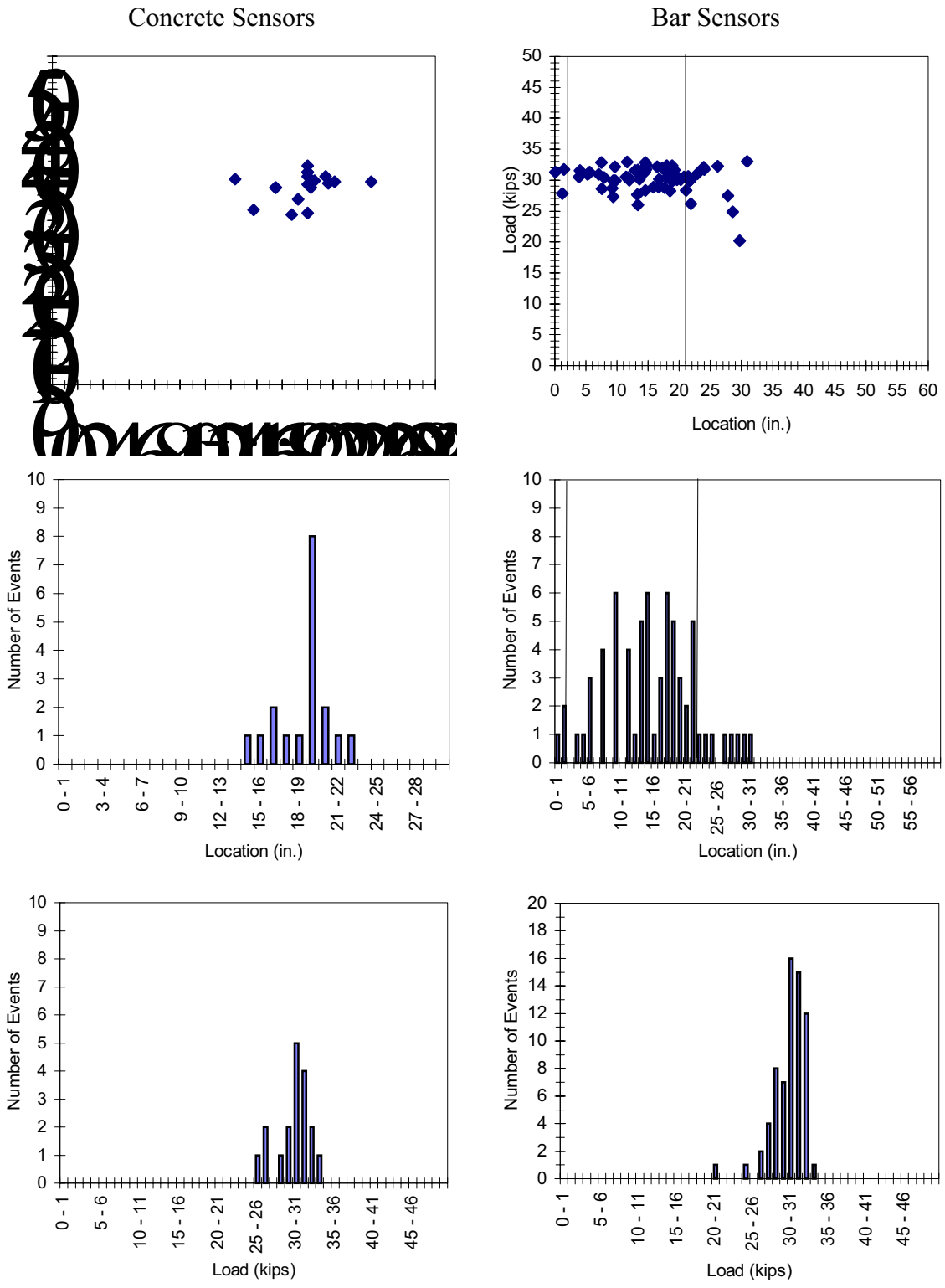

Figure F.54 2M2-6-2-47.0-3

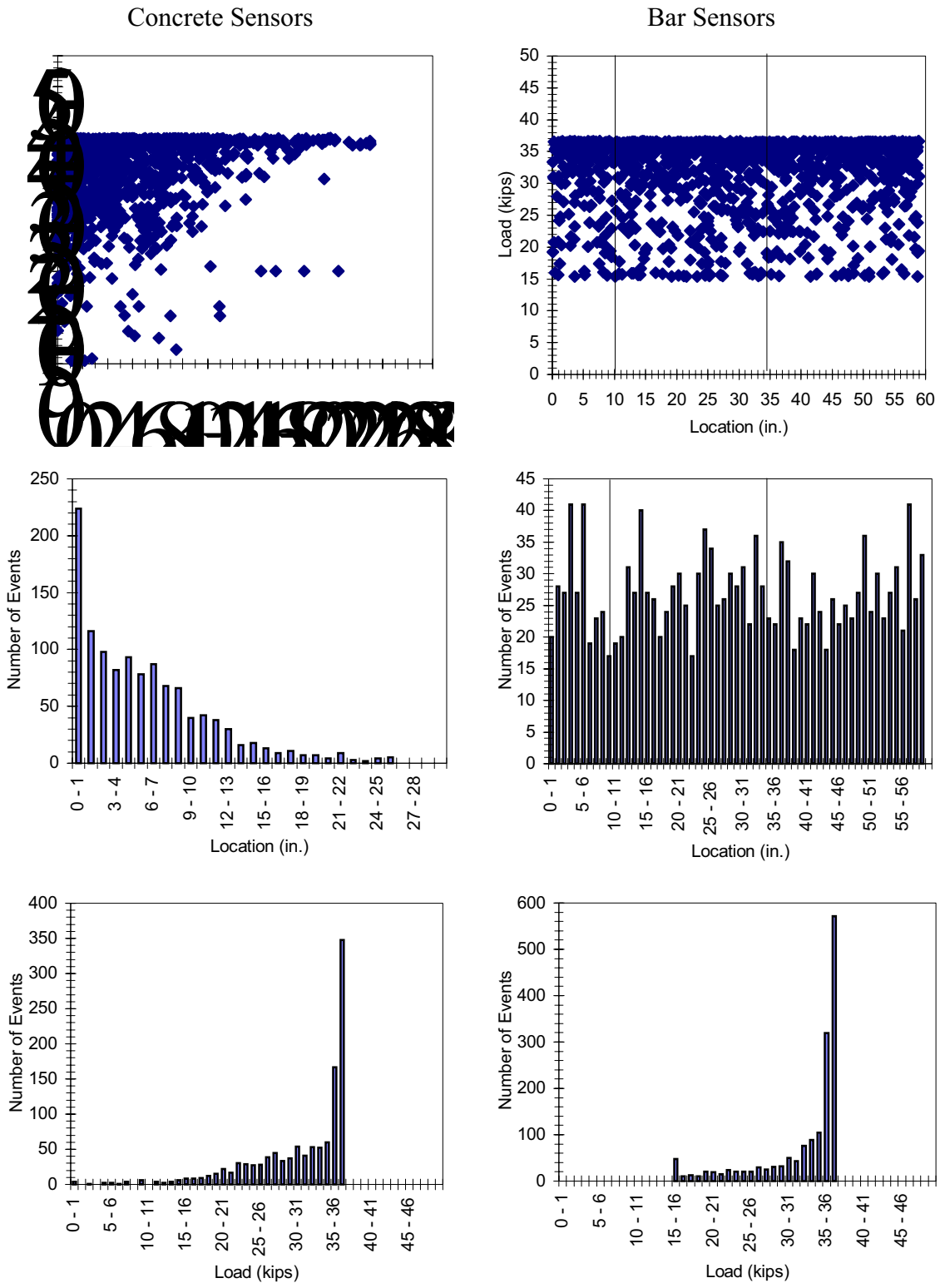

Figure F.55 2M2-6-2-25.0-1

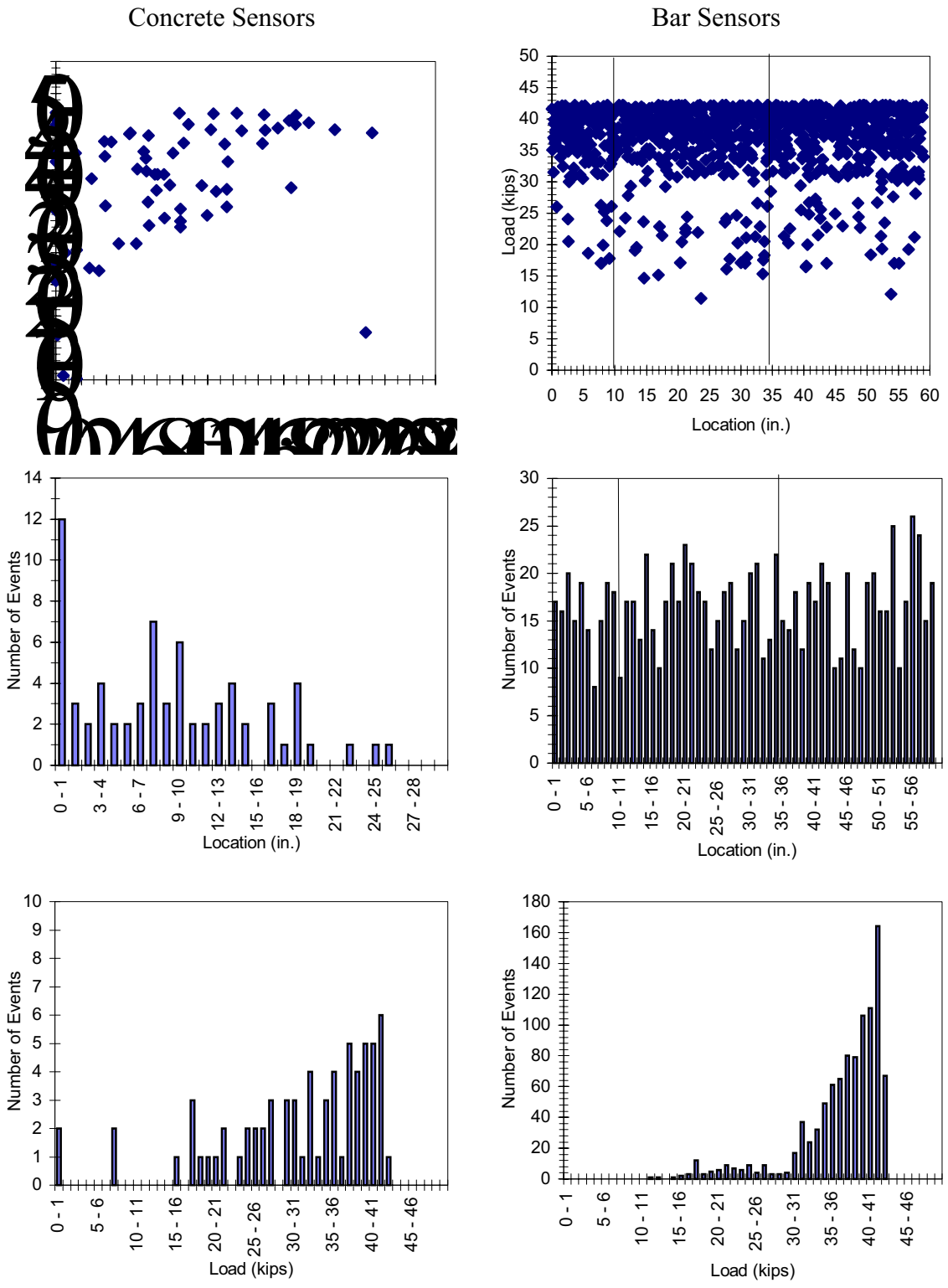

Figure F.56 2M2-6-2-25.0-2

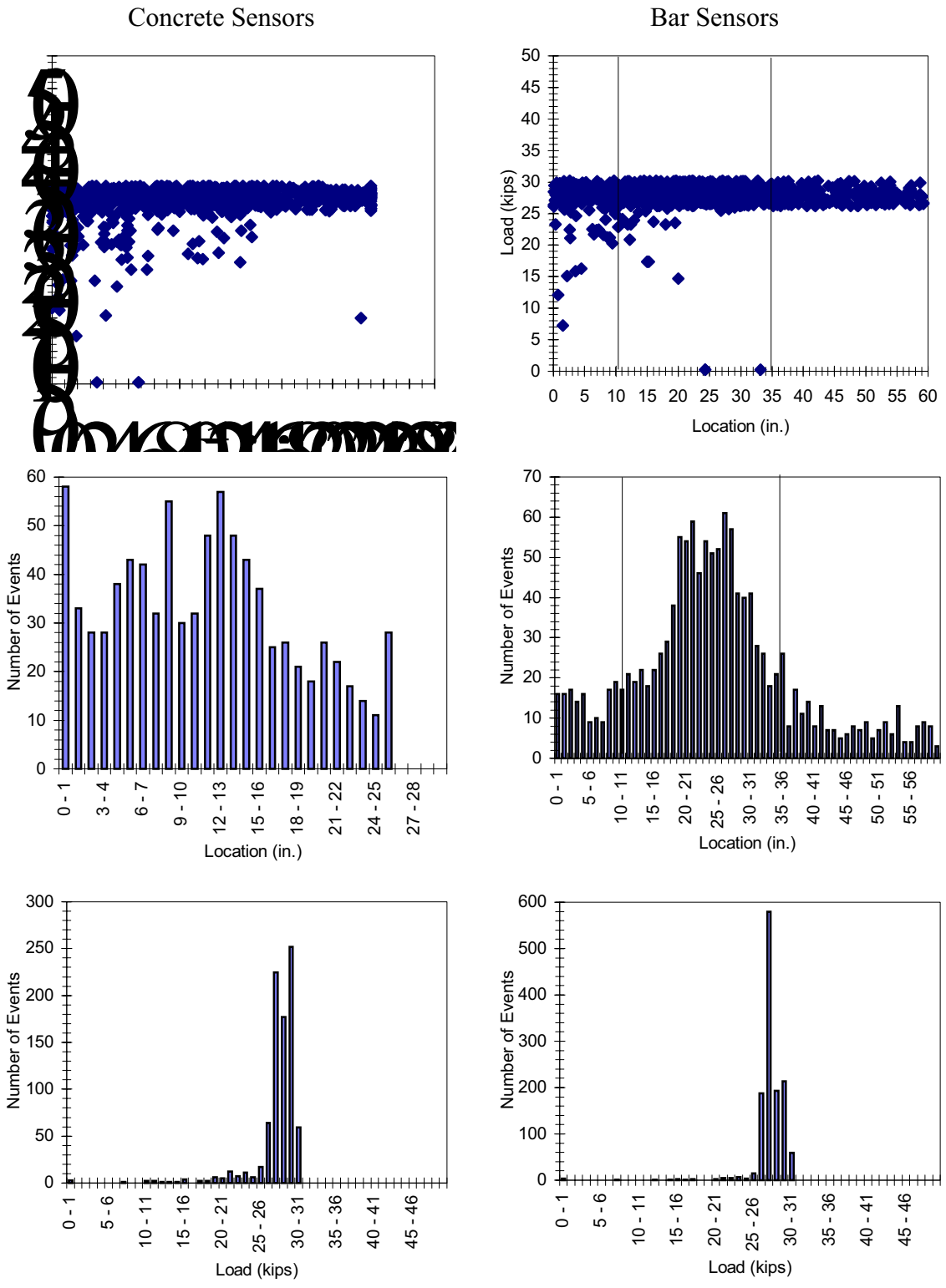

Figure F.57 2M2-6-2-25.0-3

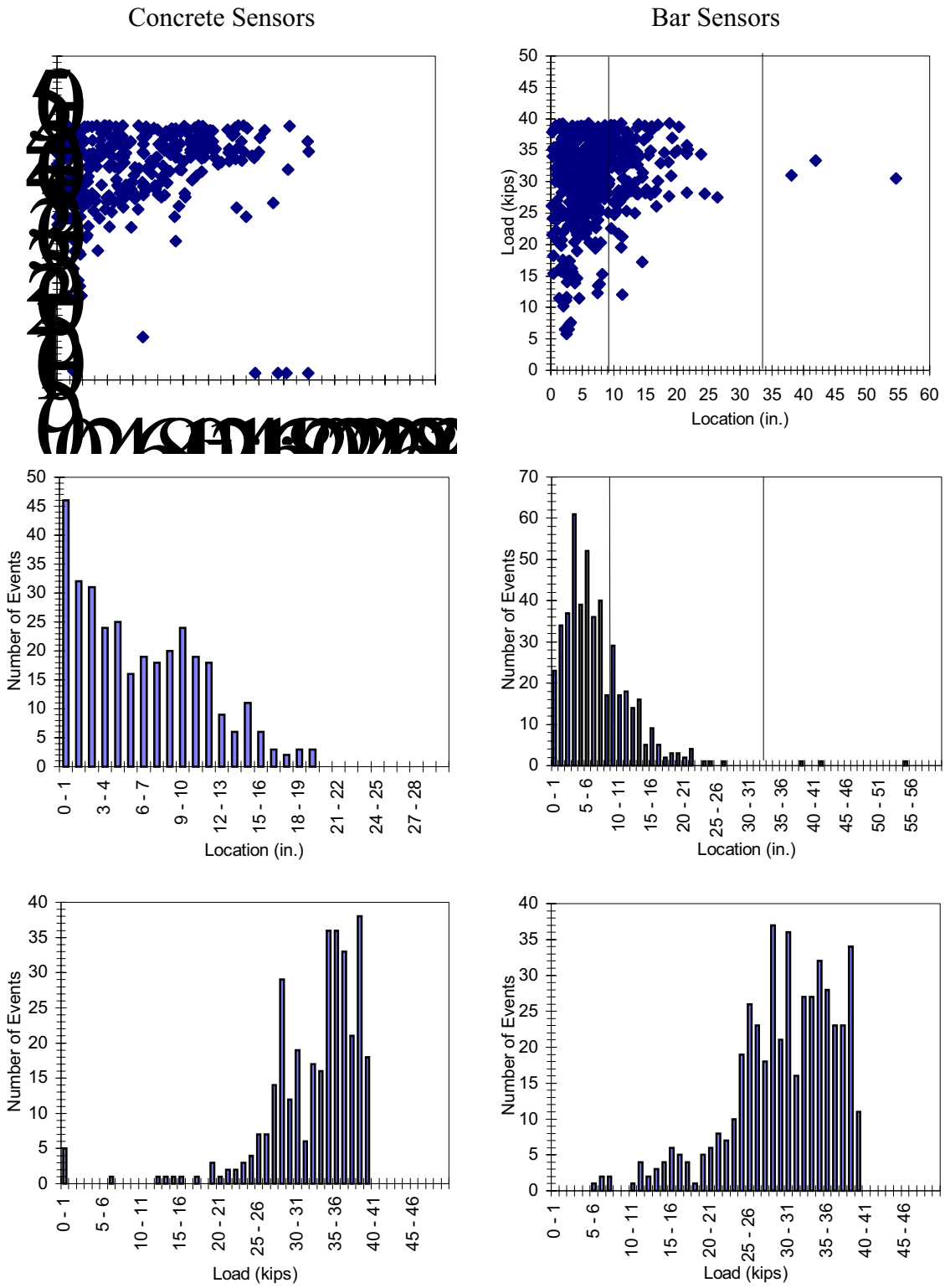

Figure F.58 2M2-6-2-25.0-4

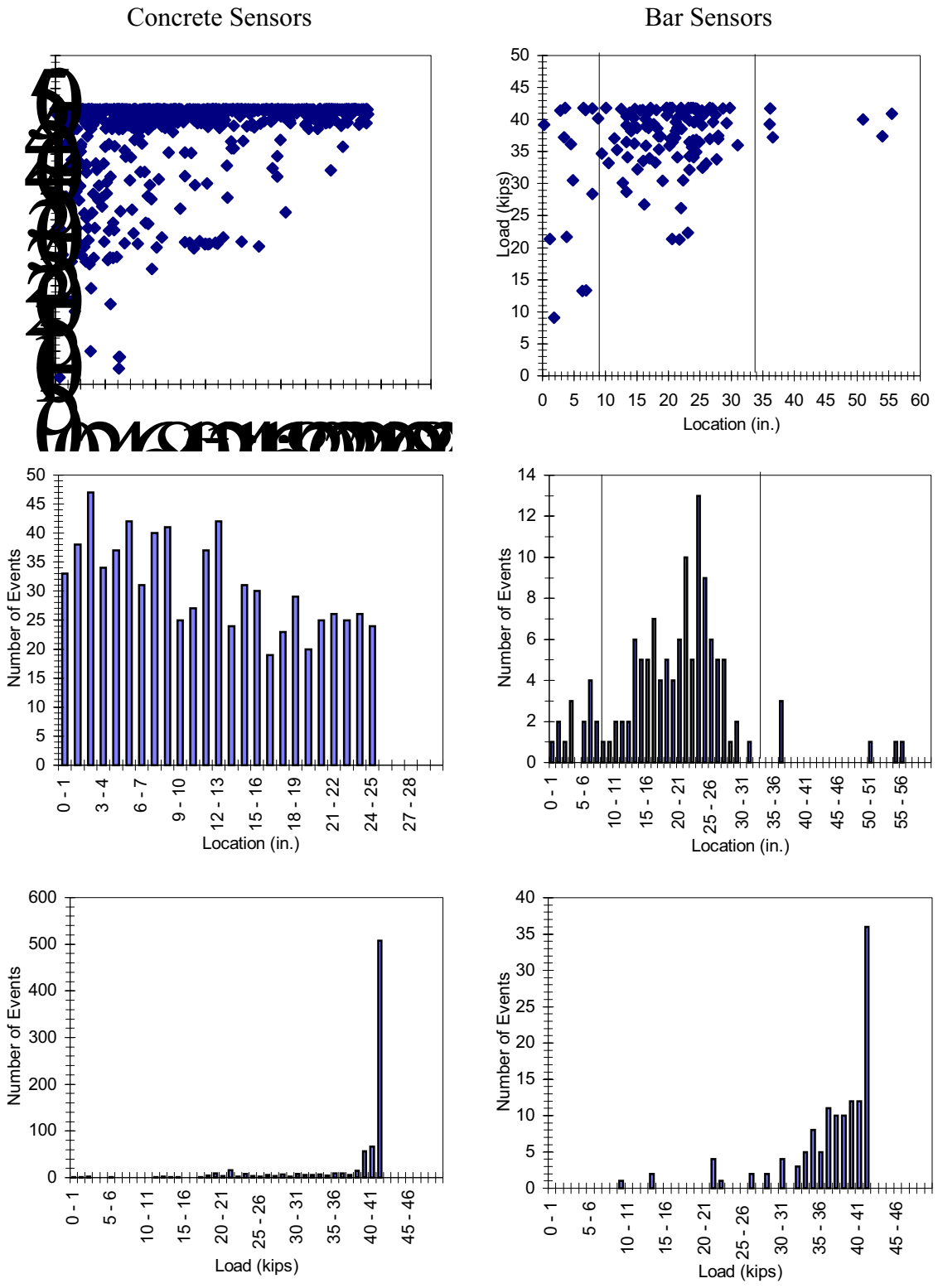

Figure F.59 2M2-6-2-25.0-5

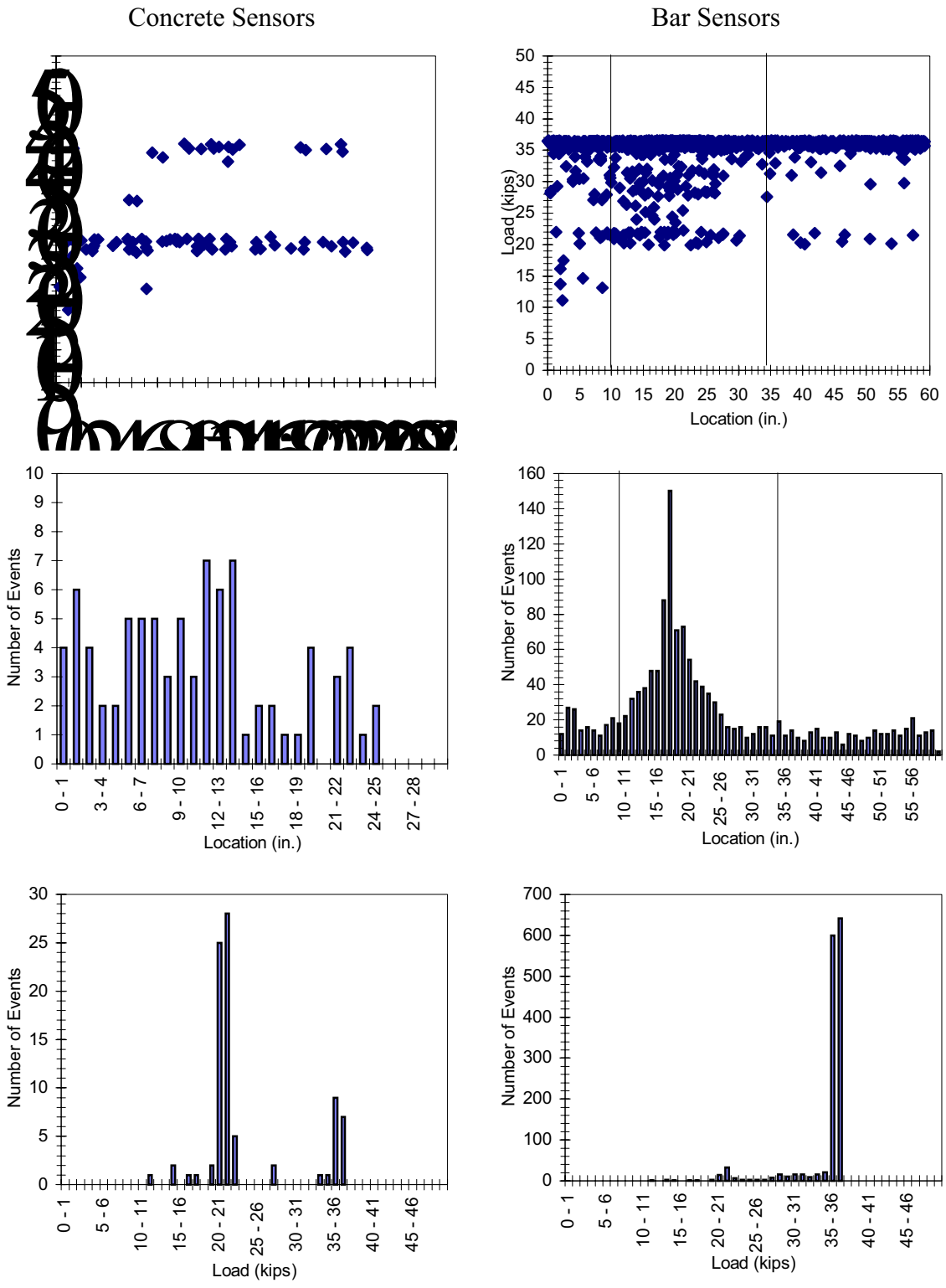

Figure F.60 2M2-6-2-25.0-6

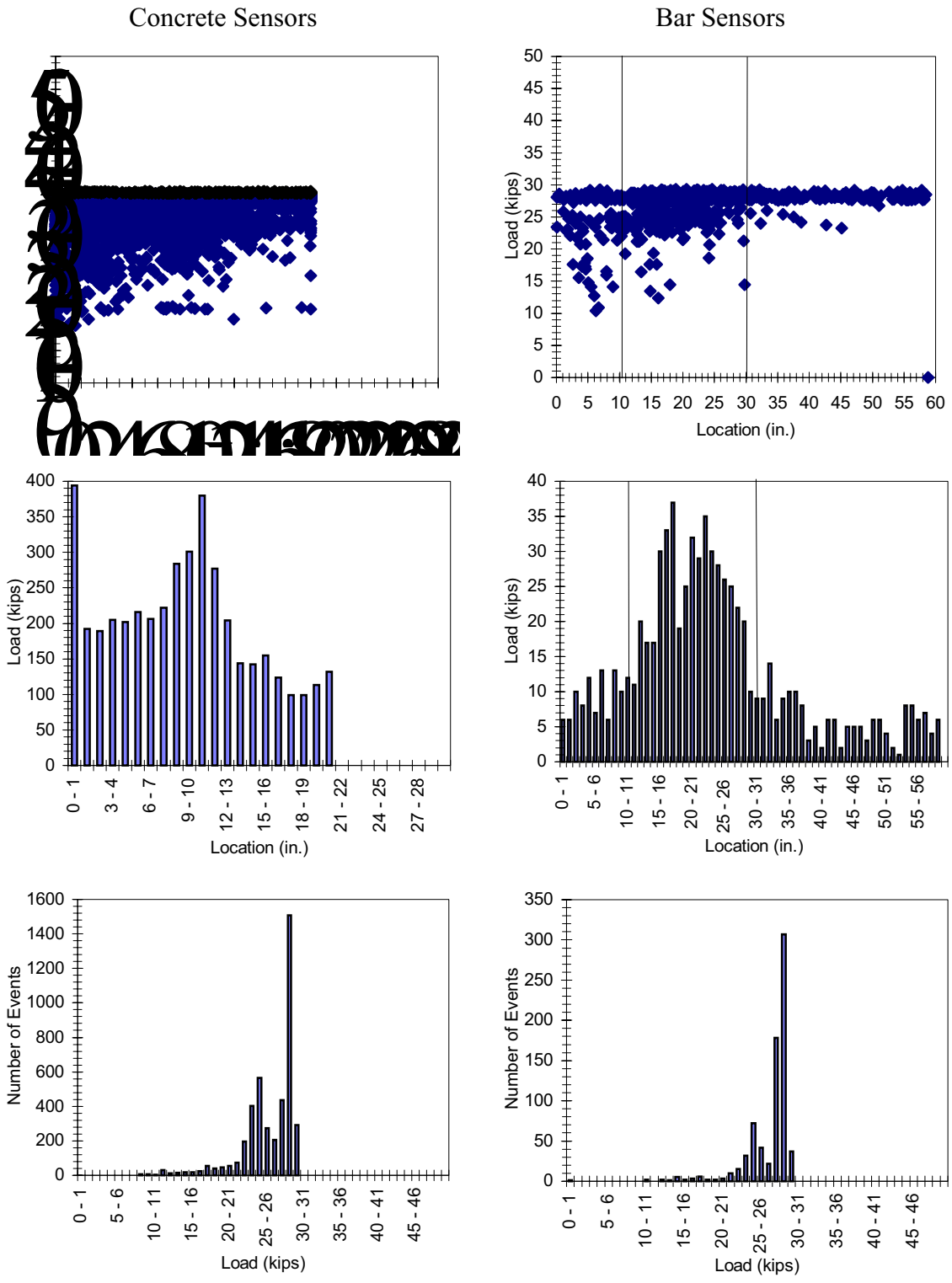

Figure F.61 2M2-6-2-20.0-1

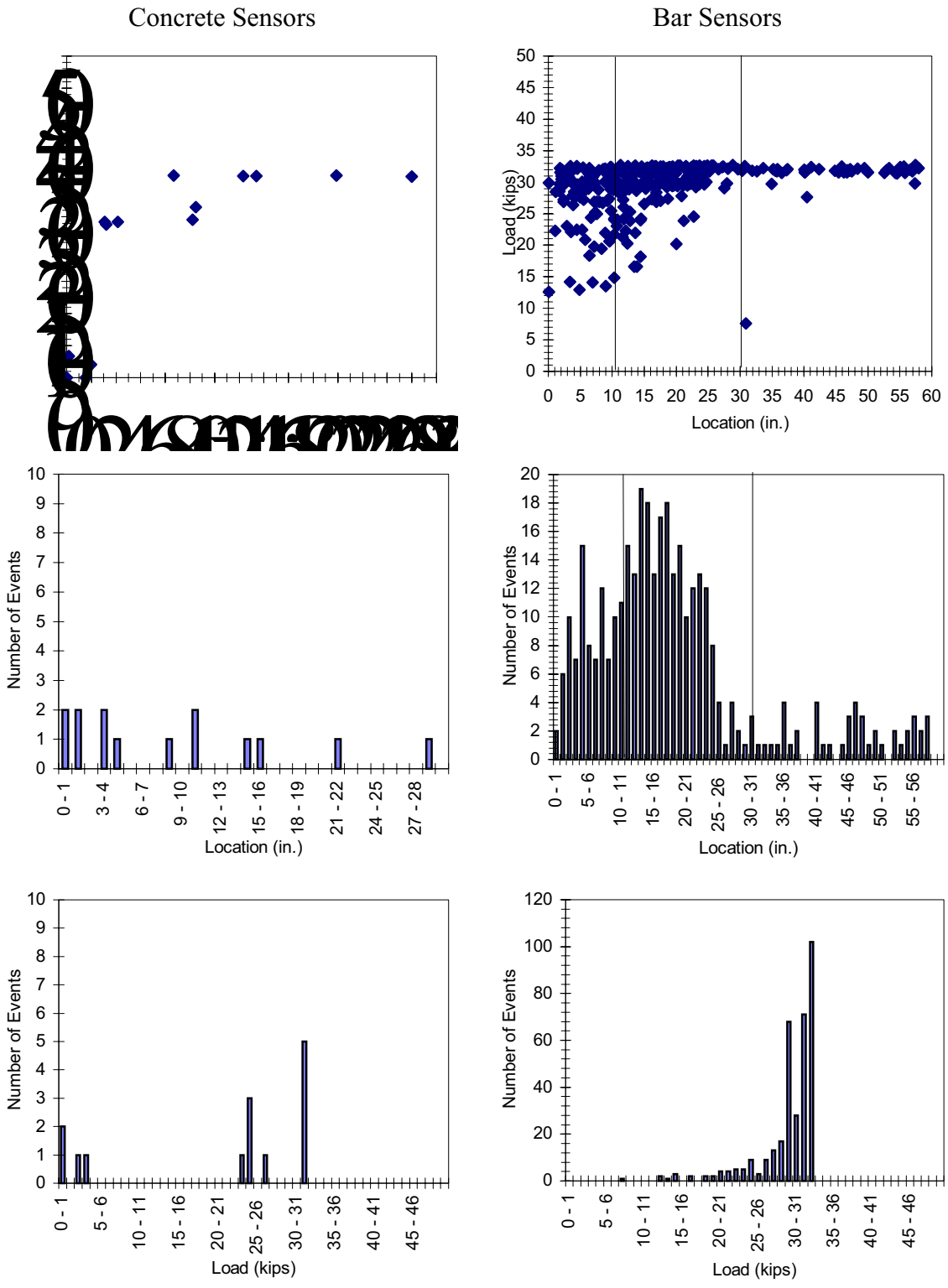

Figure F.62 2M2-6-2-20.0-2

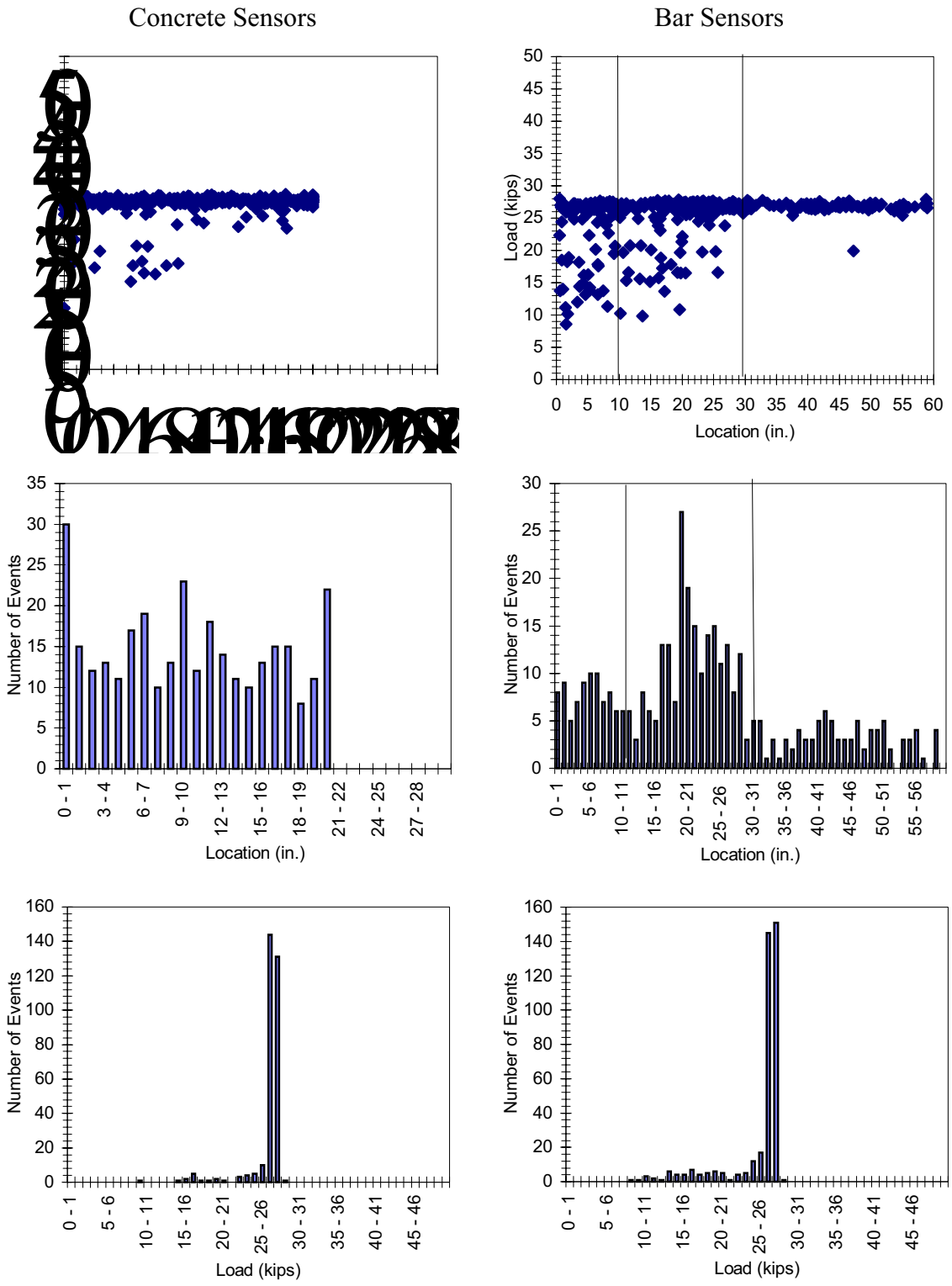

Figure F.63 2M2-6-2-20.0-3

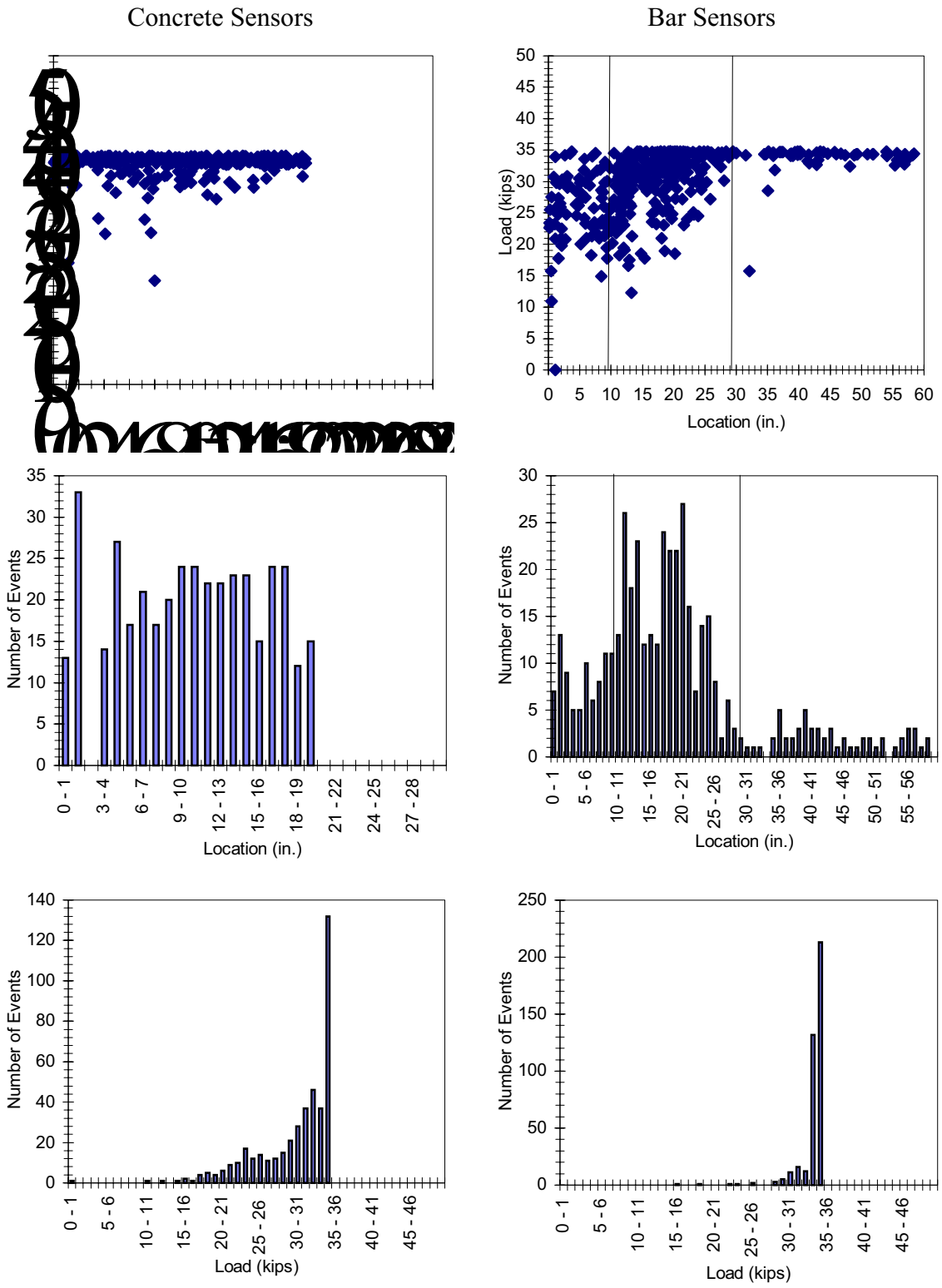

Figure F.64 2M2-6-2-20.0-4

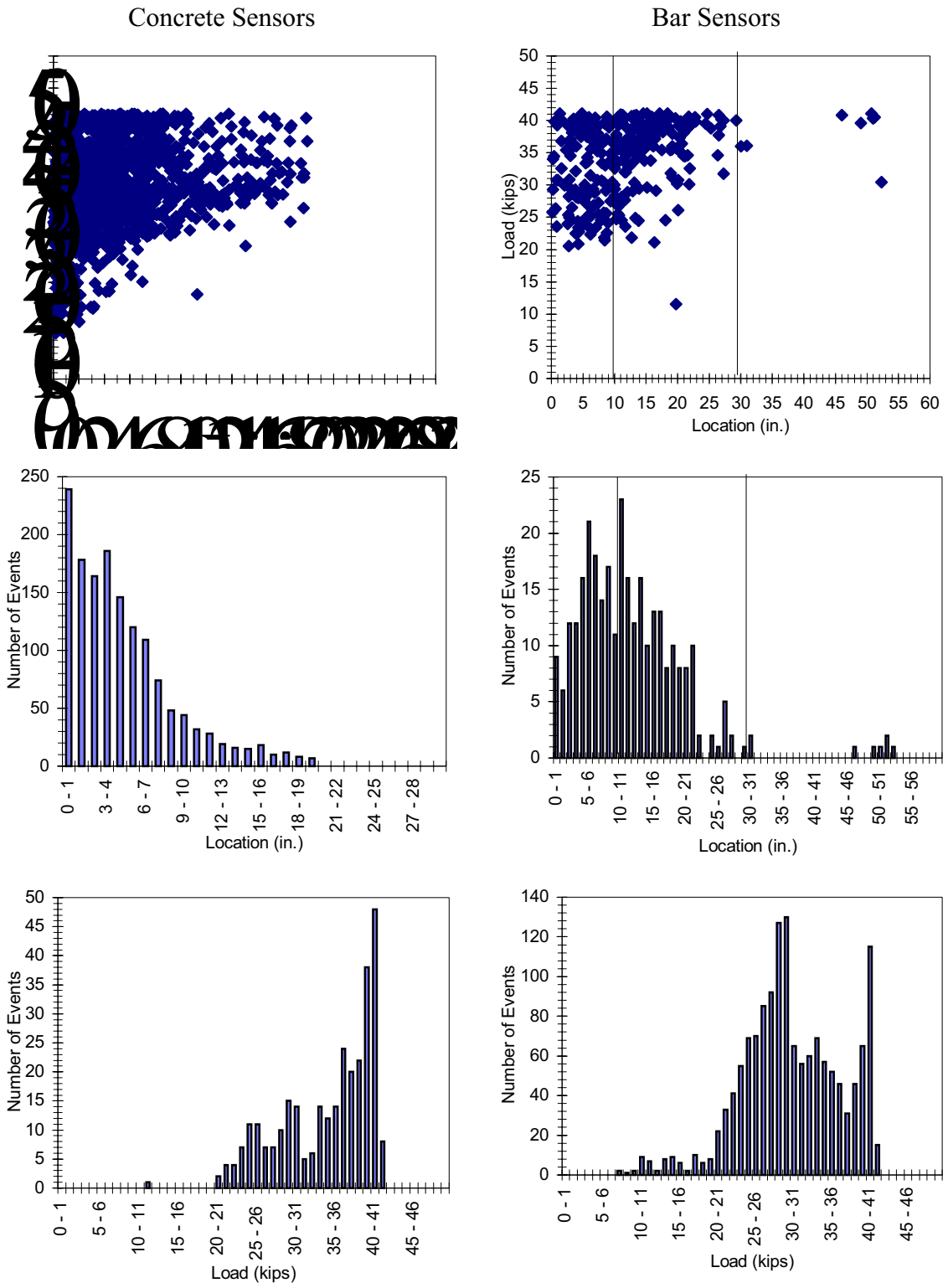

Figure F.65 2M2-6-2-20.0-5

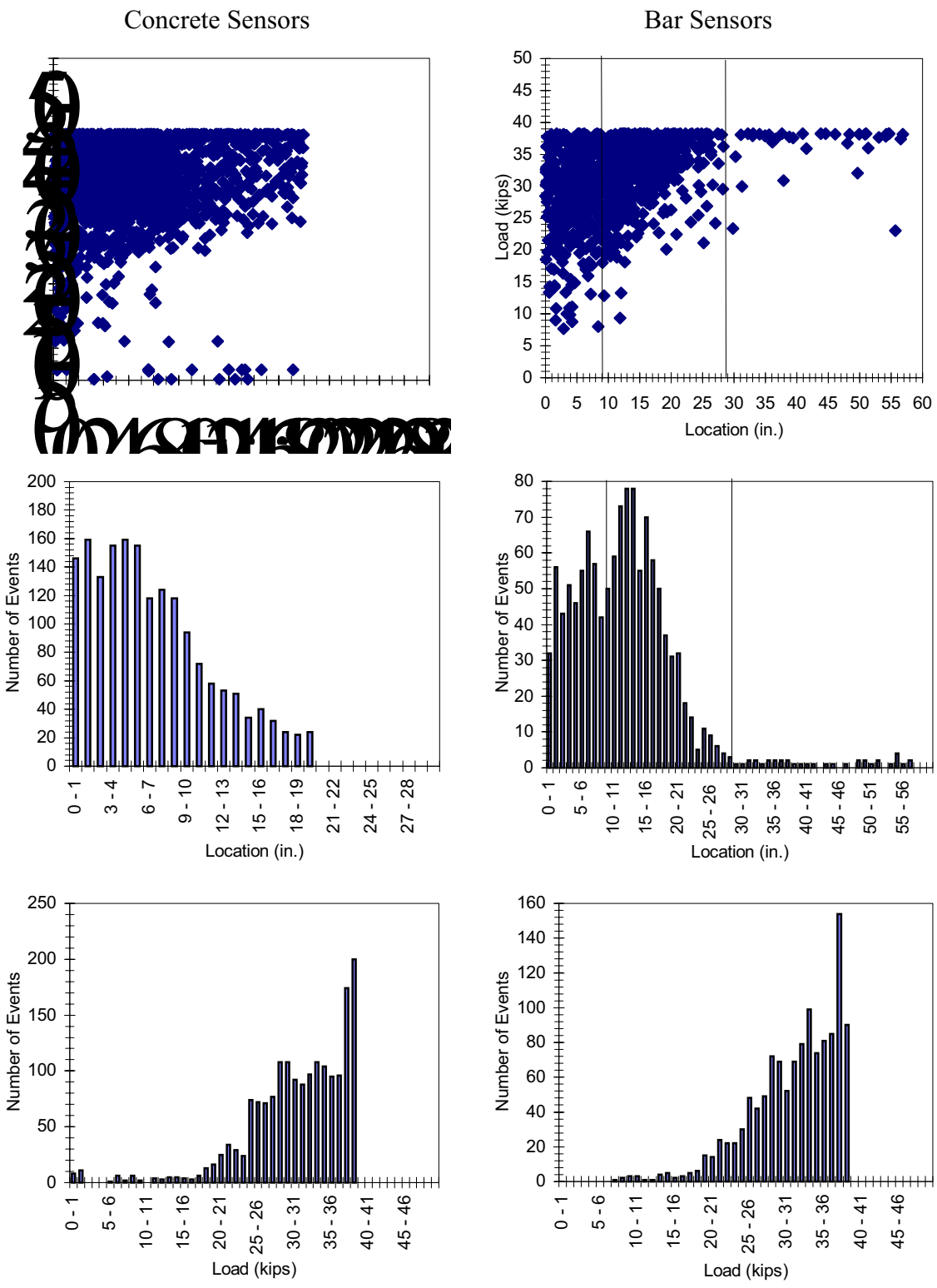

Figure F.66 2M2-6-2-20.0-6

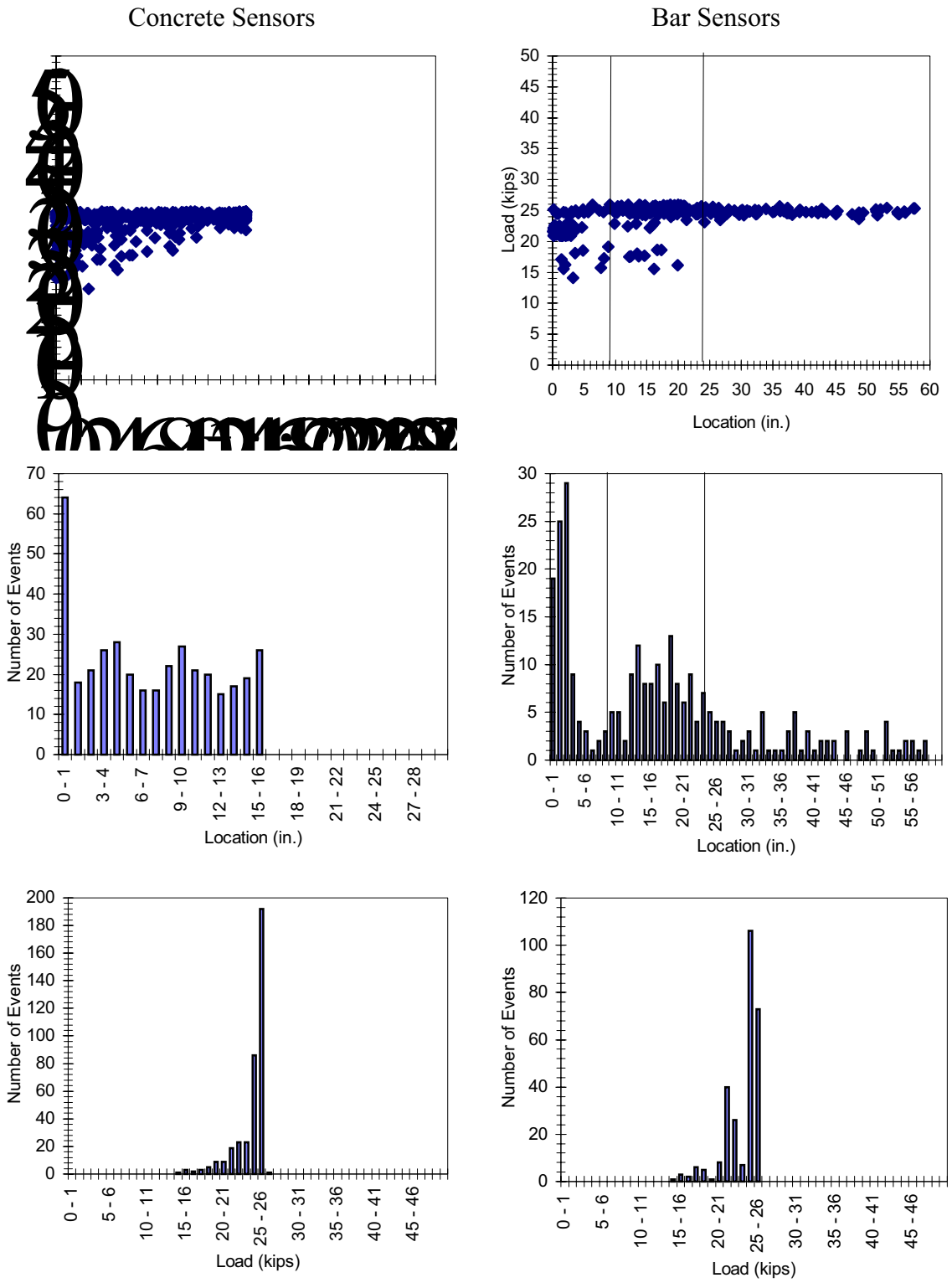

Figure F.67 2M2-6-2-15.0-1

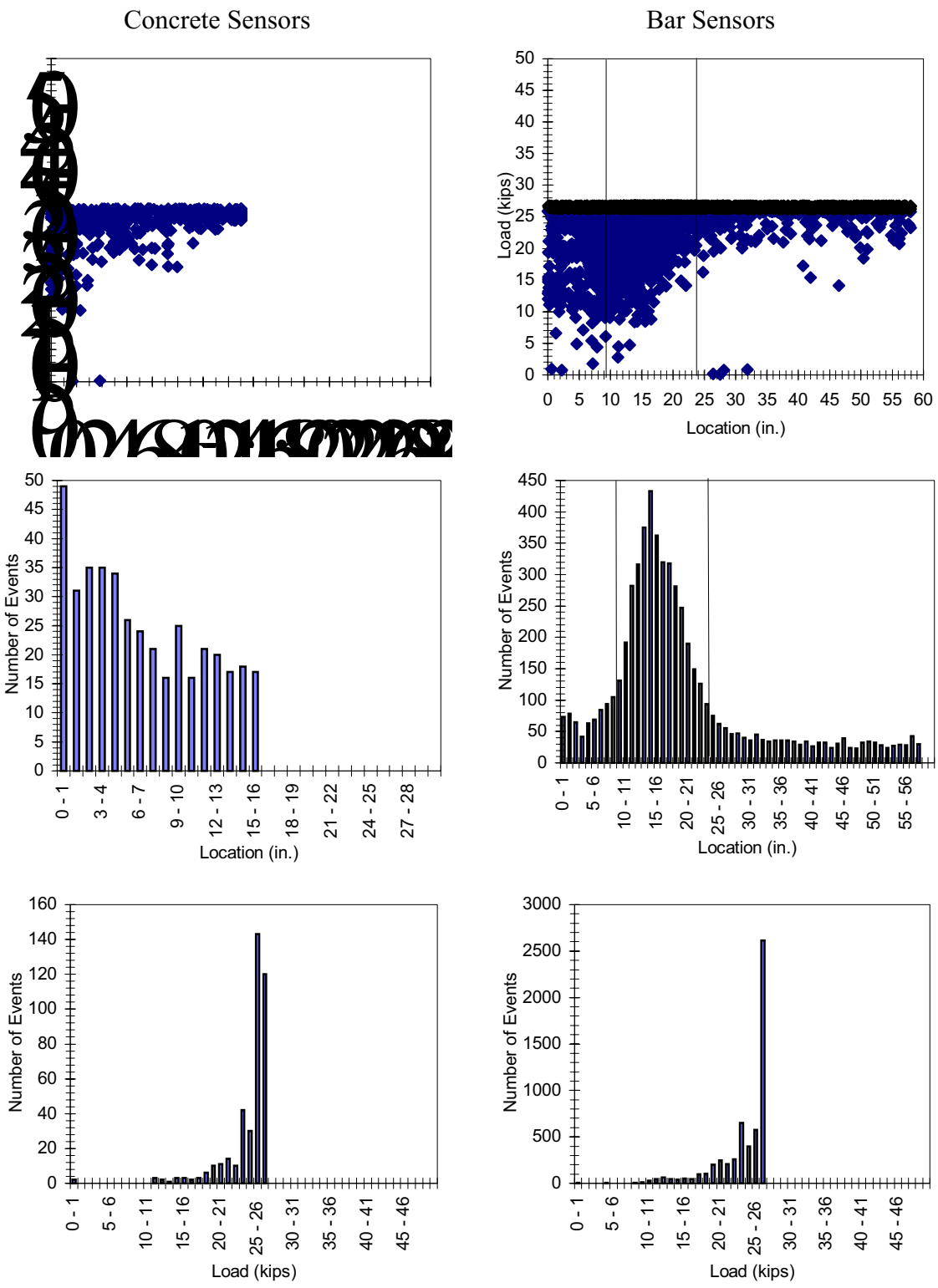

Figure F.68 2M2-6-2-15.0-2

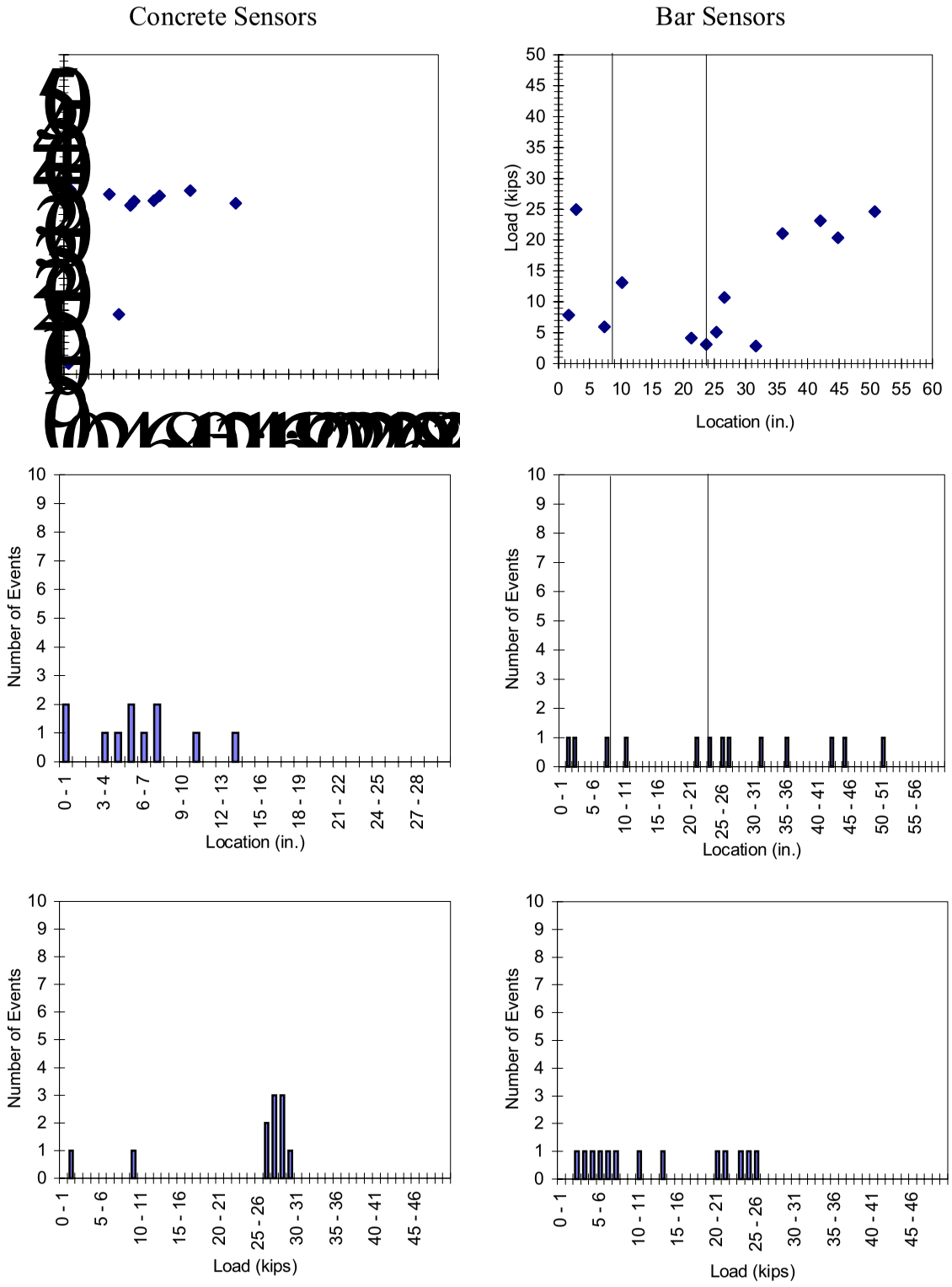

Figure F.69 2M2-6-2-15.0-3

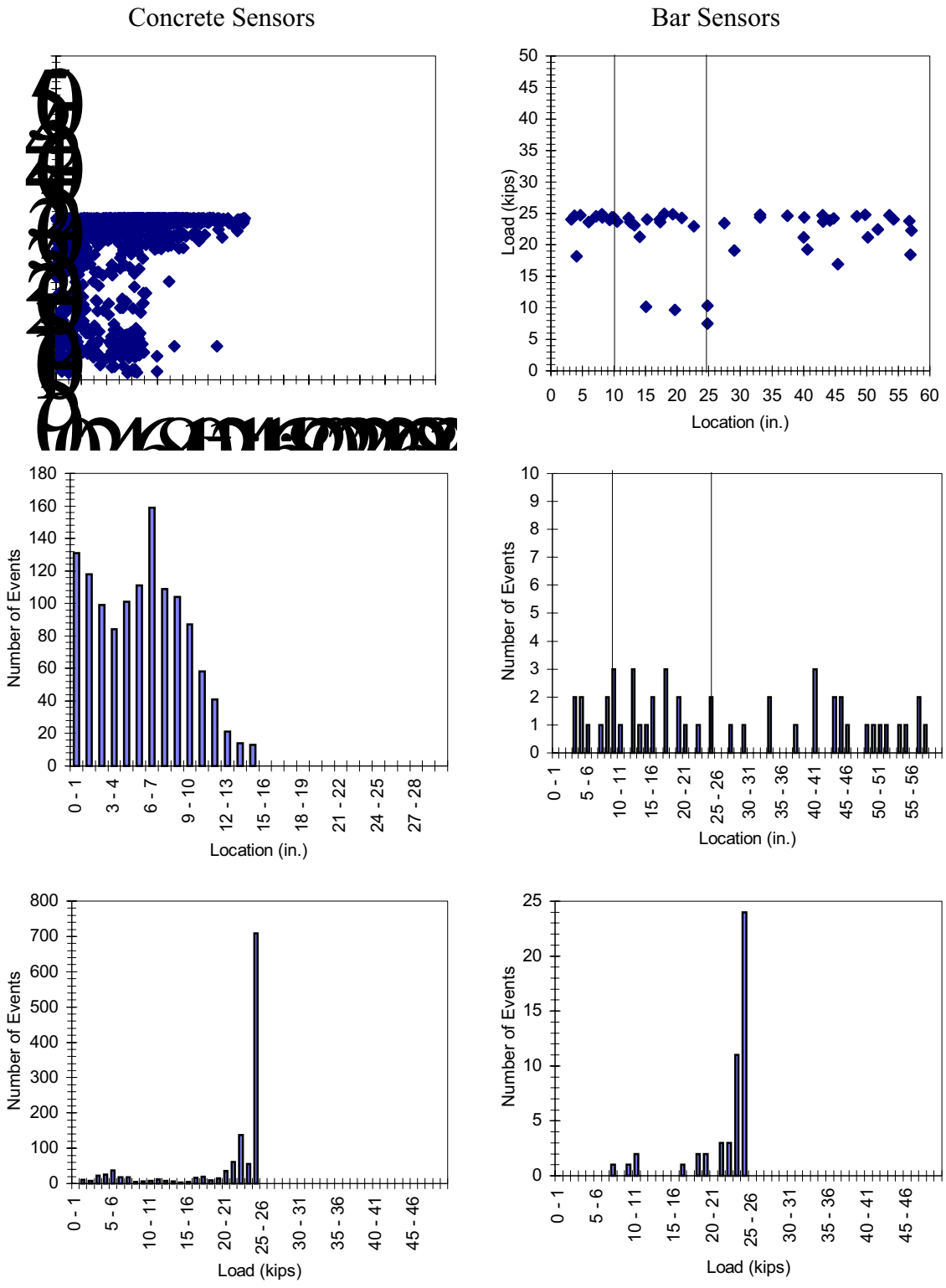

Figure F.70 2M2-6-2-15.0-4

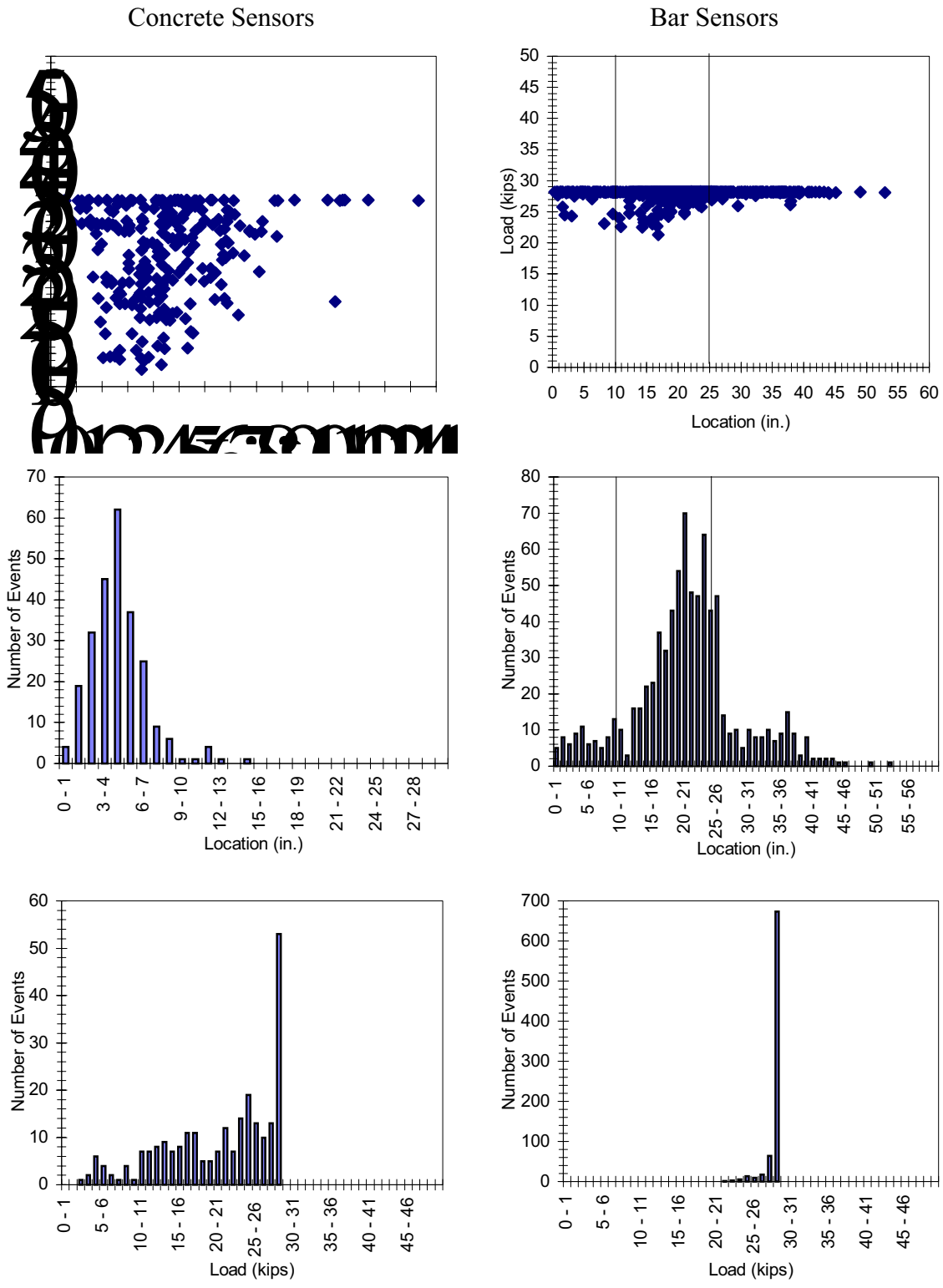

Figure F.71 2M2-6-2-15.0-5

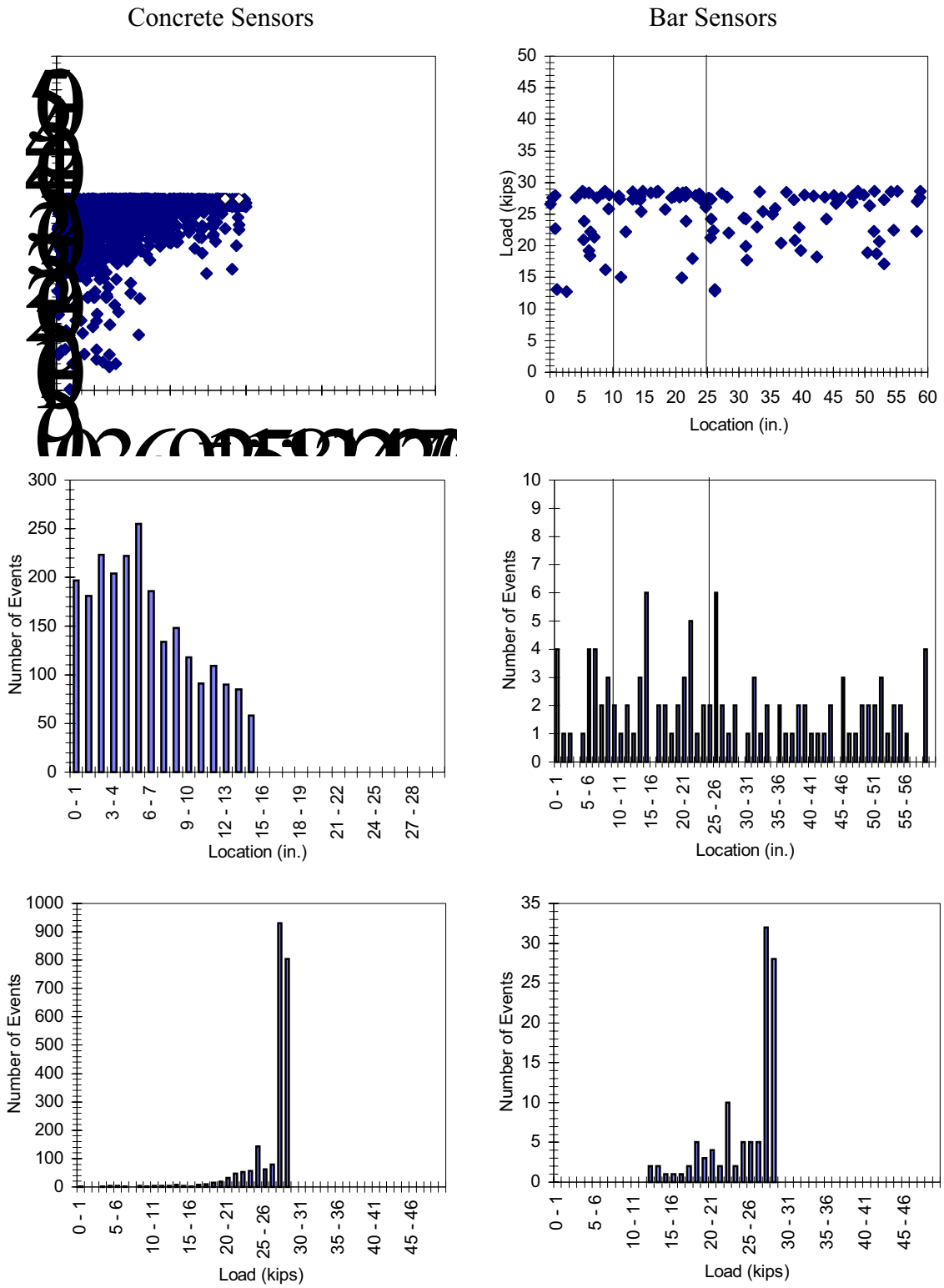

Figure F.72 2M2-6-2-15.0-6